Improved spectroscopic representations of molecules for astronomical studies

Methane and Magnesium Oxide

Kyriaki Kefala

A dissertation submitted in partial fulfillment
of the requirements for the degree of
Doctor of Philosophy
of
University College London.

Department of Physics and Astronomy
University College London

December 20, 2025

I, Kyriaki Kefala, confirm that the work presented in this thesis is my own. Where information has been derived from other sources, I confirm that this has been indicated in the work.

Declaration of Research Publications

This thesis includes research publications that I have authored or co-authored. The following is a complete list of them, categorized on the basis of their relevance to this thesis.

Publications Included in this Thesis

The following papers contain work that is directly incorporated into this thesis:

- McKemmish, L. K., Bowesman, C. A., Kefala, K., Perri, A. N., Syme, A. M., Yurchenko, S. N., & Tennyson, J. (2024). A hybrid approach to generating diatomic line lists for high resolution studies of exoplanets and other hot astronomical objects: updates to ExoMol MgO, TiO, and VO line lists. RAS Techniques and Instruments, 3(1), 565-583 [1]. The relevant chapters are 3 and 4

- Kefala, K., Boudon, V., Yurchenko, S. N., & Tennyson, J. (2024). Empirical rovibrational energy levels for methane. Journal of Quantitative Spectroscopy and Radiative Transfer, 316, 108897 [2]. The relevant chapters are 5 and 6.

- Yurchenko, S. N., Owens, A., Kefala, K., & Tennyson, J. (2024). ExoMol line lists–LVII. High accuracy ro-vibrational line list for methane (CH_4). Monthly Notices of the Royal Astronomical Society, 528(2), 3719-3729 [3]. The relevant chapters are 5 and 6.

Additional Publications

The following papers have been co-authored by me but are not directly included in this thesis:

- Tennyson, J., Yurchenko, S. N., Zhang, J., Bowesman, C. A., Brady, R. P., Buldyreva, J., Chubb, K. L., Gamache, R. R., Gorman, M. N., Guest, E. R., Hill, C., Kefala, K., Lynas-Gray, A. E., Mellor, T. M., McKemmish, L. K., Mitev, G. B., Mizus, I. I., Owens, A., Peng, Z., Perri, A. N., Pezzella, M.,

Polyansky, O. L., Qu, Q., Semenov, M., Smola, O., Solokov, A., Somogyi, W., Upadhyay, A., Wright, S. O. M., & Zobov, N. F. (2024). The 2024 release of the ExoMol database: molecular line lists for exoplanet and other hot atmospheres. Journal of Quantitative Spectroscopy and Radiative Transfer, 326, 109083 [4].

- Yurchenko, S. N., Bowesman, C. A., Brady, R. P., Guest, E. R., Kefala, K., Mitev, G. B., Owens, A., Perri, A. N., Pezzella, M., Smola, O., Solokov, A., Zhang, J., & Tennyson, J. (2024). ExoMol line lists–LX. Molecular line list for the ammonia isotopologue $^{15}NH_3$. Monthly Notices of the Royal Astronomical Society, 533(3), 3442-3456 [5].

The work presented in this thesis is my own, except where due acknowledgment is made.

Abstract

This work is conducted within the framework of the ExoMol project, which provides molecular line lists for species of astrophysical interest. With the growing application of high-resolution Doppler spectroscopy and cross-correlation techniques, there is an increasing demand for line lists with enhanced spectroscopic accuracy. To meet this need, ExoMol integrates theoretical predictions with empirical spectroscopic data, and improves the accuracy of key molecular parameters.

This thesis mainly focuses on the use of experimental data in order to improve theoretical calculations. The core methodology is the MARVEL (Measured Active Rotational-Vibrational Energy Levels) approach, which constructs self-consistent sets of empirical energy levels from high-resolution experimental spectra, by performing a least-squares fitting procedure.

In this thesis, new MARVEL analyses have been carried out for methane (CH_4) and magnesium oxide (MgO), both of which are of significant interest in atmospheric and astrophysical contexts. For methane, which is a key molecule in planetary atmospheres, a comprehensive compilation of high-resolution experimental data was processed to yield a complete and accurate set of empirical rovibrational levels. Similarly, for MgO, which is relevant especially for terrestrial environments, a full MARVEL treatment was performed for the first time. Additionally, this work includes an updated MARVEL analysis for titanium monoxide (TiO), a molecule of great importance in the spectra of exoplanets.

Finally, this thesis introduces a systematic procedure to assign quantum numbers to previously unassigned or partially assigned experimental methane transitions

drawn from the literature. Using the ExoMol MM line list as a reference, newly assigned transitions were incorporated into the MARVEL framework, enabling the derivation of additional empirical energy levels. This iterative process leads to further improvements in the accuracy and completeness of the methane spectroscopic model, advancing the quality of data available for high-resolution spectroscopic applications.

Impact statement

This thesis contributes to the field of molecular spectroscopy through the refinement of high-resolution molecular line lists, for the molecules methane (CH_4), magnesium oxide (MgO), and titanium oxide (TiO). These species play vital roles in the characterisation of planetary and exoplanetary atmospheres, substellar objects, and in the interpretation of remote sensing data across the solar system and beyond. High-quality line lists are essential for the reliable retrieval of molecular abundances, temperature profiles, and atmospheric compositions of exoplanets. A central theme of this work is the extensive use of experimental data to refine variational calculations, improving the accuracy and reliability of the resulting spectroscopic models.

For all three studied molecules, experimentally derived energy levels were incorporated through the MARVEL (Measured Active Rotational-Vibrational Energy Levels) procedure to enhance the spectroscopic accuracy of the line lists. This approach allows line positions to reach accuracies suitable for high-resolution applications ($R \geq 100,000$), ensuring reliable interpretation of observational data.

Magnesium oxide is expected to form in the high-temperature atmospheres of rocky exoplanets. This work improves the spectroscopic precision of existing ExoMol data to enable future detections of MgO, which may serve as a tracer of the atmospheric composition of ultra-hot super-Earths, commonly known as lava worlds.

Titanium oxide is a very significant molecule for understanding the thermal structures of M-dwarfs and hot Jupiters, among various other astronomical environments. It contributes to high-altitude optical opacity, strongly absorbing stellar radiation and leading to the heating of the upper atmosphere. This may induce thermal inversions in exoplanet atmospheres. The update of the Toto line list for TiO will hopefully enable more precise spectral modelling of such atmospheres and help understand the dynamics of hot exoplanets.

Methane, which is the primary molecule studied in this thesis, is one of the key

absorbers in the atmospheres of exoplanets and cool stars, and it is important for the study and classification of brown dwarfs. Improving the accuracy of spectroscopic data for methane helps refine models of atmospheric chemistry and potential biosignatures.

In addition, it is a species vital for climate change science, as it is a potent greenhouse gas with significant impact on Earth's climate. The improvement of the methane line list may help enhance the precision of satellite-based retrieval algorithms, which rely on detailed spectroscopic data, and better constrain the methane abundances in our planet's atmosphere.

An iterative strategy is proposed in this thesis to improve methane spectroscopy by systematically extending accurate energy level coverage to higher vibrational states.

Acknowledgements

I would like to express my gratitude to my supervisor, Professor Jonathan Tennyson, for his enthusiasm, patience, and guidance throughout the years. It has been an honour working with him. I am also sincerely thankful to my co-supervisor, Professor Sergey Yurchenko, whose insight and contagious passion for science made this project all the more enjoyable.

I would like to thank Dr. Tibor Furtenbacher and Professor Atilla G. Császár for their valuable contribution through MARVEL which was a vital part of this thesis.

My heartfelt thanks go to my colleagues and friends in the ExoMol group for making my Ph.D. journey such a memorable and rewarding experience. Thank you to Dr. Tony Lynas Gray, Dr. Oleg Polyansky, Dr. Apoorva Upadhyay, Dr. Charles Bowesman, Dr. Georgi Mitev, Dr. Mike Semenov, Elizabeth Guest, Dr. Jingxin Zhang, Armando Perri, Dr. Marco Pezzela, Qinghe Ni, Dr. Ryan Brady, Alex Smola, Dr. Alec Owens, Dr. Andrei Sokolov. I also thank my family, partner, and friends for their encouragement and support. Special thanks to Savvas, Alexis, Kyriaki, Aggelos.

This work was supported by the European Research Council (ERC), whose financial support is gratefully acknowledged.

Contents

1 Introduction **25**

1.1 Molecular Spectroscopy 25

1.1.1 The Born-Oppenheimer approximation 29

1.1.2 Rotational motion 32

1.1.3 Vibrational motion 36

1.1.4 Ro-vibrational motion 39

1.1.5 Selection Rules 40

1.1.6 Rotational Transitions 41

1.1.7 Electronic Transitions 41

1.1.8 Vibrational Transitions 46

1.1.9 Raman Selection Rules 47

1.2 Spectroscopy of Exoplanets 48

1.2.1 Transit spectroscopy 54

1.2.2 High-Resolution Doppler Spectroscopy 58

1.2.3 Direct Imaging 61

2 ExoMol **63**

2.1 Data provided 64

2.2 Methodology 68
2.2.1 Nuclear Motion Calculations 69
2.2.2 Hybridisation of the Line Lists 70
2.2.3 MARVEL 70
2.2.4 Isotopic Extrapolation 74
2.2.5 Predicted Shifts 75

3 Magnesium Oxide **76**

3.1 Motivation 76
3.2 Quantum numbers and selection rules 77
3.3 A new MgO MARVEL analysis 78
3.4 Overview of experimental sources 80
3.5 Uncertainties 84
3.6 Predicted shift energy levels 85
3.7 Isotopologue-extrapolation energy levels 88
3.8 Outlook 91

4 Titanium Oxide **96**

4.1 Motivation 96
4.2 Quantum numbers and selection rules 98
4.3 2024 MARVEL update 99
4.4 Uncertainties 105
4.5 Outlook 106

5 MARVEL project on Methane **111**

5.1 Motivation 111

5.2 Quantum numbers and selection rules 115

5.3 Overview of Experimental Sources 121

5.4 Raman spectra 137

5.5 Magic numbers 139

5.6 MARVEL energy uncertainties 139

5.7 Reassignment of spectra 140

5.8 The MARVEL network 142

5.9 MARVELous Methane 148

5.10 Outlook 151

6 Assignment of methane spectra **153**

6.1 Methodology 156

6.2 The experimental sources 161

6.3 CH_4 MARVEL update 179

6.4 Outlook 186

7 General Conclusions **192**

Bibliography **197**

List of Figures

1.1 Schematic energy level diagram illustrating the combination difference (CD) method. Observed transitions $\tilde{\nu}_{ik}$ and $\tilde{\nu}_{jk}$ share a common level E_k. The difference of the two observed wavenumbers equals the energy separation between E_i and E_j expressed in wavenumber units. 27

1.2 Comparison of the harmonic (dashed red) and Morse (solid blue) potential curves. The vibrational energy levels for both potentials are indicated by horizontal lines. For the Morse potential, the energy levels are labelled on the right, with quantum numbers $v = 0, 1, 2, \ldots$ showing the anharmonic nature of the potential as the levels become progressively closer together at higher energies. The dissociation energy of the molecule is marked by a grey dashed line. 39

1.3 Simplified illustration of rotational energy levels and transitions for two vibrational states of a diatomic molecule. The plot shows rotational energy levels for the ground (v=0, green lines) and first excited (v=1, red lines) vibrational states. Arrows represent transitions between rotational levels, with the P, Q, and R branches in blue, yellow, and pink, respectively. 42

1.4 Franck–Condon principle: Electronic transitions occur vertically between vibrational levels. Δ_{FC} indicates the displacement between equilibrium positions. Figure credit: [6]. 45

1.5 Morse potential energy curve for a diatomic molecule illustrating vibrational energy levels and types of scattered radiation observed in Raman spectroscopy. Green arrow: Rayleigh scattering (elastic); red arrow: Stokes Raman scattering (energy transferred to the molecule); blue arrow: anti-Stokes Raman scattering (energy transferred from the molecule). Figure credit:[7] 47

1.6 Plot of exoplanet mass versus orbital period for confirmed detected exoplanets. The mass is given as a projected value along the line of sight, where M is the planet's mass and i is the orbital inclination angle. The orbital period is shown in days. The different markers and colours indicate the detection methods for every planet. The magenta lettered circled points correspond to the planets of our Solar System. Figure is from the NASA Exoplanet Archive (exoplanetarchive.ipac.caltech.edu) 50

3.1 The MARVEL (Ma) energy uncertainties for $^{24}Mg^{16}O$ as a function of energy. 79

3.2 The predicted shifts (updated- calculated energy) for the X $^1\Sigma^+$, $v = 1$ state of X $^1\Sigma^+$ as a function of the $J(J+1)$ quantum number. The fitting was done using two linear segments. The blue points correspond to real obs. − calc. values and the red to PS. 86

3.3 The updated MARVEL (Ma) and predicted shift (PS) energies for the X $^1\Sigma^+$, A $^1\Pi$, a $^3\Pi$, B $^1\Sigma^+$ electronic states of $^{24}Mg^{16}O$ as a function of the J quantum number. The 'o' symbol indicates f parity and the '+' symbol indicates e parity. 87

3.4 The predicted shifts (updated- calculated energy) for the B $^1\Sigma^+$, $v = 1$ state of B $^1\Sigma^+$ as a function of the $J(J+1)$ quantum number. The blue points correspond to real obs. − calc. values and the red to PS. 88

3.5 The energy distribution for the rovibronic states of $^{24}Mg^{16}O$ as a function of energy source type in each electronic state. 92

3.6 The transition source type for $^{24}Mg^{16}O$, i.e. the cumulative density of transitions as a function of intensity depending on energy source type, computed at 2000 K using the program EXOCROSS [8]. Colours indicate the source type of the transition, defined by the pair of energy-level origins (calculated, MARVEL, or predicted shifts), irrespective of whether a given label refers to the upper or lower level. 93

3.7 The $^{24}Mg^{16}O$ absorption cross section computed at 2000 K using the program EXOCROSS [8] with Gaussian line profiles of 1.0 cm^{-1} half-width half-maximum. The black cross section shows all transitions in the line list with decomposition into dominant electronic bands. 93

3.8 The $^{24}Mg^{16}O$ absorption cross section computed at 2000 K using the program EXOCROSS [8] with Gaussian line profiles of 1.0 cm^{-1} half-width half-maximum. The black cross section shows all transitions in the line list, whereas the orange cross section shows only MARVEL (Ma) experimental transitions (with variational intensities), and the blue cross section shows all possible transitions between MARVEL (Ma) and predicted shift (PS) energy levels (with variational intensities). 94

3.9 The $^{24}Mg^{16}O$ absorption cross section computed at 296 K using the program EXOCROSS [8] with Gaussian line profiles of 1.0 cm^{-1} half-width half-maximum. The black cross section shows all transitions in the line list, whereas the orange cross section shows only MARVEL (Ma) experimental transitions (with variational intensities), and the blue cross section shows all possible transitions between MARVEL (Ma) and predicted shift (PS) energy levels (with variational intensities). 94

4.1 The updated MARVEL (Ma) and predicted shift (PS) energies for the lowest electronic states of $^{48}Ti^{16}O$ as a function of the J quantum number. Blue and magenta points indicate the "Ma" energies of e and f parity, respectively. Green and yellow points indicate the "PS" energies of e and f parity, respectively. 105

4.2 The MARVEL (Ma) energy uncertainties for $^{48}Ti^{16}O$ as a function of energy. 108

4.3 The black cross section shows all transitions in the new 2024 Toto line list, whereas the pink cross section shows only MARVEL (Ma) experimental transitions (with variational intensities). The blue cross section shows the Ma – Ma cross section produced from the 2021 Toto line list (with variational intensities). 109

5.1 The tetrahedral symmetry of the CH_4 molecule. Figure Credit: [9]. . 116

5.2 The four normal vibrational modes. Figure Credit: [10]. 116

5.3 The first eight vibrational polyads of methane and the number of vibrational levels and sublevels in each one. Figure Credit: [11]. . . 117

5.4 The distribution of the experimental sources utilized, across the several polyad bands with respect to line position in cm^{-1}. Green color is for the cold bands and magenta for the hot bands. 131

5.5 The MARVEL energy uncertainties with respect to the energy with and without the application of the bootstrap method. The width of the violins indicates the number of energy levels in each energy range. 141

5.6 The $^{12}C^{1}H_4$ MARVEL energy levels for the first eight polyads obtained in this work. The symbols denote the different symmetries; A: A_1, A_2, E: E, F: F_1, F_2. 145

5.7 Difference between the MARVEL energies (obs) and the a. Effective Hamiltonian [12] (blue), b. Variational calculations (pink) [13]. . . . 147

5.8 Difference between the MARVEL energies (obs) and the MeCaSDa database (calc). 149

6.1 MM stick spectrum at 296K generated with EXOCROSS [8]. 157

6.2 Assigned lines from 12HaBeMi [14] at 573 K, distinguishing "Ma" (light blue) and "Ca" (dark red) labelled transitions. 158

6.3 Large obs. – calc. values between experimental 21YoBeDu spectral lines and matched "Ca" MM lines. 159

6.4 Residuals (obs – calc) for assigned transitions in the 21YoBeDu dataset. Label "Ma"/"Ca" detones that the matching MM line is linked to a MARVELised/calculated upper level. 162

6.5 Stick spectra of methane as reported in 21YoBeDu [15], grouped into two panels by temperature range. Assigned lines are in pink, unassigned in green. 163

6.6 Residuals (obs – calc) for assigned transitions in the 21MaYuSu dataset. 166

6.7 Stick spectrum of 21MaYuSu at 296K. Pink: assigned (validated through MARVEL), Blue: assigned (not validated), Green: unassigned lines. 167

6.8 Top subplot: Experimental data from 20YaLiPl. Bottom subplot: MM data. Pink lines indicate matched transitions, light blue lines represent unassigned experimental lines, and black lines show MM transitions that do not match any 20YaLiPl lines. 168

6.9 Residuals (obs – calc) for assigned transitions in the 20YaLiPl dataset. Label "Ma"/"Ca" detones that the matching MM line is linked to a MARVELised/calculated upper level. 169

6.10 Top subplot: Experimental 573 K data from 12HaBeMi. Bottom subplot: MM lines. Pink lines indicate matched transitions, light blue lines represent unassigned experimental transitions. 170

6.11 The 1073 K spectrum from 12HaBeMi [14], with blue lines indicating transitions previously assigned at 573 K. These matches can help guide new assignments at higher temperatures. 171

6.12 Top subplots: Experimental data from 05Brown. Bottom subplots: MM data. Pink lines indicate matched transitions, and black lines show MM transitions that do not match any 05Brown lines. 172

6.13 Top subplot: Experimental data from 97Pine. Bottom subplot: MM P and Q branches in the same range. 173

6.14 Top subplot: Experimental data from 88Brown. Bottom subplot: MM data. Pink lines indicate matched transitions, and black lines show MM transitions that do not match any 05Brown lines. 174

6.15 Top subplot: Experimental data from 88Margolis. Bottom subplot: MM data. Pink lines indicate matched transitions, light blue lines represent unassigned experimental lines, and black lines show MM transitions that do not match any 88Margolis lines. 176

6.16 Residuals (obs – calc) for assigned transitions in the 88Margolis dataset. Label "Ma"/"Ca" detones that the matching MM line is linked to a MARVELised/calculated upper level. 177

6.17 Top subplot: Experimental transitions from 85HiLoBr. Bottom subplot: The corresponding MM transitions. 178

6.18 Top subplot: Experimental transitions from 82HuLoRo. Bottom subplot: The corresponding MM transitions. 178

6.19 Distribution of newly assigned and validated methane transitions as a function of wavenumber, binned in intervals of 100 cm^{-1}. The height of each bar indicates the number of transitions found within that wavenumber range. 184

6.20 Newly assigned MARVEL energy levels (in cm^{-1}) as a function of rotational quantum number J. Each point represents an energy level, with colour indicating the polyad to which it belongs. The size of each circle reflects the number of combination differences (CDs) confirming that level (maximum CDs =14). 185

6.21 Comparison of the percentage of MARVELised states before and after incorporating new transitions. 187

6.22 Residuals between MARVEL energy levels and those computed by TROVE, with respect to J, for polyads 0–6. 188

List of Tables

1.1 Regions of the electromagnetic spectrum in order of increasing frequency, with approximate values and associated molecular transition types. Table from [16]. 27

2.1 Transitions file specification. 64

2.2 Specification of the `.states` file. 64

2.3 Summary of data provided by the ExoMol Database [4]. 65

2.4 Datasets created by the ExoMol project and included in the ExoMol database: recommended line lists only. Line lists denoted with a ✔ are suitable for high resolution studies [4]. 65

2.5 Source type abbreviations used to describe energy levels in hybrid (MARVELized) line lists. 71

3.1 Overview of the MgO MARVEL compilation energy levels (EL) and comparison against DUO variational calculated energy levels ($|Ma - Ca|$), in cm^{-1}. 79

3.2 A part of the final `.states` file for $^{24}Mg^{16}O$ 81

3.3 Experimental data for MgO used in our analysis. State': Upper electronic state, State": Lower electronic state, *v*':upper state vibrational quantum number, *v*": lower state vibrational quantum number, wavelength range and mean line position uncertainty given in cm^{-1}, V/A: number of validated experimental transitions/total number of transitions. 82

3.4 Experimental data for MgO considered but not used in this analysis. 83

3.5 An extract of the final `.states` file for $^{25}Mg^{16}O$. 89

3.6 An extract of the final `.states` file for $^{24}Mg^{17}O$. 89

3.7 An extract of the final `.states` file for $^{24}Mg^{18}O$. 89

3.8 An extract of the final `.states` file for $^{26}Mg^{16}O$. 90

4.1 Experimental data for TiO used in our analysis. State': Upper electronic state, State": Lower electronic state, *v*':upper state vibrational quantum number, *v*": lower state vibrational quantum number, wavelength range and mean line position uncertainty given in cm^{-1}, V/A: number of validated experimental transitions/total number of transitions. 106

4.2 Overview of the 2024 TiO MARVEL energy levels (EL) and comparison against DUO variational energy levels ($|Ma - Ca|$) in cm^{-1}. 107

4.3 A part of the final `.states` file for $^{48}Ti^{16}O$. 108

5.1 Symmetries of the fundamental vibrational modes of methane in T_d. 118

5.2 Vibrational Polyads and their Associated Levels 120

5.4 Experimental data for $^{12}C^{1}H_4$ used in our analysis. Wavelength range and mean line position uncertainty are given in cm^{-1}. A/V: number of available transitions/number of validated transitions. "given" indicates an uncertainty provided in the source. "CD" means no uncertainty was given, so it was derived using combination differences or CDs. "Inc" means the uncertainty was increased. See section 5.6 for comments on individual sources. 122

5.3 Information on the number of experimental sources and transitions per vibrational band included in our input list of transitions. Average uncertainty is given in cm^{-1}. A/V: total number of available transitions/number of validated transitions. 130

5.5 Experimental $^{12}C^{1}H_4$ papers not used in MARVEL analysis 132

5.6 Magic Numbers. Wavenumber values were selected from the Effective Hamiltonian energy values by Amyay et al. (16AmLoPi) [12]. 140

5.7 Summary of the MARVEL energies. Energy range is in cm^{-1}. MU/MUb: The Mean Energy Uncertainty before (MU) and after bootstrap (MUb). Mean obs. – calc. in cm^{-1}: 'obs' is referring to the MARVEL value and 'calc' to the calculated value by Yurchenko et al. [3] 142

5.8 List of partly assigned experimental sources used in this work, and the sources we used for their full assignments. 143

5.9 Specific lines reassigned because they were not validated. 144

5.10 Details of the connections of the two E energy levels with large residuals. The obs. − calc. values are in cm^{-1}. The subscript $_T$ is for the comparison with the TheoReTS variational calculations, $_{EH}$ is for the comparison with the Effective Hamiltonian values, and $_M$ is for the comparison with the MeCaSDa energies. The quantum numbers are: p, J, C, α. 150

5.11 Details of the connections of the two A_2 energy levels with large residuals. The obs. − calc. values are in cm^{-1}. The subscript $_T$ is for the comparison with the TheoReTS variational calculations, $_{EH}$ is for the comparison with the Effective Hamiltonian values, and $_M$ is for the comparison with the MeCaSDa energies. The quantum numbers are: p, J, C, α. 150

6.1 Summary of experimental sources collected. Each entry lists the source, spectral range in wavenumbers cm^{-1}, and number of provided spectral lines. 154

6.2 Overview of methane spectroscopic sources evaluated, including reference, spectral range in cm^{-1}, total and assigned line counts, experimental method, and temperature of measurement. 161

6.3 Energy Level: $P = 5$, $J = 4$, $C = F_1$, $\alpha = 146$. Avg Energy Value: E = 7171.650221 cm^{-1}derived from a MARVEL run. 161

6.4 Comparison of assigned transitions (J branch and $C^{'}$) with those reported in 21YoBeDu [15]. Only transitions where discrepancies in quantum number assignments occur are shown. 164

6.5 Comparison of assigned transitions ($P^{'} - P^{''}$, J branch, and $C^{''}$) with those reported in 81BrToHu [17]. Only transitions where discrepancies in quantum number assignments occur are shown. 179

6.6 Summary of updates in the MARVEL compilation. For each source, the wavenumber range, associated polyad bands, number of assigned and validated lines (A/V), and the mean uncertainty used are provided. 180

6.7 Lower-state quantum number discrepancies between Ding et al. [18] and the MM assignments ($J''C''\alpha''$). 181

6.8 Summary of total input transitions per polyad band ($P' - P''$) including number of transitions and ranges the rotational quantum number J. 183

6.9 Summary of MARVEL energy levels per polyad. For each polyad, the table lists the total number of energy levels, the range of rotational quantum numbers J, the wavenumber energy range (cm^{-1}), the number of states defined by more than one transitions, and the mean uncertainty (cm^{-1}) of the energy levels. 184

6.10 Sources considered but not used in the assignment and MARVEL update project. The wavenumber range in cm^{-1}, and reason for exclusion are listed. 189

6.11 Summary of experimental sources for future work. 190

Chapter 1

Introduction

1.1 Molecular Spectroscopy

Molecular spectroscopy is the study of the interaction between electromagnetic radiation and matter. Electromagnetic radiation can be described in terms of massless particles called photons. Each photon carries a specific amount of energy given by the relation $E = hv$, where E is energy in Joules (J), v is frequency in Hz, and h is Planck's constant ($h = 6.63 \cdot 10^{-34}$ Js).

This fundamental relationship was first proposed by Max Planck in 1900 during his work on blackbody radiation, as the experimental data disagreed with the classical view that matter and energy behave continuously. Later, in 1905 Einstein proposed that light itself is quantised, consisting of discrete packets of energy called photons. This was crucial in explaining the photoelectric effect and paved the way for the development of quantum theory.

In molecules, internal energy arises from various types of motion, including electronic transitions, vibrations, and rotations. These motions are also quantised, meaning that molecules can only exist in specific energy states. Transitions between these states occur when a molecule absorbs or emits a photon of energy that exactly matches the energy gap between the levels, with the frequency of the corresponding radiation given by $v = \Delta E/h$. These transitions between quantised energy levels are the basis of molecular spectra. Each transition corresponds to a specific energy

change ΔE and a certain probability of occurrence also characterises each transition. The spectral line resulting from such a transition has a wavelength $\lambda = hc/\Delta E$. In spectroscopy, wavelength is often expressed in centimeters, and it's common to use the wavenumber instead, defined as $\tilde{\nu} = 1/\lambda$ in units cm^{-1}. Wavenumber is directly proportional to energy. As a result, a collection of spectral lines (spectrum) is produced, each representing a distinct transition. The pattern and position of these lines provide a unique fingerprint of the molecule, revealing information about its structure, bonding, and energy levels. The type of transition that a molecule undergoes determines the region of the electromagnetic spectrum in which it absorbs or emits radiation. Electronic transitions, which involve relatively large energy changes, typically occur in the ultraviolet or visible regions. Vibrational transitions require less energy and are observed in the infrared region, while rotational transitions correspond to smaller energy changes and appear in the microwave region. In increasing frequency, the regions of the spectrum are illustrated in Table 1.1.

The Rydberg-Ritz combination principle describes an important feature of molecular spectra [19]. This empirical rule states that it is possible to find pairs of spectral lines with the property that the sum or difference of their wavenumbers is also an observed spectral line. This principle is very important because it forms the basis for *combination differences* (CD), where the difference between the wavenumbers of two transitions that share an energy level yields the energy separation of the other two levels involved (see Figure 1.1). Therefore, spectral lines can be predicted from existing lines, and the self-consistency of the energy levels can be evaluated.

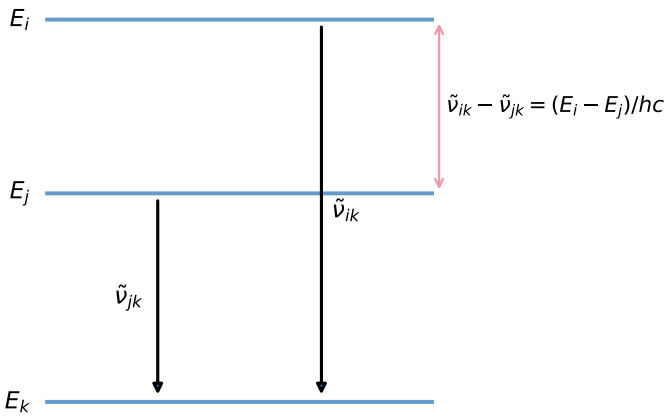


Figure 1.1: Schematic energy level diagram illustrating the combination difference (CD) method. Observed transitions $\tilde{\nu}_{ik}$ and $\tilde{\nu}_{jk}$ share a common level E_k. The difference of the two observed wavenumbers equals the energy separation between E_i and E_j expressed in wavenumber units.

Table 1.1: Regions of the electromagnetic spectrum in order of increasing frequency, with approximate values and associated molecular transition types. Table from [16].

Region	**Frequency (Hz)**	**Wavelength**	**Transition Types**
Radio	$3 \cdot 10^6 - 3 \cdot 10^{10}$	10 m – 1 cm	Nuclear spin, electron spin
Microwave	$3 \cdot 10^{10} - 3 \cdot 10^{12}$	1 cm – 100 μm	Rotational
Infrared (IR)	$3 \cdot 10^{12} - 3 \cdot 10^{14}$	100 μm – 1 μm	Vibrational
Visible and Ultraviolet (UV)	$3 \cdot 10^{14} - 3 \cdot 10^{16}$	1 μm – 10 nm	Electronic
X-ray	$3 \cdot 10^{16} - 3 \cdot 10^{18}$	10 nm – 100 pm	Inner-shell electronic
γ-ray	$3 \cdot 10^{18} - 3 \cdot 10^{20}$	100 pm – 1 pm	Nuclear transitions

In the radio frequency region, the transitions arise from the interaction of the magnetic moment of a nucleus or an electron with an external magnetic field. The resulting absorption spectra are described as nuclear magnetic resonance (NMR) and electron spin resonance (ESR), respectively. The radio region also includes hyperfine structure transitions, which result from the interaction between the nuclear spin and the electron spin. A well-known example is the 21 cm line of neutral hydrogen which arises from a spin-flip transition in the ground state. This line serves

as a key probe of atomic hydrogen in the interstellar medium. Molecular species can also exhibit hyperfine splitting. The hydroxyl radical (OH) for example, shows hyperfine transitions near 18 cm. These lines are often observed in star-forming regions and can also appear as maser emission (microwave amplification by stimulated emission of radiation).

In the microwave region, we can observe an absorption or emission spectrum as a result of the rotation of a molecule that has a permanent electric dipole. Such molecules include, for example, all diatomic molecules composed of non-identical nuclei (heteronuclear). Emission arises from the radiation produced by the rotating dipole, while absorption occurs due to the interaction between the dipole and the electric field of the incident radiation. One way to measure microwave spectra is by millimeter-wave absorption spectroscopy, where a tunable source of radiation is passed through a low-pressure gas sample and the absorption of specific rotational transitions is detected [20].

In the infrared region, transitions are caused by vibrational motion of the molecular bonds that lead to a change in the dipole moment. The absorbed energy corresponds to the excitation of vibrational modes within the molecule, such as stretching and bending of chemical bonds.
These transitions are commonly measured using Fourier-transform infrared (FTIR) spectroscopy [21], which offers broadband coverage by recording an entire spectrum simultaneously through an interferometer. For higher resolution and sensitivity, laser-based techniques are used. These include tunable diode laser absorption spectroscopy (TDLAS) [22], which uses a narrow-linewidth tunable laser to scan specific absorption lines, and cavity ring-down spectroscopy (CRDS) [23], which is very good for measuring weak transitions. Advanced methods include dual-comb spectroscopy (DCS) [24], that uses two optical frequency combs [25] to enable broadband, fast, and high-resolution measurements. Techniques like optical-optical double-resonance (OODR) spectroscopy [26, 27] achieve very high resolution by using a narrow-linewidth pump laser to selectively excite molecules to specific vibrational states, followed by a frequency comb probe that drives and measures tran-

sitions from those excited states. This technique is especially effective for accessing weak or congested transitions in highly excited states of polyatomic molecules.

Raman spectroscopy can also be used to probe vibrational transitions that involve changes in molecular polarizability. Since Raman and IR spectroscopy follow different selection rules (see subsection 1.1.5), they provide complementary information about the vibrational structure of molecules. Relevant nonlinear Raman methods include stimulated Raman spectroscopy [28] and coherent anti-Stokes Raman scattering (CARS) [29, 30].

Ultraviolet (UV) and visible radiation possesses sufficient energy to excite electrons from one electronic energy level to another. The resulting spectra arise from the interaction of an incident electromagnetic field with electronic charge distributions in the molecule, leading to electronic transitions.
Traditionally, grating-based and monochromator-based spectrometers have been widely used to measure such electronic absorption spectra in the UV-visible range [31]. Laser-based techniques such as laser-induced fluorescence spectroscopy are also used [32], where molecules are excited by the laser to an electronically excited state and detection is based on spontaneous emission as molecules relax to lower states. Other methods include resonance-enhanced multiphoton ionisation (REMPI) and its two-photon variant (R2PI) [33, 34].

X-rays can eject electrons from inner atomic orbitals (such as the K or L shells). The resulting transitions, when electrons from higher levels fall to fill these vacancies, emit X-ray radiation.

Gamma rays have the highest energy in the electromagnetic spectrum and can induce transitions within atomic nuclei. These transitions are typically observed in nuclear decay processes and are studied in nuclear spectroscopy.

1.1.1 The Born-Oppenheimer approximation

We now turn to the quantum mechanical principles that explain the transitions of a molecule. The Schrödinger equation is central to determining the energy levels

and wavefunctions of molecules, which correspond to the rotational, vibrational, and electronic states observed in spectroscopy. Generally, the *Born-Oppenheimer approximation* (BO) is used, which assumes that the motions of the nuclei and electrons can be treated separately due to their mass difference. As a result, the total internal energy of a molecule is often expressed as the sum of two components: electronic and ro-vibrational energy. This separation simplifies the problem, as it allows us to focus on the nuclear dynamics while treating the electronic energy separately. The BO approximation can fail in regions where the electronic and nuclear motions become strongly coupled, typically when two electronic states are close in energy, leading to nonadiabatic effects.

The time-independent Schrödinger equation for a molecule is written like this

$$\hat{\mathrm{H}}\Psi(\vec{r},\vec{R}) = E\Psi(\vec{r},\vec{R}) \tag{1.1}$$

where E is the total energy, the $\vec{R}$ are the nuclear coordinates and $\vec{r}$ the electronic coordinates, and Ψ is the total molecular wavefunction, which depends on both. The Hamiltonian operator consists of several terms: kinetic energy of the nuclei ($\hat{\mathrm{T}}_{\mathrm{nuc}}$), kinetic energy of the electrons ($\hat{\mathrm{T}}_{\mathrm{el}}$), potential energy from electron–electron repulsion (V_{ee}), potential energy from nucleus–nucleus repulsion (V_{NN}), potential energy from electron–nucleus attraction (V_{Ne}), as

$$\hat{\mathrm{H}} = \hat{\mathrm{T}}_{\mathrm{nuc}} + \hat{\mathrm{T}}_{\mathrm{el}} + \mathrm{V}_{\mathrm{ee}} + \mathrm{V}_{\mathrm{NN}} + \mathrm{V}_{\mathrm{Ne}}. \tag{1.2}$$

The electrons are much less massive than the nuclei; hence, we can consider the nuclei to be stationary relevant to the motion of the electrons. This is the Born-Oppenheimer (BO) approximation, and it allows us to fix the nuclei at certain coordinates $\vec{R}$. The total wavefunction can then be separated in the electronic and the nuclear part, as

$$\Psi(\vec{r},\vec{R}) = \psi_{\mathrm{el}}(\vec{r};\vec{R})\psi_{\mathrm{nuc}}(\vec{R}) \tag{1.3}$$

where $\vec{R}$ is now a parameter, not a variable, and the electronic wavefunction $\psi_{\text{el}}(\vec{r};\vec{R})$ depends on the electronic coordinates $\vec{r}$.

The electronic Schrödinger equation for the fixed nuclei geometry can be solved as

$$\hat{\text{H}}_{\text{el}}(\vec{r};\vec{R}),\psi_{\text{el}}(\vec{r};\vec{R}) = E_{\text{el}}(\vec{R})\psi_{\text{el}}(\vec{r};\vec{R}). \tag{1.4}$$

$\hat{\text{H}}_{\text{el}}$ includes all the electronic terms of the Hamiltonian $(\hat{\text{T}}_{\text{el}} + \text{V}_{\text{ee}} + \text{V}_{\text{Ne}})$ from Equation 1.2. The total energy of each state depends on the nuclear configuration. This equation is solved for each configuration, leading to a potential energy surface (PES) upon which the nuclei move, given by $E_{\text{el}}(\vec{R})$.

Once the electronic energy has been determined for a particular electronic state, we can rewrite the Equation 1.1 as

$$[V(\vec{R}) + \hat{\text{T}}_{nuc}(\vec{R})]\psi_{\text{nuc}}(\vec{R}) = E\psi_{\text{nuc}}(\vec{R}). \tag{1.5}$$

where we have set $\text{V}(\vec{R}) = \text{V}_{\text{NN}}(\vec{R}) + E_{\text{el}}(\vec{R})$.

If we consider the case of a diatomic molecule of nuclei a and b, Equation 1.5 is written as

$$\left(-\frac{\hbar^2}{2m_a}\nabla_a^2 - \frac{\hbar^2}{2m_b}\nabla_b^2 + \text{V}(R) - E\right)\psi_{\text{nuc}}(\vec{R}_a,\vec{R}_b) = 0, \tag{1.6}$$

where $\vec{R}_a$ and $\vec{R}_b$ are the position vectors of the two nuclei, and the potential energy only depends on the internuclear separation $R = |\vec{R}_a - \vec{R}_b|$. This two body problem can be reduced to one body motion by rewriting the kinetic energy in terms of the reduced mass

$$m_{red} = \frac{m_a m_b}{m_a + m_b}. \tag{1.7}$$

The kinetic energy operator will then be equal to

$$-\frac{\hbar^2}{2(m_a+m_b)}\nabla^2_{\vec{R}_{CM}} - \frac{\hbar^2}{2m_{red}}\nabla^2_{\vec{R}} \tag{1.8}$$

where $\vec{R}_{CM}$ is the centre of mass coordinate and $\vec{R} = \vec{R}_a - \vec{R}_b$ is the relative coordinate between the two nuclei. We can neglect the translational motion of the whole molecule as it is not interesting for the spectrum, and get the equation for the internal motion:

$$\left[-\frac{\hbar^2}{2m_{red}}\nabla^2_{\vec{R}} + \mathrm{V}(R) - E\right]\psi_{\mathrm{nuc}}(\vec{R}) = 0. \tag{1.9}$$

The potential $\mathrm{V}(R)$ only depends on the magnitude of R, so the problem has spherical symmetry. It is therefore convenient to express $\vec{R}$ in spherical coordinates (R,θ,ϕ), where R is the internuclear distance, and (θ,ϕ) describe the orientation of the molecular axis in space. As a first approximation, we can separate the rotational and vibrational motions of the nuclei:

$$\begin{aligned}\psi_{\mathrm{nuc}}(\vec{R}) &= \psi_{\mathrm{vib}}(R)\psi_{\mathrm{rot}}(\theta,\phi)\\ E &= E_{\mathrm{vib}} + E_{\mathrm{rot}}.\end{aligned} \tag{1.10}$$

1.1.2 Rotational motion

Expressing the Laplacian operator in spherical coordinates gives:

$$\left[-\frac{\hbar^2}{2m_{red}R^2}\frac{\partial}{\partial R}\left(R^2\frac{\partial}{\partial R}\right) + \frac{\vec{L}^2}{2m_{red}R^2} + \mathrm{V}(R)\right]\psi_{\mathrm{nuc}}(\vec{R}) = E\psi_{\mathrm{nuc}}(\vec{R}), \tag{1.11}$$

where we have substituted the squared angular momentum in spherical coordinates

$$\vec{L}^2 = -\hbar^2\left[\frac{1}{sin\theta}\frac{\partial}{\partial\theta}\left(sin\theta\frac{\partial}{\partial\theta}\right) + \frac{1}{sin^2\theta}\frac{\partial^2}{\partial\phi^2}\right]. \tag{1.12}$$

Solving the angular part of the nuclear Schrödinger equation (1.11) leads to the identification of the rotational wavefunctions as spherical harmonics

$$\psi_{\mathrm{rot}}(\theta,\phi) = \mathrm{Y}_{JM_J}(\theta,\phi). \tag{1.13}$$

The spherical harmonics are the eigenfunctions of the squared angular momentum operator $\hat{\mathrm{L}}^2$ and its projection onto the molecular axis $\hat{\mathrm{L}}_{\mathrm{z}}$ with eigenvalues $\hbar^2 J(J+1)$, and $\hbar M_J$, respectively. The rotational angular momentum quantum number J

takes integer values J = 0,1,2,.. and M_J ranges from $-J$ to J with integer steps and has a total of $2J+1$ possible values. The eigenvalues are, therefore:

$$E_{\text{rot}} = \frac{\hbar^2}{2m_{red}R^2}J(J+1). \tag{1.14}$$

In the *rigid rotor approximation*, the molecule rotates while the two atoms maintain a constant distance between them. This way, we can fix R to be a constant R_0, where the subscript indicates the vibrational level, and write Equation 1.14 in terms of the moment of inertia of the molecule $I_0 = m_{red}R_0^2$.

$$E_{\text{rot}} = \frac{\hbar^2}{2I_0}J(J+1) = B_0J(J+1). \tag{1.15}$$

Here we defined the rotational constant of the molecule as:

$$B_0 = \frac{\hbar^2}{2I_0}. \tag{1.16}$$

We notice from Equation 1.15 that the separation between the rotational levels increases with the rotational quantum number J. The differences between the energy levels give us the rotational spectrum. The transition frequency between rotational levels J and $J+1$ is given by

$$f_{J\to J+1} = E_{\text{rot},J+1} - E_{\text{rot},J} = 2B_0(J+1). \tag{1.17}$$

The bond length R_0 represents the average internuclear separation in the vibrational ground state and is slightly larger than the equilibrium bond length R_e because of zero-point vibrations. Consequently, B_0 is slightly smaller than B_e defined at R_e. As J increases, centrifugal distortion must be included because rotation stretches the bond and increases the moment of inertia. To describe this effect, it is convenient to work about the equilibrium geometry R_e. In a classical picture, we equate the

centrifugal force with the binding force at the new bond length:

$$E_{\text{rot}} = \frac{L^2}{2m_{red}R_e'^2} + \frac{1}{2}k(R_e' - R_e)^2 \tag{1.18}$$

where the force constant is the second derivative of the potential at the equilibrium bond length, $k = \frac{d^2V}{dR^2}\Big|_{R_e}$. Replacing the squared angular momentum with the eigenvalues of the operator $\hat{L}^2$, we obtain the expression for the rotational energy that accounts for the centrifugal distortion as:

$$E_{\text{rot}} = B_e J(J+1) - D_e J^2(J+1)^2 \tag{1.19}$$

where:

$$D_e = \frac{4B_e^3}{\hbar^2\omega_e^2} \tag{1.20}$$

and ω_e being the vibrational angular frequency. The constant $B_e = \hbar^2/(2m_{red}R_e^2)$ is the equilibrium rotational constant, which is larger than the experimentally observed B_0 defined for the vibrational ground state.

To generalise the discussion of rotational motion to rigid *polyatomic* molecules, we describe the rotation in terms of the principal moments of inertia. In the rigid-rotor approximation, these are taken in equilibrium geometry, analogous to the definition of B_e for diatomic molecules. The corresponding rotational constants are usually denoted by A, B and C. We describe rotation by writing the Hamiltonian as

$$H_{\text{rot}} = \frac{J_a^2}{2I_a} + \frac{J_b^2}{2I_b} + \frac{J_c^2}{2I_c} \tag{1.21}$$

where we have chosen an orthogonal set of principal axes, in which the moment of inertia matrix is diagonal. The moments of inertia are I_a, I_b, I_c corresponding to the three perpendicular axes of rotation, so that

$$I_a \leq I_b \leq I_c. \tag{1.22}$$

The angular momentum components in this coordinate system are

$$J_a = I_a \omega_a \tag{1.23}$$

$$J_b = I_b \omega_b \tag{1.24}$$

$$J_c = I_c \omega_c \tag{1.25}$$

and the rotational constant introduced in Equation 1.15 becomes

$$A = \frac{\hbar^2}{2I_A} \tag{1.26}$$

$$B = \frac{\hbar^2}{2I_B} \tag{1.27}$$

$$C = \frac{\hbar^2}{2I_C} \tag{1.28}$$

with

$$A \geq B \geq C. \tag{1.29}$$

The relation between I_a, I_b, I_c determines how molecules are classified into four different types of rotors.

1. **Linear molecules** (e.g. CO_2 have $I_a = 0, I_b = I_c$. Their energy levels within the rigid rotor approximation are given by

$$E_{\text{rot}} = BJ(J+1) \tag{1.30}$$

2. **Spherical top molecules** have $I_a = I_b = I_c$. They are high symmetry molecules (e.g. CH_4), their rotational energy levels are

$$E_{\text{rot}} = BJ(J+1) \tag{1.31}$$

   like the linear molecules.

3. **Symmetric top molecules** have one unique moment of inertia and two others equal to each other: $I_a = I_b \neq I_c$. If the unique moment of inertia is smaller

than the other two, the molecule is a prolate symmetric top (e.g. CH_3I, NH_3) with the unique axis being the a axis, and $A > B = C$. If the unique moment is larger than the other two, the molecule is an oblate symmetric top (e.g. B_3F), and the unique axis is the c axis, with $A = B > C$. Their energy levels are

$$E_{\text{rot}} = BJ(J+1) + (A-B)K^2 \tag{1.32}$$

for the prolate top, where K is the projection of J to the a axis, and

$$E_{\text{rot}} = BJ(J+1) - (B-C)K^2 \tag{1.33}$$

for the oblate top, where K is the projection of J to the c axis.

4. **Asymmetric top molecules** have three unequal moments of inertia: $I_a \neq I_b \neq I_c$. Most molecules fall into this category. Unlike the other rotor types, their rotational energy levels cannot be expressed with a simple analytical formula and must be determined numerically by solving the rigid rotor Hamiltonian. The energy levels are typically labeled using the quantum numbers J, K_a, K_c, which serve as approximate labels based on the limiting cases of prolate and oblate symmetric tops. Spectroscopic transitions in asymmetric tops are often more complex, producing dense rotational spectra.

1.1.3 Vibrational motion

The radial part of the Equation 1.11 is

$$\left[\frac{-\hbar^2}{2m_{red}}\frac{d^2}{dR^2} + \mathrm{V}(R)\right]\psi_{\text{vib}}(R) = E_{\text{vib}}\psi_{\text{vib}}(R). \tag{1.34}$$

The potential function $\mathrm{V}(R)$ can be approximated to have a parabolic form for bound states of the molecule, near the bottom of the potential. Near the minimum R_e (equilibrium bond length), the Taylor expansion of the potential gives

$$\mathrm{V}(R) = V(R_e) + \frac{dV}{dR}\Big|_{R_e}(R-R_e) + \frac{1}{2}\frac{d^2V}{dR^2}\Big|_{R_e}(R-R_e)^2 \Rightarrow \tag{1.35}$$

$$\mathrm{V}(R) = \frac{1}{2}k(R-R_e)^2, \tag{1.36}$$

where we set the minimum of the potential to be zero, $V(R_e) = 0$. The first derivative of the potential vanishes $\frac{dV}{dR}\Big|_{R_e} = 0$ at $R = R_e$, and the second derivative defines the force constant $k = \frac{d^2V}{dR^2}\Big|_{R_e}$.This leads to a form of the potential that gives *harmonic oscillator solutions*. Equation 1.11 becomes

$$\left[\frac{-\hbar^2}{2m_{red}}\frac{d^2}{dR^2} + \frac{1}{2}k(R-R_e)^2\right]\psi_{\mathrm{vib}}(R) = E_{\mathrm{vib}}\psi_{\mathrm{vib}}(R). \tag{1.37}$$

The solution for the energy levels of the harmonic oscillator is

$$E_{\mathrm{vib}} = \hbar\omega_e\left(v + \frac{1}{2}\right), \tag{1.38}$$

where the angular harmonic frequency is $\omega_e = \sqrt{k/m_{red}}$ and the vibrational quantum number v takes integer values = 0,1,2... Equation 1.38 shows that there is a zero point energy of $\frac{1}{2}\hbar\omega_e$, and that the vibrational levels have equal distance between them.

The harmonic oscillator model provides a useful first approximation for describing the potential energy of a real molecule, but it falls short of capturing the full complexity of molecular behaviour. In reality, the potential is much steeper at short bond lengths as a result of exchange interaction. At longer bond lengths, the attractive Coulomb forces between the electrons and nuclei gradually weaken as the atoms move apart, eventually reaching the dissociation limit where the bond breaks. This means there is a finite number of energy levels in contrast to the harmonic oscillator case. Also, unlike the evenly spaced energy levels of a harmonic oscillator, the vibrational energy levels in an anharmonic system become progressively closer as the vibrational quantum number v increases. To better describe real molecular

behaviour, the cubic and quartic terms of the potential are treated as perturbations to the harmonic Hamiltonian. In cm^{-1} this leads to the following expansion:

$$E_{\mathrm{vib}} = \omega_e \left(v+\frac{1}{2}\right) - \omega_e x_e \left(v+\frac{1}{2}\right)^2 + \omega_e y_e \left(v+\frac{1}{2}\right)^3 + O(v^4) \tag{1.39}$$

As a result, the separation between the vibrational levels is not constant. The coefficients appearing in Equation 1.39 are known as vibrational spectroscopic constants and provide an empirical description of anharmonic effects in molecular vibrations. Specifically, ω_e is the harmonic vibrational wavenumber, corresponding to the fundamental frequency of the harmonic oscillator. The constant x_e is the first-order anharmonicity constant, which accounts for the decrease in vibrational level spacing with increasing vibrational quantum number. Higher-order anharmonic corrections are described by constants such as y_e, which become significant only at higher vibrational excitation. These constants are characteristic of a given electronic state and are determined experimentally.

An empirical expression for potential energy that is often used to describe the electronic state potential is the Morse Potential, defined as:

$$\mathrm{V}(r) = D\left[1 - e^{-\alpha(R-R_e)}\right]^2, \tag{1.40}$$

where D is the well depth. Figure 1.2 illustrates the difference between the harmonic and Morse potential. A diatomic molecule has only one vibrational mode corresponding to the stretching of the bond along the internuclear axis. However, polyatomic molecules, possess many more vibrational degrees of freedom. A nonlinear molecule with N atoms has $3N-6$ normal modes of vibration, and a linear molecule has $3N-5$. These normal modes represent collective motions of atoms that oscillate harmonically about the equilibrium geometry. Each normal mode is an independent motion characterised by a single frequency, either IR active, Raman active, or inactive, depending on symmetry. For example, in water H_2O, three vibrational modes appear in IR and Raman: symmetric stretch ($\sim 3650\ \mathrm{cm}^{-1}$), bend ($\sim 1595\ \mathrm{cm}^{-1}$), and asymmetric stretch ($\sim 3755\ \mathrm{cm}^{-1}$) [16].

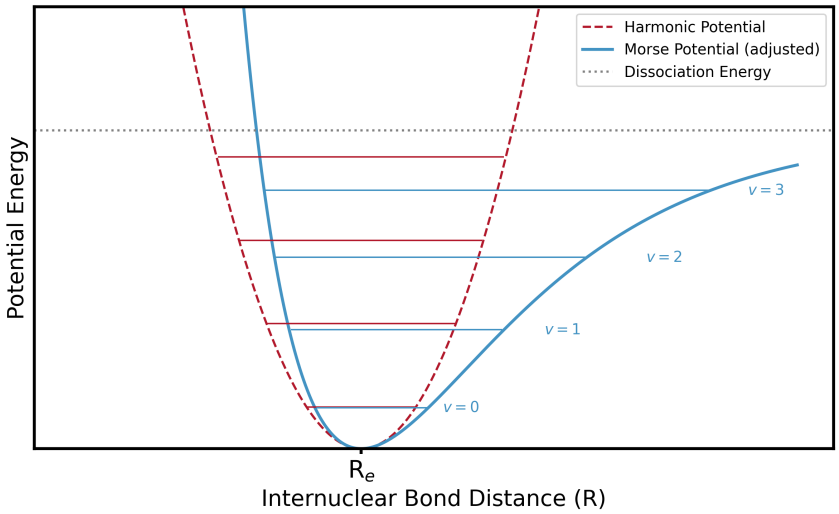


Figure 1.2: Comparison of the harmonic (dashed red) and Morse (solid blue) potential curves. The vibrational energy levels for both potentials are indicated by horizontal lines. For the Morse potential, the energy levels are labelled on the right, with quantum numbers $v = 0, 1, 2, \ldots$ showing the anharmonic nature of the potential as the levels become progressively closer together at higher energies. The dissociation energy of the molecule is marked by a grey dashed line.

1.1.4 Ro-vibrational motion

By solving the Schrödinger equation with the Morse potential, we can get a more complete expression for the energy corresponding to both the *ro-vibration* (vibration and rotation) of a diatomic molecule:

$$E_{rv} = \omega_e \left(v + \frac{1}{2}\right) + B_e J(J+1) - \omega_e x_e \left(v + \frac{1}{2}\right)^2 - D_e J^2 (J+1)^2 - \tag{1.41}$$

$$a_e \left(v + \frac{1}{2}\right) J(J+1) + \ldots. \tag{1.42}$$

The spectroscopic constant B_e is the equilibrium rotational constant. The constant D_e is the centrifugal distortion constant, which accounts for the non-rigid nature of the molecule and describes the stretching of the bond due to rotation at high J values. The constant a_e is the vibration–rotation interaction constant, reflecting the dependence of the rotational constant on vibrational excitation, arising from the increase of the average bond length as the vibrational quantum number increases.

The rotational constant for a vibrational state v can be expressed as

$$B_v = B_e - a_e\left(v+\frac{1}{2}\right)+\ldots. \tag{1.43}$$

Each term in this expression accounts for corrections to the idealised models: anharmonicity in vibration, non-rigidity in rotation, and the interaction between the vibration and rotation. Ro-vibrational spectra appear as series of sharp lines in the infrared region, and their spacing provides direct information about bond strengths and moments of inertia.

1.1.5 Selection Rules

The likelihood that a molecule transitions between energy levels upon absorbing a photon is called the transition probability. It depends on the properties of the initial and final states, and how effectively the photon can interact with these states to cause a transition. Selection rules help determine whether a particular transition is permitted.

In the dipole approximation, an external electric field $\vec{E}$ is assumed to interact uniformly with a molecule. The interaction is described by the interaction Hamiltonian $\hat{\mathrm{H}}_{\mathrm{int}} = -\hat{\mu}\cdot\vec{E}$, where the dipole moment operator is $\hat{\mu} = q\cdot\vec{r}$. The negative sign indicates that the interaction lowers the energy of the system when the electric field aligns with the dipole moment. The transition probability is determined by the matrix element of the dipole moment operator between the initial (ψ_i) and final (ψ_f) wavefunctions. If the matrix element $\langle\psi_f|\hat{\mu}|\psi_i\rangle$ has a non-zero value, the transition is dipole allowed, otherwise, it is dipole forbidden. It may be observed, although weak from other mechanisms such as magnetic dipole or electric quadrupole interactions. The electric dipole transition probability is then expressed as:

$$P = |\langle\psi_f|\hat{\mu}|\psi_i\rangle|^2. \tag{1.44}$$

1.1.6 Rotational Transitions

Only molecules with a non-zero dipole moment can interact with electromagnetic radiation via electric dipole transitions. Applying this to the four molecule categories mentioned in subsection 1.1.2 we have:

Linear Molecules lack a permanent dipole moment when homonuclear (e.g., N_2, O_2), and they do not exhibit a pure rotational spectrum. However, polar linear molecules (e.g., CO, HCl) do.

Spherical Top Molecules have highly symmetric charge distributions (e.g., CH_4, SF_6) and possess no permanent dipole moment. As a result, they do not exhibit an allowed pure rotational spectrum in the context of dipole-allowed transitions.

Symmetric Top Molecules have one unique principal moment of inertia. If they possess a permanent dipole moment along the unique axis (e.g., CH_3Cl), they exhibit a pure rotational spectrum.

Asymmetric Top Molecules have a permanent dipole moment and exhibit pure rotational spectra (e.g., H_2O).

The intensity of rotational transitions is proportional to μ^2, so, molecules with large permanent dipoles have more intense transitions. The selection rule for a dipole allowed rotational transition is

$$\Delta J = -1, 0, 1, \;\; J' + J'' \neq 0, \tag{1.45}$$

steming from the fact that a photon contains one unit of angular momentum. For symmetric tops there is also the non-rigorous rule $\Delta K = 0$. Equation 1.45 leads to the R ($\Delta J = +1$), Q ($\Delta J = 0$), and P ($\Delta J = -1$) branches as illustrated in Figure 1.3.

1.1.7 Electronic Transitions

The electronic state notation

$$^{2S+1}\Lambda^{+/-}_{\Omega,(g/u)} \tag{1.46}$$

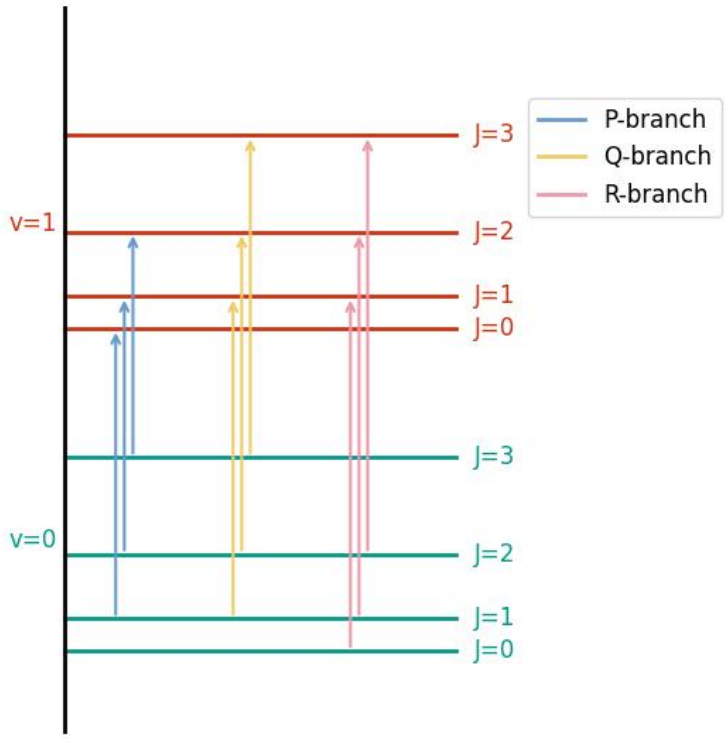


Figure 1.3: Simplified illustration of rotational energy levels and transitions for two vibrational states of a diatomic molecule. The plot shows rotational energy levels for the ground (v=0, green lines) and first excited (v=1, red lines) vibrational states. Arrows represent transitions between rotational levels, with the P, Q, and R branches in blue, yellow, and pink, respectively.

for diatomic molecules is defined based on the symmetry properties and angular momentum of the electronic wavefunctions.

1. Λ is the projection of the orbital angular momentum on the internuclear (usually z) axis. The associated symbols are: Σ for $\Lambda = 0$, Π for $\Lambda = \pm 1$, Δ for $\Lambda = \pm 2$, Φ for $\Lambda = \pm 3$ etc.

2. The multiplicity factor $2S+1$ comes from the total spin S of the electrons. It indicates the number of possible spin orientations.

3. Ω is the projection of the total angular momentum along the internuclear axis: $\Omega = |\Lambda + \Sigma|$ where Σ is the projection of the total spin S on the internuclear axis.

4. The g/u label (from the German gerade = even, ungerade = odd) applies only to homonuclear diatomic molecules which have a center of inversion. A wavefunction is g if it is symmetric under the inversion through the center, or u if it is antisymetric under inversion through the center.

5. The $+/-$ symbols apply only to Σ states and indicate the parity under reflection through a plane containing the internuclear axis. The $+$ sign indicates the wavefunction is symmetric to the reflection in that plane, and $-$ antisymmetric.

Electronic transitions happen when a molecule undergoes a transition from one potential energy curve to another. Typically they are accompanied by a transition to a different rotational and vibrational state as well. The selection rules for electronic transitions are a consequence of the symmetry properties of the molecular wavefunctions and the transformation behavior of the electric dipole operator under the relevant symmetry operations.

1. The spin selection rule applies to all molecules and requires that the total spin remain unchanged during an electronic transition:

$$\Delta S = 0. \tag{1.47}$$

This can be shown by writing the total electron wavefunction as $\psi = \psi_{\text{space}}\psi_{\text{spin}}$. The dipole moment operator $\hat{\mu}$ then acts on it as

$$\hat{\mu}\,\psi_{\text{el}} = \hat{\mu}\,\psi_{\text{spin}}\,\psi_{\text{space}} = \psi_{\text{spin}}\hat{\mu}\,\psi_{\text{space}} \tag{1.48}$$

since $\hat{\mu}$ acts only on the spatial part of the wavefunction. Consequently, from Equation 1.44, the probability has non-zero value only if the final spin wavefunction is the same as the initial one. The orthogonality of different spin states would otherwise make the integral zero.

2. For diatomic molecules, the change in the projection of the orbital angular

momentum along the internuclear axis (Λ) must satisfy:

$$\Delta\Lambda = 0, \pm 1. \tag{1.49}$$

This rule stems from the fact that the electric dipole operator carries angular momentum with quantum number $l = 1$.

3. Parity conditions refer to how the molecular wavefunction changes under inversion through the symmetry axis. For homonuclear diatomics, since they have an inversion center, a subscript g or u is used to show the symmetry with respect to the inversion operator. The dipole moment operator is antisymmetric (ungerade) under this inversion. The integral Equation 1.44 needs to be symmetric overall to be non-zero, and this happens when one wavefunction is gerade and the other ungerade.

   For heteronuclear diatomics, and specifically for states with $\Lambda = 0$, reflection through a vertical plane is a valid symmetry operation. The electric dipole operator is symmetric under such reflection, so initial and final states must transform the same way under this operation for the integral to be non-zero. This means that the allowed transitions are $\Sigma^+ \leftrightarrow \Sigma^+$, $\Sigma^- \leftrightarrow \Sigma^-$.

For polyatomic molecules, the selection rules for electronic transitions cannot be framed in terms of Λ, g/u, or reflection labels, since there is no unique internuclear axis and often no inversion center. Instead, selection rules are derived from the symmetry properties of the molecule, which are described by point groups and analysed using group theory.

An electronic transition is allowed if the direct product of the *irreducible representations* (Γ) of the initial electronic state, the dipole moment operator, and the final electronic state contains the symmetric representation of the molecule's point group:

$$\Gamma_{\text{initial}} \otimes \Gamma_{\hat{\mu}} \otimes \Gamma_{\text{final}} \supset \Gamma_{\text{totally symmetric}} \tag{1.50}$$

Here, $\Gamma_{\hat{\mu}}$ represents the transformation symmetry of the electric dipole moment op-

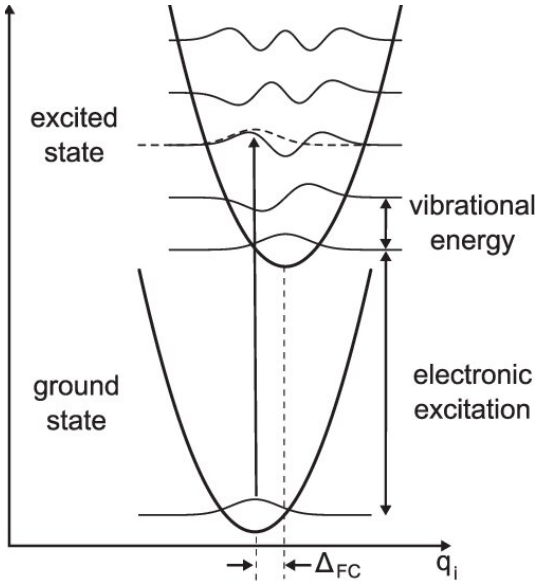


Figure 1.4: Franck–Condon principle: Electronic transitions occur vertically between vibrational levels. Δ_{FC} indicates the displacement between equilibrium positions. Figure credit: [6].

erator. For example, in most point groups, the dipole components (μ_x, μ_y, μ_z) transform as the same irreducible representations as the Cartesian coordinates (x, y, z).

In CH_4 (methane), for instance, the ground electronic state transforms as the totally symmetric representation A_1 of the T_d point group. If an excited electronic state transforms as an irreducible representation that does not appear in the decomposition of $A_1 \otimes F_2$, then the transition is forbidden by symmetry.

During an electronic transition, the likelihood of a simultaneous vibrational transition is determined by the Franck–Condon principle. This principle states that electronic transitions occur on timescales much faster than nuclear motion, meaning the nuclei remain effectively fixed during the transition. This is consistent with the BO approximation. As a result, the atomic positions and bond lengths are assumed unchanged at the moment of transition. In potential energy diagrams, where energy is plotted against internuclear distance, such transitions (vibronic transitions) are plotted as vertical lines as in Figure 1.4.

As a result of this approximation we can write the wavefunctions of the initial

and final states of a transition as products:

$$\psi_i = \psi_{\mathrm{nuc,i}}(\vec{R})\,\psi_{\mathrm{el,i}}(\vec{r};\vec{R}) \tag{1.51}$$

$$\psi_f = \psi_{\mathrm{nuc,f}}(\vec{R})\,\psi_{\mathrm{el,f}}(\vec{r};\vec{R}) \tag{1.52}$$

The probability of the transition occurring is then:

$$\langle \psi_{\mathrm{el,f}}|\hat{\mu}|\psi_{el,i}\rangle \,\langle \psi_{\mathrm{nuc,f}}|\psi_{\mathrm{nuc,i}}\rangle\,. \tag{1.53}$$

The electronic transition dipole is taken as approximately constant with respect to R, so that the transition intensity is proportional to the square of the vibrational overlap integral,

$$I \propto \left| \int \psi^*_{v,f}(R)\;\psi_{v,i}(R)\,\mathrm{d}R \right|^2 . \tag{1.54}$$

This quantity, known as the Franck–Condon factor, represents the overlap between the vibrational wavefunctions of the initial and final states, which belong to different electronic potential energy surfaces. Consequently, the strongest transitions occur between vibrational states for which this overlap is largest. An additional overlap integral involving the rotational wavefunctions also contributes to the overall transition amplitude. This rotational factor gives rise to selection rules $\Delta J = \pm 1$ for one-photon transitions.

1.1.8 Vibrational Transitions

Transitions with $\Delta v = \pm 1$ are allowed within the harmonic oscillator approximation. For anharmonic molecules, all transitions with $\Delta v = \pm 1, \pm 2, \pm 3, \ldots$ are allowed, but the intensity becomes rapidly weaker as Δv increases. The transition from $v = 0$ to $v = 1$ is normally called the fundamental vibration, and the transitions with larger Δv are called overtones. Vibrational transitions are usually accompanied by a rotational transition. The selection rule for J is given by Equation 1.45. The $\Delta J = 0$ rule is only valid for non - Σ states of diatomics, and for polyatomic molecules. So, the rovibrational spectrum of a molecule in a Σ electronic state lacks a Q branch.

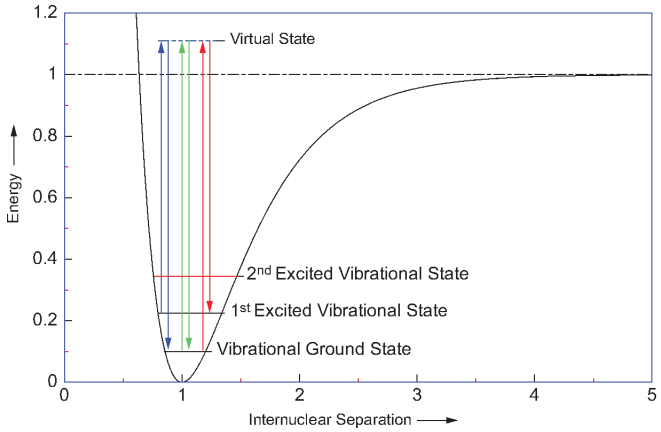


Figure 1.5: Morse potential energy curve for a diatomic molecule illustrating vibrational energy levels and types of scattered radiation observed in Raman spectroscopy. Green arrow: Rayleigh scattering (elastic); red arrow: Stokes Raman scattering (energy transferred to the molecule); blue arrow: anti-Stokes Raman scattering (energy transferred from the molecule). Figure credit:[7]

1.1.9 Raman Selection Rules

Raman spectroscopy is based on the inelastic scattering of light, known as Raman scattering. When a molecule interacts with incident photons, most photons are elastically scattered (Rayleigh scattering), but a small fraction are scattered at different energies due to excitation or de-excitation of vibrational modes. These energy differences correspond to molecular vibrational transitions Figure 1.5.

Unlike infrared (IR) spectroscopy, which requires a change in the dipole moment during vibration, Raman spectroscopy requires a change in the molecular polarizability. So, even if a vibrational mode is IR inactive, it can still be Raman-active if it changes the molecule's polarizability. This leads to the Raman selection rule: A vibrational mode is Raman active if it transforms according to the same irreducible representation as one of the components of the polarizability tensor. This contrasts with IR spectroscopy, where only modes that transform as the same irreducible representations as the components of the dipole moment vector (x, y, z) are IR-active. Due to their differing selection rules, IR and Raman spectroscopy are often complementary. Raman spectroscopy is particularly useful for studying symmetric stretching modes that may be weak or inactive in the IR spectrum. It is a powerful tool for characterising molecular vibrations in systems where fluorescence

or water absorption can interfere with IR measurements.

1.2 Spectroscopy of Exoplanets

Exoplanets are planets that orbit stars beyond our Solar System. They are typically classified into categories based on their physical properties [35]. Rocky, small planets such as Earth composed of rock, silicate, water, or carbon are called *terrestrial planets*. *Super Earths* are terrestrial planets more massive than Earth and less massive than Neptune. *Gas giants* are massive planets composed mainly of helium and hydrogen, similar to Jupiter and Saturn in our Solar System. Gas giants orbiting close to their host stars resulting in their high temperatures, are referred to as *Hot Jupiters*. The *Neptunian exoplanets* are similar in size and composition to Neptune, with atmospheres rich in hydrogen and helium. *Ice giants* are planets like Uranus and Neptune, composed primarily of water, ammonia, and methane ices. Brown dwarfs are substellar objects that can be more massive than giant exoplanets but not massive enough to sustain hydrogen fusion like stars. They share characteristics with giant exoplanets and are studied with similar spectroscopic techniques.

As of 1 May 2025, there are 5,889 confirmed exoplanets in 4,395 planetary systems [36]. The first published claims of a planet beyond the solar system date back to the 19th century. Jacob W.S. [37] suggested the presence of a planetary companion in the binary star system 70 Ophiuchi, based on observed orbital irregularities. Later, See T. J. J. [38] supported similar interpretations. These early claims were discredited by Heintz [39], who found no evidence for such companions.

In the late 1980s, several radial velocity studies searched for unseen stellar companions, many interpreted as possible brown dwarfs [40, 41], helping refine techniques later applied to exoplanet detection. The first confirmed brown dwarfs were not discovered until 1995. Gliese 229B was identified as a companion to a nearby M dwarf star [42], and Teide 1 was found in the Pleiades cluster [43]. Both were confirmed via direct imaging.

In 1992, the first confirmed exoplanets were discovered by Wolszczan and Frail

[44]. Using pulsar timing they identified two Earth-mass planets orbiting the pulsar PSR B1257+12. A third, moon-mass planet (Draugr) was detected in 1994 in the same pulsar system, adding to the first known multi-planet system beyond our solar system. In 1995, Mayor and Queloz [45] announced the discovery of 51 Pegasi b, a Jupiter-mass planet in a close orbit around a solar-type star, using radial velocity measurements. This contradicted the planet formation theories at the time, which had assumed gas giants could not form or survive near their stars. The discovery, which earned a share of the 2019 Nobel Prize in Physics, marked the beginning of the modern era of exoplanet research and was soon confirmed by independent studies [46], and it overturned the assumption that other planetary systems must resemble our own [47].

The discovery of the first multi-planet system around a main-sequence star came in 1999, when multiple planets were identified orbiting Upsilon Andromedae [48], marking a key step toward understanding the complexity of planetary systems beyond our own. In 2001, HD 28185 b became the first exoplanet found to orbit entirely within its star's habitable zone. Its mass, however, is at least six times that of Jupiter, suggesting that it is more likely a gas giant with no Earth-like surface and therefore unlikely to be habitable in the same way Earth is [49]. A major milestone in atmospheric characterisation was achieved shortly after, when Charbonneau et al. (2002) measured the atmosphere of HD 209458 b using the Hubble Space Telescope's STIS spectrograph, detecting sodium absorption in the planet's transit spectrum [50]. In 2005, the first direct detection of light from exoplanets was accomplished using the Spitzer Space Telescope, which captured infrared emission from both HD 209458 b and TrES-1, offering the first constraints on exoplanetary temperatures and atmospheres [51, 52].

Several observational techniques have been developed to detect exoplanets. Figure 1.6 shows the confirmed exoplanets plotted according to the method of their detection. The radial velocity method and transit photometry are among the most prominent detection techniques. Some of the detection techniques are analysed in the following paragraphs.

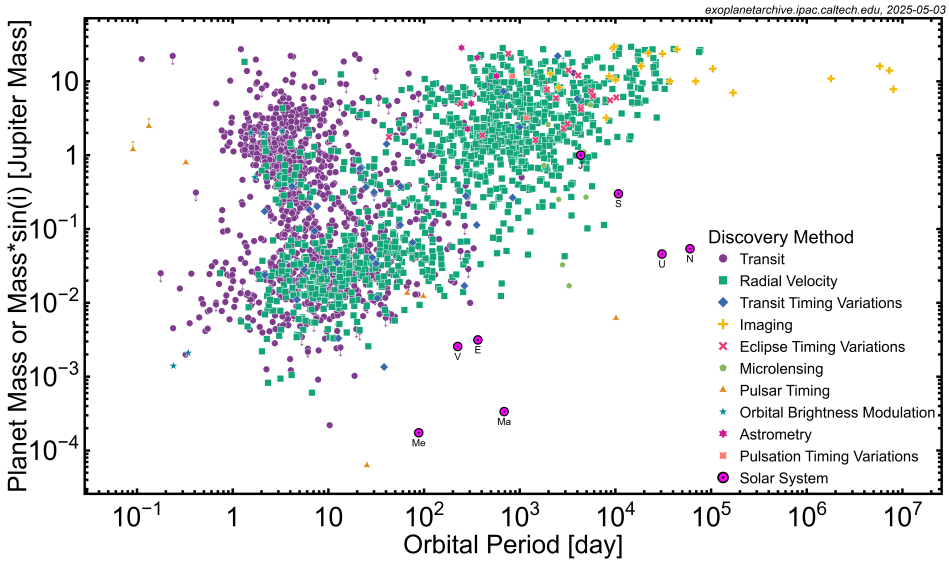


Figure 1.6: Plot of exoplanet mass versus orbital period for confirmed detected exoplanets. The mass is given as a projected value along the line of sight, where M is the planet's mass and i is the orbital inclination angle. The orbital period is shown in days. The different markers and colours indicate the detection methods for every planet. The magenta lettered circled points correspond to the planets of our Solar System. Figure is from the NASA Exoplanet Archive (exoplanetarchive.ipac.caltech.edu)

The *Radial Velocity (Doppler) Method* was used in the discovery of 51 Peg b and remains one of the most productive techniques. By observing periodic variations in a star's spectrum, we can infer the presence of a planet or brown dwarf orbiting the star and causing gravitational pull on it. The period of these variations corresponds to the planet's orbital period (P). Using Kepler's third law, the planet's distance from its host star can be determined. From this, the planet's velocity semi-amplitude (K_*) can be calculated, which, combined with the star's mass and an estimated orbital inclination, allows for the estimation of the minimum of the planet's mass (M_p) via the expression as given by Birkby [53]:

$$K_* = \left(\frac{2\pi G}{P}\right)^{1/3} \frac{M_p sin(i)}{(M_p + M_*)^{2/3}} \frac{1}{(1-e^2)^{1/2}}. \tag{1.55}$$

Here, e is the orbital eccentricity, i is the orbital inclination, G is the gravitational constant. A disadvantage of this method is that measurements are most effective when the planet's orbit is aligned with the observer's line of sight, and the calcu-

lated mass depends on the estimation of the orbital inclination. When these observations are combined with astrometric measurements, however, additional information about the inclination of the orbit can be acquired, which lowers these uncertainties. Additionally, measurements can be affected by brightness variations caused by the star itself. Ground-based observatories have contributed with instruments like High Accuracy Radial Velocity Planet Searcher (HARPS) at the European Southern Observatory's (ESO) telescope [54], High Resolution Echelle Spectrometer (HIRES) at Keck Observatory [55], and Echelle SPectrograph for Rocky Exoplanets and Stable Spectroscopic Observations (ESPRESSO) on the Very Large Telescope (VLT) [56]. These spectrographs can detect very small motions of stars, allowing the discovery of small, close-in exoplanets.

The *Transit Photometry Method* detects drops in a star's brightness when a planet passes in front of it, as observed from Earth. It is the most sensitive method and most known exoplanets have been discovered using it. Both radial velocity and transit techniques are most sensitive to large planets orbiting close to their stars. The planet's radius can be calculated based on the drop in the star's brightness, and when combined with radial velocity measurements that provide the planet's mass, the planet's density can be estimated. This, in turn, helps determine whether a planet is likely to be rocky, gaseous, or of mixed composition. A secondary transit (or occultation) happens when the planet passes behind the star from the observer's point of view. During this phase, the combined light from the system briefly decreases again, not because the star is being blocked, but because the planet's emitted or reflected light is temporarily hidden. Measuring the depth of this secondary dip, especially in infrared wavelengths, allows for the estimation of the planet's dayside temperature, thermal emission spectrum, and reflectivity (albedo). The Transit Photometry Method was used extensively by the Kepler [57] and is used by Transiting Exoplanet Survey Satellite (TESS) [58] missions.

The *Astrometry Method* involves measuring the precise positions of stars over time. If the star exhibits small, periodic shifts in its position, this can indicate the gravitational influence of an orbiting object. These positional shifts measured are

very small and require very high accuracy. So the astrometry method is technically demanding. With Gaia of the European Space Agency (ESA) [59], several exoplanets have been discovered using this technique. Furthermore, astrometry has been used to make follow-up observations for planets detected via other methods. Future missions like NASA's Nancy Grace Roman Space Telescope (RST), formerly known as WFIRST-AFTA [60] are expected to enhance astrometric capabilities further.

The *Transit Timing Variations Method* is used to detect small deviations in the timing of a planet's transits across its host star. In multi-planet systems, gravitational interactions between planets can cause these transits to occur slightly earlier or later than expected. These variations can reveal the presence of additional planets, even if they do not transit. From the amplitude and shape of the timing deviations, and by modelling the gravitational interactions of the planets, the mass ratios can be estimated, as well as the orbital periods, eccentricities, and other parameters. A notable example is the multi-planet system around Kepler-19, where a non-transiting planet was inferred through the transit timing variations of the transiting planet Kepler-19b [61]. Missions that have significantly contributed to the detection of exoplanets via this method include primarily space-based observatories such as Kepler [57], TESS [58], and CHaracterising ExOPlanets Satellite (CHEOPS) [62].

The *Pulsar Timing Method* involves the detection of planets by measuring variations in the arrival times of pulses from a rotating magnetised neutron star (pulsar). These objects emit highly regular radio pulses, with periods typically ranging from 1 ms to 15 s [61]. Deviations from the expected pulse timing indicate the presence of orbiting bodies exerting gravitational influence on the pulsar. This method is extremely sensitive and can detect planets with masses comparable to or even smaller than that of Earth. Pulsar timing for exoplanet detection is carried out by several radio telescopes and international collaborations, including but not limited to the International Pulsar Timing Array (IPTA) [63] that combine data from multiple radio telescopes.

The *Gravitational Microlensing Method* is based on the gravitational lens effect. When a star and its planet pass in front of a background star, they can act as a gravitational lens, magnifying the light from the background star. This method is particularly sensitive to planets in the habitable zone of their star and farther out and can be used to detect free-floating planets that are not bound to a star. It should be noted that, due to the transient and unique nature of each gravitational microlensing event, the results obtained are not reproducible. Ground-based surveys that have made significant contributions using this method include the Optical Gravitational Lensing Experiment (OGLE) [64], Microlensing Observations in Astrophysics (MOA) [65], and the Korea Microlensing Telescope Network (KMTNet) [66]. In the near future, the RST [67] is expected to advance this method further through high-precision space-based observations.

The *Direct Imaging Method* captures images of exoplanets by blocking out the host star's light, typically using coronagraphs or starshades. This method is most effective for detecting young, massive planets that emit thermal infrared radiation and are located far from their stars, where the star–planet contrast is larger. Moreover, targeting nearby stars is advantageous because for a given orbital separation, the angular distance between the planet and its host star is greater. Although technically challenging due to the brightness of the host star, direct imaging provides valuable insights into planetary atmospheres and orbital characteristics. Notable instruments contributing to direct imaging include the Gemini Planet Imager (GPI) [68], SPHERE on the VLT [69], and Subaru Coronagraphic Extreme Adaptive Optics System (Subaru/SCExAO) [70]. Future mission RST will include a dedicated exoplanet imaging instrument.

Research efforts in exoplanet science have progressively moved beyond detection toward atmospheric characterisation. Below, we outline the main observational techniques and the role of spectroscopy in understanding exoplanet properties.

Exoplanet atmospheric characterisation involves deciphering the composition and properties of an exoplanet's atmosphere by studying its spectrum. The diverse

chemical compositions observed in the atmospheres of solar system planets imply that exoplanetary atmospheres are likely to exhibit an even greater range of variability [71]. The main observational spectroscopic methods for studying exoplanet atmospheres are transit spectroscopy, high-resolution Doppler spectroscopy, and direct imaging.

1.2.1 Transit spectroscopy

The first atmospheric measurement was atomic sodium in the atmosphere of HD 209458b with the Hubble Space Telescope (HST) spectrograph in 2002 [50]. It was achieved with the transit method from four transits of the planet. Observations using this method have already successfully detected atomic and molecular absorption features in approximately 100 exoplanet atmospheres [72].

During a transit, when the planet passes in front of the star from the observer's line of sight, we get the *transmission spectrum*. A small fraction of starlight filters through the planet's atmosphere before reaching the observer, and the resulting spectrum reveals how the transit depth varies with wavelength [73]. Different gases in the atmosphere absorb or scatter light more or less effectively at different wavelengths, and so, the atmosphere appears to be more opaque at some wavelengths than others. Consequently, the planet seems larger where the atmosphere is more opaque.

The transmission depth at a given wavelength λ quantifies how much stellar light is blocked or absorbed by the planet and its atmosphere during a transit. It is defined by Kempton et al. [74] and Sengupta et al. [75] as:

$$D_\lambda = 1 - \frac{F_{in}}{F_*} \tag{1.56}$$

where, F_{in} the stellar flux when the planet is in transit and F_* is the out of transit stellar flux.

The in-transit stellar flux is expressed as a sum of the direct stellar flux plus a part (F_p) that is filtered through the planet's atmosphere and goes through ab-

sorption and scattering. This component depends on the atmospheric composition. Following Sengupta et al. [75], the transmission depth can then be written as

$$D_\lambda = \frac{R_{PA}^2}{R_*^2} - \frac{F_P}{F_*} \tag{1.57}$$

where R_{PA} is the radius of the planet and the atmosphere, and R_* is the stellar radius. By measuring how D_λ varies with wavelength, we can infer the composition and vertical structure of the atmosphere. Interpreting the transmission spectrum typically involves the use of a forward model, which simulates the expected atmospheric signature based on various parameters.

Broad absorption features in the infrared indicate the presence of molecules (e.g. H_2O, CH_4, CO_2) that exhibit strong spectral signatures due to their rovibrational transitions. These occur primarily in the infrared but can also extend into the visible. In the visible, atomic species such as Na and K have produce absorption lines [76, 77]. Additionally, scattering affects the transmission spectrum by attenuating stellar light, with Rayleigh scattering producing a steep slope at short wavelengths and Mie scattering from clouds or hazes flattening spectral features.

The planetary flux transmitted at wavelength λ is given by integrating the specific intensity across the atmospheric annulus:

$$F_{p,\lambda} = \int_{R_p}^{R_{PA}} I_\lambda(z) dz. \tag{1.58}$$

Here, P_P is the base radius of the planet. Using the Beer–Bouguer–Lambert law, the transmitted intensity at altitude z is

$$I(\lambda, z) = I_0(\lambda) e^{-\tau_\lambda / \mu_0} \tag{1.59}$$

where I_0 is the intensity of the incident stellar radiation, τ_λ is the optical depth along the path, and μ_0 is the cosine of the angle between the incoming ray and the surface normal.

The optical depth quantifies how much stellar radiation is attenuated via ab-

sorption and scattering as it travels through the planet's atmosphere. At altitude z it is expressed [75] as:

$$\tau(\lambda, z) = 2\int_0^{l(z)} \rho(z)\chi(\lambda, z)dl \tag{1.60}$$

where $\rho(z)$ is the atmospheric density, $\chi(\lambda, z)$ is the extinction coefficient (scattering and absorption), and $l(z)$ is the optical path length. This expression sums up the contributions to extinction.

For example, the transmission spectrum of Earth shows characteristic absorption features of molecules such as H_2O, O_2, CO_2, O_3, CH_4, and NO_2 [78]. Each of these species produces absorption bands in well-known spectral regions. For instance, ozone absorbs at ~ 4.5 and $\sim 9\,\mu$m, carbon dioxide has a steep feature at $\sim 2.7\,\mu$m, and water vapour absorption is prominent mainly in the mid infrared [79, 80]. Earth's transmission spectrum has been observed indirectly. During a total lunar eclipse, sunlight passes through Earth's atmosphere and reaches the Moon after being refracted and filtered. Observations of the Moon during such eclipses capture a transmission spectrum of Earth's atmosphere [78]. These observations serve as important benchmarks for modelling exoplanet spectra and assessing the detectability of biosignatures on Earth-like planets.

During the planet's secondary eclipse, where the planet passes behind the host star, we get the planet's *emission* and *reflection spectrum*. By comparing the combined light from the star and planet just before eclipse with the stellar light observed during eclipse, the contribution from the planet's dayside can be isolated. Reflection dominates the visible region, where stellar photons are scattered off the planet's atmosphere or surface, while thermal emission dominates in the infrared, where the planet radiates its own heat.

The reflection spectrum provides information about the atmosphere's albedo. The emission spectrum probes the temperature structure of the dayside atmosphere along with its chemical composition [81, 82]. At each wavelength, the radiation escapes primarily from a depth where the atmosphere becomes optically thin ($\tau_\lambda \simeq 1$). This allows us to get the brightness temperature $T(\lambda)$, and assuming black body

radiation, we can then retrieve the vertical temperature profile $T(z)$ [83]. The temperature profile helps identify possible thermal inversions. Also, by fitting synthetic spectra based on the temperature profile, and varying molecular abundances, one can retrieve the chemical composition and assess the presence of clouds, hazes, or non-equilibrium processes.

Reflected light spectra reveal the planet's albedo and surface or cloud properties but provide no information about temperature or vertical distribution of gases. In contrast, thermal emission spectra contain information about both the temperature structure and atmospheric composition, though interpreting them is more complex. Each method has its strengths and limitations, so combining both offers a more complete view of the atmosphere. This requires observations across a wide spectral range, from visible to mid-infrared [84].

Challenges in obtaining emission spectra include low contrast between the planet's faint infrared light and the bright host star, especially for small or cool planets, and contamination from the instrument and Earth's thermal background. Also, because secondary eclipse measurements rely on the planet-to-star flux ratio, any inaccuracies in the assumed stellar flux can introduce systematic errors into the derived planetary emission spectrum [85].

In addition to primary and secondary eclipse observations, monitoring the total brightness of the star–planet system over the full orbital period, known as a *phase curve*, provides insight into the planet's emission at different phase angles. This measured light effectively combines the planet's true brightness map and how its visible surface is projected toward the observer at each point in the orbit [86]. A large variation in brightness over the orbit means there is a strong temperature contrast between the dayside and nightside, whereas a small variation suggests more efficient heat redistribution. Therefore, such observations can constrain atmospheric dynamics and temperature contrasts between the dayside and nightside [87]. For example, shifted thermal hotspots can be detected, caused by winds. First observed on HD 189733b [87, 88], such hot spot shifts have since been detected in several other

hot Jupiters, confirming predictions made by 3D atmospheric circulation models [89]. Because they require uninterrupted, high-precision measurements over multiple days, these observations are typically conducted from space [84]. Combined with eclipse and transit data, phase curves contribute to a more complete picture of an exoplanet's atmospheric structure and climate.

Transit spectroscopy is particularly effective for studying hot Jupiters and Neptune-sized planets, whose large, extended atmospheres generate strong spectral features. Characterising the atmospheres of smaller, Earth-sized exoplanets is more challenging. Also, this method is most effective for close-in planets, as the probability and frequency of transit events decrease significantly with orbital distance [90]. Another issue regarding this method is that hazes and clouds can obscure or flatten spectral features [91]. High-resolution spectroscopy offers a potential solution to this problem [92, 93].

Earlier missions like the Hubble Space Telescope (HST) and Spitzer laid the foundation for exoplanet atmospheric studies [50, 94]. Building upon these achievements, the James Webb Space Telescope (JWST) (0.6 to 28.5 μm) has expanded our observational capabilities, enabling the study of cooler planets and the detection of a broader variety of atmospheric molecules. Early JWST observations, such as those of WASP-96b, revealed clear water vapour features that surpass the sensitivity of previous instruments [95]. In addition, JWST achieved the first thermal emission detection from a temperate rocky exoplanet, TRAPPIST-1b [96].

The future ESA's ARIEL mission, launching in 2029, will survey around 1,000 exoplanets in the infrared range of 1.95 to 7.8 μm [97]. ARIEL aims to characterise atmospheric composition, temperature structures, and clouds to better understand planet formation and evolution.

1.2.2 High-Resolution Doppler Spectroscopy

High-resolution ground-based spectroscopy, when combined with Doppler techniques, offers a powerful method for probing the atmospheres of exoplanets [98–

101]. The planet's lower mass compared to the star's means that its orbital motion produces a much more pronounced change in its radial (line-of-sight) velocity over the course of its orbit. As a result, the planet's spectral lines are Doppler-shifted by tens to hundreds of kilometers per second as it moves, while the stellar lines remain relatively stationary over the same timescale [53]. This large, time-dependent Doppler shift allows the planet's faint spectral features to be separated from both the bright stellar spectrum and the telluric lines. Consequently, high-resolution Doppler spectroscopy has proven especially effective for detecting and characterising exoplanet atmospheres.

The signal-to-noise as given by Snellen et al. [102] is:

$$S/N = \frac{S_{pl}}{\sqrt{S_* + \sigma_{bg}^2 + \sigma_{RN}^2 + \sigma_{Dark}^2}} \sqrt{N_{lines}} \tag{1.61}$$

where S_{pl} is the planet signal, S_* is the stellar signal, and $\sigma_{bg}, \sigma_{RN}, \sigma_{Dark}$ are the photon noise from the sky and telescope background, the read-out noise, and the noise from the dark current from the instrument. Their units are photons per resolution element, which is defined by the spectrograph's resolution $R = \lambda/\Delta\lambda$. N_{lines} is a multiplication factor that takes into account the number and strength of the spectral lines detected and is also dependant on the spectral resolution.

Time-series observations from the ground are used to follow the planet's orbit and track changes in its radial velocity. Especially for close-in planets for which the Doppler shifts are significant, the separation of the planet's spectral lines from the host star's and the telluric lines is simpler than the case of large orbital separation ($\alpha > 1AU$). When the signal from the planet is isolated, the noise has to be reduced. To increase the S/N ratio, the *cross-correlation* technique is used. High-Resolution Cross-correlation Spectroscopy (HRCCS) is used to detect signals from exoplanets that are buried within noisy or contaminated stellar and telluric spectra. It involves cross-correlating observed high-resolution spectra with model templates of expected molecular absorption features. Essentially, cross-correlation is an operation that measures the similarity between two signals (or functions) as a function

of a shift (τ) applied to one of them. One signal ($f(t)$) is compared to another ($g(t+\tau)$) and the degree of similarity is measured at each step:

$$R_{fg}(\tau) = \int f(t)g(t+\tau)d\tau. \tag{1.62}$$

A high value of the cross-correlation function (CCF) $R_{fg}(\tau)$ indicates that the two signals are well correlated in that shift.

The accuracy of the template spectrum critically depends on the quality of molecular line lists [53, 103]. A line list includes line positions, strengths, and opacities at various temperatures and pressures. Such data come from laboratory measurements or from theoretical quantum chemistry calculations. In addition to accurate line positions and intensities, reliable modelling of spectral line shapes is essential. Molecular absorption lines are broadened by several physical mechanisms, including thermal (Doppler) broadening due to molecular motion and pressure (collisional) broadening arising from intermolecular interactions. Accurate broadening parameters are particularly important for high-resolution cross-correlation analyses, as they determine the detailed shape of spectral lines. Incorrect broadening widths or temperature dependences can weaken the correlation signal even when line positions are accurate. This is especially relevant for hot exoplanet atmospheres, where pressure and temperature vary strongly with altitude.

Several databases provide molecular line lists, such as HITRAN [104], HITEMP [105], and ExoMol [4]. The reliability of cross-correlation results is highly sensitive to the precision of these line lists. In high-resolution spectroscopy ($R \sim 100\,000$) even small inaccuracies in line positions can lead to significant mismatches, reducing the effectiveness of signal detection [106, 107].

Each observed spectrum is cross-correlated with the model template across a range of trial radial velocities. By stacking the CCFs over a series of spectra taken at different orbital phases, a strong signal emerges when the correct radial velocity semi-amplitude of the planet (K_p) is assumed. This alignment enhances the S/N ratio and allows for the detection of specific molecules, such as CO, as

demonstrated in the case of HD 209458b [99] and τ Boötis b [108]. Typically, a 5σ S/N ratio is considered a strong detection [109].

Several ground-based instruments have been important in advancing high-resolution Doppler spectroscopy for exoplanetary atmospheric characterisation. Notable facilities include the VLT equipped with CRIRES+ (an upgraded version of CRIRES with greatly enhanced wavelength coverage) [110], the CARMENES dual-channel spectrograph at Calar Alto Observatory [111], Keck Observatory's NIRSPEC (Near-Infrared Spectrograph) [112], and Subaru Telescope's InfraRed Doppler spectrograph [113]. These ground-based observatories can achieve the required spectral resolution to isolate planetary absorption features, despite the challenges posed by telluric absorption. The space-based spectrograph ANDES (Atmospheric and Near-Infrared Exoplanet Spectrograph) [114], proposed for the Extremely Large Telescope (ELT), is expected to operate in 2028 and further expand the potential for characterising exoplanet atmospheres.

1.2.3 Direct Imaging

For planets with large angular separations from their star as seen from Earth, the Doppler shifts change very little over a night's observation, making time-resolved Doppler detection less effective. However, if their angular separation from their star is resolvable, their spectra can be analysed through direct imaging using high-contrast imaging techniques such as adaptive optics or coronagraphy [102, 115]. The planet's spectrum is fainter than the stellar and the telluric spectral lines, but it is very localised in the image, which helps isolate it and directly observe the planet's thermal emission, particularly in the near-infrared (NIR). This is especially effective for young, self-luminous giant planets ($T \geq 1\,000K$) [116, 117]. Although such systems are rarer than transiting exoplanets, their spectra are often of higher signal-to-noise ratio and resolution due to the use of large telescopes, both ground-based (e.g., VLT, Keck Observatory) with adaptive optics and coronagraphy, and space-based observatories like JWST. The atmospheric information derived from direct imaging analysis includes temperature profiles and molecular composition,

similar to the transiting method.

The detectability of weak molecular absorption features can be further enhanced in the planet's spectrum with the use of the cross-correlation technique. Although the planet's Doppler shift does not vary significantly over a single night, it still possesses a non-zero radial velocity. Therefore, the observed spectra are cross-correlated with a model template shifted across a range of trial radial velocities to search for molecular absorption features [118]. This produces a cross-correlation map, and a strong peak in the map reveals both the planet's location and the presence of specific molecules in its atmosphere [119, 120].

Chapter 2

ExoMol

The ExoMol project [121] focuses on producing high temperature line lists for key molecular species significant in the analysis of the atmospheres of extrasolar planets and cool stars. This spectroscopic data is essential for modelling atmospheric opacities and interpreting observational spectra accurately.

Originally launched in 2012, ExoMol focused on generating line lists that were as complete as possible. Such completeness was crucial for reproducing broad-band spectra and opacity profiles, particularly in low and medium resolution applications [122]. By 2024, ExoMol had produced line lists for 67 molecules, and nearly 150 isotopologues. However, the emergence of high-resolution Doppler spectroscopy and the cross-correlation technique introduced new requirements. These methods rely not only on completeness but also on high spectroscopic accuracy of line positions and intensities. Several early ExoMol line lists, though comprehensive, lacked the precision needed for high-resolution studies that require a resolving power of $R \sim 100\,000$ [106, 107]. This challenge motivated a shift in focus for the project. The project ExoMolHD (ExoMol in high definition) starting in 2020, aims to provide molecular line lists of the necessary spectroscopic accuracy. ExoMolHD combines theoretical approaches with available laboratory data to refine molecular constants, improve line positions, and extend the existing ExoMol database.

Table 2.1: Transitions file specification.

Field	Description
i	Upper state ID
f	Lower state ID
A	Einstein A coefficient in s^{-1}
$\tilde{\nu}_{fi}$	Transition wavenumber in cm^{-1} (optional).

Table 2.2: Specification of the `.states` file.

Field	Description
i	State ID
$\tilde{E}$	Recommended state energy in cm^{-1}
$g_{\rm tot}$	State degeneracy
J	Total angular momentum quantum number, J or F (integer/half-integer)
Unc	Uncertainty in the state energy in cm^{-1}
τ	State lifetime (aggregated radiative and predissociative lifetimes) in s
(g)	Landé g-factor (optional)
(QN)	State quantum numbers, may be several columns (optional)
(Abbr)	Abbreviation giving source of state energy, see Table 2.5.
($\tilde{E}_0$)	Calculated state energy in cm^{-1} (optional)

2.1 Data provided

In the basic ExoMol format [123] a line list consists of two files: the `.states` and `.trans` files. The `.states` file lists energy levels (cm^{-1}) with corresponding quantum numbers and unique indices called state IDs. The recommended state energy $\tilde{E}$ is the either a calculated value or, if available, a value refined using MARVEL or another method (see subsection 2.2.2). The `.trans` file provides Einstein A coefficients, the upper and lower state IDs corresponding to the `.states` file, and optionally transition frequencies (cm^{-1}). The structure of these files is illustrated in Tables 2.1 and 2.2, adapted from the 2024 ExoMol updates paper by Tennyson et al. (2024) [4].

Table 2.3 provides a summary of the various datasets available for each isotopologue on the ExoMol website (www.exomol.com). Table 2.4 shows the line lists created by the ExoMol group, as adapted from the 2024 ExoMol updates paper by Tennyson et al. (2024) [4].

Table 2.3: Summary of data provided by the ExoMol Database [4].

Data type
Line lists
Absorption cross sections
Pressure broadening coefficients
Temperature dependent super-lines (histograms)
Partition functions
Cooling functions
Specific heat - heat capacity
Temperature and pressure dependent opacities
Photo-absorption continuum cross section
Photo-dissociation cross sections including VUV absorption
Spectroscopic Models

Table 2.4: Datasets created by the ExoMol project and included in the ExoMol database: recommended line lists only. Line lists denoted with a ✔ are suitable for high resolution studies [4].

Paper	Molecule	DSName		Reference
III	HCN/HNC	Harris	✔	[124]
V	NaCl	Barton		[125]
V	KCl	Barton		[125]
VII	PH_3	SAlTY		[126]
VIII	H_2CO	AYTY	✔	[127]
IX	AlO	ATP	✔	[128]
X	NaH	Rivlin		[129]
XI	HNO_3	AlJS		[130]
XII	CS	JnK	✔	[131]
XIII	CaO	VBATHY	✔	[132]
XIV	SO_2	ExoAmes	✔	[133]
XV	H_2O_2	APTY		[134]
XVI	H_2S	AYT2	✔	[135]
XVII	SO_3	UYT2	✔	[136]
XIX	$H_2{}^{17,18}O$	HotWat78	✔	[137]

Continued on the next page...

Table 2.4 – continued from previous page

Paper	Molecule	DSName		Reference
XX	H_3^+	MiZATeP	✔	[138]
XXII	SiH_4	OYT2		[139]
XXIII	PO	POPS		[140]
XXIII	PS	POPS		[140]
XXIV	SiH	SiGHTLY		[141]
XXV	SiS	UCTY		[142]
XXVI	NS	SNaSH		[143]
XXVII	C_2H_4	MaYTY		[144]
XXIX	CH_3Cl	OYT		[145]
XXX	$H_2{}^{16}O$	POKAZATEL	✔	[146]
XXXI	C_2	8states	✔	[147]
XXXII	MgO	LiTY	✔	[148]
XXXIII	TiO	Toto	✔	[149]
XXXIV	PH	LaTY	✔	[150]
XXXV	NH_3	CoYuTe	✔	[151]
XXXVI	SH	GYT	✔	[152]
XXXVII	HCCH	aCeTY	✔	[153]
XXXVIII	SiO2	OYT3		[154]
XXXIX	CO2	UCL-4000	✔	[155]
XL	$H3O^+$	eXeL	✔	[156]
XLI	KOH	OYT4		[157]
XLI	NaOH	OYT5		[157]
XLII	NO	XABC	✔	[158]
XLIII	NaO	NaOUCMe	✔	[159]
XLIV	SiO	SiOUVenIR	✔	[160]
XLV	CaH	XAB	✔	[161]
XLV	MgH	XAB	✔	[161]

Continued on the next page...

Table 2.4 – continued from previous page

Paper	Molecule	DSName		Reference
XLVI	SiN	SiNful	✔	[161]
XLVII	CaOH	OYT6	✔	[161]
XLVIII	H2CS	MOTY	✔	[162]
XLIX	AlCl	YNAT	✔	[163]
L	$H3^+$	MiZo	✔	[164]
LI	LiOH	OYT7		[165]
LII	CH^+	PYT		[166]
LIII	YO	BRYTS		[167]
LIV	AlH	AloHa	✔	[168]
LV	VO	HyVO	✔	[169]
LVI	SO	SOLIS	✔	[170]
LVII	CH4	MM	✔	[2]
LVIII	OCS	OYT8	✔	[171]
LIX	N2O	TYM	✔	[172]
LX	$^{15}NH_3$	CoYuTe-15	✔	[5]
LXI	OH	MYTHOS	✔	[173]
LXII	C3	AtLast	✔	[174]
LXIII	HDO	TBD	✔	[175]
LXIV	PN	PaiN	✔	[176]

To visualise the content of line lists, precomputed cross sections at various temperatures and zero pressure are also provided [177]. Pressure and temperature dependent opacity cross sections for all ExoMol molecules, as well as O_2, Na, and K, are available as computed by Chubb et al. [178].

Quantities such as temperature-dependent specific heat capacities and partition functions are also available for the main isotopologue of each recommended line list. Other available data include cooling functions, super-lines (temperature-binned line histograms), temperature-dependent photodissociation cross sections,

and broadening parameters for pressure-dependent line profiles [4].

ExoMol supports extensive post-processing through two main tools: ExoCross (Fortran) [8] and PyExoCross (Python) [179]. These tools enable users to export line lists in the ExoMol and HITRAN format, generate cross sections, radiative lifetimes, partition functions, specific heats, absorption and emission stick spectra, and electric dipole, electric quadrupole and magnetic dipole spectra.

ExoMol has launched a new high-resolution molecular spectroscopic database called ExoMolHR (ExoMol High-Resolution) [180] available at www.exomol.com/exomolhr. The ExoMolHR database provides line positions of low uncertainty from the ExoMol database, suitable for high-resolution studies such as line identification or simulations of high-resolution spectra. Initially, reduced line lists are constructed by scraping the ExoMol database for energy levels and transitions with uncertainties unc ≤ 0.01 cm^{-1}. Then, the transitions with resolving power $R = \lambda/\Delta\lambda \geq 100\,000$ are stored. These transitions provide the core of the database.

For each transition, ExoMolHR provides the frequency, uncertainty, Einstein A-coefficient, intensity at a user specified temperature, lower energy, total level degeneracy, angular momentum and quantum numbers for upper and lower states. The ExoMolHR database currently contains data for 55 isotopologues from 32 molecules. This number is growing rapidly with the completion of more MARVEL studies (see subsection 2.2.3).

2.2 Methodology

The general methodology used to compute molecular line lists begins with *ab initio* calculations of the potential energy (PES) and dipole moment surfaces (DMS), typically performed using quantum chemistry programs such as MOLPRO [181], which compute the electronic structure of the molecule.

2.2.1 Nuclear Motion Calculations

The PESs and DMSs serve as inputs to nuclear motion programs that solve the Schrödinger equation for the nuclei. Depending on the molecular system, different programs are used: DUO for diatomics [182], DVR3D and EVEREST for triatomics [183, 184], and TROVE for general polyatomic molecules [185].

Using the BO approximation, the nuclear Schrödinger equation (Equation 1.9) is then solved variationally using the PES:

$$\hat{\mathrm{H}}_{\mathrm{nuc}}\psi_{\mathrm{nuc}}(\vec{R}) = E\,\psi_{\mathrm{nuc}}(\vec{R}), \tag{2.1}$$

where $\hat{\mathrm{H}}_{\mathrm{nuc}}$ includes kinetic, potential energy from the PES, and additional coupling terms.

Dipole transition moments are computed using the rovibronic wavefunctions and the DMS:

$$\vec{\mu}_{if} = \langle \psi_i(\vec{R}) | \hat{\mu}(\vec{R}) | \psi_f(\vec{R}) \rangle, \tag{2.2}$$

which are then used to calculate the Einstein A coefficients, that measure the probability per unit time $(1/s)$ for spontaneous emission. In S.I. units this is expressed as [186]:

$$A_{if} = \frac{64\pi^4 \nu_{if}^3}{3hc^3} |\mu_{if}|^2, \tag{2.3}$$

where ν_{if} is the transition frequency.

From the energy levels E, the partition function can be calculated:

$$Q(T) = \sum_n g_n e^{-E_n/kT}, \tag{2.4}$$

where g_n is the degeneracy of level n, k is Boltzmann's constant, and T is temperature. The Einstein A coefficients, energy levels, and partition functions are used to compute temperature-dependent line intensities in units of cm/molecule, and finally, spectra can be simulated by applying physical conditions such as temperature and pressure.

2.2.2 Hybridisation of the Line Lists

To optimise accuracy and approach resolutions of $R = 100\ 000$ or even higher, a standard process is to refine the computed PESs by fitting to high-resolution experimental data. Empirically derived energies are used for this refinement. Additionally, the final line lists are often *hybridised* by incorporating empirically derived levels. Depending on the method used to obtain the energy levels in the final line lists, we use appropriate labels in the `.states` files as shown in Table 2.5.

For the variationally calculated energies the label used is "Ca". For data directly taken from the HITRAN database [104], the abbreviation used is HI. These data are often experimentally derived. The abbreviation Mo is used for data originating from the MoLLIST project by Bernath et al. [187], which provides empirical line lists designed for use at higher temperatures. The label "EH" is used for energy levels obtained with the effective Hamiltonian method. The "EH" energies are calculated with the use of a simplified Hamiltonian that is constructed to model the energy structure of a molecule based on observed spectra.

When available, the calculated energy levels are replaced with empirical energies derived from the MARVEL procedure (subsection 2.2.3). This process is hereby referred to as *Marvelisation*. For the MARVELised levels, the label used is "Ma". Another way to improve the quality of the predicted transitions, even when we lack experimental data, is the *Predicted Shifts* method (PS). The associated abbreviation is "PS". Details on the PS method can be found in subsection 2.2.5 and section 3.6. Finally, the "IE" label is used for the levels that have been updated using *isotopic extrapolation* method as discussed in subsection 2.2.4 and section 3.7.

2.2.3 MARVEL

To provide empirical energy levels we use the Measured Active Rotation Vibration Energy Level (MARVEL) algorithm [188–191]. MARVEL is a very important element for the work described in this thesis. The MARVEL procedure starts with the collection of a comprehensive dataset of measured spectroscopic transitions (the

Table 2.5: Source type abbreviations used to describe energy levels in hybrid (MARVELized) line lists.

Abbr	Meaning
Direct Predictions	
Ca	Calculated
Ma	MARVEL
EH	Effective Hamiltonian
Mo	MOLLIST
HI	HITRAN
Corrections	
PS	Predicted Shift
IE	Isotopologue Extrapolation

frequencies or line positions) from all relevant sources of the literature. Each transition is a connection between two energy states in the molecule; a lower state and an upper state. It is characterised by its frequency and an associated uncertainty, a measure of how precise the measurement is. It is essential that the transitions of the dataset are assigned a consistent set of quantum numbers that uniquely identify the energy states involved. To keep track of all these transitions, each one is labelled with a unique tag that specifies its origin and provides an identifier for reference.

The MARVEL algorithm interprets this dataset of spectral lines using a graph-theoretical approach. A graph is a mathematical structure made up of nodes and edges. For MARVEL, the nodes represent the molecule's discrete energy levels, while the edges represent the measured spectroscopic transitions between these levels (σ_{ij}^{obs}). The edge weights are associated with each line's uncertainty. This structure is referred to as a *spectroscopic network* (SN) [192–194]. The quantum mechanical selection rules form the connectivity of the spectroscopic network. They determine which transitions between energy levels are allowed, giving the network its specific shape and structure. Since the input transitions originate from various experimental sources with differing uncertainty estimates, previous versions of MARVEL (e.g. MARVEL3) initially grouped these transitions into segments based on the similarity of their uncertainties [191].

MARVEL minimises the residuals:

$$\sum_{ij} \frac{[(E_i - E_j) - \sigma_{ij}^{\text{obs}}]^2}{\delta_{ij}^2}. \tag{2.5}$$

Here, σ_{ij}^{obs} is the observed transition frequency, E_i and E_j are the empirical energy levels determined by MARVEL, and δ_{ij} is the uncertainty associated with the measured line. This leads to a system of linear equations

$$AX = B, \tag{2.6}$$

where,

$$A = a^T ga \tag{2.7}$$

and

$$B = a^T gY. \tag{2.8}$$

The matrix a contains elements $1, -1, 0$: 1 if E_j is the upper level of the ij_{th} transition, -1 if E_j is the lower level of the ij_{th} transition, 0 otherwise. The matrix g contains the uncertainties of the transitions, the $N \times 1$ matrix Y contains N input measured lines, and the resulting matrix X contains the energy values that connect all these transitions.

A network is considered self-consistent when all cycles within it satisfy the Ritz condition [19] within experimental uncertainty. Only self-consistent, well-connected networks can yield reliable rovibrational energy levels. Networks that do not connect with other components are called *floating networks*.

The goal is to transfer the high accuracy of the line position measurements to the empirical energy values that are determined through MARVEL. This process involves a meticulous evaluation of the self-consistency of the input transitions and their assignments, and iterative adjustments of their uncertainty values. Identifying the optimal set of transition uncertainties poses a significant challenge, however. Often, a manual increase of the transition uncertainties is required to create a self-

consistent network. This process is complicated because the uncertainties provided in experimental sources may be overly optimistic or pessimistic, making it difficult to determine the appropriate adjustments. If a transition has an overly optimistic uncertainty, MARVEL may place greater trust in it compared to another transition with a larger uncertainty, even if the latter is more accurate. Consequently, an incorrect energy may be derived for a state even though it is defined by multiple transitions.

For this reason, the most recent version (MARVEL 4) offers a feature known as the bootstrap method, which iteratively performs calculations to determine the optimal energy uncertainties [195]. MARVEL randomly increases each transition uncertainty multiple times, and for every sample, it recalculates the energies. After every calculation, it compares the resulting energies with the energies when the original uncertainties are used. Based on their difference, MARVEL assesses how reliable the final energy values are and gives a final set of suitable energy uncertainties that prevent overconfidence in potentially inaccurate measurements.

The self-consistency of the spectroscopic networks are assessed through *combination differences*; differences between pairs of transitions that share a common energy level. For example, if two transitions originate from the same lower state and lead to two different upper states, the difference in their transition frequencies should match the energy spacing between the two upper states. Agreement of such differences within uncertainty confirms the reliability of the transitions. Discrepancies can indicate experimental errors or misassignments. This is how MARVEL helps to identify outliers. Transitions are flagged as invalid if the ratio between the optimal uncertainty (i.e., the uncertainty a transition would require to be consistent with the network) and the original uncertainty exceeds a threshold of 100. These invalidated transitions are either corrected or annotated with a negative sign applied to their wavenumber values, to exclude them from further analysis by MARVEL.

The MARVEL 4 Online version [195] also offers enhanced flexibility in handling transition energy units. Unlike previous versions that exclusively used cm^{-1}, Marvel 4 Online can accommodate various units (cm^{-1}, Hz, kHz, MHz, GHz, and

THz). To support this expanded functionality, a segment file is included as an input, containing a list of source names paired with their respective units.

In practice, the MARVEL methodology is implemented using the MARVEL software written by Tibor Furtenbacher of Eotvos University, which automates the inversion of the measured transitions, iterative bootstrap uncertainty estimation (for MARVEL 4), and identification of inconsistent transitions. Nevertheless, careful preparation of the input dataset is the essential first step. Users must compile assigned spectral transitions from the literature, each including the line position, associated uncertainty, and quantum number labels. Consistency in quantum number assignment is critical, as it ensures correct construction of the spectroscopic network, and using the correct input uncertainty is important to allow MARVEL to weight transitions appropriately during the inversion. Once the dataset is prepared, MARVEL constructs the network, performs the initial inversion, and flags transitions that violate self-consistency criteria. Users should not blindly trust these flagged misassignments; manual review and, if necessary, correction are required to account for poorly estimated experimental uncertainties or other possible errors. While the software's bootstrap procedure proposes optimal energy uncertainties automatically, final verification by the user ensures the reliability of the results. In this way, the MARVEL procedure combines automated computation with targeted user data handling and oversight to ensure the highest reliability of the resulting energy levels.

2.2.4 Isotopic Extrapolation

In spectroscopic modelling, it is common practice to optimise the model for the main isotopologue of a given molecule, primarily due to the scarcity of experimentally assigned spectral data for other isotopologues. The variational line lists for other isotopologues can be constructed by adjusting the atomic masses in the model corresponding to the main isotopologue and preforming a new calculation.

Polyansky et al. [137] show that a more refined pseudo-hybrid line list for a given isotopologue can be derived by shifting each energy level regarding those in

the main variational and hybridised line lists, as expressed by the following equation:

$$\tilde{E}^{\text{iso}}_{\text{IE}} = \tilde{E}^{\text{iso}}_{\text{Ca}} + \left(\tilde{E}^{\text{main}}_{\text{obs}} - \tilde{E}^{\text{main}}_{\text{Ca}} \right), \tag{2.9}$$

Here, $\tilde{E}^{\text{main}}_{\text{Ca}}$ represents the variational energy of the main isotopologue, $\tilde{E}^{\text{iso}}_{\text{Ca}}$ is the variational energy of the isotopologue of interest, and $\tilde{E}^{\text{iso}}_{\text{IE}}$ refers to its isotopologue-extrapolated (IE) energy. $\tilde{E}^{\text{main}}_{\text{obs}}$ can originate from either MARVEL, or the Predicted Shifts method described in subsection 2.2.5. Essentially, this approach assumes that the energy residuals between the hybridised and variational line lists remain constant across all isotopologues, equivalent to assuming the Born-Oppenheimer approximation is accurate.

The energy levels that have been calculated with this method are assigned the label "IE" in the energy `.states` file.

2.2.5 Predicted Shifts

Variational line lists often extend to higher total angular momentum quantum numbers (J) than those available from experimental data, requiring extrapolations for levels beyond the observed range. Similarly, experimental data may be incomplete even within the observed J range, necessitating interpolations to fill in missing levels.

A more accurate estimation of the energy levels for unobserved rotational states can be achieved by applying a shift to the calculated energy levels. This synthetic shift can be estimated from the trends in the observed minus calculated (obs.-calc.) energy differences in that band, where "obs." refers to the experimentally-derived MARVEL energy levels and "calc." to the variationally computed energy levels. As a result, any discontinuities between MARVELised and calculated energy levels are removed. For the missing energies this is done by fitting to the obs.-calc. trends and predicting synthetic obs.-calc. values for them. Energy levels updated with this method are labelled "PS".

Chapter 3

Magnesium Oxide

3.1 Motivation

Due to the cosmic abundance of magnesium and oxygen and the strength of the bond, diatomic magnesium oxide (MgO) in the gas phase is known to be present in the upper atmosphere of Earth [196] and Mercury [197, 198], where it is believed to be produced by micrometeoroid impact. However, searches for gaseous MgO in the interstellar medium have thus far been unsuccessful [199, 200].

In its solid form, magnesium oxide is considered one of the most abundant rocks in the interiors of planets [201] and to be a component of interstellar dust [202–205]; certainly it is an important part of Earth's mantle [196], but the chemical identity of solid species is difficult to confirm remotely.

However, in ultra-hot rocky exoplanets like hot rocky super-Earths, often referred to as lava or magma worlds, the higher temperatures in the atmosphere are thought to favour the production of MgO vapour [206–209]. With high-quality spectral line lists, these hypotheses can be experimentally tested.

Li et al. [148] produced the LiTY variational line list covering the isotopologues $^{24}Mg^{16}O$, $^{24}Mg^{17}O$, $^{24}Mg^{18}O$, $^{25}Mg^{16}O$ and $^{26}Mg^{16}O$. While this line list was heavily tuned to experimental data, no formal MARVEL project was undertaken previously. In order to facilitate the detection of MgO in high-resolution studies we performed a MARVEL analysis of $^{24}Mg^{16}O$ and updated the line list to get spec-

troscopic accuracy for many of the strong spectral lines. The quantum numbers used for $^{24}Mg^{16}O$ are the electronic state, the vibrational number v, the rotational quantum number J, and the projection of the total electronic angular momentum Ω.

3.2 Quantum numbers and selection rules

Magnesium oxide is a heteronuclear diatomic molecule, and its energy-level structure is therefore much simpler than that of polyatomic systems. For a diatomic molecule, the total molecular energy is commonly separated into electronic, vibrational, and rotational contributions with additional fine-structure terms where relevant. The ground electronic state of MgO is the closed-shell singlet X $^1\Sigma^+$ and the lowest electronically excited states relevant to this work include a $^3\Pi$, which is the first excited triplet, A $^1\Pi$, and B $^1\Sigma^+$. The electronic angular momentum projection quantum number is $\Lambda = 0$ for the Σ states and $\Lambda = 1$ for the Π states. For triplet states such as a $^3\Pi$, the total spin is $S = 1$, producing three spin components $\Sigma = -1, 0, +1$, and the associated fine-structure splitting.

As a diatomic molecule, MgO has a single vibrational degree of freedom described by the vibrational quantum number $v = 0, 1, 2, \ldots$. The vibrational energies follow the approximate anharmonic expansion,

$$E_{\text{vib}} = \omega_e \left(v + \tfrac{1}{2}\right) - \omega_e x_e \left(v + \tfrac{1}{2}\right)^2 + \cdots . \tag{3.1}$$

For each vibrational level of each electronic state, rotational motion is described by the rotational quantum number J, where $J = 0, 1, 2, \ldots$. For Σ states the rotational energy reduces to the rigid-rotor expression:

$$E_r = BJ(J+1). \tag{3.2}$$

The projection of the total angular momentum along the internuclear axis is defined as

$$\Omega = |\Lambda + \Sigma|.$$

Thus, $\Omega = 1$ for singlet Π states, and $\Omega = 0, 1, 2$ for triplet Π states.

Since MgO is heteronuclear, it does not possess inversion symmetry and therefore has no gerade/ungerade classification. Instead, each rovibronic level is assigned a total parity, $+$ or $-$, and a rotationless parity, e or f. These are the parity labels used in the `.states` file in this work.

Both ^{24}Mg and ^{16}O have nuclear spin $I = 0$. Consequently, all MgO isotopologues considered in this work possess only a single nuclear-spin configuration and therefore exhibit no ortho/para distinction.

The dominant electric–dipole selection rules for heteronuclear diatomic molecules are

$$\Delta J = 0, \pm 1 \, (J = 0 \not\rightarrow J = 0), \tag{3.3}$$

$$\Delta v = \pm 1 \, \text{(fundamental transitions)}, \tag{3.4}$$

$$\Delta \Lambda = 0, \pm 1, \tag{3.5}$$

$$\Delta \Omega = 0, \pm 1. \tag{3.6}$$

For real anharmonic molecules, overtone and hot-band transitions with $\Delta v = \pm 2, \pm 3, \ldots$ also acquire non-zero intensity. Accordingly, the MgO MARVEL data set in this work includes transitions with $\Delta v > 1$ in addition to the fundamental bands.

3.3 A new MgO MARVEL analysis

A MARVEL analysis for the spectroscopic data of ^{24}Mg^{16}O was performed with results summarised in Table 3.1. A part of the final states file is shown in Table 3.2. We used Marvel4.1 and produced the MARVEL energy uncertainties with the bootstrapping method as described in [195]. The MARVEL uncertainties are shown in Figure 3.1.

A total of 1181 transitions were collected from 9 sources [20, 210–217]. 1169 of these transitions are validated through the MARVEL procedure and inverted to

Table 3.1: Overview of the MgO MARVEL compilation energy levels (EL) and comparison against DUO variational calculated energy levels ($|Ma - Ca|$), in cm^{-1}.

State	v range	J range	#ELs	Unc. range	Avg. Unc.	EL range	$\|Ma - Ca\|$ range	Mean $\|Ma - Ca\|$
X $^1\Sigma^+$	0-4	0-61	125	0-0.25	0.06	0-3042.13	0-1.54	0.07
A $^1\Pi$	0-3	1-62	368	0.001-0.25	0.09	3504.32-7055.19	0.0003-0.1	0.02
B $^1\Sigma^+$	0-1	0-42	71	0.003-0.14	0.06	20003.59-21387.62	0.00004-0.06	0.02
a $^3\Pi$	0-1	1-43	256	0.001-0.15	0.07	2551.29-4129.27	0.00006-0.33	0.03

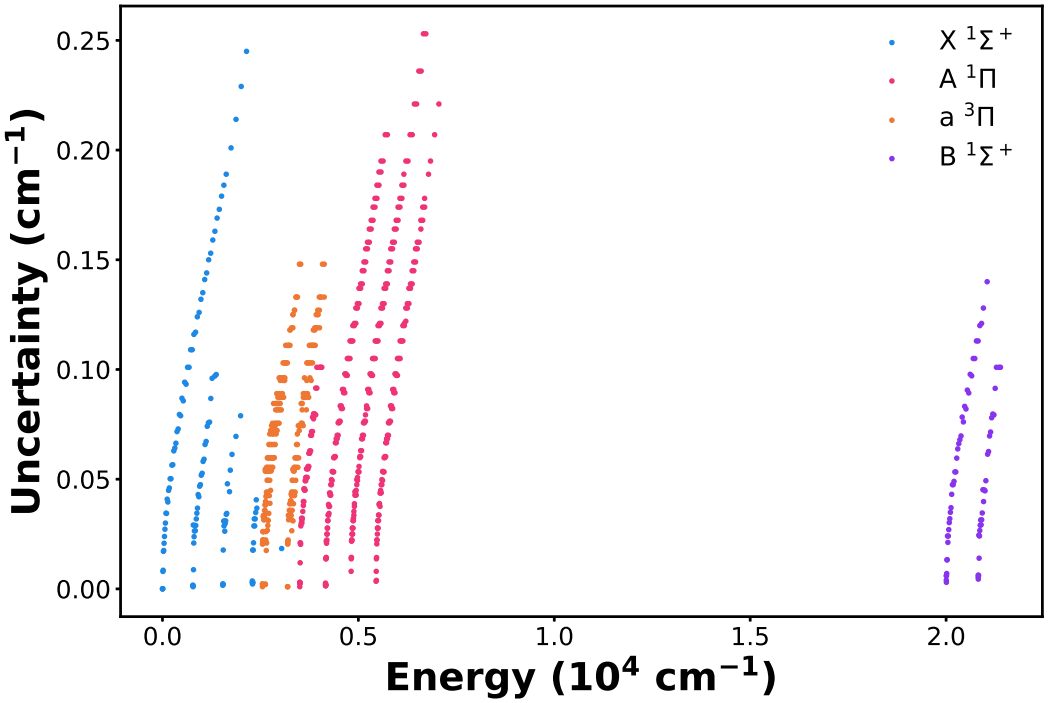


Figure 3.1: The MARVEL (Ma) energy uncertainties for ^{24}Mg^{16}O as a function of energy.

determine 820 empirical energy levels and uncertainties for the four lowest electronic states (X $^1\Sigma^+$, a $^3\Pi$, A $^1\Pi$, B $^1\Sigma^+$) and vibrational levels $v = 0 - 4$, with the highest rotational quantum number being $J_{\max} = 62$.

The relevant details can be found within section 3.4, including a full list of all the experimental data used in this analysis, a segment file connecting the sources to the wavenumber units used, a justification of the uncertainties considered for the line positions, a list of our MARVEL energy levels, and a list of papers considered but not used in the current work as well as the reasons for their exclusion.

3.4 Overview of experimental sources

Table 3.3 and Table 3.4 present all the experimental papers considered. They are given name tags composed of the last two digits of the year of their publication as well as the letters of the names of up to the first three co-authors. Further details of the papers considered and the use of the experimental data are provided below.

06KaKa [20] Observations of pure rotational transitions of MgO in the X $^1\Sigma^+$- X $^1\Sigma^+$ and a $^3\Pi$- a $^3\Pi$ systems ($v = 1-3$) are reported. The transitions are in the 7 - 14 cm^{-1} region and their uncertainty given in the paper and used in our network is $\sim 10^{-6}$ cm^{-1} .

86ToHo [212] Eight measured transitions are reported in this paper in the X $^1\Sigma^+$ electronic state for the vibrational bands ($v = 0-2$), in the 2 - 10 cm^{-1} frequency range. An uncertainty is provided in the original paper for each transition.

91CiHeBl [214] In this work twenty two observed lines are observed in the in the X $^1\Sigma^+$ electronic state. The frequency range is 731 - 806 cm^{-1}. We estimated the uncertainty from combination differences to be 10^{-3} cm^{-1} .

84StAzCa [211] Three measured transitions for the X $^1\Sigma^+$electronic state (v=0-1) and the 1.14-2.27 cm^{-1} frequency range are reported. An uncertainty is given in the original paper for each transition.

94MuRiPf [216] Observed transitions of the a $^3\Pi$ - X $^1\Sigma^+$ ($v = 0-1$) and A $^1\Pi$ - X $^1\Sigma^+$($v = 0-2$) bands are reported in this work. It is estimated that the accuracy of the data is better than 10^{-3} cm^{-1}, and we used this as the line position uncertainty.

94KaHiTa [215] This paper provides observed transitions in the infrared absorption spectrum of the A $^1\Pi$ - X $^1\Sigma^+$ system and the five vibrational bands $(1-0), (2-0), (3-0), (0-1)$. No line position uncertainty was provided in this work so it was estimated to be 0.008 cm^{-1} for the unblended and 0.016 cm^{-1} for the blended lines based on the magnitude of the combination differences.

Table 3.2: A part of the final `.states` file for $^{24}Mg^{16}O$.

i	$\tilde{E}$	$g_{\rm tot}$	J	unc	τ	g	$p_{+/-}$	$p_{e/f}$	State	v	Λ	Σ	Ω	Label	$\tilde{E}_{\rm Ca}$
1	0.000000	1	0.0	0.000000	NaN	0.000000	+	e	X(1SIGMA+)	0	0	0.0	0.0	Ma	0.000000
2	774.738739	1	0.0	0.001420	1.3596E+00	0.000000	+	e	X(1SIGMA+)	1	0	0.0	0.0	Ma	774.737704
3	1539.174552	1	0.0	0.001730	6.3331E-01	0.000000	+	e	X(1SIGMA+)	2	0	0.0	0.0	Ma	1539.136871
4	2292.687940	1	0.0	0.003610	3.9854E-01	0.000000	+	e	X(1SIGMA+)	3	0	0.0	0.0	Ma	2293.035126
5	2621.208578	1	0.0	0.004809	2.5844E-02	0.000000	+	e	a(3PI)	0	1	-1.0	0.0	PS	2621.207376
6	3037.070194	1	0.0	0.040000	2.2228E-01	0.000000	+	e	X(1SIGMA+)	4	0	0.0	0.0	Ca	3037.070194
7	3265.064334	1	0.0	0.043377	2.0867E-02	0.000000	+	e	a(3PI)	1	1	-1.0	0.0	PS	3264.977473
8	3770.264143	1	0.0	0.050000	9.7014E-02	0.000000	+	e	X(1SIGMA+)	5	0	0.0	0.0	Ca	3770.264143
9	3900.848866	1	0.0	0.030000	1.8289E-02	0.000000	+	e	a(3PI)	2	1	-1.0	0.0	Ca	3900.848866
10	4478.700487	1	0.0	0.040000	2.3189E-02	0.000000	+	e	a(3PI)	3	1	-1.0	0.0	Ca	4478.700487
11	4543.125919	1	0.0	0.060000	2.7738E-02	0.000000	+	e	X(1SIGMA+)	6	0	0.0	0.0	Ca	4543.125919

i: State counting number
$\tilde{E}$: Energy (in $\rm cm^{-1}$)
$g_{\rm tot}$: Total degeneracy
J: Total angular momentum
unc ($\Delta\tilde{E}$): Uncertainty (in $\rm cm^{-1}$)
τ: Lifetime (in s; calculated in ExoCross [8])
g: Lande g-factor
$p_{+/-}$: Total parity
$p_{e/f}$: Kronig rotationless parity
State: Electronic state
v: Vibrational quantum number
Λ: Projection of electronic orbital angular momentum on the internuclear axis
Σ: Projection of electronic spin angular momentum on the internuclear axis
Ω: Projection of the total angular momentum excluding nuclear spin along the internuclear axis
Label: Ma for experimental MARVEL energies, PS for energies from Predicted Shift method, Ca for unchanged calculated energy by Li et al. [148]
$\tilde{E}_{\rm Ca}$: DUO calculated energy by Li et al. [148]

84AzDyGe [210] Measured transitions in the band B $^1\Sigma^+$-X $^1\Sigma^+$ ($v = 1-1$, $v = 0-0$) are reported, in the 19971-20067 $\rm cm^{-1}$ range. An uncertainty is given in the original paper for each transition.

91IpCrFi [213] Observed transitions in the a $^3\Pi$-X $^1\Sigma^+$ ($v = 0-0$) and ($v = 0-1$), and D $^1\Delta$-a $^3\Pi$($v = 0-0$) and ($v = 1-1$) bands are being reported. No line position uncertainty was provided in this work so it was estimated to be 0.02 $\rm cm^{-1}$ based on the magnitude of the combination differences. We only used the a $^3\Pi$-X $^1\Sigma^+$ transitions for this project.

95MuThPf [217] Line measurements in the X $^1\Sigma^+$, a $^3\Pi$, A $^1\Pi$ states are reported in the range 1640-3510 $\rm cm^{-1}$. In the paper it is mentioned that the data accuracy is better than 10^{-3} $\rm cm^{-1}$ and this is the uncertainty we used for the line positions.

Table 3.3: Experimental data for MgO used in our analysis. State': Upper electronic state, State": Lower electronic state, v':upper state vibrational quantum number, v": lower state vibrational quantum number, wavelength range and mean line position uncertainty given in cm^{-1}, V/A: number of validated experimental transitions/total number of transitions.

Source	State'	State"	v'	v''	J range	Wavelength range	Mean Unc.	V/A
06KaKa [20]	X $^1\Sigma^+$	X $^1\Sigma^+$	1	1	6 - 11	7.9 - 12.5	10^{-6}	4/4
	X $^1\Sigma^+$	X $^1\Sigma^+$	2	2	6 - 12	7.8 - 13.5	10^{-6}	5/5
	X $^1\Sigma^+$	X $^1\Sigma^+$	3	3	6 - 12	7.7 - 13.3	10^{-6}	4/4
	a $^3\Pi$	a $^3\Pi$	0	0	7 - 13	7.02 - 13.03	10^{-6}	23/23
95MuThPf [217]	a $^3\Pi$	X $^1\Sigma^+$	0	0	0 - 15	2551.3 - 2622.95	10^{-3}	3/3
	a $^3\Pi$	X $^1\Sigma^+$	1	0	0 - 12	3193.1 - 3242.3	10^{-3}	5/5
	A $^1\Pi$	X $^1\Sigma^+$	0	0	1 - 7	3492.42 - 3504.3	10^{-3}	5/5
	A $^1\Pi$	X $^1\Sigma^+$	0	1	7 - 11	2709.13 - 2715.96	10^{-3}	2/2
	A $^1\Pi$	X $^1\Sigma^+$	1	3	2 - 14	1841.26 - 1872	10^{-3}	14/14
	A $^1\Pi$	X $^1\Sigma^+$	1	1	1 - 14	3356.9 - 3387.75	10^{-3}	4/4
	A $^1\Pi$	X $^1\Sigma^+$	1	2	1 - 9	2606.1 - 2623.34	10^{-3}	7/7
	A $^1\Pi$	X $^1\Sigma^+$	2	2	10 - 11	3249.8302	10^{-3}	1/1
	A $^1\Pi$	X $^1\Sigma^+$	3	3	0 - 6	3150.37 - 3158.23	10^{-3}	4/4
	A $^1\Pi$	X $^1\Sigma^+$	2	4	1 - 4	1775.07 - 1776.5	10^{-3}	3/3
94KaHiTa [215]	A $^1\Pi$	X $^1\Sigma^+$	1	0	1 - 57	3934.2 - 4163.8	10^{-2}	153/155
	A $^1\Pi$	X $^1\Sigma^+$	2	0	3 - 67	3970.7 - 4812.03	10^{-2}	199/200
	A $^1\Pi$	X $^1\Sigma^+$	3	0	3 - 58	5168.02 - 5452.4	10^{-2}	128/128
	A $^1\Pi$	X $^1\Sigma^+$	0	1	8 - 38	2648.6 - 3934.2	10^{-2}	87/87
	A $^1\Pi$	X $^1\Sigma^+$	2	1	11 - 32	4794.5 - 4812.03	10^{-2}	24/26
94MuRiPf [216]	a $^3\Pi$	X $^1\Sigma^+$	0	1	0 - 16	1775.4 - 1851.3	10^{-3}	12/12
	A $^1\Pi$	X $^1\Sigma^+$	0	2	0 - 15	1961.8 - 1967.03	10^{-3}	9/9
91IpCrFi [213]	B $^1\Sigma^+$	a $^3\Pi$	0	0	1 - 46	17378.3 - 27256.1	10^{-3}	326/328
	B $^1\Sigma^+$	a $^3\Pi$	0	1	0 - 49	16734.7 - 16979.1	10^{-3}	147/149
91CiHeBl [214]	X $^1\Sigma^+$	X $^1\Sigma^+$	1	0	2 - 32	733 - 805.6	10^{-3}	15/15
	X $^1\Sigma^+$	X $^1\Sigma^+$	2	1	7 - 28	738.43- 791.73	10^{-3}	7/7
86ToHo [212]	X $^1\Sigma^+$	X $^1\Sigma^+$	0	0	1 - 8	2.28 - 9.16	10^{-6}	3/3
	X $^1\Sigma^+$	X $^1\Sigma^+$	1	1	1 - 8	2.26 - 9.06	10^{-6}	3/3
	X $^1\Sigma^+$	X $^1\Sigma^+$	2	2	2 - 8	3.36 - 8.97	10^{-6}	2/2
84StAzCa [211]	X $^1\Sigma^+$	X $^1\Sigma^+$	0	0	0 - 1	1.14	10^{-5}	1/1
	X $^1\Sigma^+$	X $^1\Sigma^+$	1	1	0 - 2	1.13 - 2.27	10^{-5}	2/2
84AzDyGe [210]	B $^1\Sigma^+$	X $^1\Sigma^+$	0	0	0 - 40	19971.3 - 20062.5	10^{-3}	72/75
	B $^1\Sigma^+$	X $^1\Sigma^+$	1	1	0 - 56	20007.8 - 20066.7	10^{-3}	59/62

Table 3.4: Experimental data for MgO considered but not used in this analysis.

Source	States	Reason for exclusion
22LiMaLi [218]	-	No line measurements
21BaQiLi [219]		No line measurements
20BaQuLi [220]	-	No line measurements
18Bauschlicher [221]	-	No line measurements
17BaSc [222]	-	No line measurements
12StPeRa [223]	B $^1\Sigma^+$-X $^1\Sigma^+$	No line measurements
10MaBeYa [224]	-	No line measurements
06WaBr [34]	X $^1\Sigma^+$-E $^1\Sigma^+$, X $^1\Sigma^+$-F $^1\Pi$, X $^1\Sigma^+$-G $^1\Pi$	higher electronic states
04WaVaBe [33]	X $^1\Sigma^+$-E $^1\Sigma^+$	higher electronic state
04SoBolev [225]	-	No line measurements
03BeBuVa [226]	X $^1\Sigma^+$-F $^1\Pi$	higher electronic state
02DaDrAb [227]	B $^1\Sigma^+$-X $^1\Sigma^+$, B $^1\Sigma^+$-A $^1\Pi$	No line measurements
01DrDaAb [228]	B $^1\Sigma^+$-A $^1\Pi$	no lines measurements
01KiLiWa [229]	-	No line measurements
98SaWhKa [200]	X $^1\Sigma^+$-X $^1\Sigma^+$	two lines from 86ToHo
94GeHaTa [230]	-	No line measurements
91BoRo [231]	$d^3\Delta_2$-A $^1\Pi$, $d^3\Delta_i$-a $^3\Pi$	higher electronic state
91IpCrFi [213]	D $^1\Delta$- a $^3\Pi$	higher electronic state
89Matsui [232]	-	No line measurements
88Yarkony [233]	-	No line measurements
80BaSiYa [234]	-	No line measurements
78PaBaDo [235]	B $^1\Sigma^+$-X $^1\Sigma^+$, B $^1\Sigma^+$-A $^1\Pi$	No line measurements
77IkWoHa [236]	B $^1\Sigma^+$-X $^1\Sigma^+$, B $^1\Sigma^+$-A $^1\Pi$	not very accurate data
76AnBoPe [237]	E $^1\Sigma^+$-A $^1\Pi$	higher electronic state
76ScGa [238]		No line measurements
73Singh.b [239]	G $^1\Pi$-X $^1\Sigma^+$, G $^1\Pi$-A $^1\Pi$	higher electronic state
73Singh.a [240]	F $^1\Pi$- X $^1\Sigma^+$	higher electronic state
71MaVoCh [241]	-	No line measurements
71Singh [242]	E $^1\Sigma^+$-X $^1\Sigma^+$	higher electronic state
65TrEwxx [243]	D $^1\Delta$-A $^1\Pi$	higher electronic state
62Nicholls [244]	B $^1\Sigma^+$-X $^1\Sigma^+$, B $^1\Sigma^+$-A $^1\Pi$	No line measurements
62BrTrBe [245]	C $^1\Sigma^-$-A $^1\Pi$	higher electronic state
49LaUh [246]		No line measurements
32Mohanti [247]	-	Band heads only
30GhMaMu [248]	-	Band heads only

3.5 Uncertainties

The uncertainties for the MARVEL energy levels are illustrated in Figure 3.1. They were derived solely from the input transition uncertainties, resulting in an average value of 0.02 cm^{-1} across the four electronic states, without the bootstrap method. The input line position uncertainties were either taken as given in the individual sources, or manipulated so that they create a consistent energy level network as described in subsection 2.2.3. Details on the uncertainties used for every source are in section 3.4. However, applying the bootstrap method increased the average MARVEL energy uncertainty to 0.07 cm^{-1}.

For variationally calculated levels, the uncertainties are estimated assuming that the errors grow linearly with vibrational excitation but quadratically with rotational excitation; these assumptions are in accordance with our previous experience for a variety of species, as first adopted in [155]. We therefore estimate the uncertainties using the expression:

$$\Delta\tilde{E}_{\mathrm{Ca}} = a \cdot v + b \cdot J(J+1) + c, \tag{3.7}$$

where a, b and c are constants in units of cm^{-1}. This functional form is an empirical model chosen to reflect the observed increase in variational errors with increasing vibrational and rotational excitation. The initial minimum uncertainty determined for each electronic state is denoted by c, while a and b quantify the uncertainty scales for the vibrational v and rotational $J(J+1)$ parameters, respectively. Here, we adopted values of $a = 0.0001$ cm^{-1} and $b = 0.01$ cm^{-1} for all electronic states, $c = 0$ cm^{-1} for the ground state, and $c = 0.01$ cm^{-1} for all excited electronic states to estimate the uncertainties, with a maximum cutoff of 10 cm^{-1}. Unfortunately, due to a lack of experimental data for the b $^3\Sigma^+$ state we have little information to base the uncertainties of the energy levels in this state on; we estimated an uncertainty of 10 cm^{-1} for all energy levels in this state.

The availability of high-quality experimental data allows an assessment of the accuracy of the spectroscopic model for $^{24}Mg^{16}O$ in [148] and thus improves the

quality of our predicted uncertainties. For the four lowest-lying electronic states we find a high accuracy, with an average error of 0.029 cm^{-1} and maximum value 0.2 cm^{-1} within the states for which we had experimental data and applied the PS method (see Table 3.1 for J and v ranges). For all other cases, the errors exceed this value. For calculated levels, the errors are within 2 cm^{-1} for J values up to 140 and increase to a maximum of 10 cm^{-1} for the highest J values ($J > 300$).

3.6 Predicted shift energy levels

The predicted shift methodology has been previously employed in the construction of high-resolution line lists for AlO [249] and VO [169]. We also applied the PS method in this work to update calculated energy levels.

As is common with variational line lists, our computed levels extend to higher total angular momentum quantum numbers J than available experimental observations, and incomplete experimental data within this J range necessitate further adjustment. For the unobserved rotational states we interpolated by fitting to the obs. − calc. trends in a given spin-orbit and parity component of a vibronic state, defined by the electronic state, vibrational quantum number v, Ω and rotationless parity, and predicting synthetic obs. − calc. values for the missing levels. Specifically, for $^{24}Mg^{16}O$ this trend was captured by fitting the obs. − calc. values as a function of $J(J+1)$, either using a single linear fit or, when necessary, two separate linear segments to better represent the observed behaviour (see Figure 3.2). The apparent discontinuity in Figure 3.2 near $J = 15$ arises because low-J levels were partially constrained by experimental data incorporated into the potential energy surface by Li et al. [148], resulting in smaller obs. − calc. residuals in this region.

Energy shifts were also estimated conservatively for levels beyond the observed J range by extrapolating up to the highest J value included in the variational calculations. Similarly, this approach enables the estimation of energy levels at lower J values than those detected experimentally, which is particularly valuable when low-J transitions form dense band heads, making their assignment challeng-

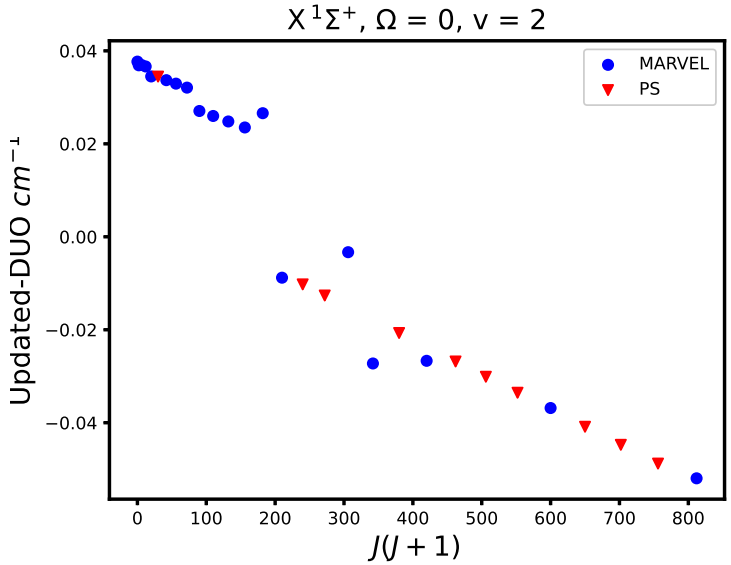


Figure 3.2: The predicted shifts (updated- calculated energy) for the X $^1\Sigma^+$, $v = 1$ state of X $^1\Sigma^+$ as a function of the $J(J+1)$ quantum number. The fitting was done using two linear segments. The blue points correspond to real obs. – calc. values and the red to PS.

ing. For the extrapolation to higher J, the predicted shifts were calculated as the mean of the last 10 obs. – calc. values within the observed range. Likewise, for extrapolation to lower J when necessary, we used the mean of the first 10 obs. – calc. values.

The uncertainties for PS levels for every state within the J range for which we have experimental data were calculated the same way as the energy values, as a fit of the MARVEL uncertainties. When extrapolating to lower J values, the PS level uncertainties were estimated to be simply equal to the standard deviation σ of the obs. – calc. Outside this range, the PS energy uncertainties were estimated as a function of the standard deviation of the known obs. – calc. data point in the band, σ. This σ value was used as a starting minimum uncertainty for the extrapolation; uncertainties were scaled for a level based on how much larger its J value was than the maximum J that occurred for the MARVEL data in that band, $J^{\mathrm{Ma}}_{\mathrm{max}}$. Taking $J_{\mathrm{ext}} = J - J^{\mathrm{Ma}}_{\mathrm{max}}$, the following equation was used:

$$\Delta\tilde{E}_{\mathrm{PS}} = a \cdot J_{\mathrm{ext}}(J_{\mathrm{ext}}+1) + \sigma, \tag{3.8}$$

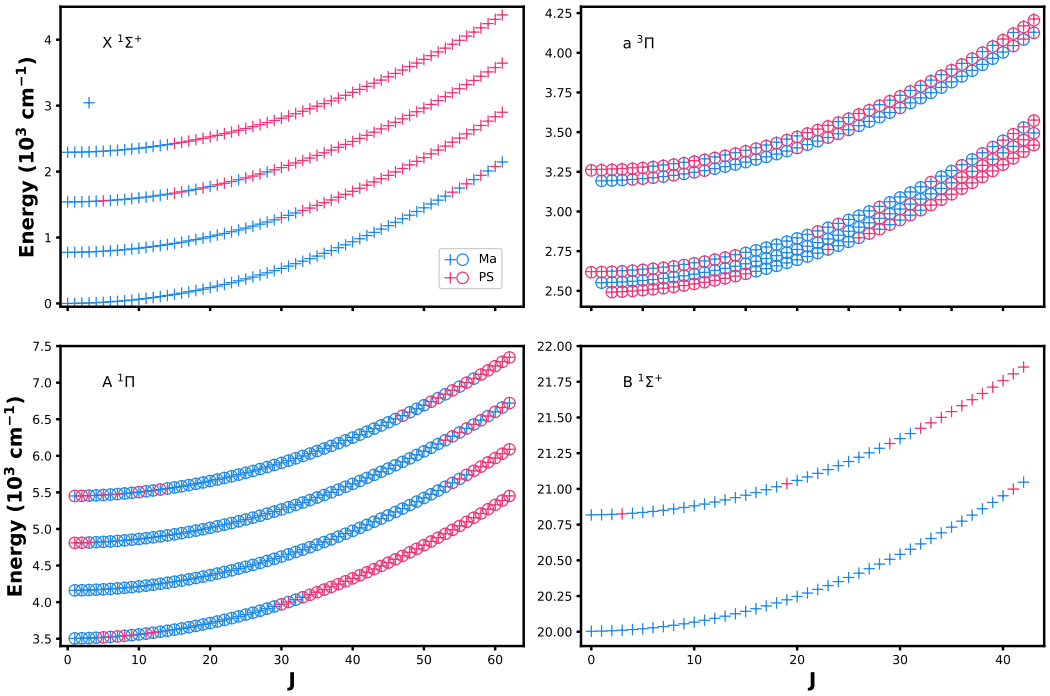


Figure 3.3: The updated MARVEL (Ma) and predicted shift (PS) energies for the X $^1\Sigma^+$, A $^1\Pi$, a $^3\Pi$, B $^1\Sigma^+$ electronic states of $^{24}Mg^{16}O$ as a function of the J quantum number. The 'o' symbol indicates f parity and the '+' symbol indicates e parity.

where a and $\tilde{E}_{\rm PS}$ are determined for each individual molecule. Where necessary, the uncertainties were extrapolated using $a = 0.0001$ cm^{-1} (see Equation 3.8) and a maximum cutoff for $\Delta\tilde{E}_{\rm PS}$ of 10 cm^{-1}. The interpolation and extrapolation of predicted energy levels from the MARVEL energies to other rotational levels of the same vibronic state is visualised most clearly in Figure 3.3. For example, for the case of B $^1\Sigma^+$ electronic state with $\Omega = 0$ and $v = 1$ the observed data range from $J = 0$ to $J = 31$. By calculating the predicted shifts we estimate the obs. $-$ calc. of the missing levels as shown in the Figure 3.4. For levels of $J > 31$, we calculated a predicted shift of -0.0235 cm^{-1}. In the case of a $^3\Pi$ electronic state with $v = 1$ and $\Omega = 0$ we only had experimental data and, hence, MARVEL energies for the e parity. For this case, we applied the predicted shifts of the e parity to the energies of the f parity, for which we lacked empirical energies.

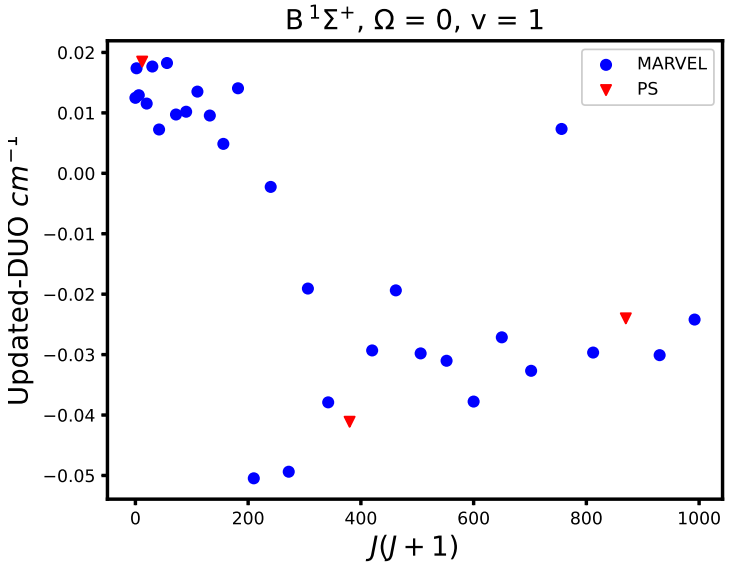


Figure 3.4: The predicted shifts (updated- calculated energy) for the B $^1\Sigma^+$, $v = 1$ state of B $^1\Sigma^+$ as a function of the $J(J+1)$ quantum number. The blue points correspond to real obs. − calc. values and the red to PS.

3.7 Isotopologue-extrapolation energy levels

The isotopologue-extrapolation (IE) method is a very effective way to provide improved accuracy for isotopologue spectra as outlined in subsection 2.2.4. This method is grounded in the well-established understanding of how nuclear mass influences vibrational energy levels, combined with the assumption that, to a high degree of approximation, the potential energy surface remains the same across isotopologues. The IE method has been used in several works [149, 249–260] in order to improve the accuracy of variational calculations for several important isotopologues.

The line lists for the $^{24}Mg^{17}O$, $^{24}Mg^{18}O$, $^{25}Mg^{16}O$ and $^{26}Mg^{16}O$ isotopologues were updated in this work, using the isotopologue extrapolation (IE) correction methodology according to the Equation 2.9. For the energy levels of the main isotopologue $^{24}Mg^{16}O$ which were updated either with a MARVEL energy (Ma) or with the predicted shifts (PS), we updated the respective level of the other four isotopologues applying the same final pseudo-experimental correction.

In total, 7017 energy levels were updated for each of the five isotopologues

Table 3.5: An extract of the final `.states` file for $^{25}Mg^{16}O$.

i	$\tilde{E}$	g_{tot}	J	unc	g	$p_{+/-}$	$p_{e/f}$	State	v	Λ	Σ	Ω	Label	$\tilde{E}_{Ca}$
1	0.000000	6	0	0.000000	0.000000	+	e	X(1SIGMA+)	0	0	0	0	IE	0.000000
638	1.125503	18	1	0.000100	0.000000	-	e	X(1SIGMA+)	0	0	0	0	IE	1.125759
1025	3.377053	30	2	0.000142	0.000000	+	e	X(1SIGMA+)	0	0	0	0	IE	3.377247
2290	6.754304	42	3	0.000173	0.000000	-	e	X(1SIGMA+)	0	0	0	0	IE	6.754408
2739	11.256836	54	4	0.015880	0.000000	+	e	X(1SIGMA+)	0	0	0	0	IE	11.257156
4004	16.885036	66	5	0.016980	0.000000	-	e	X(1SIGMA+)	0	0	0	0	IE	16.885375
4453	23.641140	78	6	0.034200	0.000000	+	e	X(1SIGMA+)	0	0	0	0	IE	23.638924
5718	31.517369	90	7	0.035000	0.000000	-	e	X(1SIGMA+)	0	0	0	0	IE	31.517628
6167	40.521272	102	8	0.041600	0.000000	+	e	X(1SIGMA+)	0	0	0	0	IE	40.521289
7432	50.643556	114	9	0.047800	0.000000	-	e	X(1SIGMA+)	0	0	0	0	IE	50.649676
7881	61.897073	126	10	0.054400	0.000000	+	e	X(1SIGMA+)	0	0	0	0	IE	61.902532
9146	74.277525	138	11	0.060000	0.000000	-	e	X(1SIGMA+)	0	0	0	0	IE	74.279569

Table 3.6: An extract of the final `.states` file for $^{24}Mg^{17}O$.

i	$\tilde{E}$	g_{tot}	J	unc	g	$p_{+/-}$	$p_{e/f}$	State	v	Λ	Σ	Ω	Label	$\tilde{E}_{Ca}$
1	0.000000	6	0	0.000000	0.000000	+	e	X(1SIGMA+)	0	0	0	0	IE	0.000000
643	1.103342	18	1	0.000100	0.000000	-	e	X(1SIGMA+)	0	0	0	0	IE	1.103598
1033	3.310571	30	2	0.000142	0.000000	+	e	X(1SIGMA+)	0	0	0	0	IE	3.310765
2307	6.621344	42	3	0.000173	0.000000	-	e	X(1SIGMA+)	0	0	0	0	IE	6.621448
2759	11.035243	54	4	0.015880	0.000000	+	e	X(1SIGMA+)	0	0	0	0	IE	11.035563
4033	16.552661	66	5	0.016980	0.000000	-	e	X(1SIGMA+)	0	0	0	0	IE	16.553000
4485	23.175837	78	6	0.034200	0.000000	+	e	X(1SIGMA+)	0	0	0	0	IE	23.173621
5759	30.897003	90	7	0.035000	0.000000	-	e	X(1SIGMA+)	0	0	0	0	IE	30.897262
6211	39.723712	102	8	0.041600	0.000000	+	e	X(1SIGMA+)	0	0	0	0	IE	39.723729
7485	49.646681	114	9	0.047800	0.000000	-	e	X(1SIGMA+)	0	0	0	0	IE	49.652801
7937	60.678773	126	10	0.054400	0.000000	+	e	X(1SIGMA+)	0	0	0	0	IE	60.684232
9211	72.815701	138	11	0.060000	0.000000	-	e	X(1SIGMA+)	0	0	0	0	IE	72.817745

for the four lowest electronic states using the IE method. The energy uncertainties for the four isotopologues were estimated as twice the uncertainty of the main isotopologue. For the cases without matches to the main (labelled as Ca in the `.states` file), Equation 3.7 was used with a maximum cutoff of 10 cm^{-1}, and with $a = 0.0001$ cm^{-1} $b = 0.01$ cm^{-1} for all electronic states, and c as the average shift for each electronic state. Tables 3.5 to 3.8 contain extracts of the states files for the isotopologues.

Table 3.7: An extract of the final `.states` file for $^{24}Mg^{18}O$.

i	$\tilde{E}$	g_{tot}	J	unc	g	$p_{+/-}$	$p_{e/f}$	State	v	Λ	Σ	Ω	Label	$\tilde{E}_{Ca}$
1	0.000000	1	0	0.000000	0.000000	+	e	X(1SIGMA+)	0	0	0	0	IE	0.000000
649	1.067541	3	1	0.000100	0.000000	-	e	X(1SIGMA+)	0	0	0	0	IE	1.067797
1043	3.203171	5	2	0.000142	0.000000	+	e	X(1SIGMA+)	0	0	0	0	IE	3.203365
2327	6.406549	7	3	0.000173	0.000000	-	e	X(1SIGMA+)	0	0	0	0	IE	6.406653
2783	10.677263	9	4	0.015880	0.000000	+	e	X(1SIGMA+)	0	0	0	0	IE	10.677583
4067	16.015714	11	5	0.016980	0.000000	-	e	X(1SIGMA+)	0	0	0	0	IE	16.016053
4523	22.424148	13	6	0.034200	0.000000	+	e	X(1SIGMA+)	0	0	0	0	IE	22.421932
5807	29.894808	15	7	0.035000	0.000000	-	e	X(1SIGMA+)	0	0	0	0	IE	29.895067
6263	38.435260	17	8	0.041600	0.000000	+	e	X(1SIGMA+)	0	0	0	0	IE	38.435277
7547	48.036236	19	9	0.047800	0.000000	-	e	X(1SIGMA+)	0	0	0	0	IE	48.042356
8003	58.710613	21	10	0.054400	0.000000	+	e	X(1SIGMA+)	0	0	0	0	IE	58.716072
9287	70.454122	23	11	0.060000	0.000000	-	e	X(1SIGMA+)	0	0	0	0	IE	70.456166

Table 3.8: An extract of the final `.states` file for $^{26}Mg^{16}O$.

i	$\tilde{E}$	g_{tot}	J	unc	g	$p_{+/-}$	$p_{e/f}$	State	v	Λ	Σ	Ω	Label	$\tilde{E}_{Ca}$
1	0.000000	1	0	0.000000	0.000000	+	e	X(1SIGMA+)	0	0	0	0	IE	0.000000
643	1.108687	3	1	0.000100	0.000000	-	e	X(1SIGMA+)	0	0	0	0	IE	1.108943
1033	3.326606	5	2	0.000142	0.000000	+	e	X(1SIGMA+)	0	0	0	0	IE	3.326800
2306	6.653412	7	3	0.000173	0.000000	-	e	X(1SIGMA+)	0	0	0	0	IE	6.653516
2757	11.088688	9	4	0.015880	0.000000	+	e	X(1SIGMA+)	0	0	0	0	IE	11.089008
4030	16.632825	11	5	0.016980	0.000000	-	e	X(1SIGMA+)	0	0	0	0	IE	16.633164
4481	23.288062	13	6	0.034200	0.000000	+	e	X(1SIGMA+)	0	0	0	0	IE	23.285846
5753	31.046626	15	7	0.035000	0.000000	-	e	X(1SIGMA+)	0	0	0	0	IE	31.046885
6204	39.916072	17	8	0.041600	0.000000	+	e	X(1SIGMA+)	0	0	0	0	IE	39.916089
7472	49.887114	19	9	0.047800	0.000000	-	e	X(1SIGMA+)	0	0	0	0	IE	49.893234
7921	60.972610	21	10	0.054400	0.000000	+	e	X(1SIGMA+)	0	0	0	0	IE	60.978069
9186	73.168273	23	11	0.060000	0.000000	-	e	X(1SIGMA+)	0	0	0	0	IE	73.170317

We directly verified the quality of our isotopologue-extrapolation correction by comparing against available experimental data. Specifically, we assessed a small part of the updated line lists for the isotopologues $^{25}Mg^{16}O$ and $^{26}Mg^{16}O$ for which we found measured spectra recorded by Kagi et al. [215] and Törring et al. [212]: Kagi et al. [215] recorded transitions in the A $^1\Pi$ – X $^1\Sigma^+$ electronic band and the $v_A - v_X = 1 - 0$ vibrational band with $J = 6 - 41$ for $^{25}Mg^{16}O$ and $J = 6 - 42$ for $^{26}Mg^{16}O$, and Törring et al. [212] published six microwave transitions with $J = 0 - 7$ for $^{26}Mg^{16}O$ with $v = 0$.

$^{26}Mg^{16}O$

For $^{26}Mg^{16}O$ the average residues in positions against experiment for four rotational X $^1\Sigma^+$-X $^1\Sigma^+$ transitions are 1.2 $\times 10^{-4}$ cm^{-1} without IE correction and 6.7$\times 10^{-6}$ cm^{-1} with IE correction, while for the rovibronic A $^1\Pi$-X $^1\Sigma^+$ band, the IE correction had a more modest reduction in errors from 0.027 cm^{-1} to 0.021 cm^{-1}. The experimental data mostly agreed with our line list energies within their mutual estimated uncertainties.

$^{25}Mg^{16}O$

Similar comparisons for $^{25}Mg^{16}O$ rovibronic A $^1\Pi$ –X $^1\Sigma^+$ transitions found that for the P and Q branches, applying the IE correction led to a reduction in average residual from 0.017 cm^{-1} to 0.012 cm^{-1}. However, the residuals associated with the R branch transition were notably larger (0.05 cm^{-1} average) and did not signif-

icantly change with applying the IE correction; the likely cause of this difference is incorrect assignments of the experimental data.

3.8 Outlook

The LiTY line list [148] for $^{24}Mg^{16}O$ was updated by incorporating 820 MARVEL (Ma), 6197 predicted shift (PS) energy levels into the line list, with 179 825 variationally calculated (Ca) energy levels retained for vibronic levels without any experimental data. 21.4% of the transitions between the MARVEL energy levels have a resolving power $R = \lambda/\Delta\lambda$ larger than 100 000. These transitions are now available in the new ExoMolHR database [180]. The distribution of energy levels within each electronic state depending on their source is shown in Figure 3.5. A consistent pattern is observed across most molecules, where the MARVEL energy levels primarily focus on the low-lying rovibronic states within each electronic state, complemented by the predicted shifts (PS) and the calculated levels.

The `.trans` files for all isotopologues were cleaned to remove negative transition frequencies. Specifically, 92, 136, 139, 131, and 127 transitions were removed for the $^{24}Mg^{16}O$ $^{24}Mg^{17}O$, $^{24}Mg^{18}O$, $^{25}Mg^{16}O$ and $^{26}Mg^{16}O$ isotopologues, respectively. The `.states` files for the $^{24}Mg^{17}O$, $^{24}Mg^{18}O$, $^{25}Mg^{16}O$ and $^{26}Mg^{16}O$ isotopologues were updated using the isotopologue extrapolation (IE) correction methodology. Due to lack of experimental data, we verified a small portion of the lines for the two isotopologues $^{25}Mg^{16}O$ and $^{26}Mg^{16}O$.

The transition source type plot for MgO is shown in Figure 3.6. This peak in Ma and PS involved transitions near $10^{-18/19}$ is atypical and indicates that some of the weaker spectral bands have been more heavily studied than the spectral band that is strongest at 2000 K. The MARVEL data for this molecule is reasonably modest with the predicted shift data crucial for dramatically extending the number of transitions whose wavenumbers are known to reasonably high accuracy.

The absorption cross section between the several electronic bands computed at 2 000 K is illustrated in Figure 3.7. The strongest transitions around 2 000 cm^{-1} or

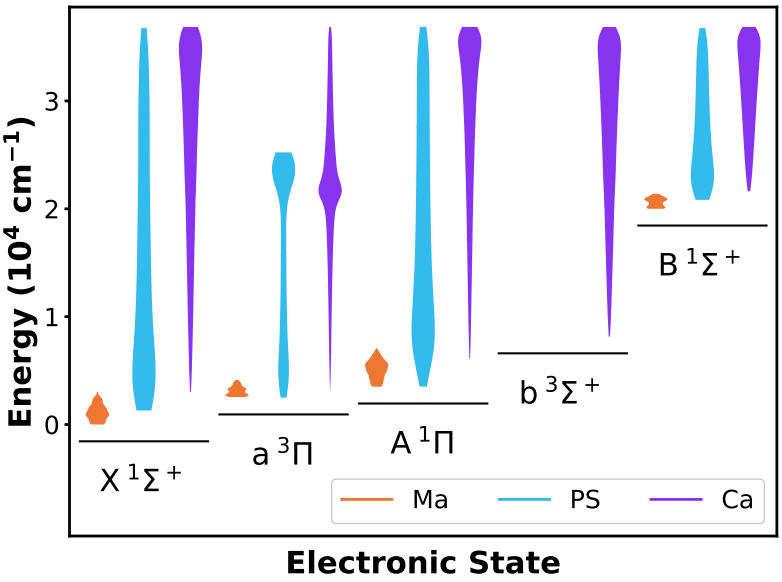


Figure 3.5: The energy distribution for the rovibronic states of $^{24}Mg^{16}O$ as a function of energy source type in each electronic state.

500 nm are the B $^1\Sigma^+$ - X $^1\Sigma^+$ band, but the hot band B $^1\Sigma^+$ - A $^1\Pi$ transition dominates for most of the visible spectra with the A $^1\Pi$ - X $^1\Sigma^+$ transition dominating the near IR region. The spin forbidden B $^1\Sigma^+$ - a $^3\Pi$ band displays significant intensity due to a $^3\Pi$ - A $^1\Pi$ spin-orbit coupling that mixes their wavefunctions. The experimentally unobserved band b $^3\Sigma^+$-a $^3\Pi$ is confirmed to be less intense than the rovibronic A $^1\Pi$ - X $^1\Sigma^+$ manifold across the full spectral region.

The high-resolution and total cross-section of MgO is shown in Figure 3.8 at 2000 K. In spectral regions where the MARVEL and total cross-sections overlap, then the line list is very suitable for high-resolution cross-correlation (HRCC). In the case of MgO, due to the limited experimental data, this region is very small (a few narrow windows between around 1.9 and 3 μm, and between 0.64 - 0.7 μm). In the absence of perturbations, predicted shift may be sufficiently reliable for HRCC especially for high signal-to-noise observations; in this case, the suitable spectral windows for HRCC in MgO extend to approximately 0.58 - 0.7 μm and 1.9 to 10 μm). Comparing with Figure 3.9 we see that in cooler temperatures the line list is potentially more suitable for high-resolution studies as the overlap becomes slightly larger.

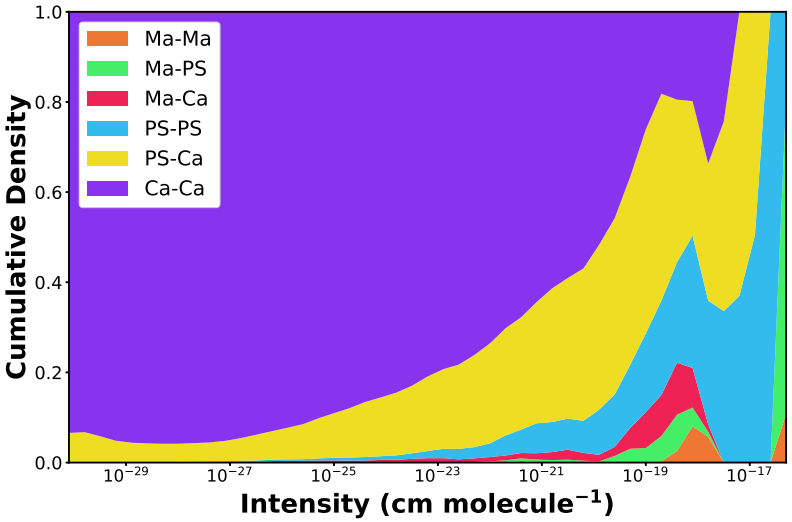


Figure 3.6: The transition source type for $^{24}Mg^{16}O$, i.e. the cumulative density of transitions as a function of intensity depending on energy source type, computed at 2000 K using the program ExoCross [8]. Colours indicate the source type of the transition, defined by the pair of energy-level origins (calculated, Marvel, or predicted shifts), irrespective of whether a given label refers to the upper or lower level.

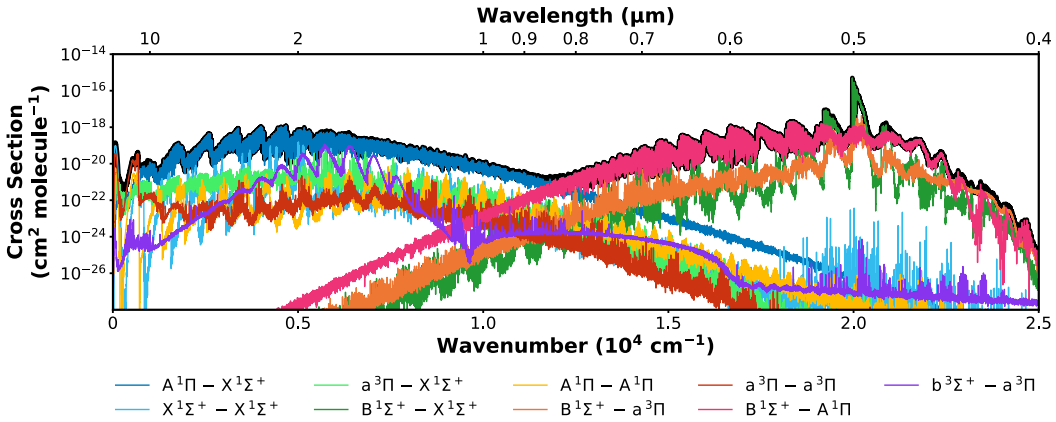


Figure 3.7: The $^{24}Mg^{16}O$ absorption cross section computed at 2000 K using the program ExoCross [8] with Gaussian line profiles of 1.0 cm^{-1} half-width half-maximum. The black cross section shows all transitions in the line list with decomposition into dominant electronic bands.

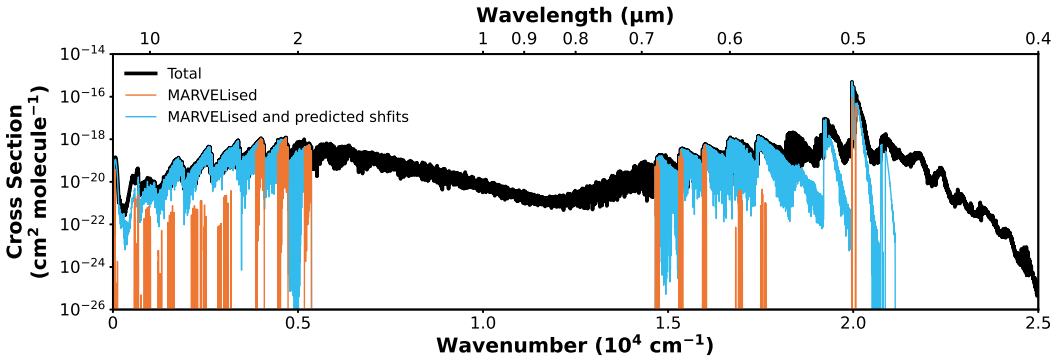


Figure 3.8: The $^{24}Mg^{16}O$ absorption cross section computed at 2000 K using the program ExoCross [8] with Gaussian line profiles of 1.0 cm^{-1} half-width half-maximum. The black cross section shows all transitions in the line list, whereas the orange cross section shows only MARVEL (Ma) experimental transitions (with variational intensities), and the blue cross section shows all possible transitions between MARVEL (Ma) and predicted shift (PS) energy levels (with variational intensities).

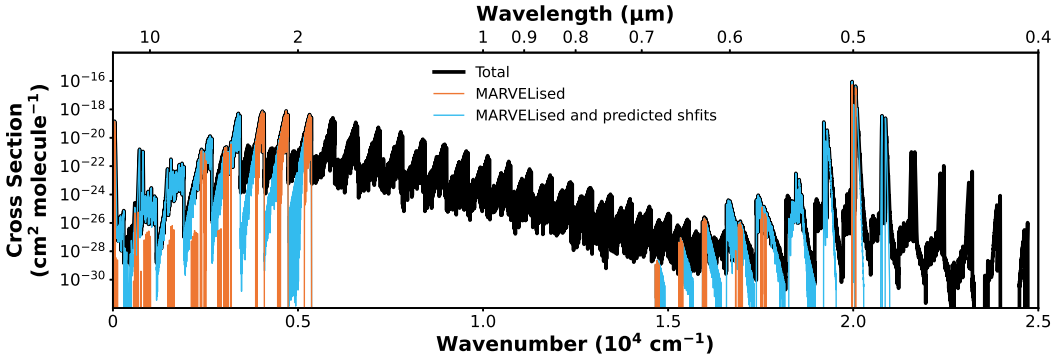


Figure 3.9: The $^{24}Mg^{16}O$ absorption cross section computed at 296 K using the program ExoCross [8] with Gaussian line profiles of 1.0 cm^{-1} half-width half-maximum. The black cross section shows all transitions in the line list, whereas the orange cross section shows only MARVEL (Ma) experimental transitions (with variational intensities), and the blue cross section shows all possible transitions between MARVEL (Ma) and predicted shift (PS) energy levels (with variational intensities).

The PS methodology used in this work enabled the extrapolation of experimental data to higher J values, offering a potentially reliable approach for HRCC detections of MgO. While the experimental data available were limited to small rotational quantum numbers, higher-resolution data for the four lowest electronic states of MgO are essential for more robust searches. Furthermore, Predicted shift methodology is only feasible if some rotational states of a given vibronic level are known. Data for the $v = 2, 3$ B $^1\Sigma^+$ state, as well as for any levels of the b $^3\Sigma^+$ electronic states, would significantly enhance the analysis. As illustrated in Figures 3.6 and 3.8, acquiring such data is a high priority for advancing high-resolution cross-correlation techniques.

Chapter 4

Titanium Oxide

4.1 Motivation

An accurate molecular line list for titanium oxide (TiO) is essential for constraining titanium abundances in low-temperature environments ($< 4000\,K$), where titanium is primarily bound in titanium oxide (TiO) molecules [251, 261–263]. TiO absorption features dominate the spectral optical and near-infrared regions [149]. This makes TiO line lists useful for probing features of several objects, including M dwarfs [264, 265], cool giant stars [266–269], and protostars [270–272]. In addition, numerous studies have investigated the presence of TiO in the atmospheres of hot Jupiters, with tentative detections reported in several cases. Evidence of TiO has been tentatively observed on planets such as WASP-69 b [273], WASP-33 b [274–276], HAT-P-41b [277, 278], WASP-127b [279], HD 209458b [280, 281], and WASP-12b [282]. However, subsequent studies have failed to confirm TiO in WASP-12b [283, 284]. For WASP-19b, a probable detection has been reported [285], but other studies have not confirmed its presence [286, 287]. It is generally accepted to also be present on the atmosphere of WASP-189 b [288, 289] and has not been detected in WASP-121b after initial evidence of its presence [290], followed by studies that suggest depletion of Ti-bearing species via a cold-trap mechanism [291–297].

The presence of TiO and vanadium oxide (VO) in these planets' atmospheres

is thought to increase the optical opaciy at high altitudes (low pressures) and to subsequently contribute to the formation of temperature inversions [298, 299], where the upper atmosphere is hotter than the lower atmosphere. The first evidence of such thermal inversions was observed by Richardson et al. [300] for HD 209458b and by Harrington et al. [301] for HD 149026b. The two molecules are expected to exist in significant quantities at temperatures exceeding $\sim$ 1400 K, creating two distinct regimes in which hot Jupiter atmospheres can be classified [299, 302, 303]: those hot enough to retain TiO and VO in the gas phase and develop temperature inversions, and those cooler where these species condense out, preventing inversions from forming. Accurately quantifying TiO abundance is essential for understanding atmospheric dynamics in hot Jupiters, requiring high-accuracy and high-completeness spectral data for reliable detection and precise measurement across different exoplanetary atmospheres [302]. Given the ongoing controversy surrounding TiO detections in some hot Jupiters [276], ensuring the completeness and accuracy of TiO spectral data is critical for robustly assessing modeling results.

Various TiO line lists have been developed [149, 304–309]. The ExoMol TiO line list, Toto, was published by McKemmish et al. [149] and contained 301 245 Ca (variational DUO) and 17 802 Ma (experimentally-derived MARVEL) energy levels for the electronic states X $^3\Delta$, a $^1\Delta$, d $^1\Sigma^+$, E $^3\Pi$, A $^3\Phi$, b $^1\Pi$, B $^3\Pi$, C $^3\Delta$, c $^1\Phi$, f $^1\Delta$, e $^1\Sigma^+$. Pavlenko et al. [251] assessed the Toto line list and found that it provides a more accurate representation of M-dwarf spectra compared to other available TiO line lists. It effectively captures the fine details in line positions and intensities, reproduces the observed band heads of TiO isotopologues, and can be used to determine Ti isotope abundances in M-star atmospheres. However, as pointed out by Hoeijmakers et al. [103] it is important to keep improving the accuracy of the line list to spectral resolutions equal or better than $\sim$ 100 000.

In mid-2021, the Toto line list for TiO was updated to correct an oversight in the original 2019 release in which the a $^1\Delta$ and e $^1\Sigma^+$ electronic states were initially not MARVELised. This 2021 update replaced the original DUO variational energy levels with experimentally-derived MARVEL energy levels for 660 energy levels in

the a $^1\Delta$ state and 98 energy levels of the e $^1\Sigma^+$ state. This update improved the high-resolution accuracy of the line list, particularly in the spectral regions dominated by transitions involving these states, particularly 2000 – 2500 cm^{-1} (4 – 5 μm), 3000 – 3500 cm^{-1} (2.8 – 3.3 μm), 9000 – 9500 cm^{-1} (1.05 – 1.10 μm), 10 000 – 10 500 cm^{-1} (0.95 – 1.00 μm), 11 000 – 11 500 cm^{-1} (0.87 – 0.91 μm).

Here, I report on updates to the Toto line list for all isotopologues. The 2021 update is superseded by the 2024 update which was published by McKemmish et al. [1]. Specifically, in this 2024 TiO update, we construct a hybridised line list by combining the calculated variational DUO energy levels (Ca) from the 2019 Toto spectroscopic model [149], an updated MARVEL compilation (Ma) and new predicted shift energy levels (PS). This update also provides uncertainty estimates for all energies, which were not present in the original 2019 line list. The spectroscopic model for TiO has not been refit for this update.

4.2 Quantum numbers and selection rules

Titanium oxide is a heteronuclear diatomic molecule, and its energy-level structure is described using the same set of quantum numbers and conventions as for MgO (see section 3.2). The primary difference is the open-shell character of TiO and the larger number of low-lying electronic states relevant to this work.

The ground electronic state of TiO is the open-shell triplet X $^3\Delta$. The electronically excited states considered here include the singlet states a $^1\Delta$, d $^1\Sigma^+$, b $^1\Pi$, c $^1\Phi$, f $^1\Delta$, and e $^1\Sigma^+$, as well as the triplet states A $^3\Phi$, B $^3\Pi$, C $^3\Delta$, and E $^3\Pi$. The electronic angular momentum projection quantum number takes the values $\Lambda = 0, 1, 2$, and 3 for Σ, Π, Δ, and Φ states, respectively. All remaining quantum numbers, parity conventions, and electric–dipole selection rules for TiO are identical to those described for MgO in section 3.2. So, the quantum numbers used for ^{48}Ti^{16}O are the electronic state, the vibrational number v, the rotational quantum number J, and the projection of the total electronic angular momentum Ω.

4.3 2024 MARVEL update

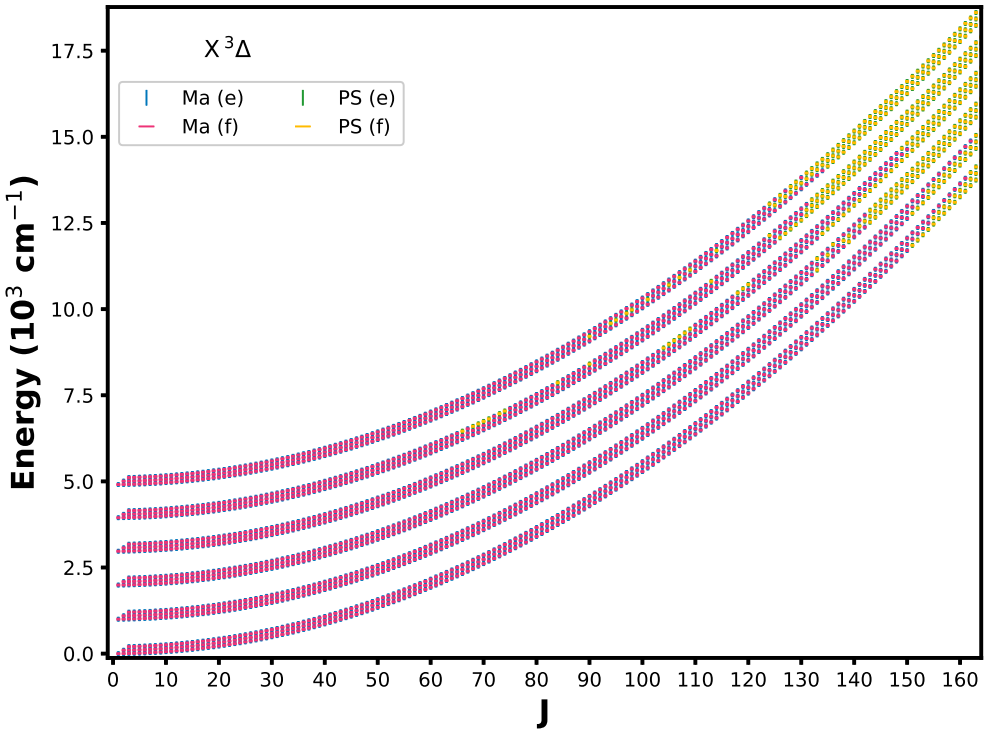
The MARVEL energy levels of $^{48}Ti^{16}O$ were first compiled by McKemmish et al. [310] and were used to update the 2019 Toto line list [149]. We performed an update on the MARVEL energies using MARVEL4.1 [195] by expanding the TiO MARVEL dataset to incorporate new experimental data for the E $^3\Pi$ – X $^3\Delta$ [311] (659 transitions, all validated) and B $^3\Pi$ – X $^3\Delta$ bands [312] (5506 transitions, all validated), as well as new experimental transitions for the X $^3\Delta$ rovibrational band were included from 19BrWaTu [313] (16 transitions, all validated) and 21WiBrDo [314] (514 transitions, all validated). For details on the experimental sources, see Table 4.1.

In cases of inconsistencies in the network, the newer data was preferred, and inconsistent older data were removed from the final spectroscopic network. Most notably, 179 lines from the 73Phillips [315] data were invalidated, which were previously found to be unreliable [310].

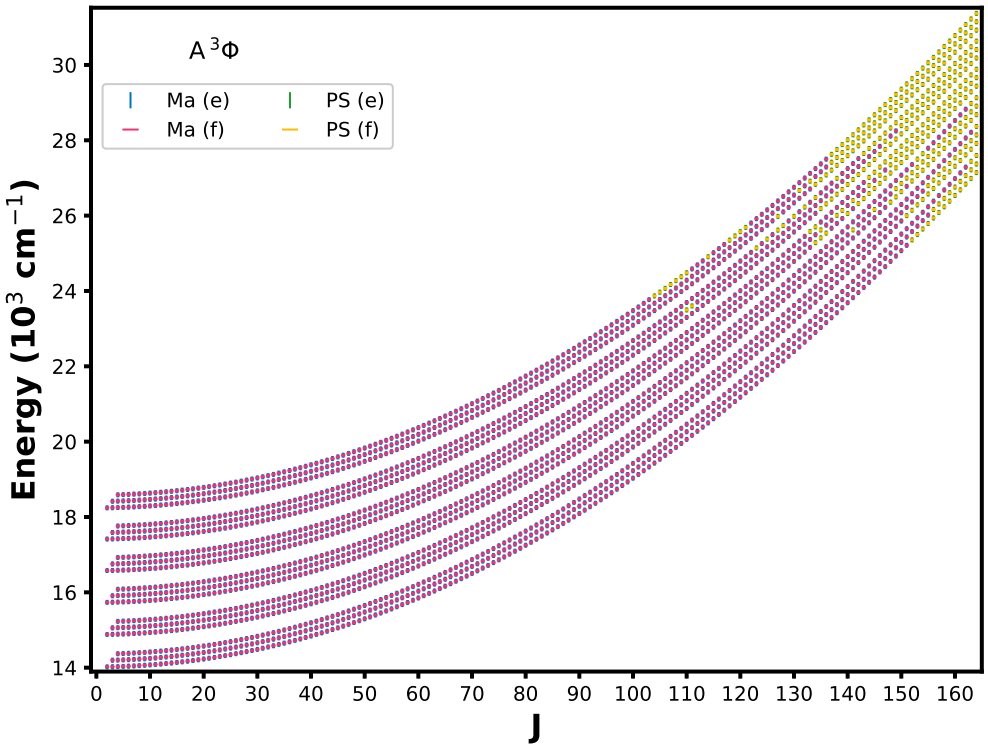
The scope of the data used is summarised in Table 4.2. The most significant difference from the 2019 MARVEL dataset is that B $^3\Pi$, $v = 2$ lines are available for the first time; there has also been a significant increase in the J range of data for the E $^3\Pi$ and B $^3\Pi$ states as expected. Furthermore, 515 out of 517 lines by Kobayashi et al. [316] and Simard et al. [317] in the band E $^3\Pi$ – X $^3\Delta$ with unresolved upper state parities were assigned e and f parities using the MARVEL energy levels. No significant changes in the X $^3\Delta$ state were identified. Both the 2019 and 2024 compilations consider 11 electronic states and the same set of vibronic levels.

In addition to the MARVEL update, the predicted shifts methodology was followed to fill gaps in observations and to estimate the energy residuals for the missing states, as well as to calculate extrapolated predicted shift uncertainties, as described in subsection 2.2.5. The MARVEL energies and the predicted shift levels with respect to the rotational quantum number J are shown in Figure 4.1 for the 11 electronic states included in this analysis.

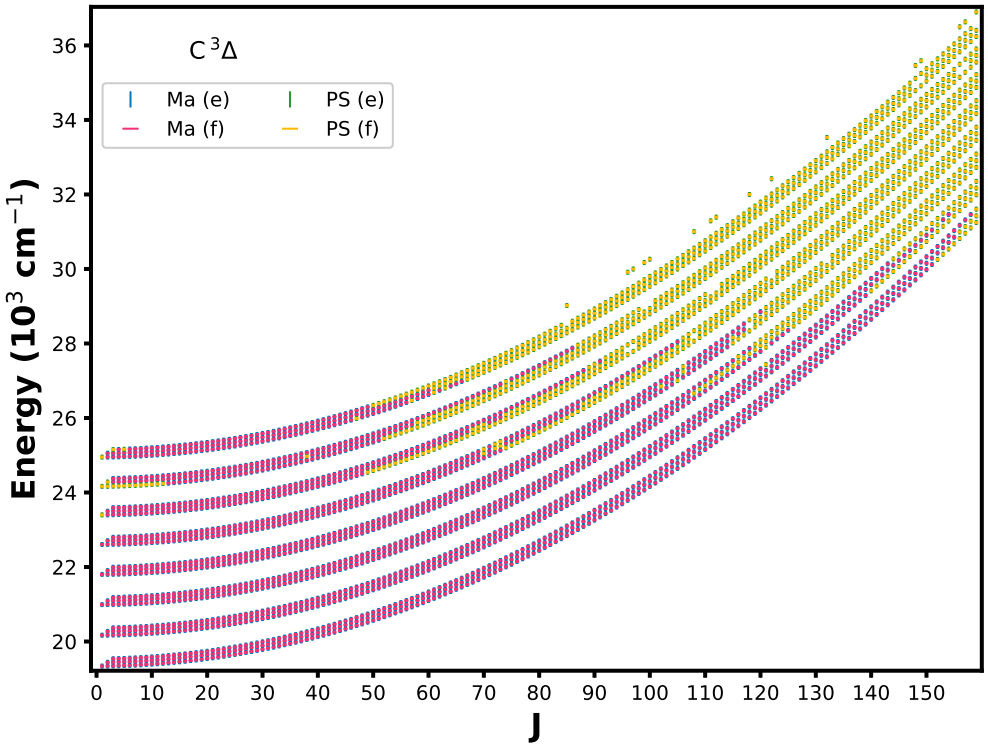
In addition, the .states files for the $^{46}Ti^{16}O$, $^{47}Ti^{16}O$, $^{49}Ti^{16}O$, and $^{50}Ti^{16}O$



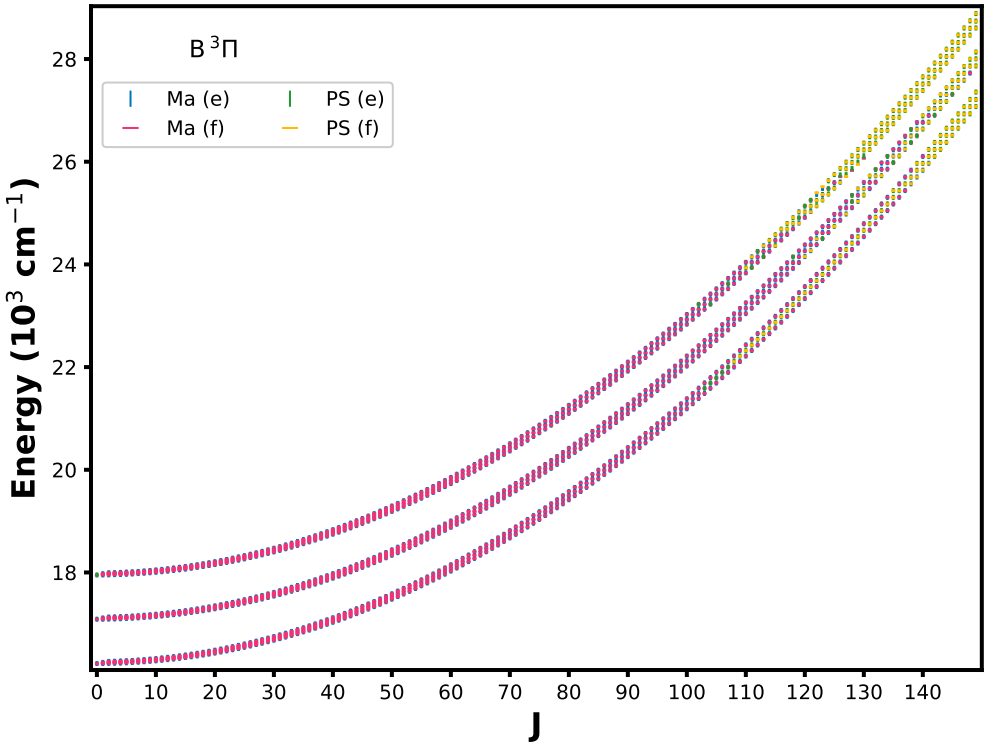
(a) $X\,^3\Delta$



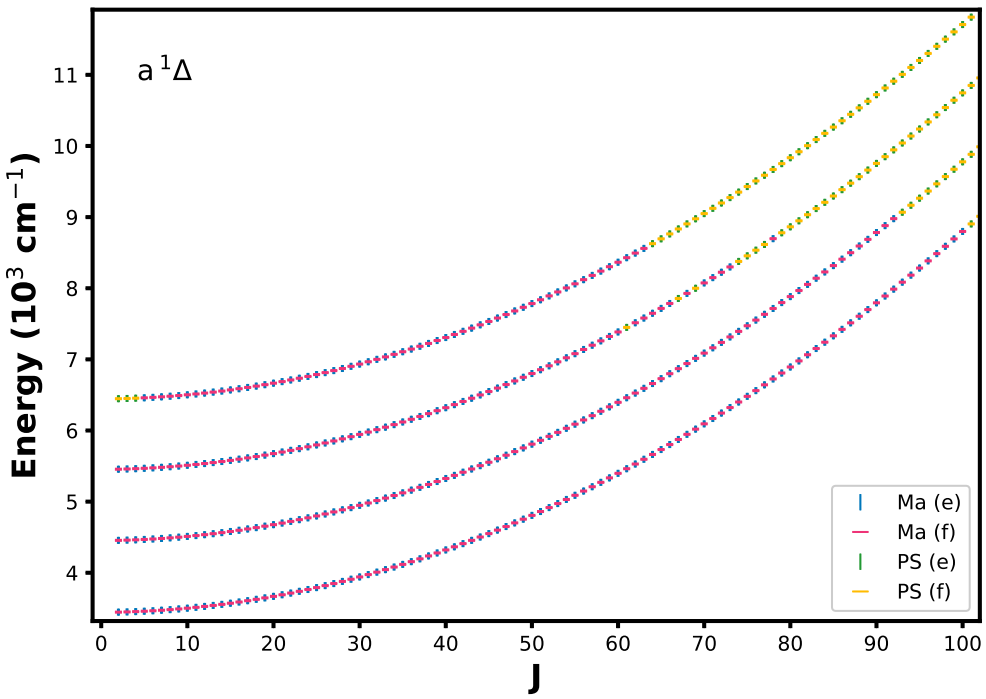
(b) $A\,^3\Phi$



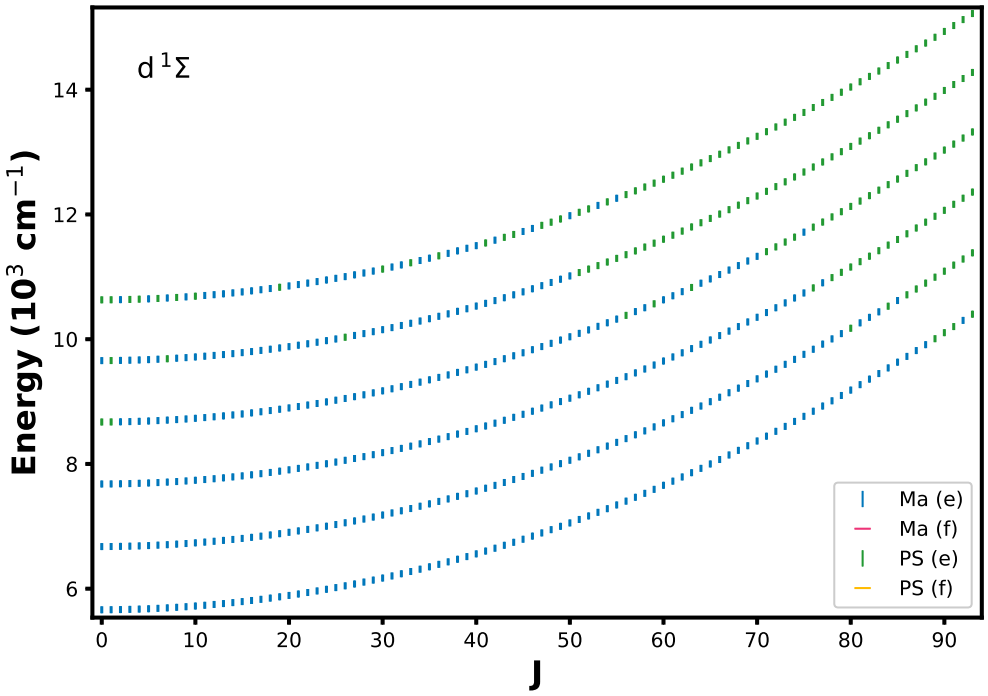
(c) $C^3\Delta$



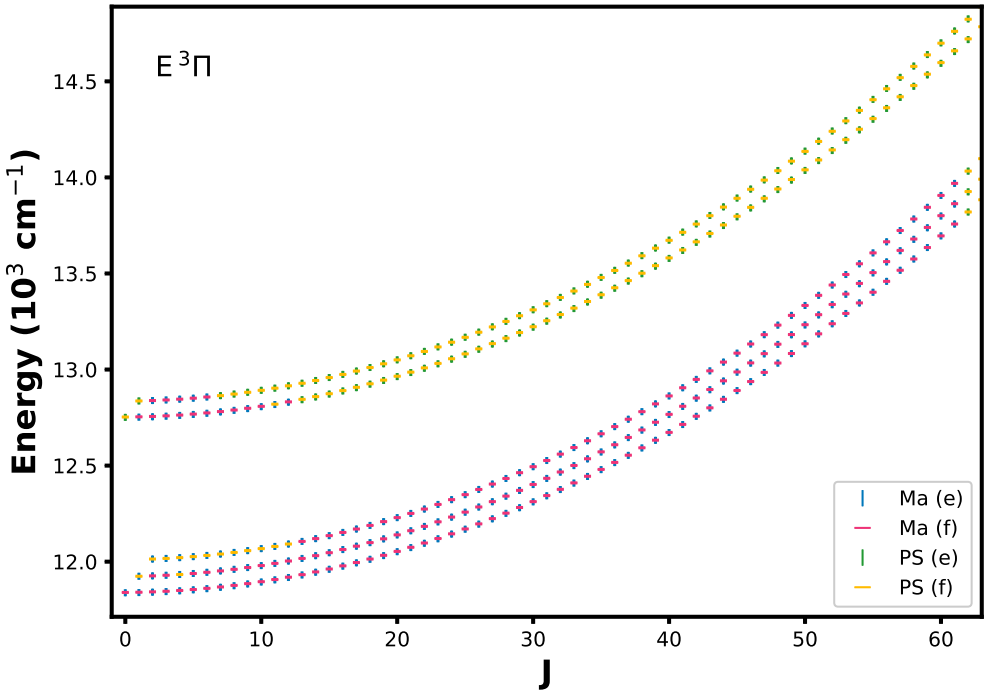
(d) $B^3\Pi$



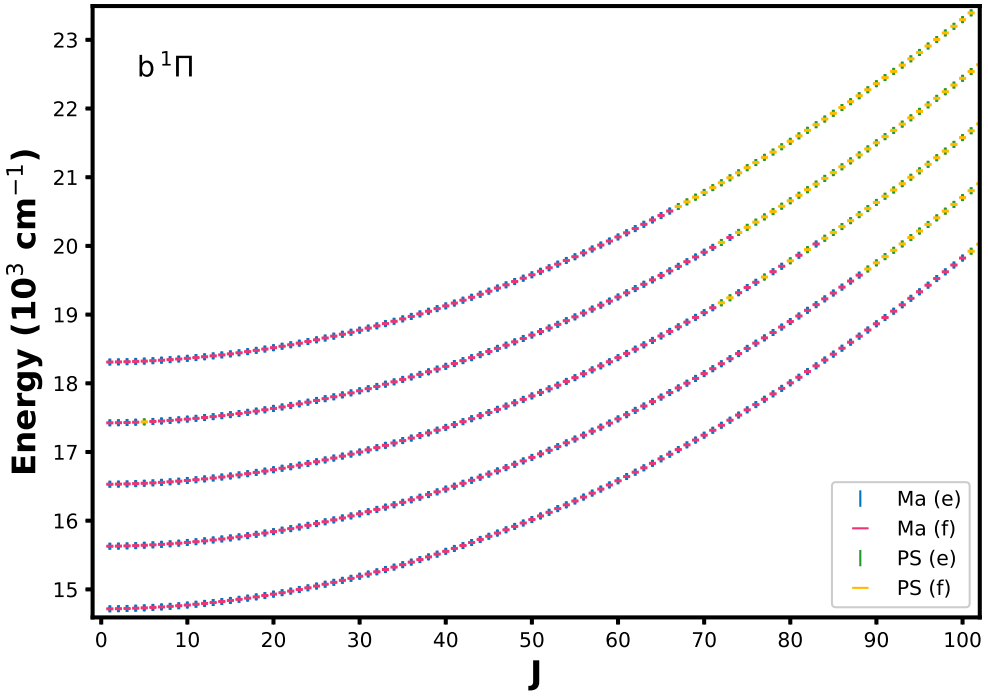
(e) $a\,^1\Delta$



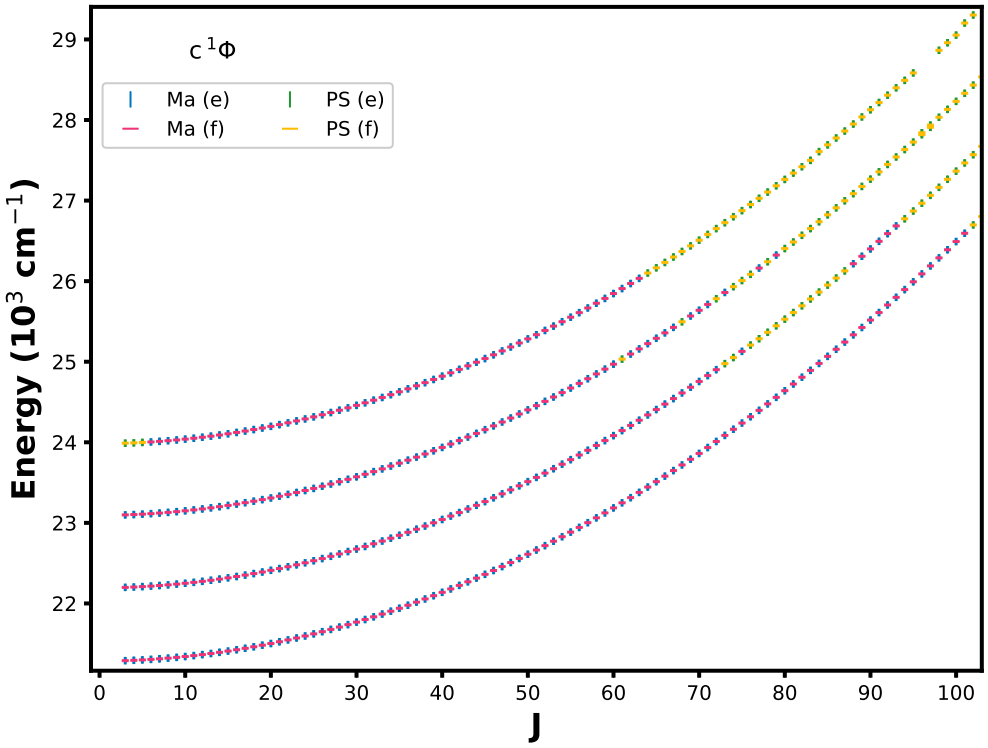
(f) $d\,^1\Sigma$


E $^3\Pi$
Energy (10^3 cm^{-1})
J
Ma (e)
Ma (f)
PS (e)
PS (f)

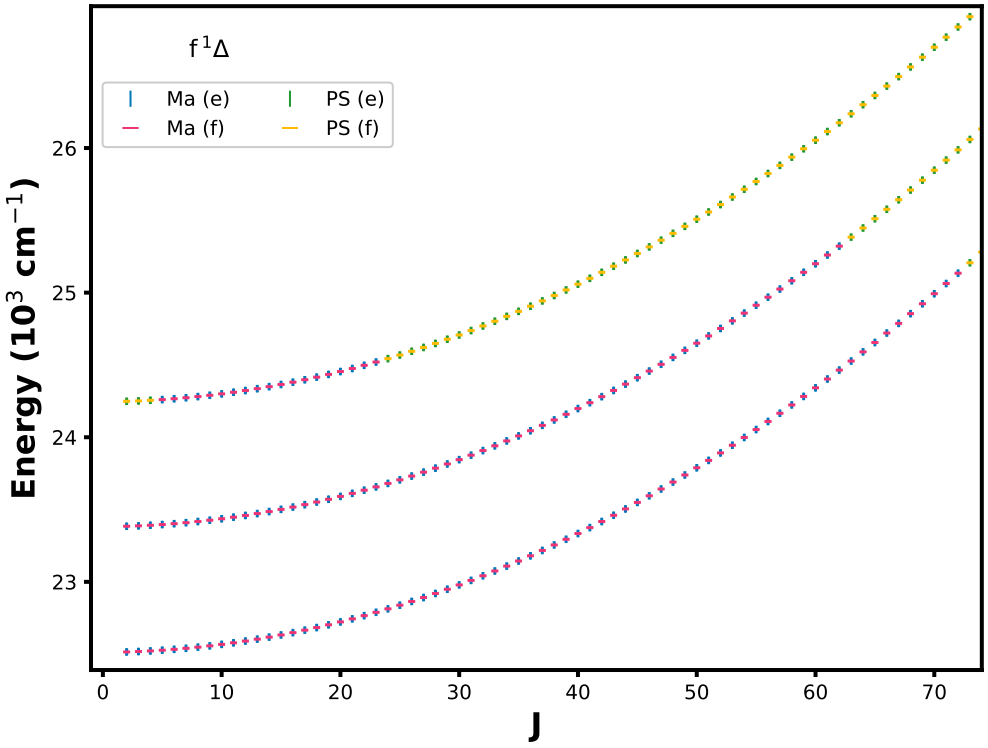
(g) $E\,^3\Pi$


b $^1\Pi$
Energy (10^3 cm^{-1})
J
Ma (e)
Ma (f)
PS (e)
PS (f)

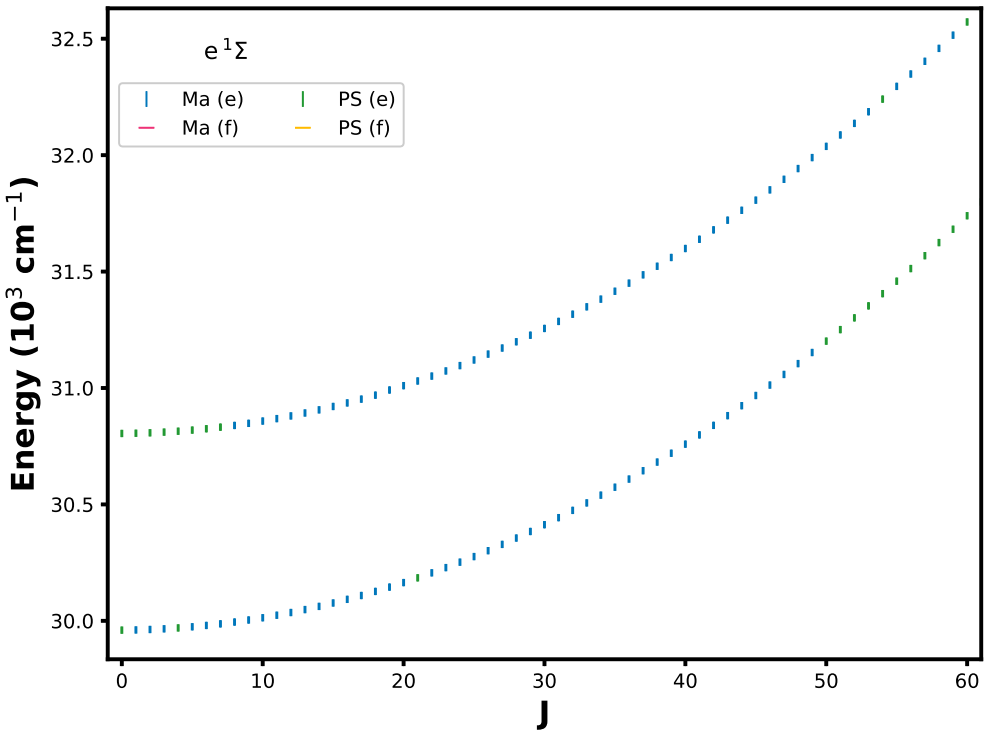
(h) $b\,^1\Pi$



(i) $C^1\Phi$



(j) $f^1\Delta$



(k) $e\,^1\Sigma$

Figure 4.1: The updated MARVEL (Ma) and predicted shift (PS) energies for the lowest electronic states of ^{48}Ti^{16}O as a function of the J quantum number. Blue and magenta points indicate the "Ma" energies of e and f parity, respectively. Green and yellow points indicate the "PS" energies of e and f parity, respectively.

isotopologues were updated using the isotopologue extrapolation (IE) correction methodology, as outlined in subsection 2.2.4.

This analysis, as well as the details on the hybridisation of the line list are not part of this thesis as they were conducted by colleagues and co-authors Dr. Charles A. Bowesman and Armando N. Perri.

4.4 Uncertainties

We use MARVEL4.1 to produce the MARVEL energy uncertainties shown in Figure 4.2. MARVEL4.1 allows for the uncertainties in the energies to be calculated using a bootstrapping approach, as described by Tennyson et al. [195].

This method accounts for inconsistencies between multiple transitions to or from a given level by applying an increase to the level's final uncertainty. Accord-

Table 4.1: Experimental data for TiO used in our analysis. State': Upper electronic state, State": Lower electronic state, v':upper state vibrational quantum number, v": lower state vibrational quantum number, wavelength range and mean line position uncertainty given in cm^{-1}, V/A: number of validated experimental transitions/total number of transitions.

Source	State'	State"	v'	v''	J range	Wavelength range	Mean Unc.	V/A
20BeCaxx [311]	$E\,^3\Pi$	$X\,^3\Delta$	0	0	13 - 61	11682.9 - 11854.0	$5 \cdot 10^{-2}$	659/659
21CaBexx	$B\,^3\Pi$	$X\,^3\Delta$	0	0	0 - 102	15711.7 - 16233.2	$5 \cdot 10^{-2}$	1752/1752
[312]	$B\,^3\Pi$	$X\,^3\Delta$	1	0	0 - 161	16326.1 - 17096.4	$5 \cdot 10^{-2}$	1862/1862
	$B\,^3\Pi$	$X\,^3\Delta$	2	0	160	16773.8	$5 \cdot 10^{-2}$	1/1
	$B\,^3\Pi$	$X\,^3\Delta$	2	1	0 - 130	16385.5 - 16958.0	$5 \cdot 10^{-2}$	1891/1891
19BrWaFu	$X\,^3\Delta$	$X\,^3\Delta$	0	0	7 - 12	253229.0 - 384151.1	$3 \cdot 10^{-1}$	14/14
[313]	$X\,^3\Delta$	$X\,^3\Delta$	1	1	8 - 10	286512.7 - 318333.0	$1 \cdot 10^{-1}$	2/2
21WiBrDo	$X\,^3\Delta$	$X\,^3\Delta$	1	0	1 - 33	971.2 - 1031.8	$5 \cdot 10^{-4}$	207/207
[314]	$X\,^3\Delta$	$X\,^3\Delta$	2	1	1 - 38	971.8 - 1026.9	$5 \cdot 10^{-4}$	176/176
	$X\,^3\Delta$	$X\,^3\Delta$	3	2	1 - 34	971.8 - 1013.6	$5 \cdot 10^{-4}$	89/89
	$X\,^3\Delta$	$X\,^3\Delta$	4	3	4 - 30	977.5 - 1000.8	$5 \cdot 10^{-4}$	42/42

ingly, the uncertainties in the MARVEL energy levels present in the 2024 update that were also present in the 2019 data set have uncertainties on average 14% larger. These uncertainty changes have a large standard deviation of 87% however, with uncertainties in the extreme cases being up to 200 times smaller or 50 times larger in the 2024 MARVEL data. These uncertainties are incorporated into the 2024 TiO line list update for the MARVELised energy levels.

4.5 Outlook

The Toto MARVEL compilation [149] was updated by including measured transitions from four new sources for the X $^3\Delta$ rovibrational, B $^3\Pi$ – X $^3\Delta$ and E $^3\Pi$

Table 4.2: Overview of the 2024 TiO MARVEL energy levels (EL) and comparison against DUO variational energy levels ($|Ma-Ca|$) in cm^{-1}.

State	v range	J range	EL range	#ELs
	Unc range	Avg. Unc	$\|Ma-Ca\|$ range	Mean $\|Ma-Ca\|$
X $^3\Delta$	0 - 5	1 - 162	0 - 14878	5000
	0.0000 - 7.92	0.40	0.0000 - 5.50	0.19
a $^1\Delta$	0 - 3	2 - 100	3446 - 8978	638
	0.0215 - 2.02	0.12	0.0001 - 7.45	0.12
d $^1\Sigma^+$	0 - 5	0 - 92	5661 - 12259	402
	0.0273 - 0.36	0.06	0.0002 - 0.28	0.05
E $^3\Pi$	0 - 1	0 - 61	11838 - 13969	386
	0.0100 - 0.10	0.04	0.0022 - 1.82	0.69
A $^3\Phi$	0 - 5	2 - 163	14021 - 28825	5152
	0.0002 - 8.06	0.48	0.0000 - 3.19	0.36
b $^1\Pi$	0 - 4	1 - 100	14717 - 20507	806
	0.0245 - 1.20	0.08	0.0002 - 1.05	0.15
B $^3\Pi$	0 - 2	0 - 148	16224 - 27727	2275
	0.0080 - 3.62	0.16	0.0011 - 68.2	4.25
C $^3\Delta$	0 - 7	1 - 158	19341 - 31462	4756
	0.0010 - 6.32	0.28	0.0001 - 11.1	0.50
c $^1\Phi$	0 - 3	3 - 101	21290 - 26685	608
	0.0245 - 2.31	0.13	0.0001 - 8.27	0.20
f $^1\Delta$	0 - 2	2 - 72	22515 - 25321	302
	0.0245 - 0.15	0.05	0.0004 - 0.63	0.08
e $^1\Sigma^+$	0 - 1	1 - 59	29960 - 32515	98
	0.0582 - 0.11	0.07	0.0107 - 3.57	0.77

Table 4.3: A part of the final `.states` file for ^{48}Ti^{16}O.

i	$\tilde{E}$	g_{tot}	J	unc	τ	g	$p_{+/-}$	$p_{e/f}$	State	v	Λ	Σ	Ω	Label	$\tilde{E}_{\text{Ca}}$
1	5661.898155	1	0	0.041180	7.6104E+03	0.000000	+	e	d(1SIGMA+)	0	0	0	0	Ma	5661.946212
2	6675.291935	1	0	0.042330	2.9150E-02	0.000000	+	e	d(1SIGMA+)	1	0	0	0	Ma	6675.201129
3	7678.749695	1	0	0.050790	1.4712E-02	0.000000	+	e	d(1SIGMA+)	2	0	0	0	Ma	7678.740969
4	8672.576682	1	0	0.045563	9.9027E-03	0.000000	+	e	d(1SIGMA+)	3	0	0	0	PS	8672.544044
5	9656.625935	1	0	0.055780	7.5003E-03	0.000000	+	e	d(1SIGMA+)	4	0	0	0	Ma	9656.588560
6	10630.952776	1	0	0.050239	6.0608E-03	0.000000	+	e	d(1SIGMA+)	5	0	0	0	PS	10630.852666
7	11595.314399	1	0	0.365317	5.1027E-03	0.000000	+	e	d(1SIGMA+)	6	0	0	0	Ca	11595.314399
8	11838.204653	1	0	0.010000	3.7253E-06	0.000000	+	e	E(3PI)	0	1	-1	0	Ma	11839.872151
9	12293.863078	1	0	4.684229	3.5418E-01	0.000000	+	e	D(3SIGMA-)	0	0	0	0	Ca	12293.863078
10	12549.951692	1	0	0.415317	4.4199E-03	0.000000	+	e	d(1SIGMA+)	7	0	0	0	Ca	12549.951692
11	12751.138832	1	0	0.016147	3.6251E-06	0.000000	+	e	E(3PI)	1	1	-1	0	PS	12752.897046
12	13268.347028	1	0	4.734229	1.4200E-01	0.000000	+	e	D(3SIGMA-)	1	0	0	0	Ca	13268.347028

i: State counting number
$\tilde{E}$: Energy (in cm^{-1})
g_{tot}: Total degeneracy
J: Total angular momentum
unc ($\Delta\tilde{E}$): Uncertainty (in cm^{-1})
τ: Lifetime (in s; calculated in ExoCross [8])
g: Lande g-factor
$p_{+/-}$: Total parity
$p_{e/f}$: Kronig rotationless parity
State: Electronic state
v: Vibrational quantum number
Λ: Projection of electronic orbital angular momentum on the internuclear axis
Σ: Projection of electronic spin angular momentum on the internuclear axis
Ω: Projection of the total angular momentum excluding nuclear spin along the internuclear axis
Label: Ma for experimental MARVEL energies, PS for energies from Predicted Shift method, Ca for unchanged calculated energy by [149]
$\tilde{E}_{\text{Ca}}$: DUO calculated energy by [149]

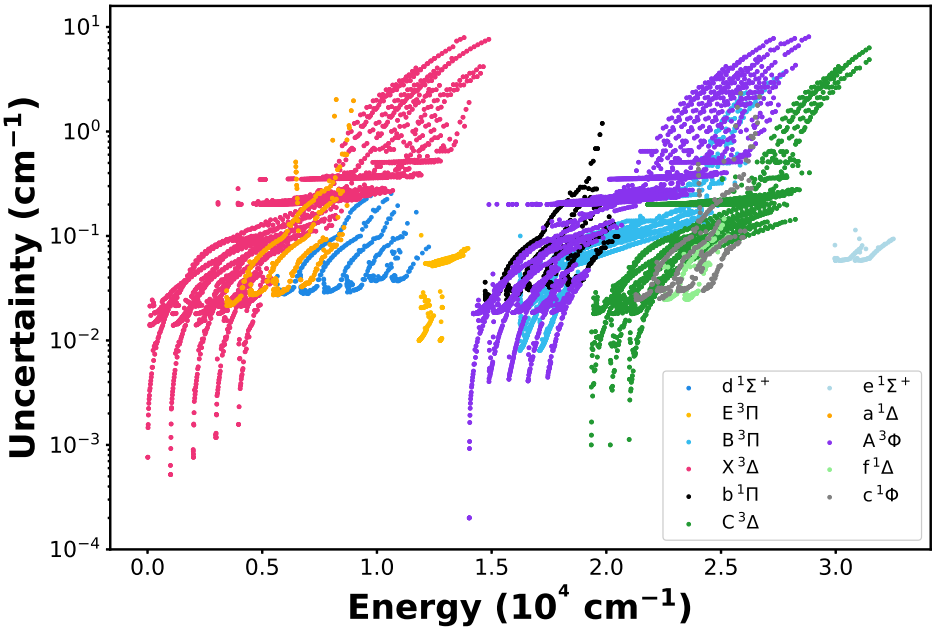


Figure 4.2: The MARVEL (Ma) energy uncertainties for ^{48}Ti^{16}O as a function of energy.

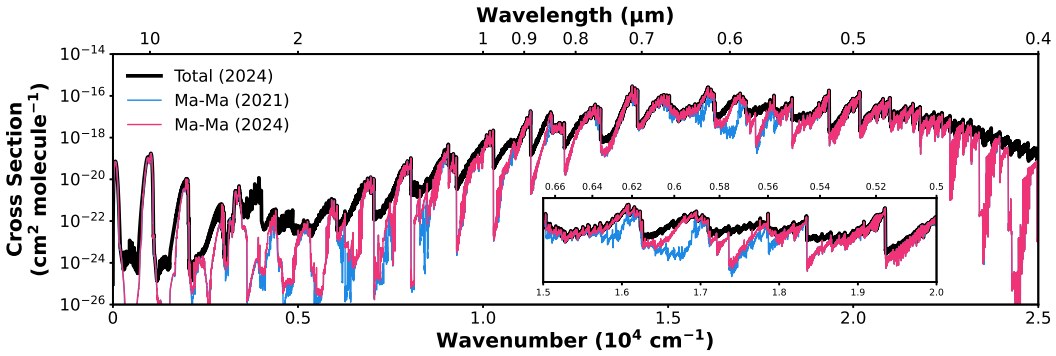


Figure 4.3: The black cross section shows all transitions in the new 2024 Toto line list, whereas the pink cross section shows only MARVEL (Ma) experimental transitions (with variational intensities). The blue cross section shows the Ma – Ma cross section produced from the 2021 Toto line list (with variational intensities).

– X $^3\Delta$ bands (see Table 4.1). This updated MARVEL data set was then used to rehybridize the 2021 Toto line list for each isotopologue with novel predicted shift calculations.

The 2024 TiO MARVEL compilation contains 12 164 energy levels from 61 509 validated (62 935 total) transitions compared to 2019 compilation of 10 761 energy levels from 51 547 validated (56 240 total) transitions. The updated states file also includes 17001 predicted shifts (PS) energy levels and 263821 variationally calculated (Ca) energy levels. Part of the final states file is shown in Table 4.3. 31 % of the transition between the Ma levels have resolving power larger than 100 000. These transitions are now available in the new ExoMolHR database [180].

Figure 4.3 shows the high-res vs total cross-section for ^{48}Ti^{16}O with the new 2024 Toto line list, as well as the partial cross sections for transitions between only MARVEL (Ma) states using the 2024 and 2021 Toto line lists. There is very high MARVEL coverage for TiO between 450 nm - 1.5 μm (6000 – 22 000 cm^{-1}) (fig. 4.3). The high MARVEL coverage of the strong spectral lines for most of the visible and near-IR region means a wide spectral window is possible for high-resolution cross-correlation (HRCC) studies. This new update added experimental data supporting HRCC between 590 and 630 nm (15 870 – 16 950 cm^{-1}), which corresponds to the B $^3\Pi$ – X $^3\Delta$ rovibronic transitions. Possible improvements for

the future could be in the 565 - 580 nm (17 200 – 17 700) cm^{-1} region, which would require experimental data for transitions involving B $^3\Pi$, $v = 3$ levels.

Chapter 5

MARVEL project on Methane

5.1 Motivation

Methane ($^{12}C^{1}H_4$) is the simplest stable hydrocarbon molecule, with wide-ranging implications in atmospheric and astrophysical chemistry. Methane on Earth has biological, and geological origins. It is produced by methanogenic microorganisms on wetlands as a metabolic byproduct [318]. A natural reservoir of methane exists in the permafrost regions and beneath the oceans in the form of methane hydrates [319, 320]. Methane is central in atmospheric chemistry, and its presence in the atmosphere affects the planet's temperature and climate system. The concentration of methane in the troposphere has been increasing after a decade of constant value [321–324] and annual increases in methane are accelerating [325], making it an important global warming species [326]. In particular, since the preindustrial era, the tropospheric concentration of $^{12}C^{1}H_4$ has more than doubled [327, 328]. Methane also contributes substantially to tropospheric ozone production, which itself is a key component to driving climate change [329].

Methane has been identified as the second anthropogenic greenhouse gas after carbon dioxide [330, 331]. Its atmospheric lifetime is notably shorter than that of carbon dioxide, primarily due to its reactivity with hydroxyl radicals (OH). Despite that, it is a ~ 28 times more potent greenhouse gas over a 100-year period [328, 332], contributing significantly to heat-trapping in the atmosphere [330].

Global methane emissions stem from a variety of human activities, surpassing those originating from natural processes. In particular, about 60% of global methane is derived from human activities [322]. These anthropogenic sources include emissions from agriculture, biomass burning, the gas and oil industry, large-scale deforestation, industrial processes, combustion, and wastewater treatment. In contrast, the number of natural methane sinks remains limited [333], and the primary methane sink is atmospheric oxidation from hydroxyl radicals [325]. It is crucial to gain deeper insight into how methane is removed from the atmosphere to evaluate ways to strengthen these natural processes and establish the scale of removal needed.

At the same time, precise measurement and monitoring of methane concentrations are of paramount importance for researchers dedicated to combating climate change [327, 334], and of great complexity due to the diversity of methane sources and the geographical disparity of emissions. Monitoring of $^{12}C^{1}H_4$ is typically achieved using infrared observations [335]. Instruments are generally based on absorption optical techniques [323, 336]. Fourier Transform Infrared (FTIR) spectroscopy [337, 338], Tunable Diode Laser Absorption Spectroscopy (TDLAS) [22], Frequency Comb Spectroscopy [339], Cavity Ring Down Spectroscopy [340], Correlation Spectroscopy [341], High Spectral Resolution Lidar [342] are some of the main methodologies employed, and they use spectroscopy databases to obtain accurate values for line strengths and line broadenings.

Methane's role in atmospheric chemistry and climate impact is not limited to Earth; methane is notably abundant within our Solar System [343]. Primarily found on the outer planets, methane is prevalent in the atmospheres of Jupiter [344], Saturn [345], Uranus [346], and Neptune [347]. It has also been detected on Venus [348] and several moons, including Titan [349–351] and Triton [352–355], which renders it invaluable for atmospheric analysis and modelling. In addition to these celestial bodies, methane has sparked extensive debates regarding its presence and significance on Mars [356–362], as well as its origin on the Martian surface [363] and seasonal variations [364]. Moreover, it has been detected in some distant ob-

jects like comets [365, 366] by flyby missions and ground observations, as well as Pluto [367].

The primary focus and motivation for this study is the importance of methane in the characterisation of extrasolar planets. It is one of the key absorbers in the atmospheres of exoplanets and cool stars, and it is important for the study and classification of substellar objects (brown dwarfs) [368–370]. The quality of methane line lists has been proven to be crucial for the atmospheric retrievals of such objects [122, 371]. Type T brown dwarfs are fundamentally defined by the presence of methane, which dominates their infrared absorption spectra [372–374]. This defining characteristic has even led to them being referred to as 'methane dwarfs' [375]. The T brown dwarfs are distinguished from warmer types (L) by the strong absorption signatures of methane in the NIR $1-2.5\,\mu m$ region [376–378]. This is a direct consequence of thermochemical equilibrium; at temperatures below $\sim 1500\,K$, methane becomes the most stable carbon-bearing molecule, replacing carbon monoxide (CO) as the dominant carrier of carbon [379]. This transition, driven by the $CH_4 \rightleftharpoons CO$ equilibrium reaction, marks the shift from L to T dwarfs. Consequently, measuring methane's abundance is essential for determining the key C/O ratio [380]. L dwarfs, in contrast, exhibit strong metal-hydride bands, prominent neutral alkali absorption features, and weak or absent TiO and VO absorption [381]. However, weak methane absorption features of the strong ν_3 band can been observed in L dwarfs [382–384], indicating the onset of this chemical transition at the cooler end of the L-dwarf sequence. Methane is also dominant in the spectra of Y dwarfs which have even lower temperatures ($\sim 300-500\,K$), and are characterized also by strong ammonia absorption features and condensation of H_2O clouds [385–387].

Substantial advances in exoplanet discovery have ignited a strong interest within the scientific community to identify exoplanets that may be inhabited or possess habitable conditions. High-resolution infrared spectroscopy ($R \geq 100\,000$) is a crucial tool for understanding the chemical composition of the atmosphere of such planets. Recognizing and detecting biosignatures is one of the main goals of

researchers in this field. Methane is considered a biosignature for terrestrial planets [388, 389], which means that it can be a very good indicator of the presence of life beyond Earth, and maybe a sign of early Earth-like environments.

The gas giants known as hot Jupiters are expected to contain methane, along with other molecules such as water and carbon monoxide [390]. In fact, after its original detection in HD 189733b by Swain et al. [391] with the use of transit spectroscopy, methane has been observed in the atmospheres of hot Jupiters, including HD 209458b [392], XO-1b [393], HD 102195b [394], and it has also been suggested to be present in WASP-69b [395] and HAT-P-12 b [396].

Warm Neptunes like GJ 436b and GJ 3470b are expected to exhibit methane-rich atmospheres, although its abundance on these planets has occasionally been a subject of debate [397–400]. The Q-branch band head of CH_4 was detected in the atmosphere of the warm Neptune WASP-107b, where methane is found to be highly depleted, significantly more than predicted by chemical equilibrium models [401]. Tentative indications of CH_4 in the atmosphere of the warm Neptune HAT-P-11b have also been reported [402, 403].

Strong evidence of CH_4 was also reported in other exoplanetary atmospheres including the warm Jupiter WASP 80b [404, 405], the habitable zone, sub Neptune and possible Hycean world K2-18 b [406], the young Jovian planet 51 Eridani b [407] from direct imaging, the gas giant HR 8799 b [408].

The importance of methane has led to the construction of numerous line lists [13, 14, 104, 105, 409–413], and plenty of experimental works aimed at accurately characterizing methane's spectral properties. In the current analysis, a large number of such works have been utilized (see section 5.3). The first ExoMol line list for methane "10to10" by Yurchenko & Tennyson [410] containing almost 10 billion transitions, was constructed to describe the opacity of methane for temperatures up to 1500 K. An extension of the "10to10" line list was made in 2017 by Yurchenko et al. [414] to higher temperatures up to 2000 K using the super-lines approach [415]. The completeness of this line list at higher temperatures allowed for the identifi-

cation of methane spectral features in T type dwarfs [416]. The line list was also used to model the bright T4.5 brown dwarf 2MASS 0559-14, and agreed very well with observations [122]. "10to10" has been used in several studies of exoplanetary atmospheres [417], including HR 8799 b [408], WASP -189b [418], KELT 1b [419], WASP-127 b, WASP-79 b, WASP-62b [420], HD 209458b [421], WASP -43b [422], GJ 1214 b [423], WASP 39b [424], HAT-P-18b [425], 55 Cancri e [426], LTT 9779 b [427], WASP -76b [428], WASP-12b [429], 51 Eridani b [430] and has been implemented in several atmospheric retrieval codes [431–433]. The "10to10" line list improved methane high-temperature absorption data by making it more complete, in a time when existing laboratory spectra mostly came room-temperature measurements. However, it lacks the accuracy needed, especially in the weak lines in the near-infrared (NIR), for high-resolution spectroscopy of brown dwarfs and exoplanets [371, 434–436]. This motivated the development of the MARVEL project for methane, with the goal of producing highly accurate experimental energy levels to support accurate atmospheric modelling in astrophysical and planetary applications.

5.2 Quantum numbers and selection rules

Methane has tetrahedral symmetry (see Figure 5.1) where the carbon atom is at the centre of mass and the hydrogen atoms are on the four vertices of a regular tetrahedron. It is a spherical top molecule since the moment of inertia about any axis passing through the centre of mass is the same. Within the rigid rotor approximation, it has the same energy level structure as linear molecules [437, 438],

$$E_r = BJ(J+1) \tag{5.1}$$

Methane belongs to the symmetry group T_d with five irreducible representations A_1, A_2, E, F_1, and F_2 [438]. We can decompose the symmetry of the ro-

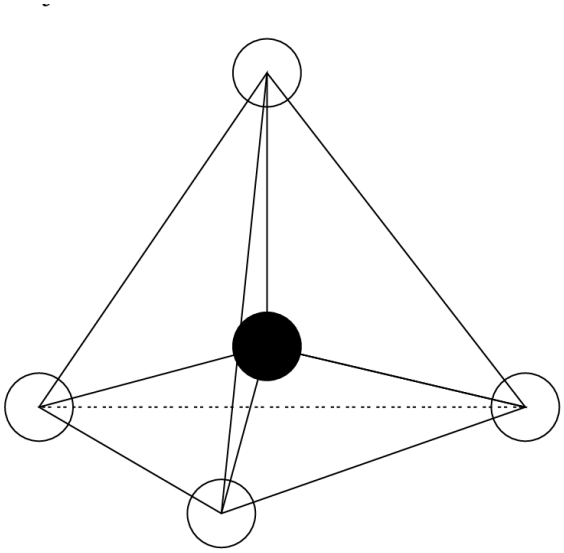


Figure 5.1: The tetrahedral symmetry of the CH_4 molecule. Figure Credit: [9].

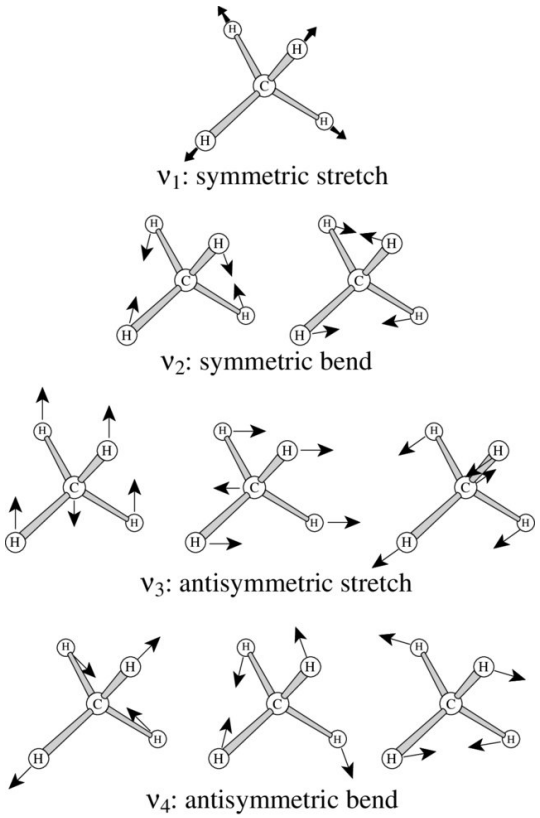


Figure 5.2: The four normal vibrational modes. Figure Credit: [10].

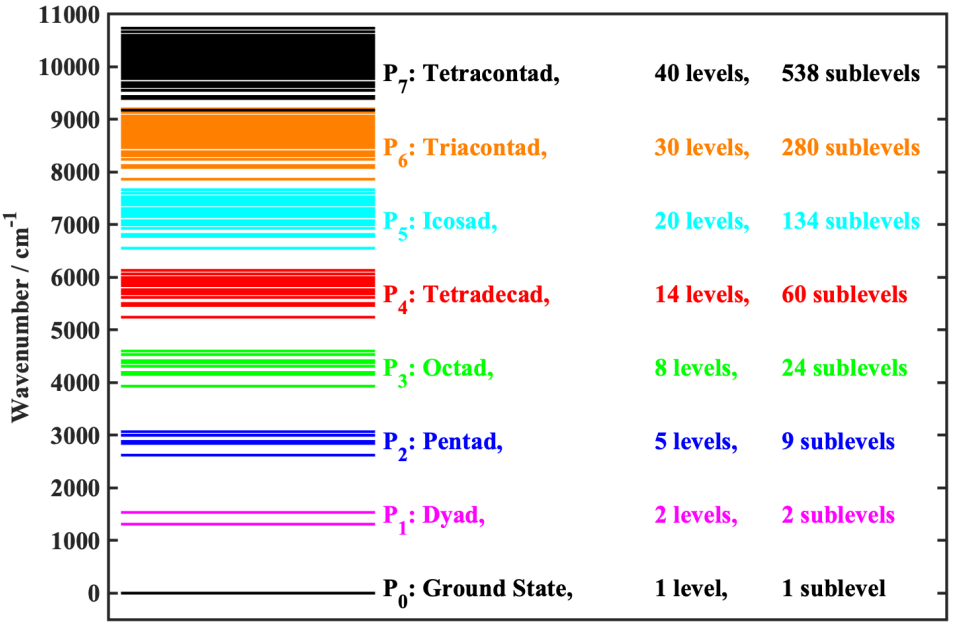


Figure 5.3: The first eight vibrational polyads of methane and the number of vibrational levels and sublevels in each one. Figure Credit: [11].

vibrational states in terms of these representations as:

$$\Gamma = 5A_1 \oplus 5A_2 \oplus 2E \oplus 3F_1 \oplus 3F_2. \tag{5.2}$$

We use the quantum number C to label the symmetry species of ro-vibrational states, corresponding to one of the five irreducible representations. The coefficients in Equation 5.2 are the nuclear statistical weights [439], which have effect on the transition strengths.

Methane has nine vibrational degrees of freedom (3N-6) and four normal modes of vibration (see Figure 5.2): The non-degenerate symmetric C-H stretching vibration ν_1 (A_1 symmetry), the doubly degenerate C-H bending vibration (E symmetry) known as the ν_2 mode, and two triply degenerate modes (F_2 symmetry); the ν_3 mode corresponds to the C-H stretching vibration, while the ν_4 mode is associated with the C-H bending vibration. Each vibrational level is identified by a set of nine normal quantum numbers. The quantum numbers v_1, v_2, v_3 and v_4 describe the excitations of the four normal modes ν_1, ν_2, ν_3 and ν_4, respectively. The quantum numbers l_2, l_3 and l_4, describe the vibrational angular momenta of ν_2, ν_3

Table 5.1: Symmetries of the fundamental vibrational modes of methane in T_d.

mode	Components	Symmetry	$\tilde{\nu}$ cm^{-1}	Type
ν_1	1	A_1	2916.45	Symmetric stretch
ν_2	2	E	1533.33	Symmetric bend
ν_3	3	F_2	3019.49	asymmetric stretch
ν_4	3	F_2	1310.76	asymmetric bend

and ν_4, while the non-degenerate ν_1 mode does not carry an associated angular momentum quantum number. Finally, the m_3 and m_4 denote the multiplicity indices of the degenerate modes [410]. The fundamental frequency wavenumbers are shown in Table 5.1.

The four normal mode wavenumbers $\tilde{\nu}_i$ exhibit the following approximate relation:

$$\tilde{\nu}_1 \simeq \tilde{\nu}_3 \simeq 2\tilde{\nu}_2 \simeq 2\tilde{\nu}_4 \simeq 3000\,\mathrm{cm}^{-1}. \tag{5.3}$$

This leads to the vibration energies of methane being grouped in a polyad structure [440]. The integer polyad number P is defined as

$$P = 2(v_1 + v_3) + v_2 + v_4 \tag{5.4}$$

and is numbered with increasing energy starting with $n = 0$ for the Monad, $n = 1$ for the Dyad, $P = 2$ for the Pentad, $P = 3$ for the Octad, *etc*. The first eight polyads of methane with the number of levels and sublevels within each one are shown schematically in Figure 5.3. Each polyad is labeled with a Greek prefix for the number of the levels. Here a vibrational level is defined simply by the quantum numbers (v_1, v_2, v_3, v_4) while the sublevels comprise all the vibrational angular momentum or symmetry products that are allowed for this vibrational level. Thus, the vibrational level (v_1, v_2, v_3, v_4) is split into several sublevels as soon as it is not just one fundamental level. For instance, "$2\nu_3$" or level (0,0,2,0) has three sublevels A_1, E and F_2. The degeneracy exhibited by three of the normal modes results in an increasing number of vibrational sublevels as the molecule is excited. The levels of each polyad are listed on Table 5.2 for the 8 first polyads, which are relevant to this

study.

In the case of higher polyads, the number of sublevels m within a particular symmetry species tend to closely approximate a regular representation, with a ratio of $m(A_1) : m(A_2) : m(E) : m(F_1) : m(F_2)$ equal to $1 : 1 : 2 : 3 : 3$ [441].

The total angular momentum of the molecule is denoted J. This quantum number characterises the rotational motion of the molecule and can take non-negative integer values: $J = 0, 1, 2..$.

Methane is classified into three nuclear spin isomers: meta ($I = 2$, A_1, A_2), ortho ($I = 1$, F_1, F_2) and para ($I = 0$, E).

The full assignment using the normal mode quantum numbers albeit being theoretically most appropriate gets quickly very complicated with the vibrational excitations. In addition, the different vibrational states become strongly mixed, and the assignment of a set of normal mode quantum numbers to a particular state is no longer well-defined. As a practical alternative, the full set of four rotation-vibration quantum numbers used for the assignment of methane lines in this work is

$$P, J, C, \alpha. \tag{5.5}$$

Here, the counting number α counts the levels with the same (C, J) within a polyad from lowest to highest energy.

The electric dipole transitions follow specific selection rules determined by their symmetry:

$$A_1 \leftrightarrow A_2 \, , E \leftrightarrow E \, , F_1 \leftrightarrow F_2 \tag{5.6}$$

with the standard rotational angular momentum selection rules:

$$\Delta J = -1, 0, 1, \;\; J' + J'' \neq 0, \tag{5.7}$$

leading to the three well-known P, Q and R branches, respectively.

The symmetric ν_1 stretching (A_1) and the asymmetric ν_2 bending (E) modes

Table 5.2: Vibrational Polyads and their Associated Levels

P	Name	Vibrational Levels
0	Monad	Ground State
1	Dyad	$\nu_2\,,\nu_4$
2	Pentad	$\nu_1\,\nu_2\,,\nu_2+\nu_4\,,2\nu_4\,,2\nu_2$
3	Octad	$3\nu_2\,,3\nu_4\,,2\nu_2+\nu_4\,\nu_2+\nu_3\,,\nu_3+\nu_4\,,\nu_2+2\nu_4\,,\nu_1+\nu_4\,,\nu_1+\nu_2$
4	Tetradecad	$4\nu_4\,,\nu_2+3\nu_4\,,\nu_1+2\nu_4\,,\nu_3+2\nu_4\,,2\nu_2+2\nu_4\,,\nu_2+\nu_3+\nu_4\,,4\nu_2\,,$ $\nu_1+\nu_3\,,3\nu_2+\nu_4\,,\nu_1+2\nu_2\,,2\nu_3\,,2\nu_1\,,2\nu_2+\nu_3\,,\nu_1+\nu_2+\nu_4$
5	Icosad	$5\nu_4\,,5\nu_2\,,\nu_2+2\nu_3\,,\nu_1+\nu_2+\nu_3\,,\nu_4+2\nu_3\,,3\nu_2+2\nu_4$ $\nu_2+2\nu_1\,,\nu_4+2\nu_1\,,4\nu_2+\nu_4\,,\nu_2+4\nu_4\,,\nu_1+3\nu_2\,,$ $3\nu_2+\nu_3\,,\nu_1+\nu_3+\nu_4\,,2\nu_2+\nu_3+\nu_4\,,\nu_1+3\nu_4\,,2\nu_2+3\nu_4\,,$ $\nu_3+3\nu_4\,,\nu_1+2\nu_2+\nu_4\,,\nu_2+\nu_3+2\nu_4\,,\nu_1+2\nu_2+\nu_4$
6	Triacontad	$6\nu_2\,,\nu_2+5\nu_4\,,2\nu_2+4\nu_4\,,\nu_3+4\nu_4\,,\nu_1+4\nu_4\,,2\nu_1+2\nu_4\,,$ $\nu_2+\nu_3+3\nu_4\,,\nu_1+\nu_3+2\nu_4\,,3\nu_2+3\nu_4\,,5\nu_2+\nu_4\,,4\nu_2+\nu_3$ $\nu_1+2\nu_2+2\nu_4\,,2\nu_3+2\nu_4\,,3\nu_1\,,4\nu_2+2\nu_4\,,2\nu_2+\nu_3+2\nu_4\,,$ $\nu_1+\nu_2+\nu_3+\nu_4\,,\nu_1+2\nu_3\,,\nu_2+2\nu_3+\nu_4\,,2\nu_1+2\nu_2\,,$ $3\nu_2+\nu_3+\nu_4\,,2\nu_2+2\nu_3\,,6\nu_4\,,\nu_1+\nu_2+3\nu_4\,,3\nu_3\,,2\nu_1+\nu_3$ $\nu_1+4\nu_2\,,2\nu_1+\nu_2+\nu_4\,,\nu_1+3\nu_2+\nu_4\,,\nu_1+2\nu_2+\nu_3\,,$
7	Tetracontad	$7\nu_4\,,\nu_2+6\nu_4\,,\nu_1+5\nu_4\,,\nu_3+5\nu_4\,,2\nu_2+5\nu_4\,,\nu_1+\nu_2+4\nu_4\,,$ $3\nu_2+4\nu_4\,,\nu_2+\nu_3+4\nu_4\,,2\nu_1+3\nu_4\,,\nu_1+\nu_3+3\nu_4\,,3\nu_1+\nu_4\,,$ $\nu_1+4\nu_2+\nu_4\,,2\nu_3+3\nu_4\,,2\nu_2+\nu_3+3\nu_4\,,2\nu_1+\nu_3+\nu_4\,,$ $4\nu_2+3\nu_4\,,\nu_1+\nu_2+\nu_3+2\nu_4\,,\nu_1+3\nu_2+2\nu_4\,,3\nu_2+2\nu_3\,,$ $\nu_2+2\nu_3+2\nu_4\,,\nu_1+2\nu_3+\nu_4\,,3\nu_2+\nu_3+2\nu_4\,,\nu_2+3\nu_3\,,$ $5\nu_2+2\nu_4\,,\nu_1+2\nu_2+\nu_3+\nu_4\,,3\nu_3+\nu_4\,,2\nu_1+3\nu_2\,,6\nu_2+\nu_4\,,$ $2\nu_2+2\nu_3+\nu_4\,,4\nu_2+\nu_3+\nu_4\,,\nu_1+5\nu_2\,,7\nu_2\,,2\nu_1+\nu_2+2\nu_4\,,$ $\nu_1+2\nu_2+3\nu_4\,,3\nu_1+\nu_2\,,\nu_1+\nu_2+2\nu_3\,,5\nu_2+\nu_3\,,$ $2\nu_1+2\nu_2+\nu_4\,,\nu_1+3\nu_2+\nu_3\,,2\nu_1+\nu_2+\nu_3$

lead to no change in the dipole moment and as such, are infrared inactive. Only the two F_2 modes ν_3, ν_4 (and more generally, all F_2 vibrational sublevels) are infrared active for transitions starting in the ground vibrational state, as a first approximation. The ro-vibrational transitions of the IR non-active bands get intensities through ro-vibrational interactions with IR active states.

In this analysis, we have used transitions both from Raman and infrared spectra. The selection rules for the Raman spectrum of methane follows: all four vibrational modes are active and the rotational selection rules in the general case are:

$$\Delta J = -2, -1, 0, 1, 2, \tag{5.8}$$

leading to the five O, P, Q, R and S branches. One should notice however that for the A_1 vibrational sublevels, such as ν_1 fundamental band, there is only a Q Raman branch ($\Delta J = 0$).

5.3 Overview of Experimental Sources

In this work, we compiled all the available experimental spectroscopic data up until July 2023 and put them through the MARVEL procedure in order to determine a dataset of empirical rovibrational energy levels with experimental accuracy. We built the dataset of the observational spectra from lowest to highest polyads testing with MARVEL at each step. In particular, for our final runs, we used the MARVEL4 Online version [195]. Finally, the ExoMol MM methane line list was improved by Yurchenko et. al. [3] with the use of empirical energy levels in place of the computed values with the variational program TROVE [442], and by fitting the PES with the empirical energies.

A MARVEL (Measured Active Rotational Vibrational Energy Levels) analysis of the available spectroscopic data on methane ($^{12}C^{1}H_4$) was performed. A total of 82 173 measured rovibrational transitions were gathered from 96 literature sources and put through the MARVEL procedure which led to the determination of 23 292 empirical energy levels with uncertainties, up to ~ 9900 cm^{-1} covering the lowest

eight polyads. A comparison with Effective Hamiltonian (EH) evaluated levels, variational calculations by the TheoReTS project, and the MeCaSDa database is performed.

A comprehensive collection of high-resolution spectra of $^{12}C^{1}H_4$ has been assembled for this study. A total of 279 research articles were reviewed, and from this pool, 96 were selected for inclusion in our current research. A summary of these selected sources, along with details regarding their observational data is presented in Table 5.3 and Table 5.4, and their distribution among different polyad bands is shown in Figure 5.4.

Notably, in our compilation we have 11 sources with pure rotational transitions [11, 443–452]. Pure rotational transitions in methane can be observed due to slight asymmetries introduced by centrifugal distortion and vibration–rotation coupling.

Information about the sources that were considered but ultimately excluded from our analysis can be found in Table 5.5. Comments related to Table 5.4, especially referring to the assignment of unassigned lines are found in section 5.7. For discussion on the treatment of the uncertainties refer to section 5.6.

Table 5.4: Experimental data for $^{12}C^{1}H_4$ used in our analysis. Wavelength range and mean line position uncertainty are given in cm^{-1}. A/V: number of available transitions/number of validated transitions. "given" indicates an uncertainty provided in the source. "CD" means no uncertainty was given, so it was derived using combination differences or CDs. "Inc" means the uncertainty was increased. See section 5.6 for comments on individual sources.

Source	Polyad Band	Wav. Range	A/V	Mean Unc.
				Origin
23DuViGa [453]	$P_6 - P_2$ $P_7 - P_3$	5909 – 6216	22/19	5.0E-03 CD
23RiTeJo [454]	$P_2 - P_0$	3009 – 3015	12/12	4.7E-04 given

Continued on the next page...

Source	Polyad Band	Wav. Range	A/V	Mean Unc. / Origin
22GeHjBo [455]	$P_1 - P_0$ $P_2 - P_1$	1250 – 1379	711/711	1.9E-02 given
22RoNiMa [456]	$P_3 - P_0$ $P_4 - P_1$	4100 – 4300	11337/11311	7.5E-03 CD
21FoRuSiVtype [457]	$P_4 - P_0$	5972 – 6047	24/24	4.9E-05 given
21FoRuSi [457]	$P_6 - P_2$	5910 – 6057	8/8	1.0E-04 giv
21FoRuSi (pump) [457]	$P_2 - P_0$	3028.75	1/1	5.0E-04 CD
21OkInOk [458]	$P_4 - P_2$	3017 – 3019	10/10	7.1E-08 given
21LiDiLi [459]	$P_1 - P_0$	1396 – 1398	8/8	1.0E-03 CD
20YaLiPl [460]	$P_4 - P_0$	6076 – 6078	6/6	6.3E-05 given
20NiRoTh [461]	$P_3 - P_0$ $P_4 - P_1$	4300 – 4600	9749/9734	9.0E-03 inc
19Pine [462]	$P_2 - P_0$	3012 – 3019	66/66	3.9E-05 inc
19LiYaFe [463]	$P_4 - P_0$	6105 – 6108	11/11	1.7E-07 given
19YaLiFe [464]	$P_4 - P_0$	6076.1	1/1	1.2E-06 given
19RoNiTh [465]	$P_3 - P_0$ $P_4 - P_1$	3760 – 4100	6835/6722	5.0E-03 CD
19NiPrRe [466]	$P_6 - P_0$	8736 – 9160	329/329	5.0E-03 inc
18MaZhCa [467]	$P_4 - P_0$	4975 – 4985	32/32	2.0E-03 inc

Continued on the next page...

Source	Polyad Band	Wav. Range	A/V	Mean Unc. Origin
18GhMoKa [468]	$P_4 - P_0$	5695 – 5850	2066/2039	1.5E-03 given
18GoPrKa [469]	$P_4 - P_0$	6076 – 6078	6/6	1.8E-07 given
18YaLiFe [470]	$P_4 - P_0$	6077 – 6078	2/2	9.8E-07 given
18KoMaEs [471]	$P_2 - P_0$	2885 – 3123	35/35	1.1E-05 given
18NiThDa [472]	$P_4 - P_0$ $P_5 - P_2$	5550 – 5815	3356/3337	1.0E-03 CD
17NiThDa [473]	$P_4 - P_0$	5300 – 5550	2843/2839	1.5E-03 CD
17BrCuHi [443]	$P_0 - P_0$ $P_1 - P_1$	37 – 85	10/10	8.9E-06 given
17HaPrNi [474]	$P_3 - P_0$	4300 – 4492	59/55	1.0E-04 CD
17HaPrNi(2) [474]	$P_3 - P_0$	4300 – 4482	102/102	6.2E-04 given
16NiReTa [475]	$P_5 - P_0$	6539 – 6800	2333/2333	1.0E-03 CD
16DeMaRe [476]	$P_4 - P_0$	6076 – 6078	12/12	3.8E-05 given
16ReNiCa [477]	$P_5 - P_0$	6294 – 6781	299/299	1.0E-03 CD
16AmLoPi[a] [12]	$P_1 - P_0$ $P_2 - P_1$	1100 – 1488	5062/5062	2.7E-03 given
15NiLyMi [411]	$P_4 - P_0$	5550 – 6205	1928/1927	5.0E-03 given
15DeBeSm [478]	$P_3 - P_0$	4499 – 4629	302/300	3.9E-04 given

Continued on the next page...

Source	Polyad Band	Wav. Range	A/V	Mean Unc. / Origin
14SmBePr [479]	$P_1 - P_0$	1398 – 1645	154/151	5.4E-05 giv
14NiThRe [480]	$P_4 - P_0$	4801 – 5300	2725/2716	3.0E-03 CD
13NiBoWe [481]	$P_4 - P_0$	4885 – 6205	1177/1159	1.0E-03 given
13AbIwOk [482]	$P_2 - P_0$	2894 – 3105	150/150	1.4E-07 giv
13DaNiTh [483]	$P_2 - P_0$	4600 – 4869	1570/1561	1.0E-03 CD
13CaLeWa [484]	$P_4 - P_0$	5855 – 6244	3400/3379	1.5E-03 CD
13ZoGiBa [485]	$P_4 - P_0$	5870 – 6138	348/341	1.2E-03 given
12CaWaMo [486]	$P_5 - P_0$	6256 – 6789	2512/2489	1.5E-03 given
12TaQu [487]	$P_5 - P_0$	7509 – 7564	19/19	1.0E-03 given
11NiThRe [488]	$P_5 - P_0$	6256 – 6789	717/717	2.4E-03 CD
11BaGiSw [489]	$P_2 - P_0$	2905 – 3049	132/132	9.2E-06 given
11OkNaIw [490]	$P_2 - P_0$	2943 – 3019	54/54	7.7E-08 given
10NiLyMi [491]	$P_4 - P_0$	5550 – 6205	2544/2543	5.0E-03 given
10SmBePr [492]	$P_1 - P_0$	1159 – 1495	435/435	7.2E-04 inc
10BoPiRo [444]	$P_0 - P_0$ $P_1 - P_1$	59 – 277	193/193	3.0E-03 CD

Continued on the next page...

Source	Polyad Band	Wav. Range	A/V	Mean Unc. Origin
09AlBaBoBr-PentDyad [11]	$P_2 - P_1$	1189 – 1931	1046/1046	1.0E-03 inc
09AlBaBoBr-OctadGs [11]	$P_3 - P_0$	3518 – 4747	7898/7896	5.0E-03 inc
09NiLyPe [493]	$P_4 - P_0$	5556 – 6181	449/441	1.0E-03 CD
09AlBaBoBr-DyadGs [11]	$P_1 - P_0$	1088 – 1752	1189/1182	5.0E-03 inc
09AlBaBoBr-OctadDyad [11]	$P_3 - P_1$	2334 – 3299	1707/1707	2.0E-03 inc
09TaKoSa [494]	$P_2 - P_0$	2947 – 2959	12/12	3.6E-07 given
09AlBaBoBr-PentadGs [11]	$P_2 - P_0$	2466 – 3275	2246/2246	5.0E-03 inc
09ScKaGa [495]	$P_5 - P_0$	7478 – 7564	24/23	1.0E-03 CD
05Brown [496]	$P_5 - P_0$	7478 – 7564	26/25	1.0E-03 inc
05PrBrMa [497]	$P_3 - P_0$	4100 – 4635	1432/1402	2.8E-04 inc
02HiQu [498]	$P_5 - P_0$	7478 – 7553	23/22	1.0E-03 given
02GrFiTo [499]	$P_2 - P_0$	3182 – 3225	100/100	4.2E-04 given
01HiRoLoToa [500]	$P_3 - P_0$	3848 – 3872	96/90	7.0E-04 given
01RoHiLo [501]	$P_4 - P_0$	4909 – 5272	189/184	1.0E-03 CD
01HiRoLoTob[b] [500]	$P_3 - P_0$	3797 – 4100	206/205	1.0E-04 CD

Continued on the next page...

Source	Polyad Band	Wav. Range	A/V	Mean Unc. / Origin
00FeChJoBr [502]	$P_2 - P_0$	2884 – 3150	257/256	2.0E-04 given
98ErTyKr [503]	$P_2 - P_0$	2947.8	1/1	6.6E-09 given
98GeHeHi [504]	$P_4 - P_0$	5577 – 6077	22/15	1.0E-03 CD
98BrKaRu [505]	$P_1 - P_0$ $P_2 - P_1$ $P_3 - P_2$ $P_4 - P_3$	1260 – 1334	285/275	2.0E-03 inc
97MaBeSa[c] [506]	$P_4 - P_2$ $P_4 - P_0$	2868 – 6058	66/61	8.7E-03 given
93HiBaBr [507]	$P_2 - P_1$ $P_3 - P_2$ $P_1 - P_0$	1262 – 1276	40/40	1.5E-03 given
92HiLoBr [508]	$P_3 - P_0$ $P_2 - P_1$	1382 – 4653	434/431	7.0E-03 inc
92PuWe [450]	$P_0 - P_0$ $P_2 - P_2$	0.3 – 0.6	18/18	9.3E-07 giv
92BeSaCa[c] [509]	$P_2 - P_0$	2910 – 2921	82/81	1.0E-03 given
92KrLiWe [510]	$P_2 - P_0$	2947.9	1/1	6.6E-09 given
91MiLaSt[c] [511]	$P_2 - P_0$	3063 – 3067	13/13	5.7E-04 given
91Jouvard [512]	$P_2 - P_0$	3063 – 3071	37/37	1.0E-03 CD

Continued on the next page...

Source	Polyad Band	Wav. Range	A/V	Mean Unc. / Origin
88Brown [513]	$P_3 - P_0$	3876 – 3891	12/10	1.1E-04 given
87HiLoCh [449]	$P_1 - P_1$	4 – 9	14/14	2.8E-06 given
87OlBaHi [448]	$P_1 - P_1$	0.4 – 0.6	6/6	1.5E-05 given
85ChKlNi [514]	$P_2 - P_0$	2947 – 2948	3/3	1.5E-07 given
85Dreizler[d] [11]	$P_0 - P_0$	0.16 – 0.76	7/7	1.0E-03 CD
85OlAnBa [446]	$P_0 - P_0$	0.26 – 0.51	27/27	2.1E-06 given
83DeFrPr [515]	$P_4 - P_2$	3034 – 3068	10/1	1.0E-01 given
82JeRo [516]	$P_1 - P_0$	1170 – 1317	49/49	1.0E-02 CD
82ChGoKl [514]	$P_2 - P_0$	2947.9	1/1	1.0E-07 given
81DoKoTa [514]	$P_2 - P_0$	2947.9	1/1	4.6E-08 giv
80ItOz [517]	$P_0 - P_0$	0.00027	1/1	6.0E-13 giv
80KnEdPe [518]	$P_2 - P_0$	2947.9	1/1	1.0E-07 giv
80ClDaRu [514]	$P_2 - P_0$	2947.9	1/1	4.6E-07 given
79DaPiRo [519]	$P_2 - P_0$	2937 – 3068	30/30	5.0E-04 CD
79PiDu [520]	$P_1 - P_0$	1259 – 1307	128/123	1.2E-02 inc

Continued on the next page...

Source	Polyad Band	Wav. Range	A/V	Mean Unc. / Origin
79ReCa [521]	$P_1 - P_0$	1292 – 1307	89/81	1.0E-02 inc
79DoKoTa [514]	$P_2 - P_0$	2947.9	1/1	3.3E-07 given
76BlEdJo [522]	$P_2 - P_0$	2947.9	1/1	1.4E-06 given
76Pine [523]	$P_2 - P_0$	2916 – 3123	155/149	5.0E-04 given
75HoGeOz [447]	$P_0 - P_0$	0.6 – 0.64	3/3	6.6E-06 given
75ChBe[c] [524]	$P_1 - P_0$	1359 – 1771	196/193	6.1E-02 inc
73Curl [445]	$P_0 - P_0$	0.01 – 0.04	2/2	6.6E-07 given
73HoGeOz [452]	$P_0 - P_0$	0.3 – 0.5	3/3	3.3E-06 given
73TaUeSh [451]	$P_2 - P_2$	0.5	1/1	3.3E-07 given
72EvDaWe [514]	$P_2 - P_0$	2947.9	1/1	1.6E-06 given
MAGIC[e]	$P_0 - P_0$	10 – 3105	10/10	6.0E-03

[a] The $P_3 - P_2$ and $P_4 - P_3$ lines were inconsistent with the rest of the network, so they were not included.

[b] Lines assigned by Rodina et al. [465].

[c] Raman lines.

[d] Published in [11] from private communication.

[e] Refer to section 5.5.

Table 5.3: Information on the number of experimental sources and transitions per vibrational band included in our input list of transitions. Average uncertainty is given in cm^{-1}. A/V: total number of available transitions/number of validated transitions.

Bands	A/V	Sources	Av. Unc. (cm^{-1})
$P_0 - P_0$	143/143	9*	0.002262
$P_1 - P_0$	3452/3433	12	0.008287
$P_1 - P_1$	140/140	4	0.002144
$P_2 - P_0$	3406/3397	29	0.003453
$P_2 - P_1$	5932/5931	6	0.003850
$P_2 - P_2$	16/16	2	0.000001
$P_3 - P_0$	32369/32308	13	0.006160
$P_3 - P_1$	1699/1699	1	0.002000
$P_3 - P_2$	149/149	2	0.001907
$P_4 - P_0$	21154/21028	21	0.002323
$P_4 - P_1$	7316/7275	3	0.007303
$P_4 - P_2$	31/17	3	0.015161
$P_4 - P_3$	44/34	1	0.002000
$P_5 - P_0$	5953/5927	8	0.001381
$P_5 - P_1$	22/22	1	0.001000
$P_6 - P_0$	329/329	1	0.005000
$P_6 - P_2$	26/26	2	0.003492
$P_7 - P_3$	4/2	1	0.005000

* Excluding the "magic" numbers explained in section 5.5

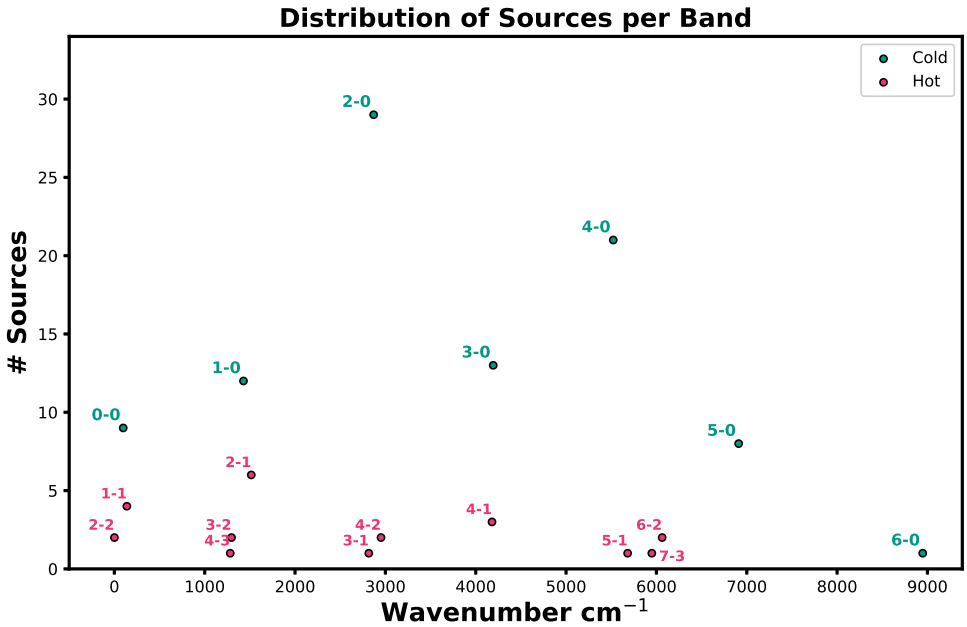


Figure 5.4: The distribution of the experimental sources utilized, across the several polyad bands with respect to line position in cm^{-1}. Green color is for the cold bands and magenta for the hot bands.

Table 5.5: Experimental $^{12}C^{1}H_4$ papers not used in MARVEL analysis

Source	Wavenumber range cm^{-1}	Comments
48NePlBe [525]	5900 – 6200	old measurements
52BoThWi [526]	2700 – 3200	low accuracy
55FeRoWe [527]	1300 – 1800	old measurements
60RaEaSk [528]	5983 – 6115	not fully assigned low accuracy
65MoGaMo [529]		no line measurements
65Moret [530]		no line measurements
66HeMoGo [531]		low accuracy
66McDowell [532]		low accuracy
70ClSt[c] [533]		no line measurements
70HeHuAn [534]	2884 – 3141	different assignments low accuracy
70OzYiKh [535]		no line measurements
71HuDa [536]	2884 – 3141	different assignments low accuracy
71HuPo [537]	1225 – 1376	different assignments low accuracy
72BaSuHu [538]	2884 – 3139	low accuracy
72Bobin [539]	5891 – 6107	not fully assigned low accuracy
72Botineau [540]	1225 – 1400	low accuracy
72RoOzKu [541]	100 – 180	no line measurements
73BeFaCh [542]		no line measurements
73BoFo [543]	2840 – 3167	no new measurements
73CaDe [544]		not accurate J assignments low accuracy

Continued on the next page...

Source	Wavenumber range cm^{-1}	Comments
73CuOkSm [545]		no new measurements
73DaMa [546]		no line measurements
73Susskind [547]		no new measurements
75Berger [548]	1271 – 1311	different assignments low accuracy
75BoHi [549]		different assignments low accuracy
75Champion [550]	1481 – 1747	no line measurements
75RoOz [551]		no new measurements
75TaDaPo [552]	3019 – 3021	different assignments
76GrRo [553]		no new measurements
76HaBoUe [554]		no new measurements
77AlKoSm [555]		no new measurements
77Berger[c] [556]		different assignments
77Champion [557]		no line measurements
77ToBrHu [558]	2862 – 3000	different assignments
78BoGu [559]	4157 – 4425	different assignments low accuracy
78ChHuSc [560]		no new measurements
78HuBrTo [561]	2700 – 2862	unassigned lines
78MaHeBy[c] [562]		no line measurements
78OwPaDo[c] [563]	2916 – 2918	not fully assigned
78OzRo [564]	94 – 145	low accuracy
79BlGoLu [565]	1120 – 1800	low accuracy
79BoBr [566]		no line measurements
79GrRo [567]		no new measurements
79GrRoPi [568]		not fully assigned
79KoPrSm [569]		no measurements provided

Continued on the next page...

Source	Wavenumber range cm^{-1}	Comments
80ChPiBe [570]		no new measurements
80HiDeCh [571]		low accuracy
80Jennings [572]		no measurements provided
80OrRo [573]		no new measurements
80VaEsOw [574]		no measurements provided
81GhHeLo [575]	2832 – 3018	low accuracy
81HuBrTo [576]		difficult to scan table
81OzGeRo [577]	0.00026 – 0.64	no new measurements
81Robiette [578]		no new measurements
81ToBrHu [579]	2385 – 3200	no line measurements
82BrRo [580]		no new measurements
82BrToRo [581]	2700 – 3000	difficult to scan
82LoBrRo [582]	2460 – 2675	different assignments
82LuPiPiCh [583]		no line measurements
82RaCa [584]		no new measurements
82PoPaCh [585]	2250 – 3250	no line measurements
83BrMaNo [586]		no new measurements
83FrIlFi[c] [587]	2916 – 2917	different assignments
83VaGiVa.a [588]		unassigned lines
85BrTo [589]		no line measurements
85GrLa [590]		no line measurements
85ThFaKo[c] [591]		low accuracy
86KeCoSm [592]		no new measurements
87Kim [593]		no line measurements
86TyChPi [594]		no new measurements
89BrLoHi [595]		no new measurements
89VaCh [596]	1270 – 1317	not fully assigned
90VaCh [597]	1332 – 1350	no new measurements

Continued on the next page...

Source	Wavenumber range cm^{-1}	Comments
91RoCh [598]		no new measurements
92BrMaCh [599]		no new measurements
92Pine [600]	3012 – 3018	we used the lines from [462]
92SaCaDo[c] [601]	2916 – 2917	no new measurements
92SmRiDe [602]		no new measurements
96OuHiLo [603]		no new measurements
98WeCh [604]		no line measurements
00MeDoMe [605]	2942 – 2982	not fully assigned low accuracy
01NaMi [606]	3009 – 3039	not fully assigned low accuracy
02BrCa [607]	10635 – 13300	no line measurements
05GhBu [608]		no new line measurements
05JoChSa [30]	1200 – 5500	no line measurements
05MoChVa [609]	2914 – 2922	no new line measurements
06BoMeMa[610]	2931 – 2996	no new line measurements
06BoReLo [440]		no line measurements
07JoGaCh[c] [611]	2905–2925	no line measurements
07RuWoHa [612]	2990 – 3070	not fully assigned low accuracy
07WiOrOz [613]	0.06 – 0.24	no line measurements
10HoSkSa [614]		not fully assigned low accuracy
10TrHaTo [615]	6000	no new line measurements
10ZiWh [616]		no line measurements
12SaAuPi [617]	59 – 288	no new line measurements
12YuFaYa [618]		no new line measurements
13ThDaAn [323]		no new line measurements

Continued on the next page...

Source	Wavenumber range cm^{-1}	Comments
13TyTaRe [619]		no line measurements
14ReNiTY [620]		no line measurements
14UlBeAl [441]	1000 – 12500	no line measurements
15LiWaTa [621]		no new line measurements
15MaKcVa[c] [622]	882 – 3434	unassigned
15ReNiTy [623]		no line measurements
17ReNiTy [13]		no line measurements
18NiPrRe [624]		no line measurements
18Petrov [625]		no new line measurements
18ReNiBe [626]	0 – 3400	no line measurements
19BuAmBe [627]		no line measurements
19DeGhHo [628]		no new line measurements
19GhHeBe [629]		no new line measurements
19KiMaPe [630]		no new line measurements
20GiNaTu [631]		no new line measurements
20HaGoRe [413]		no line measurements
20PeMaZa [632]		no line measurements
21CuHiMo [633]		no new line measurements
21FaArVa [634]		no new line measurements
21FoRuSib [635]	3028 – 6058	no new data
21EsFa [636]	2884–2969	no new line measurements
22ZhXuWa [637]	3225 – 3857	no line measurements
23MaThCa [638]		no line measurements
23VaDeKa [639]		no new line measurements

[c] Raman lines

In some instances, we found lines that were measured in earlier works and documented elsewhere, or they were assigned in later publications. Here are details for such cases:

83DeFrPr and **83DeFrPrb** [515, 640]: We used the lines as published and assigned in 97MaBeSa [506].

81DoKoTa [641]: Measurements of one F-symmetry line at 88 THz were published in 85ChKlNi [514]. We could not find the original papers 79DoKoTa [642] and 81DoKoTa [641] (references 6 and 8 of [514] respectively).

98BrKaRu [505]: We used the more recent assignments from 16AmLoPi [12].

02HiQu [498]: We got the full assignments from 12TaQu [487].

05Brown [496]: We got the full assignments of 27 of the published lines from 12TaQu [487].

09ScKaGa [495]: We got the full assignments of 27 of the published lines from 12TaQu [487].

13AbIwOk [482]: We got the full assignments from 18AmBo [643].

13CaLeWa [484]: The transitions were published unassigned, but have been assigned in other works; we used 3436 lines assigned by 17NiChRe [644], and 2445 lines by 16NiReTa [475].

5.4 Raman spectra

The following data sources provided Raman spectra we evaluated and considered in our analysis. We included 379 Raman transitions in total. The sources we used are the following:

75ChBe [524] reported 196 ν_2 Raman transitions in the range 1360-1770 cm^{-1} belonging to the O,P,R, and S branches which were assigned by Gray et al. (76GrRo) [553] and Champion (77Champion) [557].

92BeSaCa [509] reported 83 ν_1 and $\nu_2+\nu_4$ Raman lines in the range 2911-2921 cm^{-1} belonging in the Q branch.

91MiLaSt [511] reported 13 ν_2 Raman lines in the range 3063-3066 cm^{-1} belonging to the Q Branch.

94HiChTo [512] reported 37 $2\nu_2$ Raman lines in the Q branch and the range 3063-3070 cm^{-1} from a thesis by J.M. Jouvard, University of Bourgogne (1991).

97MaBeSa [506] measured 21 $2\nu_1 - \nu_1$ Raman lines in the Q branch. In addition, they reported 4 Raman lines in the $2\nu_3 - \nu_3$ band in the R and P branches and the 2800-6000 cm^{-1} range that are originally from 83DeFrPr [515], as well as 6 lines from 83DeFrPrb [640]. The 83DeFrPrb lines were not validated by MARVEL.

92SaCaDo [601] reported 45 ν_1 Raman lines that have also been published and assigned by Bermejo et al. 92BeSaCa [509], as well as 13 lines by Koslov et al. (79KoPrSm) [569] and 6 lines by Graener et al. (85GrLa) [590]. The assignments of these lines were also done using lines by Bermejo, et al. (92BeSaCa) [509].

The following Raman sources were not used. It is possible that some of these sources could have been recovered by assigning them ourselves, but given their low accuracy, they were unlikely to provide significant value to this analysis.

85ThFaKo [591]: The Raman lines reported were not used because of low accuracy.

78OwPaDo [563]: 32 ν_1 Raman lines were measured in the 2916-2918 cm^{-1} range with assignments without counting numbers. **70ClSt** [533]: No measured wavenumbers.

75Champion [550]: Only calculated values were provided.

78MaHeBy [562]: No measured wavenumbers.

15MaKcVa [622]: Measured Raman spectra were reported at temperatures ranging from 300 K to 860 K covering the $882 - 1791$ cm^{-1} and $2548 - 3434$ cm^{-1} regions without assignments.

77Berger [556]: Raman ν_3 lines were reported ranging from 2850 cm^{-1} to 3100 cm^{-1}. The lines were assigned in this source as well as by Champion et al. (80ChPiBe) [570] but the counting numbers follow a different convention that we could not use.

83FrIlFi [587]: ν_1 Raman Q branch lines were reported from 2916 to 2917

cm^{-1} assigned with a different convention for the counting numbers.

06JoChSa [30]: No measured wavenumbers.

82LoBrRo [582]: Measurements of $2\nu_4$ Raman transitions in the 2460-2675 cm^{-1} region were published. The assignments were different and due to low accuracy, we were not able to include them in the analysis at this stage.

07JoGaCh [611]: No measured wavenumbers.

5.5 Magic numbers

To interconnect previously unlinked networks, including the ortho, para, and meta networks, we use artificial transitions that we call 'magic numbers'. In addition to these, the two measured transitions from Itano et al. [517] and Ozier et al. [535] physically link the E (para) and F (ortho) networks.

We used some magic numbers to link unconnected components (refer to section 5.8). Specifically, the first three (MAGIC.1, MAGIC.2, MAGIC.3) were used to link the ortho (F), para (E), and meta (A) networks, the next three (MAGIC.4, MAGIC.5, MAGIC.6) were used to improve the connection between unlinked networks, and the last four (MAGIC.7 to MAGIC.10) connected the first four larger energy components. For this work, the Effective Hamiltonian wavenumber values by Amyay, et al. (16AmLoPi) [12] were used as magic numbers, which are listed in Table 5.6.

5.6 MARVEL energy uncertainties

When running MARVEL we have to include line position uncertainties. We started by using the uncertainties given in the experimental sources, where available. To make the network self-consistent though, we increased some of these initial uncertainties, and when missing in the original papers, we estimated them by assessing the degree of their agreement with the rest of the network (Combination Differences). The last column of Table 5.4 shows the origin of the uncertainty adopted

Table 5.6: Magic Numbers. Wavenumber values were selected from the Effective Hamiltonian energy values by Amyay et al. (16AmLoPi) [12].

Wavenumber (cm^{-1})		Upper State				Lower State				Label
Value	**Unc**	P'	J'	C'	α'	P''	J''	C''	α''	
10.481641	0.000001	0	1	F_1	1	0	0	A_1	1	MAGIC.1
31.442100	0.000001	0	2	E	1	0	0	A_1	1	MAGIC.2
31.442366	0.000001	0	2	F_2	1	0	0	A_1	1	MAGIC.3
62.878129	0.000001	0	3	A_2	1	0	0	A_1	1	MAGIC.4
104.772781	0.000001	0	4	A_1	1	0	0	A_1	1	MAGIC.5
62.875738	0.000001	0	3	F_1	1	0	0	A_1	1	MAGIC.6
2179.816	0.030	0	20	E	1	0	0	A_1	1	MAGIC.7
2620.967	0.010	0	22	E	1	0	0	A_1	1	MAGIC.8
3104.763	0.010	0	24	A_2	1	0	0	A_1	1	MAGIC.9
3104.752	0.010	0	24	F_2	2	0	0	A_1	1	MAGIC.10

for each source. These input transition uncertainties are used by the MARVEL algorithm to derive the uncertainties for the final energy levels (see Table 5.7 for the mean energy uncertainty per polyad). This manual handling of the transition uncertainties was the first method we followed, but a more sophisticated way to deal with this is the bootstrap method, for which we performed 100 iterations [195]. The MARVEL energy uncertainties with and without the bootstrap method are presented in Figure 5.5. Without the bootstrap method, MARVEL yielded an average energy uncertainty of 0.0036 cm^{-1} based purely on the stated input uncertainties. However, when the bootstrap method was applied, the average energy uncertainty increased slightly to 0.0049 cm^{-1} suggesting that the input uncertainties are too low for the cases of polyad 0, 1, and 2. Interestingly, this increase in uncertainty on bootstrapping is very similar to that found for other systems (e.g. N_2O [195].

5.7 Reassignment of spectra

Regarding the line assignments, we faced the challenge that some sources used different conventions for the non-rigorous quantum number α, or the lines provided were not assigned fully or at all. For those without assignments, we either assigned

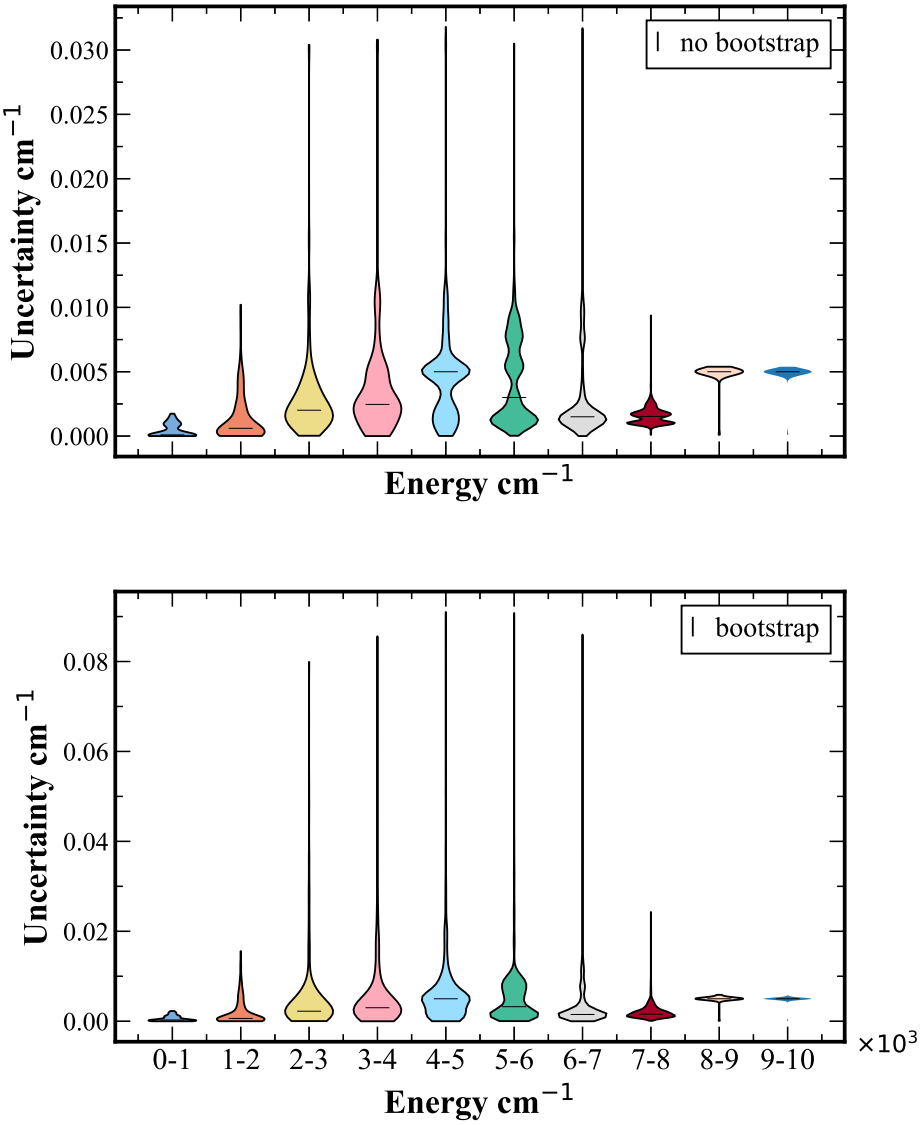


Figure 5.5: The MARVEL energy uncertainties with respect to the energy with and without the application of the bootstrap method. The width of the violins indicates the number of energy levels in each energy range.

Table 5.7: Summary of the MARVEL energies. Energy range is in cm^{-1}. MU/MUb: The Mean Energy Uncertainty before (MU) and after bootstrap (MUb). Mean obs. – calc. in cm^{-1}: 'obs' is referring to the MARVEL value and 'calc' to the calculated value by Yurchenko et al. [3]

Polyad	Energy range cm^{-1}	# E.L.	max J	MU/MUb	Mean obs. – calc.
P_0	0 – 3628.25	247	26	0.005/0.01	-0.0114
P_1	1310.7 – 5054.83	1088	27	0.005/0.01	0.0093
P_2	2587.04 – 6239.03	3154	27	0.005/0.009	0.0184
P_3	3870.48 – 7017.60	7708	23	0.005/0.006	0.0099
P_4	5121.72 – 7417.90	8232	18	0.002/0.002	0.0022
P_5	6377.52 – 7903.64	2528	15	0.001/0.001	-0.1193
P_6	8562.46 – 9629.88	333	10	0.005/0.005	-0.1769
P_7	9832.06 – 9986.23	2	4	0.005/0.005	-0.3876

them ourselves or excluded them, leaving them for a future project (see chapter 6). In particular, Table 5.8 shows a list of sources that provided unassigned or partly assigned transitions, or transitions with different notations. The second column of the table shows the other sources we used to help fully assign these lines and convert them to our notation scheme. Table 5.9 presents a few cases where we changed the assignment of a line based on the resulting MARVEL network.

5.8 The MARVEL network

Out of a total of 82 173 transition frequencies assessed, 308 were not validated and were assigned a negative wavenumber in the input line list. At this stage, six artificial transitions were included called "magic" numbers (the first six in Table 5.6). Three of them to connect the different nuclear spin isomers, and three to improve the network connectivity as explained above in section 5.5. This resulted in a spectroscopic network comprising 81 865 lines, separated into 305 sub-networks, which I will refer to as as *components* here. The largest component consisted of 80 598 transitions connecting 23 060 energy levels, with 109 of these components containing one single transition linking two levels.

The next four components were two E symmetry, one A_1/A_2, and one F_1/F_2

Table 5.8: List of partly assigned experimental sources used in this work, and the sources we used for their full assignments.

Source	Used for assignment
$P_1 - P_0$	
79PiDu [520]	72Botineau [540] and 16AmLoPi [12]
82JeRo [516]	16AmLoPi [12]
$P_2 - P_0$	
72EvDaWe [645]	09AlBaBo [11]
76Pine [523]	EH fit [12]
76BlEdJo [522]	09AlBaBo [11]
79DaPiRo [519]	several other sources
80KnEdPe [518]	09AlBaBo [11]
80ClDaRu [646]	09AlBaBo [11]
92KrLiWe [510]	09AlBaBo [11]
92PuWe [450]	EH fit [12]
98ErTyKr [503]	09AlBaBo [11]
00FeChJo [502]	09AlBaBo [11]
18KoMaEs [471]	13TyTaRe [619]
$P_3 - P_0$	
88Brown [513]	EH fit [12]
$P_4 - P_0$	
10NiLyMi [491]	mainly 15NiLyMi [411]
13ZoGiBa [485]	EH fit [12]
16DeMaRe [476]	EH fit [12]
18GoPrKa [469]	16DeMaRe [476].
18YaLiFe [470]	several other sources
19LiYaFe [463]	HITRAN [104], EH fit [12]
19YaLiFe [464]	HITRAN [104], 13ZoGiBa [485], 13CaLeWa [647]
20YaLiPl [460]	several other sources
$P_5 - P_0$	
12CaWaMo [486]	HITRAN [648]
12TaQu [487]	HITRAN [104], 15ReNiTy[623], 02HiQu [498].
16ReNiCa [477]	several other sources
$P_4 - P_2$	
21OkInOk [458]	several other sources, EH fit [12]
$P_6 - P_2$	
21FoRuSi [457]	several other sources, EH fit [12]

Table 5.9: Specific lines reassigned because they were not validated.

Source	Line position cm^{-1}	Old assignment	New assignment
Line tag		$P', J', C', \alpha', P'', J'', C'', \alpha''$	
05PrBrMa [497]			
05PrBrMa.218	4286.9494	3, 4, F_2, 41; 0, 5, F_1, 1	3, 4, F_2, 41; 0, 5, F_1, 2
05PrBrMa.157	4492.21562	3, 4, F_2, 52; 0, 3, F_1, 1	3, 4, F_2, 58; 0, 5, F_1, 1
05PrBrMa.957	4509.85664	3, 10, A_1, 37; 0, 9, A_2, 1	3, 10, A_2, 35; 0, 9, A_1, 1
05PrBrMa.1196	4522.04973	3, 11, F_1, 117; 0, 10, F_2, 3	3, 11, F_2, 114; 0, 10, F_1, 2
10NiLyMi [491]			
10NiLyMi.1575	5998.2405	4, 10, F_2, 325; 0, 10, F_1, 2	4, 10, F_2, 326; 0, 10, F_1, 2
13NiBoWe [481]			
13NiBoWe.1198	5940.473	4, 8, F_2, 180; 0, 8, F_1, 1	4, 8, F_2, 181; 0, 8, F_1, 1
13CaLeWa [647]			
13CaLeWa.1094	5931.3501	4, 8, F_1, 207; 0, 7, F_2, 1	4, 8, F_1, 208; 0, 7, F_2, 1
15NiLyMi [411]			
15NiLyMi.2170	6102.64367	4, 10, F_2, 325; 0, 9, F_1, 3	4, 10, F_2, 326; 0, 9, F_1, 3
17HaPrNi [474]			
17HaPrNi(2).74	4417.887686	3, 7, F_1, 66; 0, 6, F_2, 1	3, 7, F_1, 66; 0, 6, F_2, 2
17HaPrNi(2).54	4427.8182	3, 8, F_2, 75; 0, 7, F_1, 1	3, 8, F_2, 75; 0, 7, F_1, 2
17HaPrNi(2).31	4432.66252	3, 8, F_2, 76; 0, 7, F_1, 1	3, 8, F_2, 76; 0, 7, F_1, 2
17HaPrNi.53	4469.326872	3, 6, F_2, 80, 0, 7, F_1, 1	3, 6, F_2, 80; 0, 7, F_1, 2
17HaPrNi.57	4489.942539	3, 4, F_2, 56, 0, 5, F_1, 1	3, 4, F_2, 56; 0, 5, F_1, 2
18GhMoKa [468]			
18GhMoKa.911	5753.75715	4, 8, F_1, 207; 0, 9, F_2, 1	4, 8, F_1, 208; 0, 9, F_2, 1

symmetry networks which consisted of 103, 57, 48, and 44 transitions respectively. To establish connections between them and the largest component four new magic numbers were added (the last four in Table 5.6). We connected only these four to the largest network because the next was a much smaller one consisting of only 29 transitions. As a result, we ended up with 81872 validated transitions in total separated into 301 components, the largest one of which includes 80854 transitions that link 23 292 energy levels.

The distribution of energy levels according to their symmetries is as follows: 21.4% are of A_1/A_2 symmetry, 18.4% are of E symmetry, and 60.2% are of F_1/F_2 symmetry. This is consistent with the ratio 1 : 1 : 2 : 3 : 3 expected at highly excited

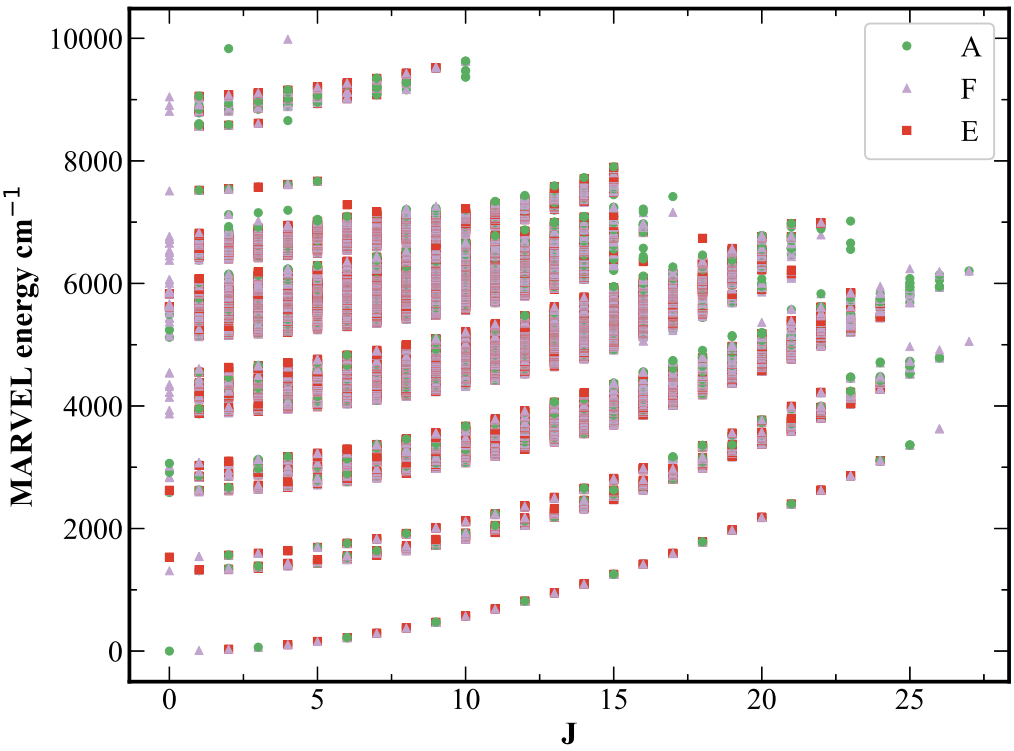
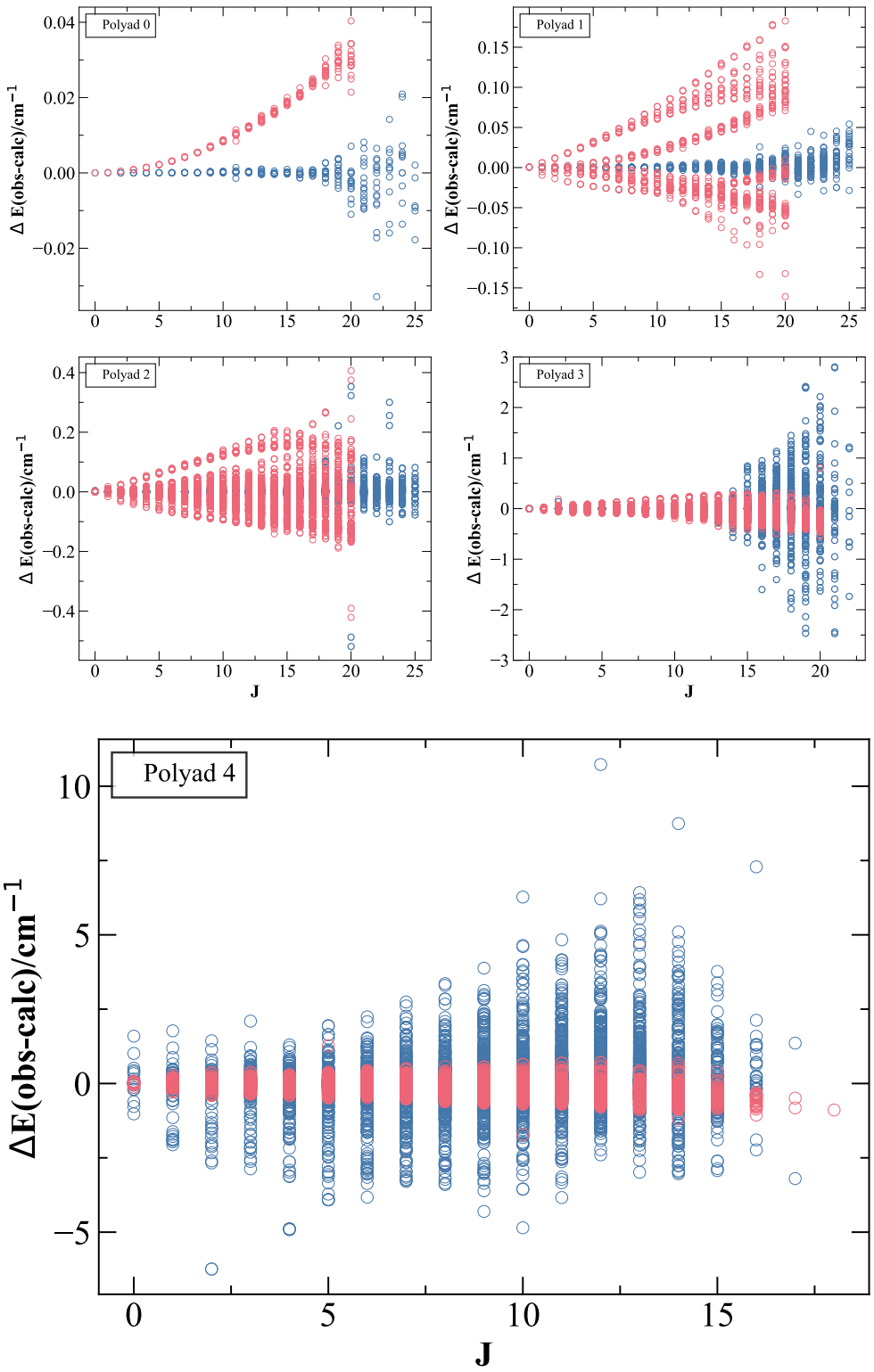
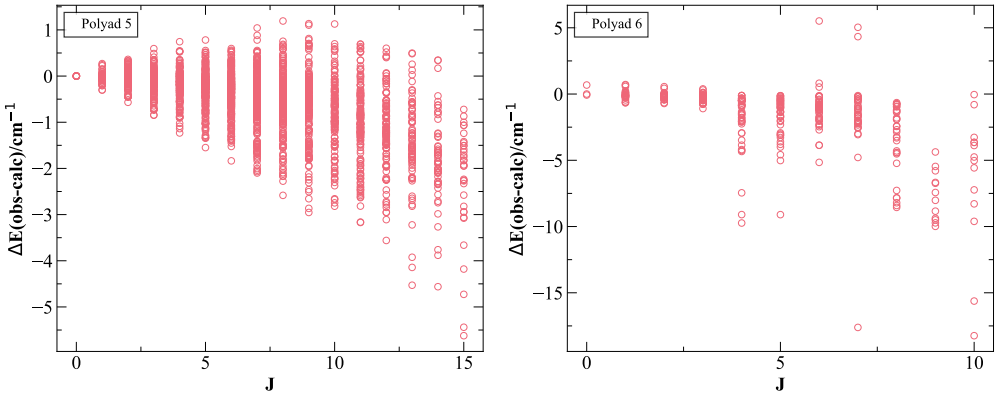


Figure 5.6: The $^{12}C^{1}H_4$ MARVEL energy levels for the first eight polyads obtained in this work. The symbols denote the different symmetries; A: A_1, A_2, E: E, F: F_1, F_2.

states. The energy distribution with respect to J is illustrated in Figure 5.6. Relevant details (wavenumber range, J range, average energy uncertainties, number of energy levels) are given in Table 5.7.



(a) Polyad 0, 1, 2, 3, 4.



(b) Polyad 5 and 6.

Figure 5.7: Difference between the MARVEL energies (obs) and the a. Effective Hamiltonian [12] (blue), b. Variational calculations (pink) [13].

We compared our empirical rovibrational energy levels to the Effective Hamiltonian results of 16AmLoPi [12] and variational energies (purely calculated) from the TheoReTS project [13] as shown in Figure 5.7. We also compared with calculated levels from the MeCaSDa database [649] as shown in Figure 5.8.

For the first two polyads the agreement with the Effective Hamiltonian energies is very good for $J \leq 17$ with a maximum difference of less than 0.007 cm^{-1}. For the next two polyads, the agreement with the Effective Hamiltonian energies is very good for $J \leq 15$ with a maximum difference of less than 0.014 cm^{-1}. Regarding the comparison with the TheoReTS variational energies, the agreement is always within 1 cm^{-1} for the first five polyads. Additionally, in polyad 3 the TheoReTS energies exhibit better agreement with the MARVEL energies than the Effective Hamiltonian energies in high J values. The comparison with the MeCasDa database follows a similar trend to the one with the Effective Hamiltonian results as seen in Figure 5.8. The differences grow with J and polyad P in all cases and grow more in the cases of polyad 5 and polyad 6 where our data are limited. For polyad 2 Figure 5.7 shows a difference of $\simeq 0.4$ cm^{-1} between MARVEL and the Effective Hamiltonian energies, as well as the TheoReTS energies for four $J = 20$ levels. These differences are much smaller when compared with MeCaSDa. These four levels, comprising two E levels and two A_2 levels, are part of two weakly coupled components within the network. Their connections to the broader network are limited, leading to less accu-

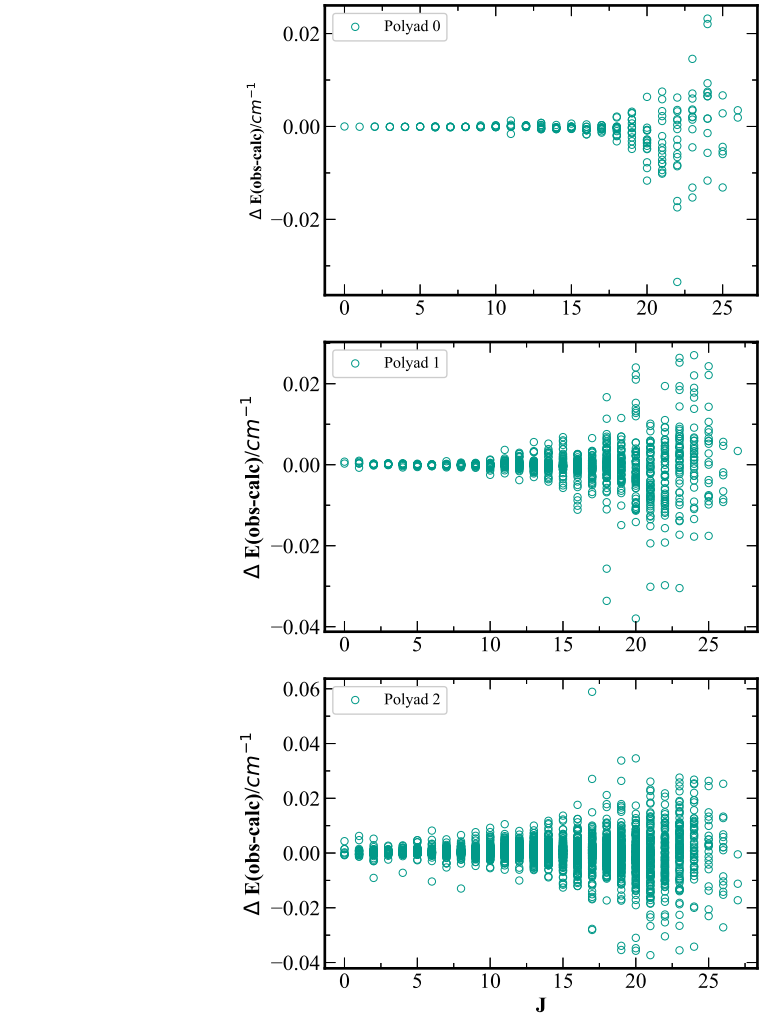
rate definitions. Additionally, the single transition defining the states (2,20,A_2,14) and (2,20,E,28) is given three different assignments in the original source [12]; it is assigned as an F line, an E line, and an A line. We note that F states are generally better defined, as they are stronger, and characterised by more transitions. More experimental data are required to resolve the above problem and enhance the accuracy of the A and E networks.

Regarding the large residuals for four polyad 2 levels, Table 5.10 and 5.11 show the connections of these levels with the rest of the network. For the two A_2 energy levels; their only connection with the network is through the level (1, 21, A_1, 5) for both of them and (1, 20, A_1, 6) for one of them. Regarding the level (1, 20, A_1, 6), it is only related through a single transition to one other level: (2, 21, A_2, 12) and this has no further links. As for the (1, 21, A_1, 5) level, it couples weakly as well with the rest of the network; it is connected with single transitions with two levels of higher energy and a single transition with the lower level (0, 22, A_2, 1) which is defined only by higher levels.

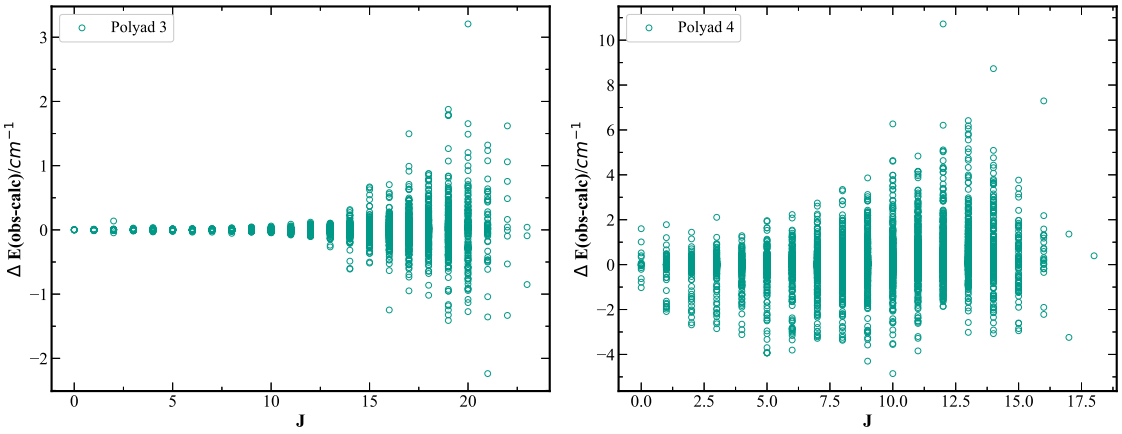
Furthermore, the two E levels have a single connection to the network through (1, 21, E, 11). This, in turn, has a weak connection with the rest of the network because it leads to three higher energy levels with single transitions and only one lower level (0, 22, E, 1) with one line. The level (0, 22, E, 1) is linked through single transitions with three higher energy levels and is defined with a single artificial transition (MAGIC number) with the ground state.

5.9 MARVELous Methane

Yurchenko et al. [3] generated the MARVELous Methane (MM) line list in 2024, which covers wavelengths $\lambda > 0.83$ μm (wavenumbers up to 12 000 cm^{-1}) and contains over 50 billion transitions between 9 155 208 states with total angular



(a) Polyads 0, 1, 2.



(b) Polyads 3, 4.

Figure 5.8: Difference between the MARVEL energies (obs) and the MeCaSDa database (calc).

Table 5.10: Details of the connections of the two E energy levels with large residuals. The obs. − calc. values are in cm^{-1}. The subscript $_T$ is for the comparison with the TheoReTS variational calculations, $_{EH}$ is for the comparison with the Effective Hamiltonian values, and $_M$ is for the comparison with the MeCaSDa energies. The quantum numbers are: p, J, C, α.

MARVEL Energy Levels	**obs-calc$_T$**	**obs-calc$_{EH}$**	**obs-calc$_M$**	**Main links**	**Secondary links**
2 20 E 28, 4974.164 cm^{-1}	0.41	-0.49	-0.003	1 21 E 11	
2 20 E 27, 4967.845 cm^{-1}	-0.39	0.35	-0.0009		
Main connecting level					
1 21 E 11, 3796.475 cm^{-1}		-0.004	-0.0004		
(1 21 E 11) links					
1. 2 22 E 14		0.013	-0.0098		1 22 E 6
2. 2 21 E 15		0.079	-0.006		-
3. 0 22 E 1		0	-0.00056		1 22 E 4 1 23 E 4 2 23 E 51 0 0 A_1 1

Table 5.11: Details of the connections of the two A_2 energy levels with large residuals. The obs. − calc. values are in cm^{-1}. The subscript $_T$ is for the comparison with the TheoReTS variational calculations, $_{EH}$ is for the comparison with the Effective Hamiltonian values, and $_M$ is for the comparison with the MeCaSDa energies. The quantum numbers are: p, J, C, α.

Energy Levels	**obs-calc$_T$**	**obs-calc$_{EH}$**	**obs-calc$_M$**	**Main links**	**Secondary links**
2 20 A_2 14, 4974.134 cm^{-1}	0.37	-0.52	-0.035	1 21 A_1 5	
2 20 A_2 13, 4967.815 cm^{-1}	-0.42	0.32	-0.031	1 21 A_1 5 and 1 20 A_1 6	
Main connecting levels					
a. 1 21 A_1 5, 3796.445 cm^{-1}		-0.03	-0.03		
b. 1 20 A_1 6, 3725.267 cm^{-1}	-0.16	-0.018	-0.038		
a. (1 21 A_1 5) links					
1. 2 21 A_2 8		0.059	-0.027		1,22,A1,3
2. 2 20 A_2 23	-0.1	-0.036	-0.025		-
3. 0 22 A_2 1		-0.03	-0.03		1 22 A_1 3 1 21 A_1 5 2 23 A_1 24 3 21 A_1 36 3 23 A_1 9
b. (1 20 A_1 6) links					
2 21 A_2 12		-0.06	-0.037		-

momentum $J \leq 60$. The line list was generated through solving the nuclear motion Schrödinger equation using the variational program TROVE for an empirically-derived potential energy surface (PES) and a new high-level *ab initio* dipole moment surface. The PES was constructed by fitting the ro-vibrational energies of CH_4 to the set of MARVEL derived energies. Moreover, the line list is adapted to high-resolution applications by replacing the calculated ro-vibrational energies with the experimentally-derived values where available. Table 5.7 shows the average obs. − calc. values for each polyad, where obs is referring to the MARVEL value and calc to the calculated with TROVE.

5.10 Outlook

We compiled a thorough database of published experimental methane spectra up to July 2023 and used them to extract accurate empirical rovibrational energy levels. We ended up with 82 173 measured transitions assembled from 96 articles. We used Combination Differences to attribute quantum numbers to transitions where they were missing, or to convert to our counting number notation where necessary. As can be seen in tables 5.4 and 5.3 we could find assigned methane spectra in the literature up to polyad 7 and mainly for cold bands. However, starting from even the lower part of the icosad (polyad 5) the number of well assigned lines starts decreasing. For polyad 7 we have almost no assigned measured transitions. This makes the confidence of the assignments that we have in these higher energies smaller, since we do not have enough combination differences starting from ~ 8000 cm^{-1}. This is something to expect, as spectral congestion in the near-infrared and visible regions because of the increasing number of interacting levels makes it harder to resolve individual lines. The 82 173 lines yielded 23 292 energy levels through the MARVEL procedure. With the bootstrap method, 66.8% of MARVEL energy levels have an uncertainty lower than or equal to 0.005 cm^{-1}.

The MM line list [3] contains over 50 billion transitions and covers the frequency range from 0 to 12 000cm^{-1} with rotational excitation up to $J = 60$. The line list is based on a new empirical potential energy surface, which was refined by

fitting to the experimentally derived energies of CH_4. The accuracy of the line list is further improved via the MARVELisation procedure, where the computed energies are replaced by the experimentally derived values as described in this chapter. Using the MARVELised energy levels only, near 1 000 000 new lines were generated of that quality. The high-resolution transitions are available in ExoMolHR [180].

Several recent studies have used the MM line list for methane to refine atmospheric models and retrievals for exoplanets. Zhang et al. [650] used it to update opacities in their analysis of JWST/NIRCam emission spectra for HD 189733b, one of the most extensively studied exoplanets, and found evidence of methane depletion. Schleich et al. [651] generated synthetic spectra to assess the impact of different temperature-pressure profile assumptions on retrieval accuracy for WASP-39b, showing that an isothermal profile does not adequately describe the atmosphere. Schmidt et al. [652] confirmed the detection of $^{12}C^{1}H_4$ ($\sim 4\sigma$) in K2-18b, using opacities from MM in their POSEIDON model and the "10to10" line list in their BeAR model, demonstrating that their methane detection is robust across retrieval frameworks. Lastly, [653] incorporated the line list into their radiative transfer model PUMAS to study aerosols in WASP-39b. Additionally, for Gl 229 B, the first T-type brown dwarf discovered, Kawashima et al. [654] obtained a C/O ratio consistent with its host star. Their study also validated molecular line lists using a high-resolution spectrum of the atmosphere, revealing a poorer fit with the ExoMol "34to10" line list [414], but better agreement with HITEMP [105] and the MM line list.

Chapter 6

Assignment of methane spectra

This project builds upon the previous work involving the Marvelisation of the MM line list performed by Yurchenko et al. [3]. The aim is to improve the line list quality through the incorporation of newly assigned experimental transitions. During the MARVEL project for methane, we compiled an extensive collection of sources containing valuable and accurate methane spectral data. Table 6.1 summarises information from 51 such sources that contain lines we did not use because they are unassigned, or partly unassigned. Our goal was to provide full quantum number assignments to as many of these lines as possible, using the MM line list (stick spectrum at 296 K shown in Figure 6.1) as a reference guide. These newly assigned transitions were then incorporated into MARVEL, allowing us to derive updated empirical energy levels. This iterative process ultimately will lead to further improvements in the MM line list. In this chapter, I present the work performed on 14 of the 51 sources incorporated into the MARVEL project update (see Table 6.2). This update includes new line assignments derived from these sources, as well as newly published assigned transitions from recent experimental studies.

Table 6.1: Summary of experimental sources collected. Each entry lists the source, spectral range in wavenumbers cm^{-1}, and number of provided spectral lines.

Sources	Wavenumber Range	# Lines
72HuPoVa [655]	4136–4288	452
77Berger [556]	2850–3100	237
78OwPaDo [563]	2916-2918	32
80PiHiBe [656]	9000–9155	108
81BrToHu [17]	2400-3200	33
82HuLoRo [657]	2930-3250	595
83FrIlFi [587]	2916–2917	13
83PiChGu [658]	2250–3260	191
84MaFrPr [659]	2940–2995	6
85HiLoBr [660]	1568-1932	13
85MaFrPr [661]	2892–2935	20
	8876–8938	10
88Brown [513]	3700-4136	223
88Margolis [662]	5500-6180	1312
89VaCh [596]	1270-1317	11
90Margolis [663]	5597–5635	1600
91CaChSt [664]	13702–13887	39
93LuLoGa [665]	11539–12756	32
94BoLiRe [666]	11220–11313	137
95CaPeJo [667]	11245–11312	30
95SiOb [668]	13470–14025	869
95TsSa [669]	11200–11335	269
96SiOb [670]	7128–7373	293
97Pine [671]	3028-3122	103
98BoRePl [672]	5500–6180	40
		15434 (800 K)
03NaBe [673]	2000–6400	22163 (1000 K)
		25727 (1273 K)

Continued on next page

Sources	Wavenumber Range	# Lines
	6775–6789	14
05Brown [496]	7467–7564	9
	9001–9111	27
07LuGo [674]	11870–11930	48
08FrWaBu [675]	5860–6185	1309
08KaGaRo [676]	5860–7700	128
09GaKaCa [677]	5852–6181	845
09ScKaGa [495]	7351–7655	3474
10CaWaKa [678]	6716–7655	12865
11MoKaWa [679]	7541–7919	5070 (80 K) 7690 (294 K)
12CaWaMo [486]	5854–7919	23138
12HaBeMi [14]	1067–4900	160840 (573K -1673 K)
12WaMoKa [680]	6717–7589	19940 (80 K) 24001 (296 K)
12GaChZh [681]	6038–6050	72
13CaLeMo [647]	5855–6183	9228
13MaPrMo [682]	7040–7378	654
15BeKaCa [683]	7908-8345	12703
15BeLiCa [684]	9028–10435	7786
15HaBeBa [412]	2600-5000	194129 (473K -1173 K)
15MaKcVa [622]	882–3434	2422
18GhVaMo [685]	5693–6257	177
18SeSiLu [686]	9057–9167	36
19WoBeRe* [687]	5200-9200	4047349 (295 K-1000 K)
20YaLiPl [460, 688]	6075–6078	90
20YaLiPlb [688]	6077	2
21MaYuSu [689]	6770-7570	23390
21YoBeDu [15]	2750-3200	300
22Lucchesini [690]	12799–12840	112

Continued on next page

Sources	Wavenumber Range	# Lines
23CaKaVa [691]	10800–14000	12800

* Compilation of measured spectra in several temperatures and resolutions.

6.1 Methodology

The general methodology we followed can be broadly described in the following steps:

1. We collect the experimental line positions along with intensities, when available, and generate the corresponding MM line list at the appropriate temperature for comparison.

2. We match individual or grouped spectral lines between the experimental data and the MM line list at the corresponding temperature, using Python tools. In more detail, as a first step, we find "trivial" matches to transitions which are already present in our database, and usually correspond to the strongest lines. These lines are the so-called "Ma"-"Ma" transitions, as they connect two levels already MARVELised in the `.states` file. Matching new measured spectral lines with such transitions gives us an idea for the accuracy of the lines in this specific source.

   The second step is to identify matches with transitions linked to "Ca" (calculated) energy levels in the MM line list. These matches are particularly valuable because including them in MARVEL yields new empirical energy levels, improving the accuracy of the line list beyond purely theoretical predictions. To illustrate this, we present a spectral segment where lines labelled as "Ma" and "Ca" have been matched between the experimental data and the MM theoretical predictions (see Figure 6.2).

3. We validate the assignments through the MARVEL procedure, mainly by checking combination differences; this involves comparing the energy differences between pairs of transitions that share a common upper or lower

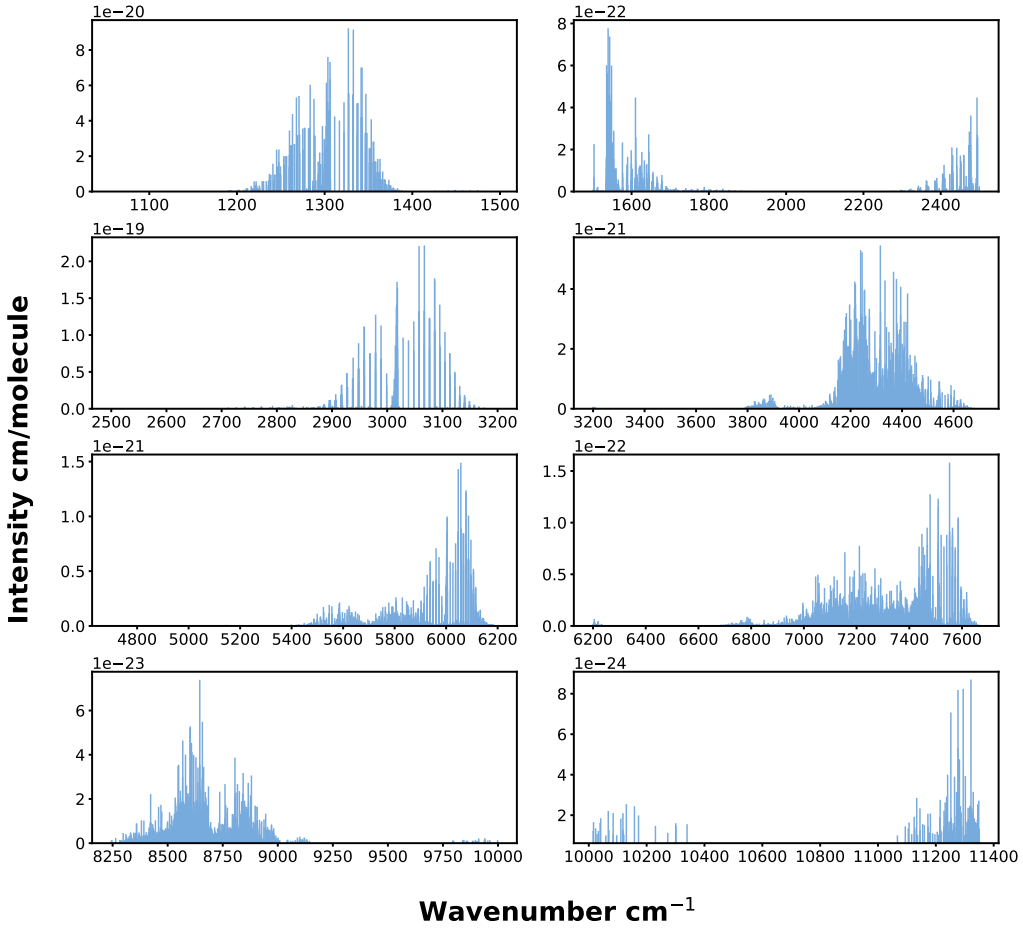


Figure 6.1: MM stick spectrum at 296K generated with ExoCross [8].

level. This step often requires revisiting and refining assignments when inconsistencies are detected. For example, one recurring difficulty involved the characteristic triplet patterns of methane, arising from its A, E, and F symmetry components. These triplets often appear as closely spaced lines in the spectrum, making it challenging to assign each transition unambiguously.

The general strategy of the codes used starts with filtering the MM lines to correspond to the approximate spectral range of each experimental dataset. This reduces computational load and excludes irrelevant transitions. We also apply a minimum intensity threshold.

Initial intensity tolerance criteria are set relatively relaxed, typically allowing

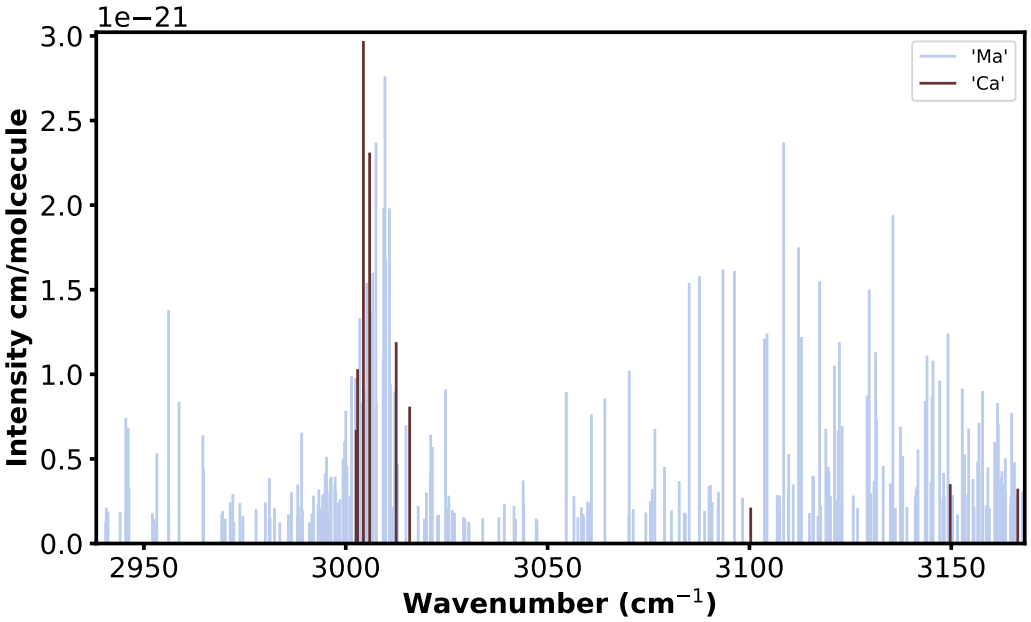


Figure 6.2: Assigned lines from 12HaBeMi [14] at 573 K, distinguishing "Ma" (light blue) and "Ca" (dark red) labelled transitions.

up to a 60-80% difference between experimental and MM intensities to accommodate uncertainties in both measurements and theoretical predictions. This allowed for multiple candidates in some cases, and then the closest match of intensity and position was chosen. Beyond numerical tolerances, stick spectra were visually assessed to strengthen assignment confidence. For instance, when a particular line's assignment was well established, differences in intensity and line position relative to neighbouring lines aided in assigning nearby transitions with greater certainty.

Line position tolerances vary depending on the specific case. We typically begin with a very strict tolerance such as the reported experimental uncertainty, to identify any obvious matches. However, in many instances, especially at higher polyads where the differences between calculations and MARVEL are more prominent, we applied a more relaxed tolerance, ranging from a few times the experimental uncertainty up to 1–4 cm^{-1}. This broader window allowed us to capture all potential candidates, after which we selected the closest match based on line position. Outliers were further scrutinised. MARVEL helped eliminate inconsistent assignments, and we also reviewed the observed–calculated (obs. − calc.) deviations

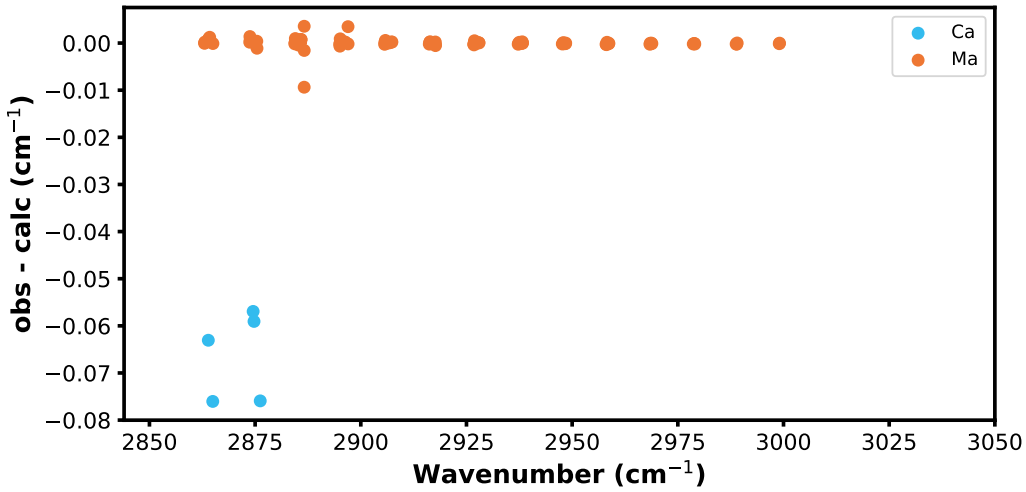


Figure 6.3: Large obs. – calc. values between experimental 21YoBeDu spectral lines and matched "Ca" MM lines.

across each source to flag any remaining mismatches. "Calc" in the context of this chapter refers to values taken from the MM line list. These may correspond either to theoretical calculations or to energy levels that have already been MARVELised. We use the term "calc" primarily to contrast with "obs", which denotes values obtained directly from the experimental datasets discussed throughout this chapter. An example of this are five lines from the source 21YoBeDu [15] that displayed obs. – calc. values between -0.05 cm^{-1}to -0.08 cm^{-1}with the MM lines that they matched with as seen in the Figure 6.3.

Even though the upper levels of these transitions were calculated, we don't expect such large obs. – calc. values in polyad 2. Therefore, these lines require reassessment, and unless a more reliable assignment can be made, they should be left unassigned at this stage.

When lower-state energies were available in the experimental source, these values were used as supplementary constraints to support or confirm assignments, applying loose matching criteria to accommodate possible deviations.

Robust quantum numbers, such as the rotational quantum number J and the symmetry label C, were fixed in the matching process if they were available from the experimental source. In cases where this strict matching failed, these quantum

number criteria were relaxed to identify plausible assignments without compromising overall accuracy.

To assist with complex line assignments involving closely spaced transitions, we used a Combination Differences (CD) method, where we computed all plausible transitions between a set of excited state energies produced by MARVEL, and lower energy states (e.g., ground vibrational states), applying the quantum number selection rules (see Equation 5.6 and Equation 5.7). These generated transitions were then matched against experimental spectral lines. This comparison helps identify which transitions are reliably assigned and which may be outliers or require reassignment.

In particular, we used this method to resolve conflicts in the assignments we attributed to some of the 21MaYuSu [689] transitions. The CD code generated all allowed transitions between polyad 5 and polyad 0 levels. For example, two such lines matched on wavenumber and loosely on lower state energy with the two measured lines labelled 21MaYuSu.2174 and 21MaYuSu.3945. The other transitions defining the same upper energy level have the tags 21MaYuSu$_{Ca}$.1259, 21MaYuSu$_{Ca}$.1679, 21MaYuSu$_{Ca}$.1351, 21MaYuSu$_{Ca}$.1527, and 21MaYuSu$_{Ca}$.15819 and have taken their assignments from MM lines connected to a "Ca" upper level. So, in total a single level is defined by these seven transitions, all from this new source. These lines form two groups that support conflicting assignments for the same upper energy level. The Table 6.3 summarises these groups:

Group 1 includes the lines 21MaYuSu.2174 and 21MaYuSu$_{Ca}$.1259. Their closely matching MARVEL energies indicate one consistent assignment of the upper energy level. Group 2 consists of the 21MaYuSu.3945 together with the lines 21MaYuSu*Ca*.1351 and 21MaYuSu*Ca*.1679. This set supports an alternative assignment for the same upper level, differing slightly in energy from Group 1.

The outliers 21MaYuSu$_{Ca}$.1527, and 21MaYuSu$_{Ca}$.15819 are transitions that do not fit clearly into either group and require reassignment. By comparing the average energies derived by these transition groups, we can identify which assign-

Table 6.2: Overview of methane spectroscopic sources evaluated, including reference, spectral range in cm^{-1}, total and assigned line counts, experimental method, and temperature of measurement.

Sources	Range	Total # lines	# Assigned lines	Method	Temperature (K)
78OwPaDo [563]	2916-2918	32	32	Stimulated Raman Gain	296 (assumed)
81BrToHu [17]	2400-3200	33	32	FTIR absorption	296
82HuLoRo [657]	2930-3250	599	599	FTIR absorption	296 (assumed)
85HiLoBr [660]	1568-1932	13	13	FTIR absorption	302
88Margolis [662]	5500-6180	1312	1254	FTIR absorption	296
88Brown [513]	3700-4136	223	223	FTIR absorption	296
89VaCh [596]	1270-1317	11	11	Tunable Diode Laser absorption	130-296
97Pine [671]	3028-3122	103	103	Difference-Frequency Laser absorption	295
	6775–6789	14	14		
05Brown [496]	7467–7564	9	9	FTS absorption	296
	9001–9111	27	26		
12HaBeMi [14]	1067–4900	3256	1124	FTIR emission	573–1673
13MaPrMo [682]	7040–7378	654	16	Tunable Extended Cavity Diode Laser absorption	28
20YaLiPl [460, 688]	6075–6078	90	56	Cavity Ring-Down absorption	296
21MaYuSu [689]	6770-7570	23390	7248	Dual-Frequency Comb absorption	296–1000
21YoBeDu [15]	2750-3200	300	240	FTIR absorption	296–1098

Table 6.3: Energy Level: $P = 5$, $J = 4$, $C = F_1$, $\alpha = 146$. Avg Energy Value: E = 7171.650221 cm^{-1}derived from a MARVEL run.

Tag	Transition	Energy Level	Diff. from Avg	Lower State	Avg. Group Energy
Group 1					
21MaYuSu.2174	7066.532488	7171.311662	-0.339	0,4,F_2,1	7171.311927
21MaYuSu_Ca.1259	7108.436188	7171.312192	-0.338	0,3,F_2,1	7171.311927
Group 2					
21MaYuSu.3945	7014.415513	7171.542612	-0.108	0,5,F_2,1	7171.543122
21MaYuSu_Ca.1351	7108.667288	7171.543292	-0.107	0,3,F_2,1	7171.543122
21MaYuSu_Ca.1679	7066.764288	7171.543462	-0.107	0,4,F_2,1	7171.543122
Outliers					
21MaYuSu_Ca.1527	7066.828288	7171.607462	-0.043	0,4,F_2,1	7171.607462
21MaYuSu_Ca.15819	7067.911688	7172.690862	1.040	0,4,F_2,1	7172.690862

ment is more consistent with the observed data and try to reassign one of the groups accordingly to a more accurate upper (and maybe lower) level.

6.2 The experimental sources

Below we consider each of the fourteen sources in turn and include details on the assignment procedure. Information about the sources can be found in Table 6.2.

1. 21YoBeDu

   The experimental data from the study by 21YoBeDu [15] consist of high-

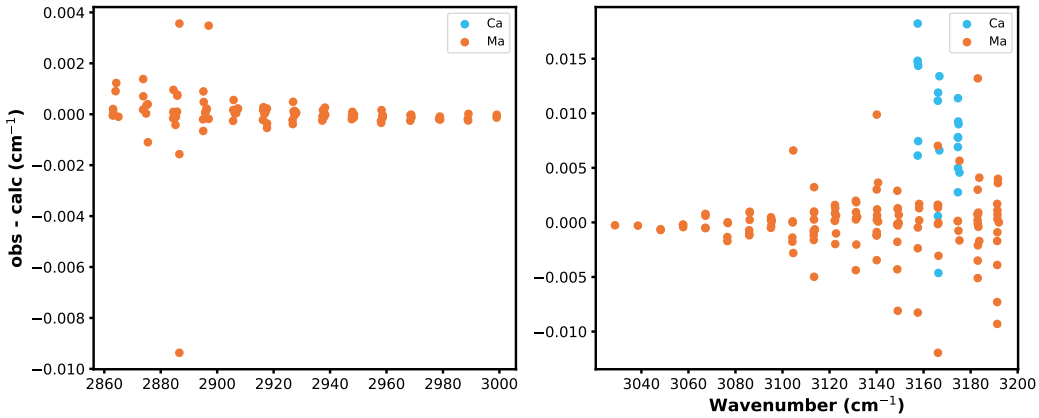


Figure 6.4: Residuals (obs – calc) for assigned transitions in the 21YoBeDu dataset. Label "Ma"/"Ca" detones that the matching MM line is linked to a MARVELised/calculated upper level.

resolution infrared measurements of methane line positions. A total of 953 lines were observed in the ν_3 vibrational band (polyad 2) over the wavenumber range of 2750–3200 cm^{-1} with average line position uncertainty 0.00015 cm^{-1}. The spectra were recorded at five different temperatures: 296 K, 463 K, 681 K, 894 K, and 1098 K, using a high-resolution Fourier transform infrared (FTIR) spectrometer. The line positions are provided assigned except for the counting numbers. To get the counting numbers we matched the experimental data with the MM lines based on matching the upper and lower quantum labels ($J^{'}$,$P^{'}$,$C^{'}$,$J^{''}$,$P^{''}$,$C^{''}$). Among candidates meeting these criteria, the match with the closest line position and best agreement in intensity was selected.

The residuals between the observed and the corresponding MM line positions (obs. – calc.) were analysed in two spectral regions. For transitions with line positions $\leq$ 3000 cm^{-1}, the mean residual was 0.0007 cm^{-1} with a standard deviation of 0.004 cm^{-1}. For transitions with line positions >3000 cm^{-1}, the mean obs-calc value was 0.001 cm^{-1} with a standard deviation of 0.004 cm^{-1}, indicating tighter agreement in this region as shown in Figure 6.4. Some transitions were observed at multiple temperatures, exhibiting very similar line position wavenumbers. After accounting for duplicates, al-

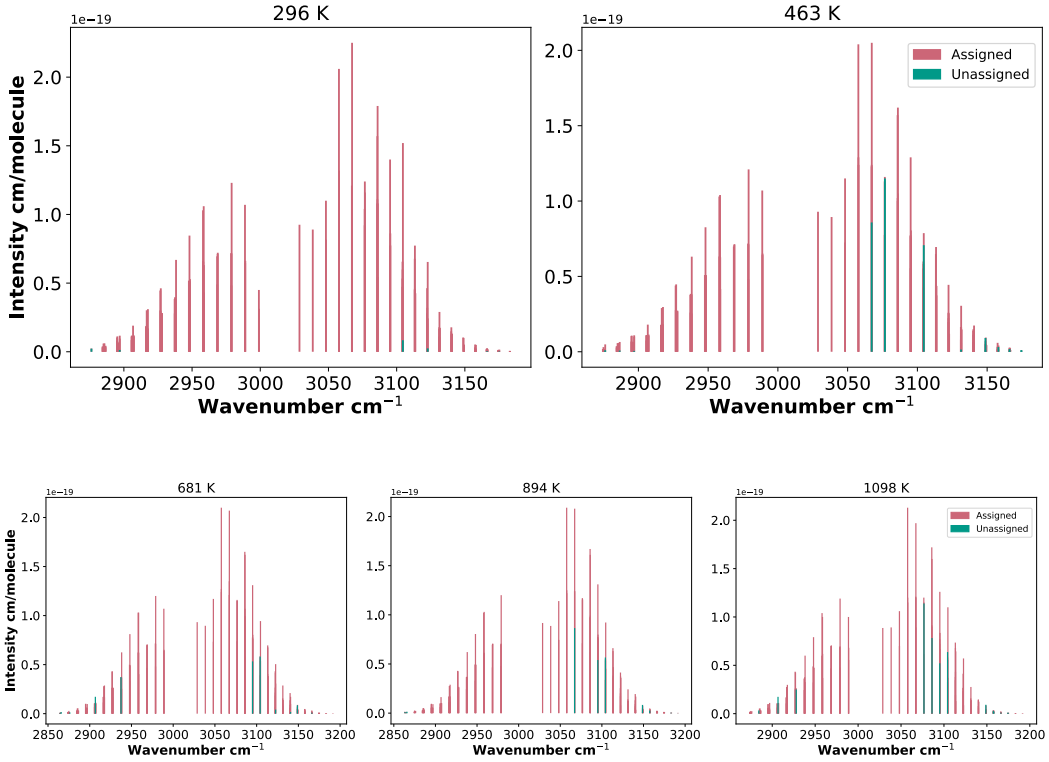


Figure 6.5: Stick spectra of methane as reported in 21YoBeDu [15], grouped into two panels by temperature range. Assigned lines are in pink, unassigned in green.

lowing their difference in wavenumber to be up to 0.005 cm^{-1}, the number of unique transitions is 300. Of these, we assigned 240 transitions fully and included them in the MARVEL procedure. We validated 234 out of the 240. One line was invalidated, and from the remaining, the 219 were validated against other lines in the network. Figure 6.5 shows the measured transitions across various temperatures, highlighting those we successfully assigned versus those that remain unassigned.

For a small number of transitions we manually increased the uncertainties from $\sim 10^{-6}$ to $\sim 10^{-4}$ to achieve better agreement with the other transitions used as input for MARVEL.

A small subset of transitions had discrepancies between our quantum number assignments and those reported in the experimental source [15]. These differences are detailed in Table 6.4.

2. 21MaYuSu

Table 6.4: Comparison of assigned transitions (J branch and $C^{'}$) with those reported in 21YoBeDu [15]. Only transitions where discrepancies in quantum number assignments occur are shown.

Line position (cm^{-1})	**Our assignment**	**Paper's assignment**
3048.1527	R(2) F_2	R(2) F_1
2999.0604	P(2) E	P(1) E
2885.3514	P(13) F_1	P(13) F_2
2885.7612	P(13) A_1	P(13) A_2
2885.8479	P(13) F_1	P(13) F_2
3157.4815	R(14) E	R(14) F_2
3166.0836	R(15) F_1	R(15) F_2
3166.7250	R(15) F_2	R(15) F_1
3174.5349	R(16) A_1	R(16) A_2
3183.0475	R(17) E	R(17) F_2
2886.6087	P(13) F_2	P(13) F_1
3113.7068	R(11) F_2	R(11) E
3157.5059	R(14) F_1	R(14) E
3148.8127	R(13) F_1	R(13) E

Malarich et al. [689] recorded methane spectra across a temperature range of 296 – 1000 K with an accuracy of approximately 10^{-5} cm^{-1} with a dual-frequency comb spectrometer. Line positions are reported along with intensities at 296 K and estimated lower-state energies (E'') for 11 647 transitions out of the 23 390 provided.

To assign complete quantum labels using MM, we performed a matching procedure based on both line position and intensity. In cases where multiple potential assignments were identified, we applied a combination difference method. This approach involved generating all plausible icosad–monad transitions using MARVEL with our full set of experimental transitions. These lines were then evaluated to identify consistent assignments.

In total, 10,275 transitions were fully assigned. Of these, 7,248 were validated with MARVEL. This means that they were either consistent with the network

of all the other transitions in our database, or the network lacked other transitions leading to the same upper levels to flag inconsistencies. Among the these transitions, 4 belong to the polyad band 6-1, while the remaining transitions fall within the 5–0 band. Since relatively few transitions have been assigned in the 5–0 band so far, some of the matches were ambiguous. Regarding the input uncertainties, we increased them to 10^{-3} cm^{-1} in order to achieve agreement with the rest of the transitions in the MARVEL network.

The residuals (measured minus MM) for the assigned lines exhibit a mean of -0.11 cm^{-1}and a standard deviation of 0.33 cm^{-1}. The obs-calc with Ma-Ma lines have a mean value of 0.0005 cm^{-1}, so the large residuals are caused by the differences of the experimental values with the calculated values. This is also shown in Figure 6.6. Notably, 6,832 of the transitions contribute new energy levels that had not been previously MARVELised, covering rotational quantum numbers from J=0 to J=16. However, due to the lack of enough assigned transitions on these high polyads, 3,626 of these transitions define new levels on their own, with no other transitions connected to the same level, making these levels more uncertain until further supporting transitions are identified. The assigned, unassigned, and assigned but not validated lines are illustrated in Figure 6.7.

3. 20YaLiPl

Yasoufi et al. [460] provide a total of 96 line positions, one of which is also measured in [688]. These measurements were performed using cavity ring-down spectroscopy. Of the 96 lines, 6 were identified in the original experimental paper corresponding to the $2\nu_3$ R(6) transition in polyad 4 and included in the earlier MARVEL project (see chapter 5) after we added counting numbers to them. The remaining 90 lines had not been assigned in the experimental study; in this work, we assigned 56 of them and validated them all through MARVEL. Among these newly assigned lines, 7 transitions belong to the 5–1 polyad band and 49 to the 4–0 polyad band. Additionally, 27 of these transitions contribute to new MARVEL energy levels, with only 3

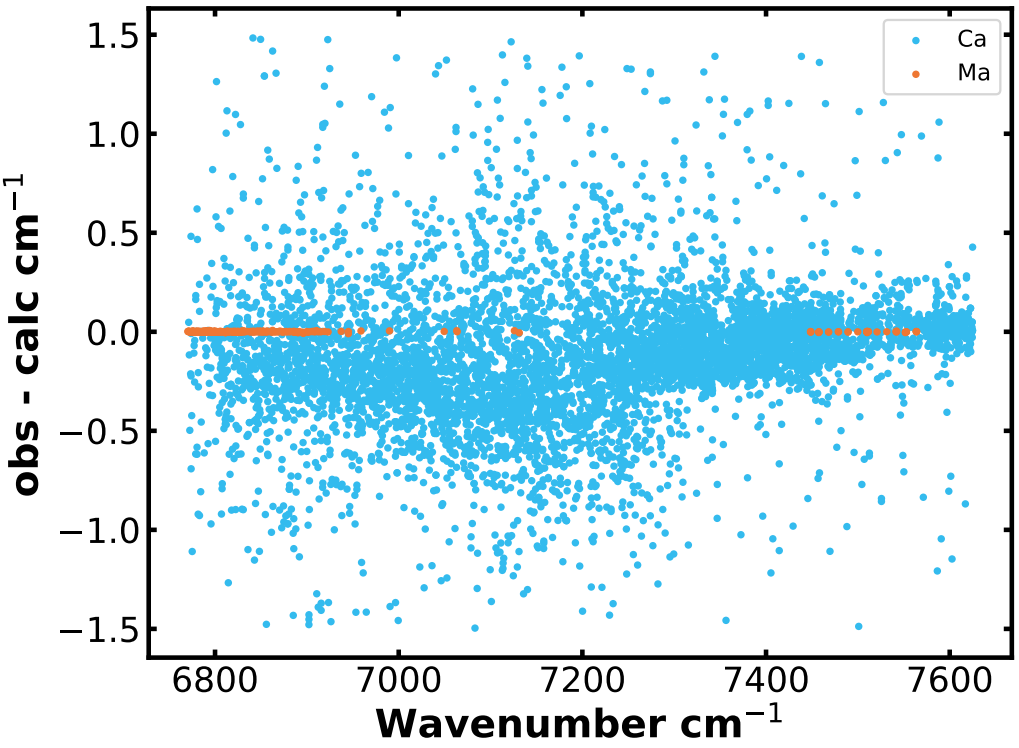


Figure 6.6: Residuals (obs – calc) for assigned transitions in the 21MaYuSu dataset.

of them supported by other transitions leading to the same levels. Figure 6.8 shows the coinciding lines between the experiment and MM, as well as the lines that do not match.

The residuals for the assigned lines have a mean value of -0.0013 cm^{-1} with a standard deviation of 0.007 cm^{-1} as shown in Figure 6.9.

4. 13MaPrMo covers the wavenumber range 7050–7350 cm^{-1} using a direct absorption tunable diode laser spectrometer. Line intensities are reported at two temperatures: 28K and 81K. The authors explicitly identified 16 of the observed transitions as R(0) transitions; however, no counting numbers were provided. Since the ground state is of A_1 symmetry, we were able to determine the appropriate counting numbers by cross-referencing with the data by Rey et al. [623].

   One line at 7152.7205 cm^{-1} was excluded from our assignment because it is identified in Rey et al. (16ReNiCa) [477] as a $^{13}CH_4$ transition.

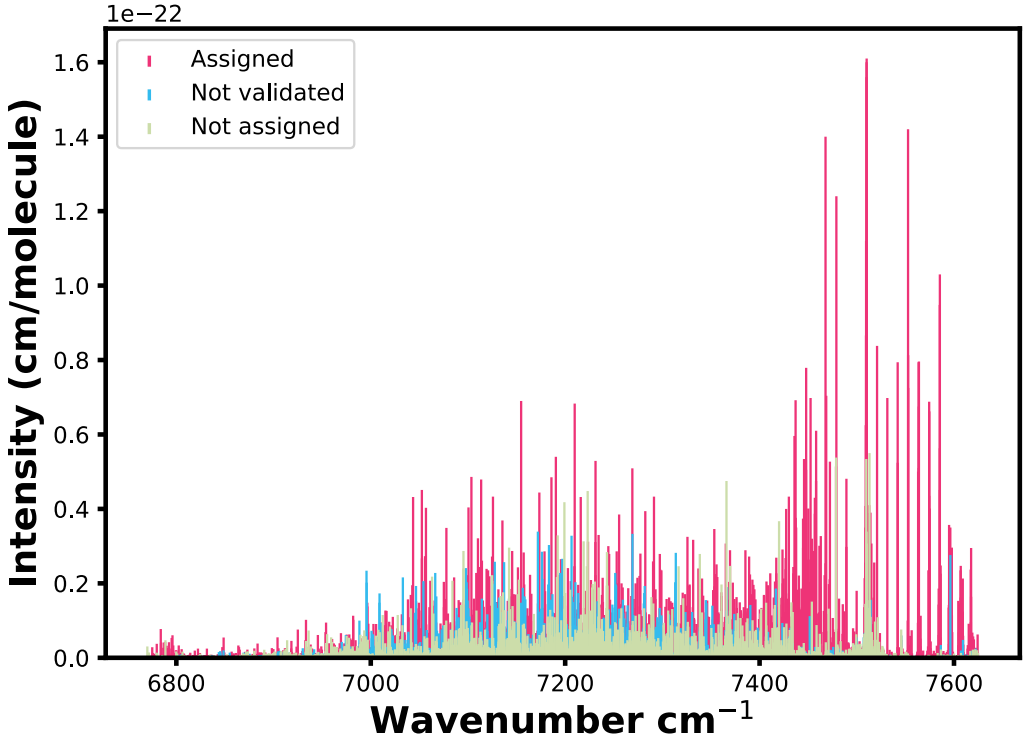


Figure 6.7: Stick spectrum of 21MaYuSu at 296K. Pink: assigned (validated through MARVEL), Blue: assigned (not validated), Green: unassigned lines.

The authors also reported 655 additional unassigned transitions with estimated lower-state energies in the supplementary material. These lines include intensity data, but due to time constraints, we were not able to assign them as part of this thesis.

In total, the 15 transitions define 15 MARVEL levels in polyad 5, $C = A_2$. Five of these are confirmed with combination differences.

5. 12HaBeMi

Hargreaves et al. [14] recorded laboratory emission spectra of hot methane using a Fourier transform infrared spectrometer over a broad temperature range from 573 K to 1673 K. The data cover both hot and cold polyad bands in the wavenumber range 1067–4900 cm^{-1}, with line position uncertainty better than 0.005 cm^{-1}. This is the uncertainty we used as input for MARVEL. Many of the observed lines are identified as HITRAN lines; the remaining

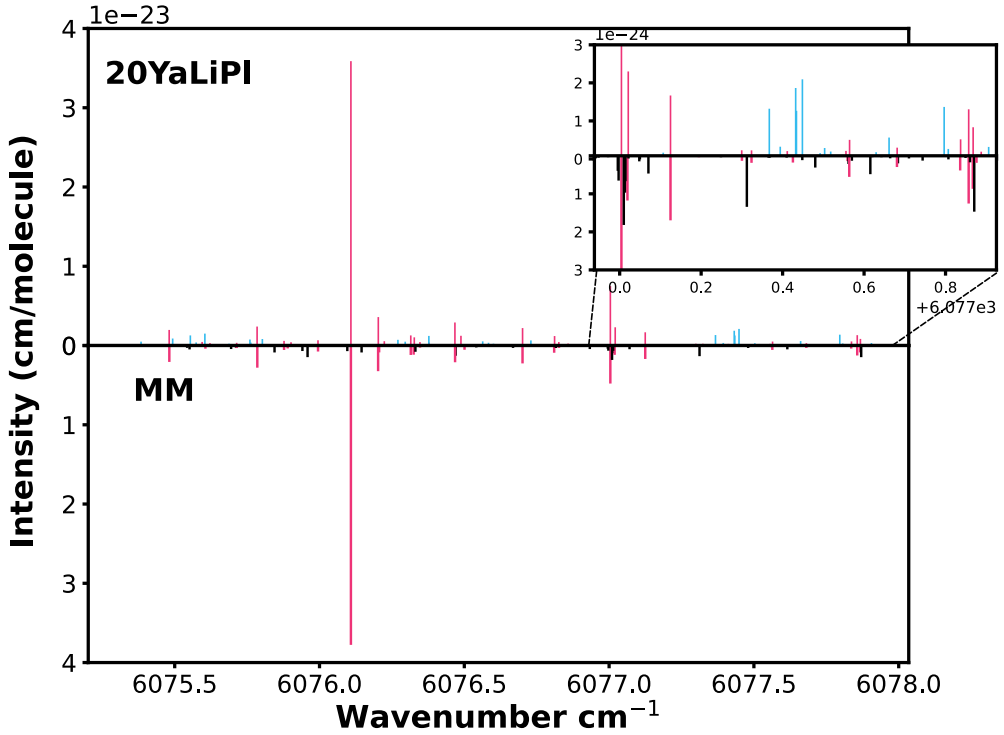


Figure 6.8: Top subplot: Experimental data from 20YaLiPl. Bottom subplot: MM data. Pink lines indicate matched transitions, light blue lines represent unassigned experimental lines, and black lines show MM transitions that do not match any 20YaLiPl lines.

lines, not found in the HITRAN database, were the focus of our assignment project.

Lower-state energies were estimated by the authors for 1923 of the lines not present in HITRAN, for the temperature 573 K. Out of 3256 lines reported at this temperature, we have successfully assigned 1124 transitions. All but 14 assigned transitions were validated against the MARVEL database—the 14 lead to floating polyad 2 and 3 levels not supported by other transitions.

The residuals between the experimental and MM line positions for the assigned lines have a mean of 0.00019 cm^{-1} and a standard deviation of 0.0039 cm^{-1}. A significant number of lines remain unassigned due to spectral congestion (see Figure 6.10).

The authors reported consistent line positions across all temperature measure-

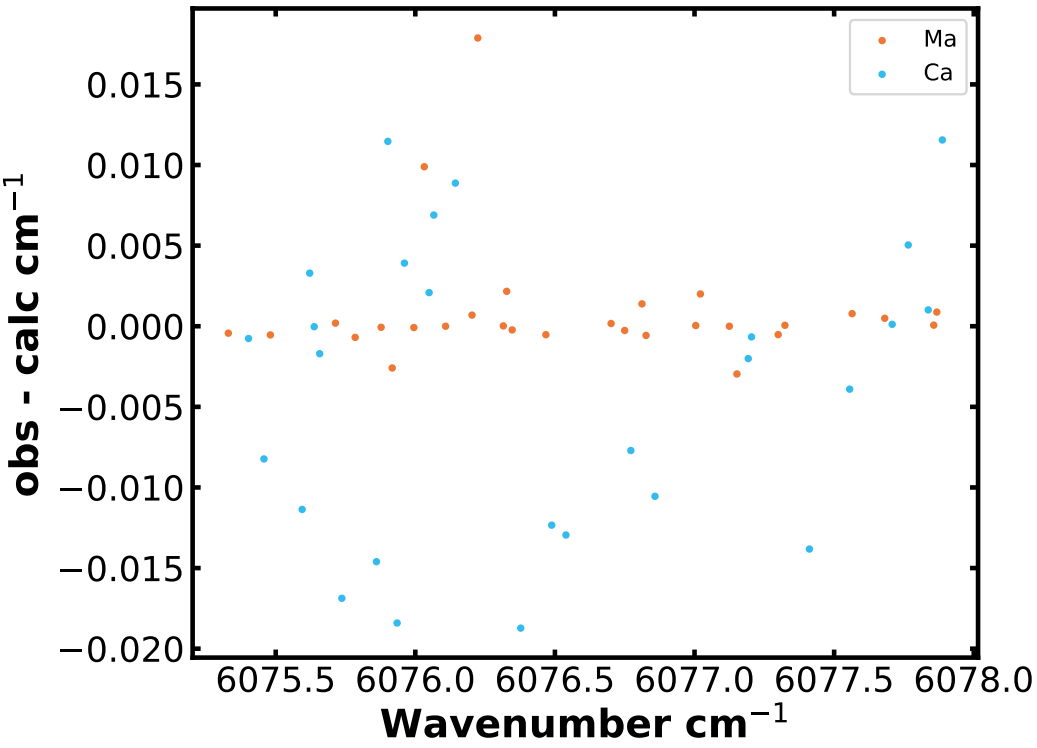


Figure 6.9: Residuals (obs – calc) for assigned transitions in the 20YaLiPl dataset. Label "Ma"/"Ca" detones that the matching MM line is linked to a MARVELised/calculated upper level.

ments, assigning the same wavenumber to transitions observed at multiple temperatures. This consistency enables a powerful strategy: starting from the well-assigned 573 K spectrum, we can track the same transitions at higher temperatures and use them as anchors to assist in assigning additional lines in these more congested spectra. We have begun applying this approach to the 673 K and 1073 K datasets. Although a full analysis is still in progress, an example plot of the 1073 K spectrum is shown in Figure 6.11, where the blue lines represent transitions successfully identified by referencing their counterparts at 573 K.

6. 05Brown

Brown et al. [496] performed Fourier Transform spectroscopy, providing a total of 87 lines across several wavenumber ranges. Specifically between 9001 and 9111 cm^{-1}, 37 lines were reported. Of these, 10 lines were already as-

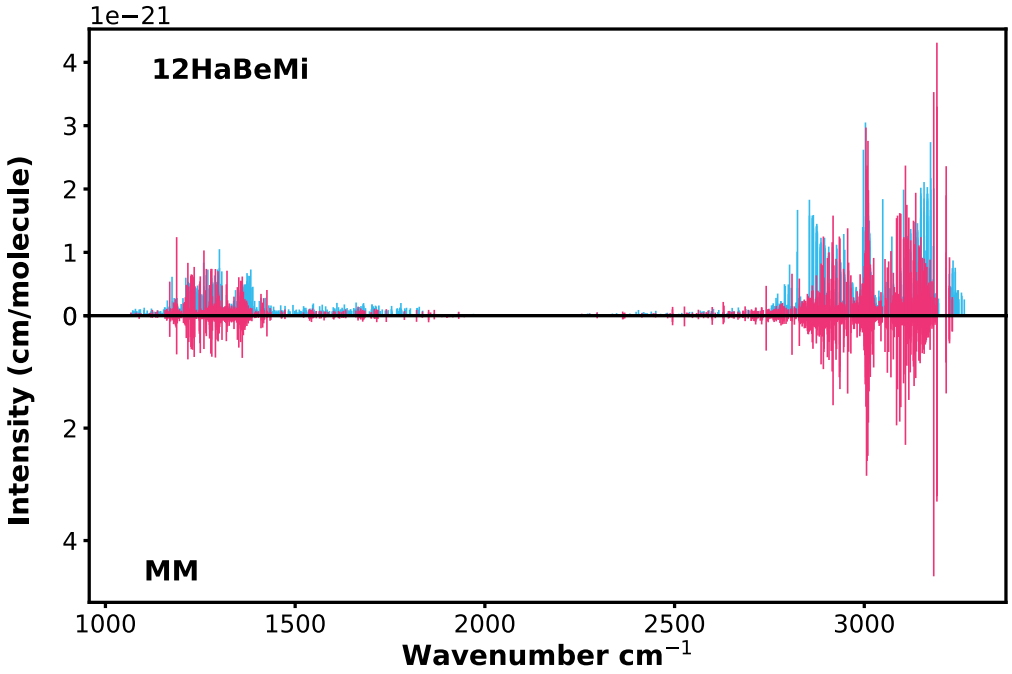


Figure 6.10: Top subplot: Experimental 573 K data from 12HaBeMi. Bottom subplot: MM lines. Pink lines indicate matched transitions, light blue lines represent unassigned experimental transitions.

signed by Nikitin et al. [466] and included in our first MARVEL project. From the remaining 27 lines, all but one were assigned in this work, as belonging to the polyad 6 band.

Between 7467 and 7564 cm^{-1} 36 lines were reported. Out of these, 27 lines were included in the initial MARVEL project after we provided full assignments by using transitions by Tanner et al. [487]. In the present project, we used lines from the newly assigned source 21MaYuSu (5–0 band) for the remaining lines. All except one were validated through MARVEL. Between 6775 and 6789 cm^{-1} 14 lines were reported, all of which have been assigned with the MM line list.

Overall, the transitions assigned from this source are connected to already MARVELised energies with only one determining a new energy level. The stick spectrum is shown in Figure 6.12. The residuals for the assigned lines have a mean value of -4.8×10^{-5} cm^{-1} with a standard deviation of 0.003

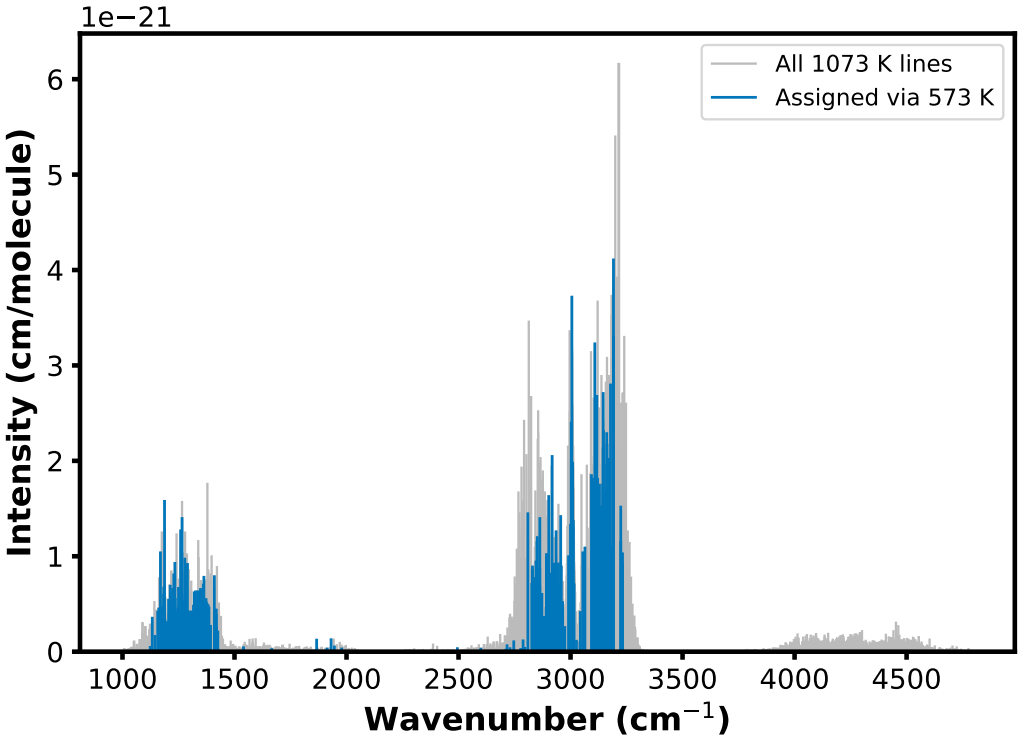
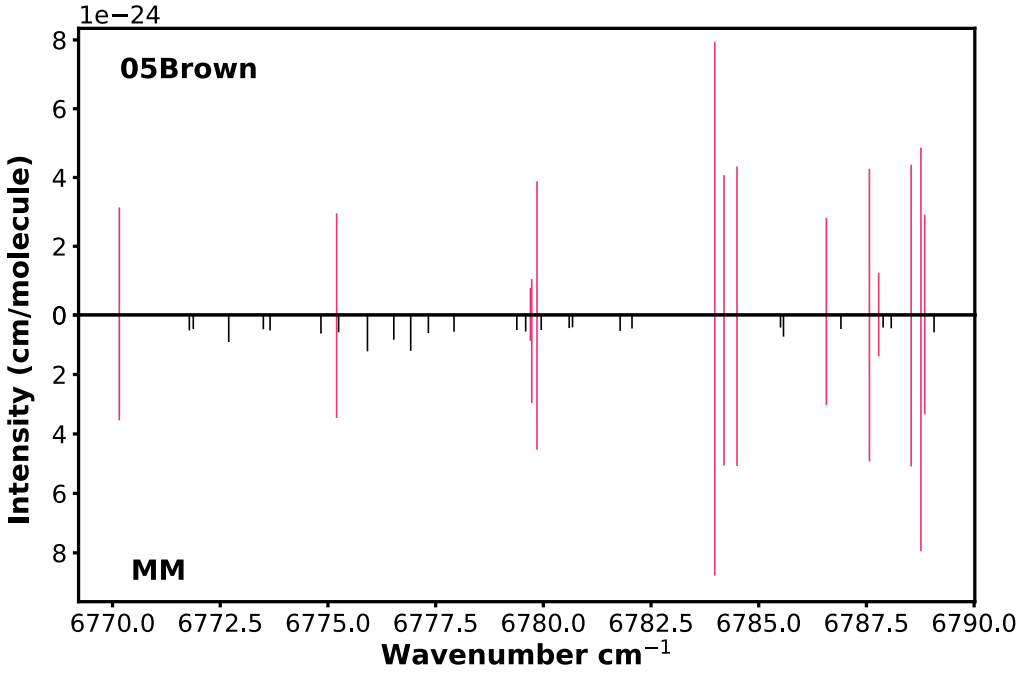


Figure 6.11: The 1073 K spectrum from 12HaBeMi [14], with blue lines indicating transitions previously assigned at 573 K. These matches can help guide new assignments at higher temperatures.

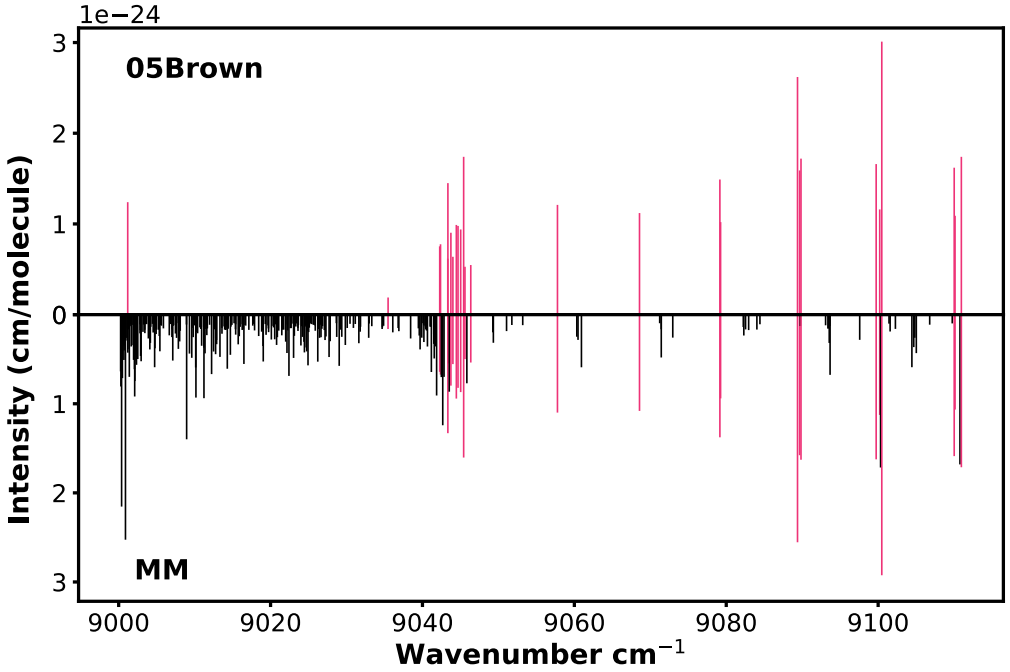
cm^{-1} for the range 9001 and 9111 cm^{-1}. For the range 6775 - 6789 cm^{-1} the residuals show a mean of -3×10^{-4} cm^{-1} with a standard deviation of 5×10^{-5} cm^{-1}.

7. 97Pine

   Pine [671] used direct absorption spectroscopy employing a difference-frequency laser to measure the ν_3 band (polyad 2) P and R branches of the methane spectrum in the range 3028-3122 cm^{-1}. Intensities are provided at room temperature, along with line positions, J assignments, and symmetries. We assigned counting numbers to the 103 lines provided based on line position and intensity at 296 K (Figure 6.13). They all contribute to energy levels that have already been MARVELised. No uncertainty is mentioned in the original source for the line positions, so we used 0.0001 cm^{-1} based on combination differences. The residuals between the experimental and the MM



(a) Range: 6775–6789 cm^{-1}



(b) Range: 9001–9111 cm^{-1}

Figure 6.12: Top subplots: Experimental data from 05Brown. Bottom subplots: MM data. Pink lines indicate matched transitions, and black lines show MM transitions that do not match any 05Brown lines.

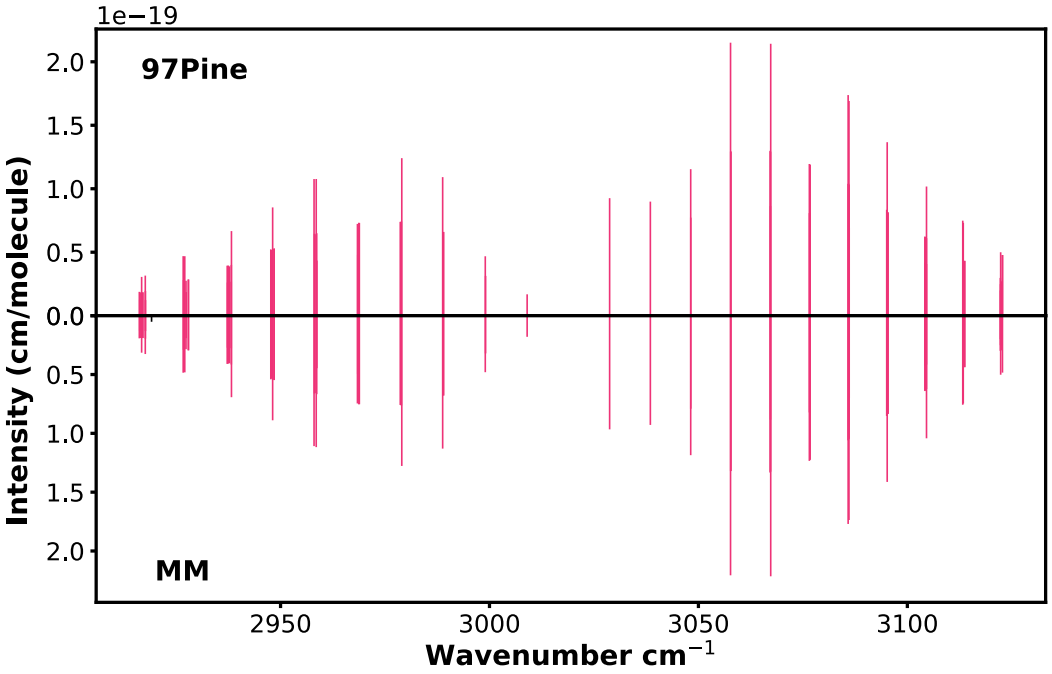


Figure 6.13: Top subplot: Experimental data from 97Pine. Bottom subplot: MM P and Q branches in the same range.

lines have a mean value of -0.0002 cm^{-1} with a standard deviation of 0.0002 cm^{-1}.

8. 89VaCh

   Varanasi et al. [596] reported measurements of 11 spectral lines in the v_4 vibrational band using a tunable diode laser at several temperatures. All relevant quantum numbers, except for counting numbers, were provided; the missing counting numbers were straightforwardly assigned by cross-referencing with other sources in our database. No new MARVEL energy levels were derived from these transitions. Although line position uncertainties were not reported in the original study, we adopted a value of 0.001cm^{-1}, based on consistency with other transitions.

9. 88Brown

   Brown et al. [513] measured the methane spectrum in the range 3700-4136 cm^{-1} using Fourier transform spectroscopy. The line position uncertainties

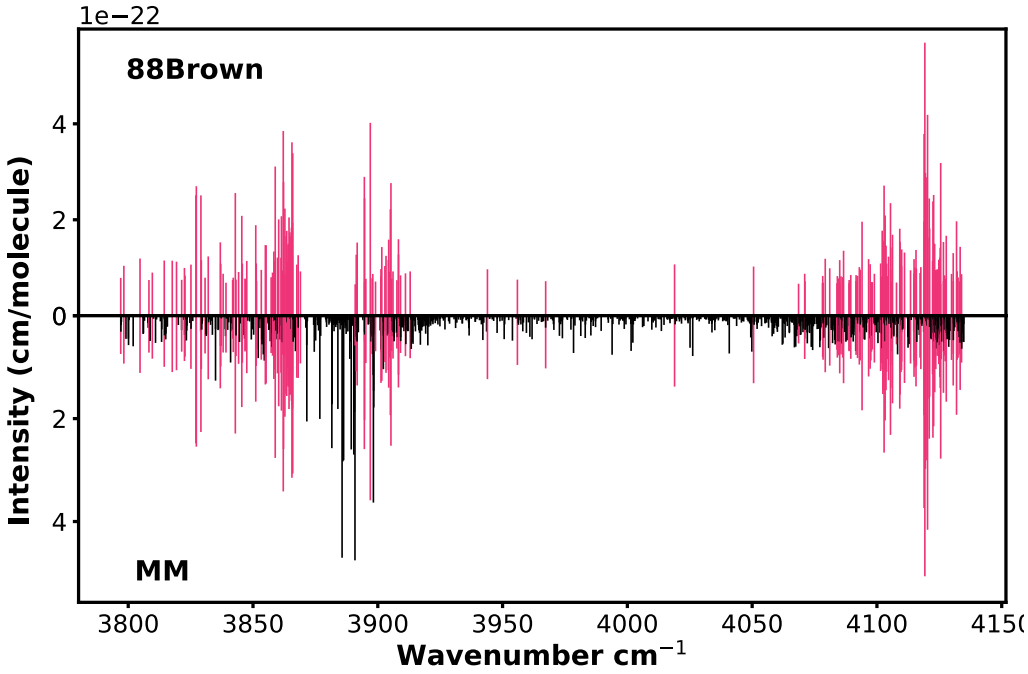


Figure 6.14: Top subplot: Experimental data from 88Brown. Bottom subplot: MM data. Pink lines indicate matched transitions, and black lines show MM transitions that do not match any 05Brown lines.

range from 0.0002 to 0.003 cm^{-1}. A total of 235 spectral lines are provided with line strengths at room temperature. Of these, 12 lines had already been incorporated into the MARVEL database, having been identified by the authors as the R(0) and R(4) transitions of the $3\nu_4$ band. In our earlier MARVEL work, we determined their symmetry assignments and the counting numbers. For the remaining 223 lines, we assigned them using the MM line list based on line position and intensity at 296 K (Figure 6.14). They correspond to transitions within the 3–0 polyad band and they all contribute to energy levels that have already been MARVELised. The residuals between the experimental and the MM lines have a mean value of -0.0001 cm^{-1} with a standard deviation of 0.003 cm^{-1}.

10. 88Margolis

Margolis et al. [662] measured line positions and intensities in the 5500–6180 cm^{-1} spectral region, covering the $2\nu_3$ band of methane, with

average line position uncertainty of 0.0002 cm^{-1}. The measurements were performed at room temperature (296 K) using high-resolution Fourier transform spectroscopy. The dataset includes 144 lines with assigned rotational quantum number J values and 1168 lines without.

In total, we assigned 1255 lines in this region (Figure 6.15). Among these, 52 lines are connected to previously calculated energy levels, thereby yielding new empirical energies in the tetradecad (polyad 4) for $J = 11$ to $J = 14$, with 7 of these lines being reinforced by additional transitions that link to the same upper levels. Notably, as illustrated in Figure 6.15, four intense features near 5690 cm^{-1} remain unassigned.

The residuals between the experimental and the MM lines have a mean value of 0.001 cm^{-1} with a standard deviation of 0.005 cm^{-1}. As shown in Figure 6.16 systematic deviations are evident. In two distinct regions along the wavenumber axis, the residuals show a clear upward drift, suggesting local discrepancies of the experimental data with the calculated values. Notably, the Q-branch transitions with J=11–14 near 5990 cm^{-1} exhibit residuals consistently between 0.01 and 0.05 cm^{-1}. In addition, a group of R(13) lines near 6141 cm^{-1} also shows similar elevated deviations.

11. 85HiLoBr

Hilico et al. [660] measured 13 lines in the hot band $v_3 - v_4$ band between 1568-1932 cm^{-1} using a Fourier transform spectrometer. We assigned counting numbers based on proximity in line position and matching values of J and symmetry with MM lines. The reported line position uncertainty is 0.002 cm^{-1}. None of these lines contributes to new empirical energy levels. The residuals between the experimental and the MM positions have a mean of 0.0004 cm^{-1} and a standard deviation of 0.0004 cm^{-1}, which likely suggests an issue with calibration. The experimental stick spectrum with the corresponding MM lines is shown in Figure 6.17.

12. 82HuLoRo

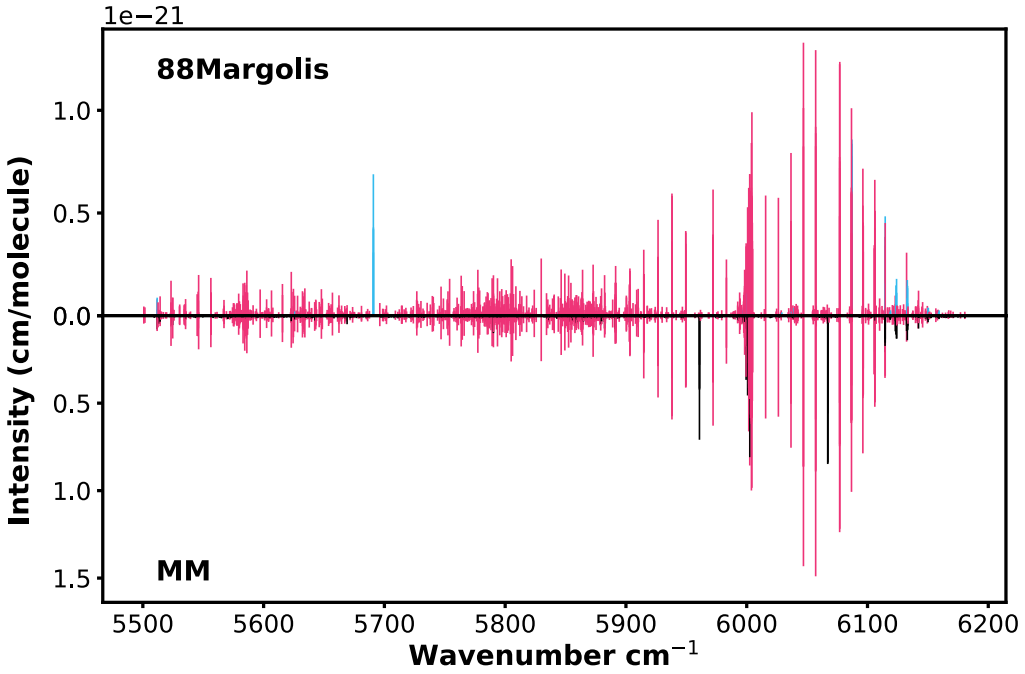


Figure 6.15: Top subplot: Experimental data from 88Margolis. Bottom subplot: MM data. Pink lines indicate matched transitions, light blue lines represent unassigned experimental lines, and black lines show MM transitions that do not match any 88Margolis lines.

Hunt et al. [657] recorded spectra using a Fourier transform spectrometer with the accuracy of line positions estimated to be 0.0005 cm^{-1} for isolated lines and 0.001 cm^{-1} for blended lines. A total of 599 lines are reported in the range 2930–3250 cm^{-1} within polyad 2. Symmetries and J assignments are provided. We assigned counting numbers to all the lines (Figure 6.18), with 88 of them yielding new MARVEL energies, but 20 of them leading to energy levels as single transitions. In addition, 7 of the newly assigned lines were not validated with MARVEL. The residuals between the experimental and the MM line positions have a mean of -0.002 cm^{-1} and a standard deviation of 0.05 cm^{-1}.

13. 81BrToHu

Brown et al. [17] reported 33 line positions and intensities in the range 2400–2100 cm^{-1} for the P and R branches of the $\nu_2+\nu_3-\nu_2$ hot band, using a Fourier transform spectrometer. The measurements were made at room

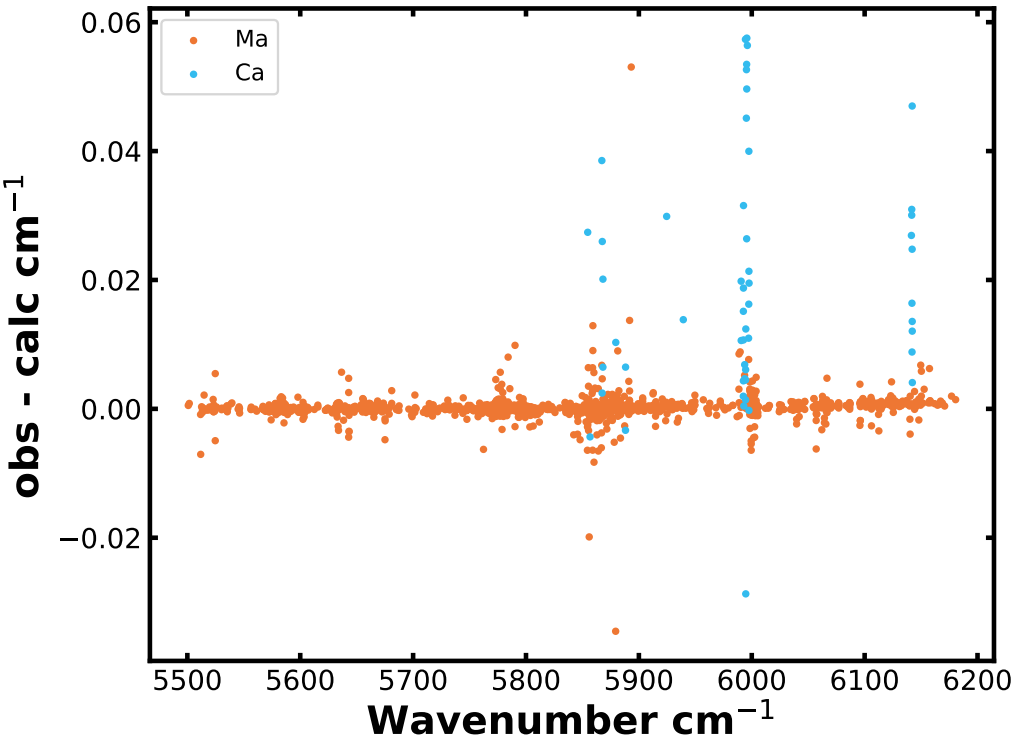


Figure 6.16: Residuals (obs – calc) for assigned transitions in the 88Margolis dataset. Label "Ma"/"Ca" detones that the matching MM line is linked to a MARVELised/calculated upper level.

temperature with estimated uncertainties of 0.001 cm^{-1}. J assignments are provided for all lines, but not symmetries C.

We successfully matched 32 of the 33 lines to transitions already present in other sources and they do not result in any new MARVEL energy levels. All lines are validated with MARVEL. The residuals between the experimental and the MM line positions have a mean of -0.001 and a standard deviation of 0.004 cm^{-1}. In Table 6.5, we highlight several lines for which our proposed quantum number assignments differ from those reported in the original work.

14. 78OwPaDo

Owyoung et al. [563] reported 32 Raman spectral lines from the ν_1 band and Q branch using direct continuous-wave stimulated Raman gain spectroscopy. The line position uncertainty is 0.01cm^{-1}, which we adopted as the input uncertainty for our MARVEL analysis. Rotational quantum numbers (J) and

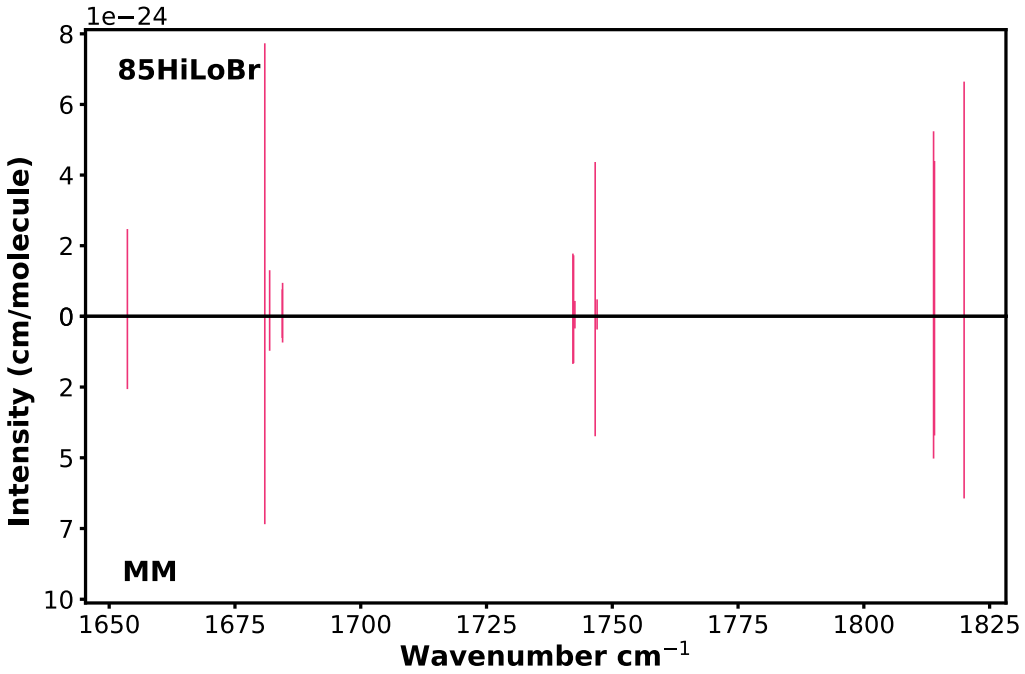


Figure 6.17: Top subplot: Experimental transitions from 85HiLoBr. Bottom subplot: The corresponding MM transitions.

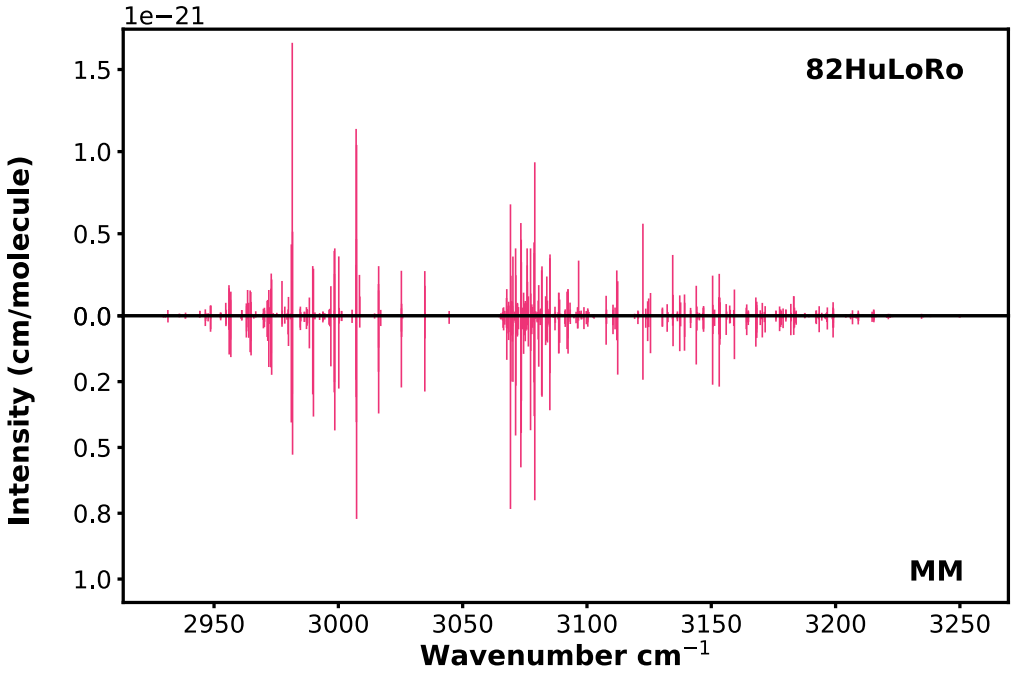


Figure 6.18: Top subplot: Experimental transitions from 82HuLoRo. Bottom subplot: The corresponding MM transitions.

Table 6.5: Comparison of assigned transitions ($P^{'} - P^{''}$, J branch, and $C^{''}$) with those reported in 81BrToHu [17]. Only transitions where discrepancies in quantum number assignments occur are shown.

Line position (cm^{-1})	Our assignment	Paper's assignment
3101.0968	3-1 R(8) E	3-1 R(9)
3101.3079	3-1 R(8) F_2	3-1 R(9)
3101.5996	3-1 R(8) F_2	3-1 R(9)
3109.2032	3-1 R(9) F_1	3-1 R(10)
3109.3033	2-0 R(8) A_1	3-1 R(10)
3109.3893	3-1 R(9) F_2	3-1 R(10)
3109.7850	2-0 R(8) F_2	3-1 R(10)

symmetry assignments were provided in the original study. We assigned counting numbers by cross-referencing these transitions with others in our database. No new MARVEL energy levels were derived from this dataset.

6.3 CH_4 MARVEL update

We incorporated into MARVEL several newly published experimental spectra for methane, including the lines we assigned, as described in the previous subsection. Since our initial MARVEL analysis, which included data published up to July 2023, we have expanded our database with the sources listed in Table 6.6 and described below.

1. 24DiCaWa

   Ding et al. [18] reported high-resolution methane spectra measured using a tunable external-cavity diode laser in combination with a stabilised optical cavity. The spectra were recorded at 296 K, with a frequency accuracy better than 6.7×10^{-5} cm^{-1}.

   A total of 20 transitions were reported with room-temperature intensities, and with full assignments for seven of them, no assignments for two, and partial

Table 6.6: Summary of updates in the MARVEL compilation. For each source, the wavenumber range, associated polyad bands, number of assigned and validated lines (A/V), and the mean uncertainty used are provided.

Source	Range (cm^{-1})	Polyad Band(s)	A/V	Mean Unc. (cm^{-1})
24HjOlSi [27]	5800–6100, 9070–9370	P_4–P_0, P_6–P_2	145/145	3×10^{-5}
24NiReCa [692]	7606–7919	P_6–P_0	1382/1382	2×10^{-3}
24NiSoPr [693]	900–1050	P_2–P_1, P_1–P_0	1246/1244	10^{-3}
24DiCaWa [18]	∼5997	P_4–P_0	15/14	2×10^{-5}
21MaYuSu [689]	6770-7570	P_5–P_0, P_6–P_1	10274/7248	10^{-3}
21YoBeDu [15]	2750-3200	P_2–P_0	234/240	10^{-4}
20YaLiPl [460]	6076–6078	P_4-P_0	62/62	7×10^{-4}
13DaNiTh [483]	4600-4869	P_2-P_0	1570/1560	1.0E-03
13MaPrMo [682]	7040–7378	P_5-P_0	15/15	3×10^{-3}
13CaLeWa [484]	5855–6244	P_4-P_0	3400/3378	1.5×10^{-3}
12HaBeMi [14]	1067–4900	P_1–P_0, P_2–P_1, P_3–P_3 P_2–P_0, P_3–P_1, P_4–P_2	1124/1124	5×10^{-3}
05Brown [496]	6775–6789, 7478–7564 9001–9111	P_5-P_0	85/86	2×10^{-3}
05PrBrMa [497]	4100–4635	P_3-P_0	1432/1398	2×10^{-3}
98BrKaRu [505]	1260–1334	P_1-P_0	285/270	2×10^{-3}
97Pine [671]	3028–3122	P_2-P_0	103/103	$\times10^{-6}$
89VaCh [596]	1270-1317	P_1-P_0	11/11	10^{-3}
88Margolis [662]	5500–6180	P_4-P_0	1255/1255	2×10^{-4}
88Brown [513]	3876–3891	P_3-P_0	235/232	10^{-4}
85HiLoBr [660]	1568–1932	P_2-P_1	13/13	2×10^{-3}
83DeFrPr [515]	3034–3068	P_4-P_2	10/0	2×10^{-3}
82HuLoRo [657]	2930–3250	P_2-P_0	599/588	5×10^{-4}
81BrToHu [17]	2400–3200	P_3-P_1, P_2-P_0	32/32	10^{-3}
78OwPaDo [563]	2916-2918	P_2-P_0	32/32	10^{-2}

assignments for the rest. Out of these 20 transitions, we provided complete quantum number assignments in the P_4-P_0 polyad band for 15 using the MM line list. One of the 15 lines was invalidated, and 12 were validated against other transitions in the network. However, a few discrepancies were observed between our assignments and those proposed in the original paper, as detailed in Table 6.7.

2. 24NiSoPr

Table 6.7: Lower-state quantum number discrepancies between Ding et al. [18] and the MM assignments ($J''C''\alpha''$).

Wavenumber (cm^{-1})	Paper Assignment	MM Assignment
5997.275347	11 A_2 1	11 F_1 2
5997.336688	11 A_2 1	11 E 1
5997.358972	11 A_2 1	11 F_2 1
5997.440732	11 A_2 1	11 F_2 3
5997.490137	11 F_2 2	11 F_1 3
5997.503450	11 A_2 1	11 F_1 1

Nikitin et al. [693] measured 1246 assigned lines in the 900–1050 cm^{-1} range and the $P_2 - P_1$, $P_1 - P_0$ polyd bands, using a Fourier transform spectrometer. The reported line position uncertainties are better than 0.001 cm^{-1}, which is the value we adopted as the input uncertainty for our MARVEL analysis.

During validation, we found that one of the reported assignments required modification: the transition labeled 24NiSoPr.907 at 1025.714936 cm^{-1} was originally labelled as a P(14) F_1 line, but further analysis indicated that it should instead be classified as a Q(13) F_2 transition. Additionally, two lines could not be confirmed through MARVEL validation, but the rest 1244 were validated with combination differences.

3. 24HjOlSi

   Optical–optical double-resonance spectroscopy was employed by Hjältén et al. [27] to measure transitions in the 9070–9370 cm^{-1} region. A total of 118 transitions were reported between the v_3 and $3v_3$ vibrational bands. In addition, 27 were measured between the vibrational ground state and the $2v_3$ state in the 5800–6100 cm^{-1} range. Altogether, 145 transitions were included in MARVEL, 92 of which were successfully validated against other lines in the MARVEL network. An average uncertainty of 10^{-5} cm^{-1} was reported and used in the MARVEL input.

4. 24NiReCa

Nikitin et al. [692] reported 1382 measured and fully assigned transitions in the wavenumber range 7606–7919 cm^{-1} and polyads $P_6 - P_0$. As the authors did not provide explicit uncertainties for the line positions, we adopted a default uncertainty of 0.002 cm^{-1} based on consistency checks using combination differences. All transitions were successfully incorporated into the MARVEL network. The MARVEL energies derived from these transitions in polyad 6 show significant discrepancies when compared with the MM calculated energies with obs-calc ranging from -8 to -13 cm^{-1} (the MM energies are larger). This is likely due to differences in the labelling of polyad numbers or counting numbers. Since no additional transitions are available to confirm or refute these assignments, we have chosen not to modify them.

In total, incorporating the transitions we assigned using the MM line list from the 14 sources described in section 6.2, along with newly published experimental data from the 4 sources detailed in section 6.3, resulted in 16,837 transitions included in MARVEL, with 3050 of them being invalidated, 9440 of them being validated by other transitions in the MARVEL network, and the rest 4347 of them leading to floating energies (defined only by these single lines). These transitions span a wavenumber range from 902 to 9111 cm^{-1}. The most densely populated region of transitions lies between 6971 and 7510 cm^{-1} (see Figure 6.19). The uncertainties of the lines vary, with a minimum of 10^{-6} cm^{-1}, a maximum of 8×10^{-3} cm^{-1}, and an average uncertainty of approximately 10^{-3} cm^{-1}.

Table 6.6 summarises the experimental sources newly included in the present MARVEL update. For each dataset, we provide the wavenumber range, associated polyad bands, the number of assigned and validated transitions (A/V), and the mean uncertainty used in the input. Here, "validated" refers to transitions that are either not inconsistent with others or have no conflicting alternatives in the dataset. The table also includes some previously incorporated sources for which the number of validated transitions has changed compared to the earlier compilation (see Table 5.4 in the previous chapter). The distribution of all the lines in several polyad bands, with the associated J ranges is shown in Table 6.8.

Table 6.8: Summary of total input transitions per polyad band ($P' - P''$) including number of transitions and ranges the rotational quantum number J.

$P' - P''$	# Transitions	Max J$'$	Min J$''$
Cold bands			
0 - 0	154	24	0
1 - 0	3948	29	0
2 - 0	4623	24	0
3 - 0	32592	23	0
4 - 0	22500	17	0
5 - 0	16262	16	0
6 - 0	1748	10	0
Hot bands			
1 - 1	126	15	1
2 - 1	7040	29	1
3 - 1	2108	20	0
2 - 2	16	12	4
3 - 2	315	15	0
4 - 1	7316	18	0
4 - 2	35	8	0
4 - 3	43	9	1
5 - 1	29	9	1
6 - 1	3	5	1
6 - 2	144	9	0
7 - 3	4	4	1

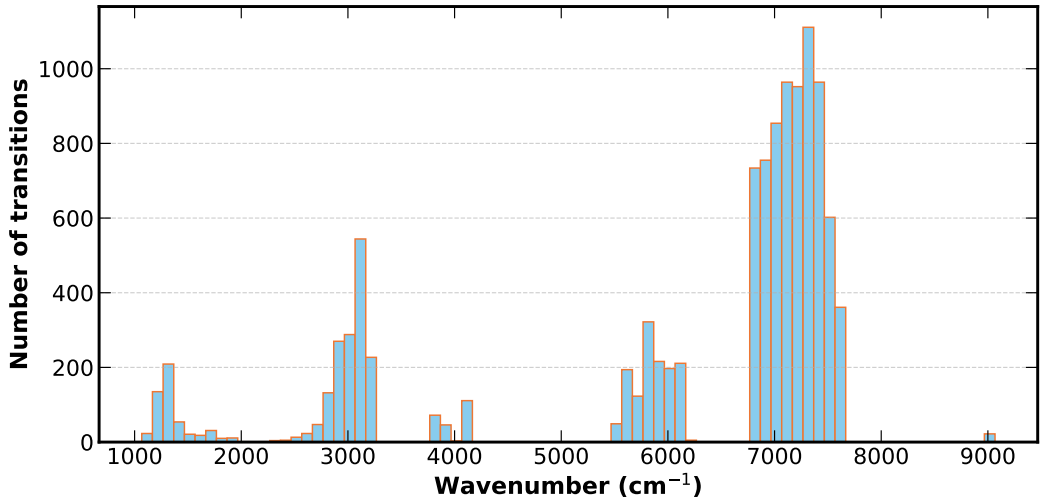


Figure 6.19: Distribution of newly assigned and validated methane transitions as a function of wavenumber, binned in intervals of 100 cm^{-1}. The height of each bar indicates the number of transitions found within that wavenumber range.

Table 6.9: Summary of MARVEL energy levels per polyad. For each polyad, the table lists the total number of energy levels, the range of rotational quantum numbers J, the wavenumber energy range (cm^{-1}), the number of states defined by more than one transitions, and the mean uncertainty (cm^{-1}) of the energy levels.

Polyad	# Levels	J range	Energy range	with CDs	Mean Unc
0	281	0-27	0 - 3904	280	0.006
1	1190	0-28	1310 - 5334	1174	0.005
2	3389	0-29	2587 - 6760	2311	0.005
3	7727	0-23	3870 - 7018	6180	0.005
4	8303	0-18	5121 - 7669	5933	0.002
5	7580	0 -16	6377 - 8783	3126	0.002
6	1332	0-10	7696 - 9630	451	0.003
7	2	2 - 4	9832 - 9987	0	0.005

In total, with this update, we derive 29 802 energy levels from 99 006 transitions. The new energy levels that were not included in the first MARVEL project are illustrated in Figure 6.20. Most of the new levels belong to polyads 5 (5 052 states) and 6 (999 states). With these additions, the total number of states in polyad 5 increases to 7 580, of which 3 126 are confirmed through combination differences (CD). For polyad 6, there are now 1 332 states in total, with 451 confirmed by CD.

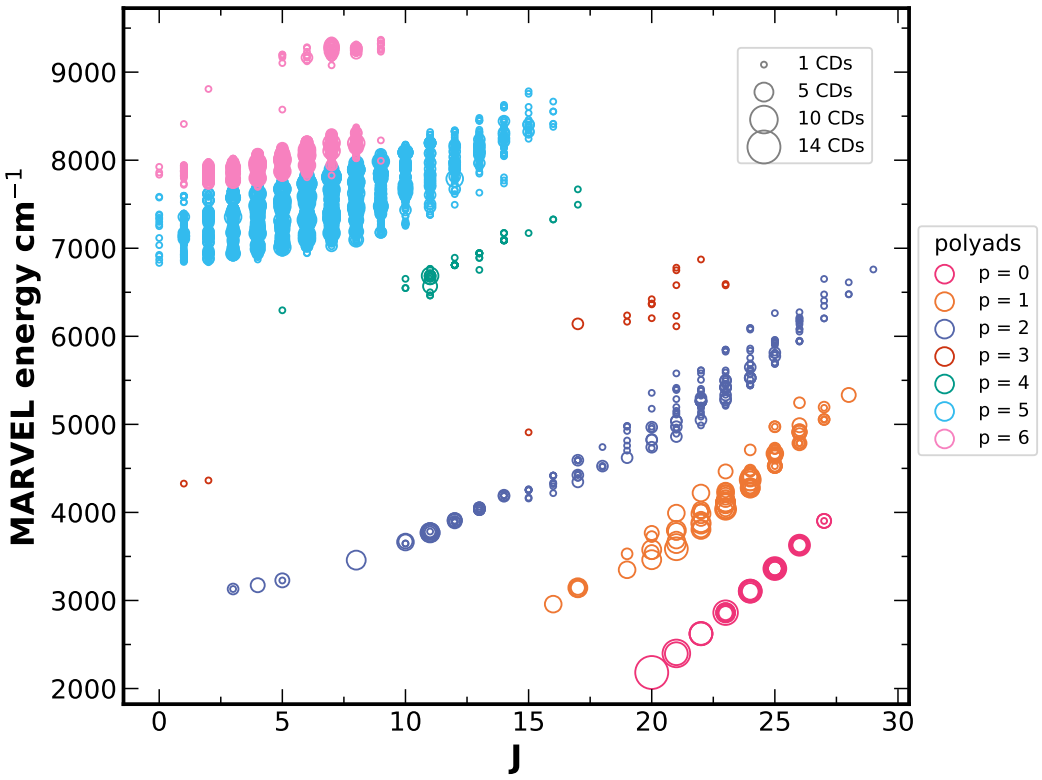


Figure 6.20: Newly assigned MARVEL energy levels (in cm^{-1}) as a function of rotational quantum number J. Each point represents an energy level, with colour indicating the polyad to which it belongs. The size of each circle reflects the number of combination differences (CDs) confirming that level (maximum CDs =14).

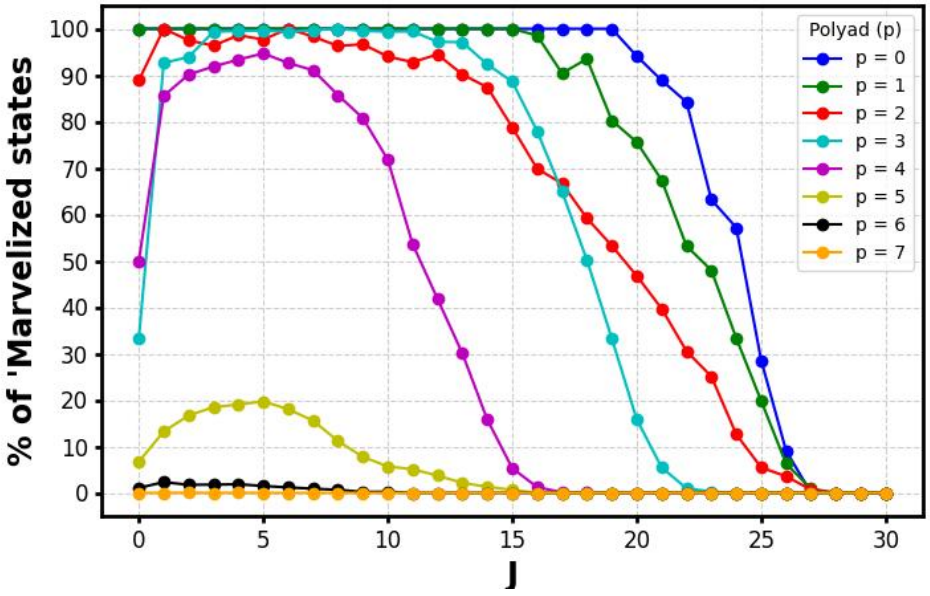
As a summary, Figure 6.21 shows the percentage of MARVELised levels in the MM `.states` file before and after this assignment and update project, in comparison to the total number of states in each polyad. The main improvements are observed in the increased number of MARVELised energies in polyads 5 and 6. The uncertainties of the MARVEL energy levels were estimated using the bootstrap method performed with 100 iterations. Table 6.9 provides a detailed overview of the energy levels for each polyad, including the count of states, the rotational quantum number J ranges, the spectral coverage in wavenumbers, and the number of energies confirmed by CDs. The relevant files (transitions, energy levels, and segment file which maps the experimental sources with the right unit) are available in https://github.com/kyrrk/Methane-Update.

6.4 Outlook

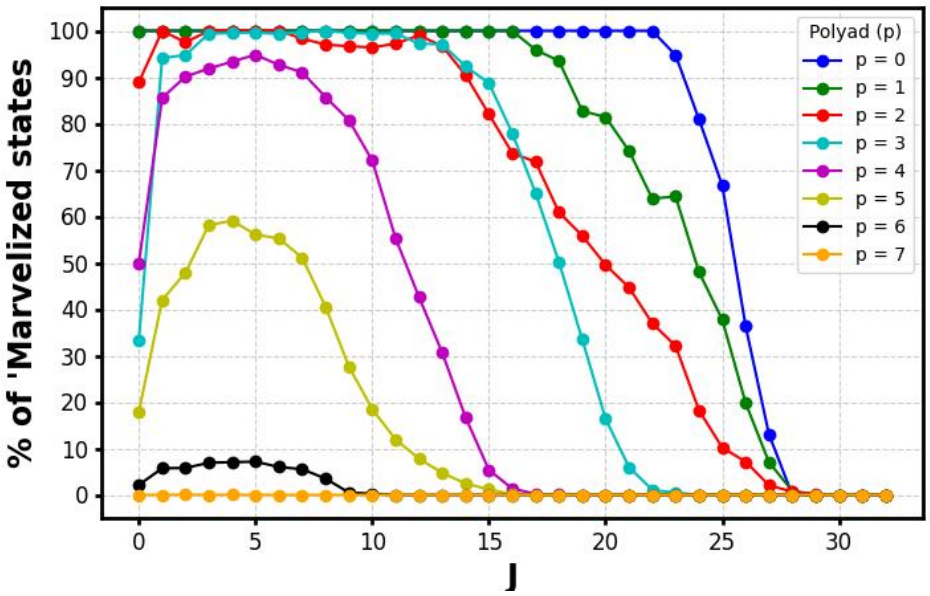
A central goal of this work is to refine the methane line list by improving the accuracy of experimentally derived energy levels at progressively higher vibrational excitations, with the ultimate aim of extending reliable coverage into the near-infrared and eventually the visible region. Through the MARVEL framework, we have begun to construct a highly accurate spectroscopic network of energy levels, validated through combination differences, and compared with theoretical predictions. This provides input for improving variational calculations.

Residuals between MARVEL and TROVE energies are found to increase with both the rotational quantum number J within a polyad and with overall vibrational excitation as seen in Figure 6.22. In polyad 4 we observe residuals as large as 0.8 cm^{-1} even at low J values. Interestingly, the corresponding MARVEL levels changed very little during this assignment project, implying that the discrepancies may arise from systematic misassignments carried over from previous work. One plausible explanation is that some transitions were mistakenly attributed to polyad 4, despite originating from nearby polyads. This case underscores the difficulty of assigning transitions in spectrally dense regions.

In polyad 6, a branch of particularly large residuals is traced to transitions included in the MARVEL input based on assignments that could not be verified against other sources. The challenge ahead is to resolve ambiguities in existing assignments and to expand coverage into higher-energy regions. Addressing both will require new experimental data, ideally under conditions that populate high-energy states more strongly. In this regard, high-temperature spectra offer a promising path forward. Data sets such as that of 12HaBeMi [14], along with other sources listed in Table 6.1, contain numerous transitions, including hot bands, that could be assigned and incorporated into the MARVEL compilation moving forward. Another promising method is the double-resonance approach, which selectively excites specific intermediate states to probe higher-lying vibrational levels. This technique can provide highly accurate transition frequencies in otherwise sparsely characterized

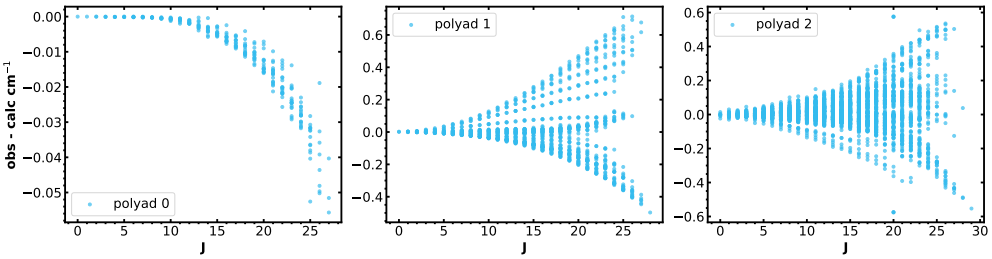


(a) Before

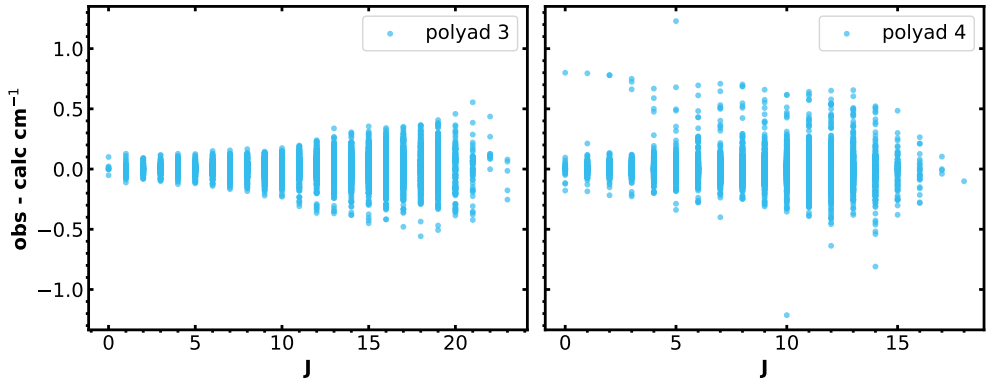


(b) After

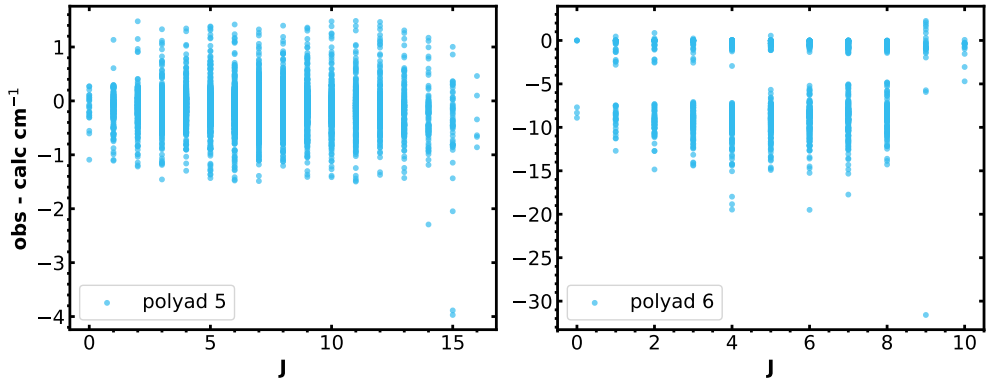
Figure 6.21: Comparison of the percentage of MARVELised states before and after incorporating new transitions.



(a) Polyads 0, 1, 2



(b) Polyads 3, 4



(c) Polyads 5, 6

Figure 6.22: Residuals between MARVEL energy levels and those computed by TROVE, with respect to J, for polyads 0–6.

Table 6.10: Sources considered but not used in the assignment and MARVEL update project. The wavenumber range in cm^{-1}, and reason for exclusion are listed.

Source	Wavenumber range	Comments
72HuPoVa [655]	4136–4288	range covered by more recent measurements
77Berger [556]	2850–3100	low accuracy
80PiHiBe [656]	9000–9155	could not assign this range
82PoPaCh [585]	2250–3250	observed energies provided
84MaFrPr [659]	2940–2995	low accuracy
85MaFrPr [661]	2892–2935, 8876–8938	low accuracy
96SiOb [670]	7128–7373	low accuracy
91CaChSt [664]	13702–13887	could not assign this range
93LuLoGa [665]	11539–12756	could not assign this range
94BoLiRe [666]	11220–11313	could not assign this range
95CaPeJo [667]	11245–11312	could not assign this range
95SiOb [668]	13470–14025	could not assign this range
95TsSa [669]	11200–11335	could not assign this range
07LuGo [674]	11870–11930	could not assign this range
15BeLiCa [684]	9028–10435	could not assign this range
22Lucchesini [690]	12799–12840	could not assign this range
23CaKaVa [691]	10800–14000	could not assign this range

regions, such as polyad 6, and can help resolve ambiguities in assignments while expanding the coverage of high-energy states [457].

It is also worth noting that several sources in Table 6.1 contain transitions involving very high polyads that were not analysed in the present study because the energy ranges provided are too high to be able to assign with confidence currently. Table 6.10 lists such articles along with all other sources we considered but ultimately did not use, as well as the reasons for their exclusion. In contrast, Table 6.11 presents sources with transitions suitable for future analysis.

Table 6.11: Summary of experimental sources for future work.

Sources	Wavenumber Range	# Lines
83FrIlFi [587]	2916–2917	13
83PiChGu [658]	2250–3260	191
90Margolis [663]	5597–5635	1600
98BoRePl [672]	5500–6180	40
03NaBe [673]	2000–6400	15434 (800 K) 22163 (1000 K) 25727 (1273 K)
08FrWaBu [675]	5860–6185	1309
08KaGaRo [676]	5860–7700	128
09GaKaCa [677]	5852–6181	845
09ScKaGa [495]	7351–7655	3474
10CaWaKa [678]	6716–7655	12865
11MoKaWa [679]	7541–7919	5070 (80 K) 7690 (294 K)
12CaWaMo [486]	5854–7919	23138
12HaBeMi [14]	1067–4900	160840 (573 K–1673 K)
12WaMoKa [680]	6717–7589	19940 (80 K) 24001 (296 K)
12GaChZh [681]	6038–6050	72

Continued on next page

Sources	Wavenumber Range	# Lines
13CaLeMo [647]	5855–6183	9228
13MaPrMo [682]	7040–7378	654
15BeKaCa [683]	7908-8345	12703
15BeLiCa [684]	9028–10435	7786
15HaBeBa [412]	2600-5000	194129 (473 K - 1173 K)
15MaKcVa [622]	882–3434	2422
18GhVaMo [685]	5693–6257	177
18SeSiLu [686]	9057–9167	36
19WoBeRe* [687]	5200-9200	4047349 (295 K–1000 K)

* Compilation of measured spectra in several temperatures and resolutions.

Chapter 7

General Conclusions

The overarching motivation for this thesis as part of the ExoMol project is to enhance the accuracy and completeness of spectroscopic data used in high-resolution cross-correlation spectroscopy (HRCCS), a powerful technique for detecting and characterising exoplanet atmospheres. We have contributed to the improvement of molecular line lists for three species of astrophysical interest: methane (CH_4), magnesium oxide (MgO), and titanium monoxide (TiO).

For MgO, we updated the LiTY line list [148] to include over 7 000 empirical (MARVEL) and semi-empirical (PS) energy levels to provide improvements to the resolving power $R = \lambda/\Delta\lambda$ of transitions. The predicted shift (PS) methodology estimates missing energies by identifying systematic trends in the differences between observed and calculated energy values (obs. $-$ calc.) across a given vibronic state. For unobserved levels, shifts were predicted via interpolation or extrapolation in J, with associated uncertainties estimated conservatively from the local uncertainties of existing MARVEL energies. In cases where experimental data existed for only one parity component, the method allowed propagation of corrections to the other.

Notably, the PS method proved especially valuable for MgO due to the sparse available experimental information. It enabled the inclusion of energy levels and uncertainties for transitions otherwise inaccessible through direct measurement, significantly improving spectral completeness. Ultimately, the updated LiTY line list for MgO is considered suitable for HRCC studies in the windows 580 - 700 nm

and 1 900 to 10 000 nm. However, the predicted shift methodology is only viable when at least some rotational transitions of a given vibronic level are experimentally known. The availability of data for the $v = 2, 3$ B $^1\Sigma^+$ state, as well as for any levels of the b $^3\Sigma^+$ electronic states, would greatly strengthen and extend the analysis.

Similarly, due to the limited availability of experimental spectra for the isotopologues $^{24}Mg^{17}O$, $^{24}Mg^{18}O$, $^{25}Mg^{16}O$ and $^{26}Mg^{16}O$, the isotopic extrapolation (IE) method was employed. This approach uses accurate energy levels from the main isotopologue $^{24}Mg^{16}O$, obtained either from MARVEL or PS, to improve the energy predictions for other isotopologues. This method relies on the assumption that the differences between observed and variational energies in the main isotopologue can be transferred to the others. This is in agreement with the Born–Oppenheimer approximation, according to which all isotopologues share essentially the same potential energy surface, since it is governed by the electronic structure and only weakly affected by changes in nuclear mass.

In total, over 7,000 energy levels per isotopologue were updated using this method, improving the expected accuracy of the resulting line lists. Uncertainties were estimated based on those of the main isotopologue, scaled conservatively to account for the extrapolation, and comparison with limited available experimental data for the isotopologues $^{25}Mg^{16}O$ and $^{26}Mg^{16}O$ was performed.

In the case of TiO, new measured rovibronic transitions were incorporated into the MARVEL framework, leading to a more complete and accurate energy level network. These MARVEL-derived energies have been used to improve the Toto line list [149], which now offers broad spectral coverage across the visible and near-infrared regions, with high resolving power in the range 450–1500 nm. While external to the work described in this thesis, the inclusion of Predicted Shift (PS) energy levels, has extended the line list's accuracy to higher rotational quantum numbers. Notably, the updated line list includes experimental data supporting HRCC studies in the 590–630 nm range (15 870–16 950 cm^{-1}).

Methane was the primary focus of this study, owing both to its critical role in

exoplanetary characterisation, atmospheric modelling, and climate physics, and to the abundance of available experimental spectroscopic data. To improve the available spectroscopic data, we performed an extensive collection of spectra from 96 experimental sources, which we processed using the MARVEL (Measured Active Rotational-Vibrational Energy Levels) procedure. This allowed us to construct a reliable set of empirical rovibrational energy levels for methane. These empirical levels were used by Yurchenko et al. [3] to refine variational calculations using the TROVE program. The resulting line list, MARVELous Methane (MM) contains over 7 million transitions with resolving power $R \geq 100000$.

Currently, Marvelised energy levels are complete and well-confirmed up to the tetradecad (polyad 4), with partial and increasingly sparse coverage in the icosad (polyad 5) and triacontad (polyad 6). As a result, the MM line list is highly accurate in far- and mid-infrared region but loses accuracy at near-infrared wavelengths. Our strategy to improve methane spectroscopy is based on an iterative approach that gradually extends accurate energy level coverage to higher vibrational excitations.

In this study, we analysed previously unassigned or partially assigned experimental spectra using the MARVELous Methane line list, allowing us to incorporate 6507 new empirical levels into the MARVEL compilation. Of these, 2009 are confirmed through combination differences. Many newly assigned states belong to polyad 5, a region previously lacking high-accuracy assignments.

The first step moving forward will be to investigate the large residuals observed in regions such as polyad 4, and to determine whether these discrepancies arise from systematic shifts or isolated misassignments. Where appropriate, we will attempt to revise or reassign affected transitions in order to correct the observed deviations between MARVEL and TROVE energy levels.

The MM line list will be updated by refitting the potential energy surface (PES) to this expanded set of empirical levels. A new hybrid line list will be generated by replacing theoretical energies with MARVEL ones wherever available. This updated line list will then serve as a reference for assigning further high-resolution spec-

tra. Table 6.11 contains 24 such experimental sources of various ranges and polyad bands. We will particularly target transitions to higher polyads (P_5,P_6 and beyond). As these new assignments are validated and incorporated into MARVEL, they will be used to refine the variational calculations again, and the accuracy and completeness of the line list will be successively improved. During this process, the quality change of the line list will be assessed by comparing with known data.

This iterative procedure ensures that each stage improves the accuracy of the next, allowing assignments to be made in increasingly higher polyads, and increasingly dense and blended spectral regions above $10,000$ cm^{-1}, eventually reaching into the visible.

The detection and characterisation of methane in the visible spectral region is important for exoplanetary science, particularly for high-resolution reflected-light spectroscopy of temperate rocky exoplanets and for understanding methane-rich atmospheres in the Solar System, including Titan and the giant planets [691, 694, 695].

One promising avenue is to use the CH_4 line list not only to refine the PES for the main isotopologue, but also to improve on the variational calculations of methane isotopologues such as $^{13}CH_4$ and CH_3D. High-quality spectroscopic data for these species are of particular importance for planetary and exoplanetary studies. The $^{13}CH_4$ isotopologue enables determination of the $^{13}C/^{12}C$ isotopic ratio in planetary atmospheres. This can provide insight into methane formation pathways on Earth [696], and may eventually inform studies of atmospheric processes and formation histories on other planets [697]. In addition, $^{13}CH_4$ is the second most abundant isotopologue of methane, making it a natural target for spectroscopic modelling. Moreover, the deuterated isotopologue CH_3D is important for the estimation of the D/H ratio, which serves as a tracer of planetary origin and evolution [698]. From a spectroscopic perspective, however, the two isotopologues differ significantly in complexity. While $^{13}CH_4$ retains the tetrahedral symmetry of CH_4, allowing its treatment within the existing MARVEL–TROVE framework with

relatively minor modifications, CH_3D exhibits reduced molecular symmetry due to isotopic substitution. This symmetry reduction lifts degeneracies and leads to a substantially more complex rovibrational structure. As a result, the empirically refined PES for $^{12}CH_4$, in combination with an ab initio electric dipole moment surface, can be directly reused to compute high-accuracy line lists for $^{13}CH_4$. This methodology was succesfully applied to water isotopologues $H_2^{17}O$ and $H_2^{17}O$ by Polyansky et al. [137] and to ammonia $^{15}NH_3$ by Yurchenko et al. [5].

In addition, the isotopic extrapolation (IE) method can be used, as there is limited available experimental data for methane isotopologues. In this approach, the obs. – calc. residuals from $^{12}CH_4$ MARVEL energy levels are used as empirical corrections applied to the calculated energy levels of the isotopologues. Since $^{13}CH_4$ retains the tetrahedral symmetry and polyad structure, the IE method is expected to yield high accuracy in this case. In contrast, for lower symmetry isotopologues such as CH_3D the extrapolation is less reliable.

Bibliography

[1] L. K. McKemmish, C. A. Bowesman, K. Kefala, A. N. Perri, A. M. Syme, S. N. Yurchenko, and J. Tennyson. A hybrid approach to generating diatomic line lists for high resolution studies of exoplanets and other hot astronomical objects: Updates to ExoMol MgO, VO and TiO line lists. *RASTI*, 3:565–583, 2024.

[2] K. Kefala, V. Boudon, S. N. Yurchenko, and J. Tennyson. Empirical rovibrational energy levels for methane. *J. Quant. Spectrosc. Radiat. Transf.*, 316:108897, 2024.

[3] S. N. Yurchenko, A. Owens, K. Kefala, and J. Tennyson. ExoMol line lists – LVII. High accuracy ro-vibrational line list for methane (CH_4). *MNRAS*, 528:3719–3729, 2024.

[4] Jonathan Tennyson, Sergei N. Yurchenko, Jingxin Zhang, Charles A. Bowesman, Ryan P. Brady, Jeanna Buldyreva, Katy L. Chubb, Robert R. Gamache, Maire N. Gorman, Elizabeth R. Guest, Christian Hill, Kyriaki Kefala, A. E. Lynas-Gray, Thomas M. Mellor, Laura K. McKemmish, Georgi B. Mitev, Irina I. Mizus, Alec Owens, Zhijian Peng, Armando N. Perri, Marco Pezzella, Oleg L. Polyansky, Qianwei Qu, Mikhail Semenov, Oleksiy Smola, Andrei ov, Wilfrid Somogyi, Apoorva Upadhyay, Samuel O. M. Wright, and Nikolai F. Zobov. The 2024 release of the ExoMol database: molecular line lists for exoplanet and other hot atmospheres. *J. Quant. Spectrosc. Radiat. Transf.*, 326:109083, 2024.

[5] S. N. Yurchenko, Charles A. Bowesman, Ryan P. Brady, Elizabeth R. Guest, Kyraki Kefala, Georgi B. Mitev, Alec Owens, Armando N. Perri, Marco Pezzella, Oleksiy Smola, Andrei Solokov, Jingxin Zhang, and J Tennyson. ExoMol Line Lists – LX: Molecular line list for the ammonia isotopologue $^{15}NH_3$. *MNRAS*, 533:3442–3456, 2024.

[6] Steve Pittner, Daniel Lehmann, Dietrich Zahn, and Veit Wagner. Charge transport analysis of poly(3-hexylthiophene) by electroreflectance spectroscopy. *Phys. Rev. B*, 87, 2013.

[7] Günter G Hoffmann. *Infrared and Raman Spectroscopy: Principles and Applications*. Walter de Gruyter GmbH & Co KG, 2023.

[8] Sergei N. Yurchenko, Ahmed F. Al-Refaie, and Jonathan Tennyson. ExoCross: A general program for generating spectra from molecular line lists. *A&A*, 614:A131, 2018.

[9] P.-L. Buono, F. Laurent-Polz, and J. Montaldi. Symmetric Hamiltonian bifurcations. In J. Montaldi and T. Ratiu, editors, *Geometric Mechanics and Symmetry: The Peyresq Lectures*, volume 306 of *London Mathematical Society Lecture Note Series*, pages 357–402. Cambridge University Press, Cambridge, 2005.

[10] Plinio Maroni. *Bond-and mode-specific reactivity of methane on Ni (100)*. PhD thesis, Verlag nicht ermittelbar, 2005.

[11] S. Albert, S. Bauerecker, V. Boudon, L. R. Brown, J.-P. Champion, M. Loëte, A. Nikitin, and M. Quack. Global Analysis of the High Resolution Infrared Spectrum of Methane $^{12}CH_4$ in the Region from 0 to 4800 cm^{-1}. *Chem. Phys.*, 356:131–146, 2009.

[12] B. Amyay, M. Louviot, O. Pirali, R. Georges, J. Vander Auwera, and V. Boudon. Global analysis of the high temperature infrared emission spectrum of $^{12}CH_4$ in the dyad (ν_2/ν_4) region. *J. Chem. Phys.*, 144:024312, 2016.

[13] Michael Rey, Andrei V. Nikitin, and Vladimir G. Tyuterev. Accurate Theoretical Methane Line Lists in the Infrared up to 3000 K and Quasi-continuum Absorption/Emission Modeling for Astrophysical Applications. *ApJ*, 847:105, 2017.

[14] Robert J. Hargreaves, Christopher A. Beale, Laurent Michaux, Melis Irfan, and Peter F. Bernath. Hot methane line lists for Exoplanet and Brown Dwarf atmospheres. *ApJ*, 757:46, 2012.

[15] Mahdi Yousefi, Peter F. Bernath, Mike Dulick, Manfred Birk, and Georg Wagner. Line parameters for hot methane ν_3 band broadened by H_2 from 296 to 1100 K. *J. Quant. Spectrosc. Radiat. Transf.*, 263:107557, 2021.

[16] C. N. Banwell and Elaine M. McCash. *Fundamentals of Molecular Spectroscopy*. McGraw-Hill, 4th edition, 1994.

[17] L R Brown, R A Toth, R H Hunt, and J W Brault. Line Assignments and Intensities of the $\nu_2 + \nu_3 - \nu_2$ Band of $^{12}CH_4$. *J. Mol. Spectrosc.*, 89:528–541, 1981.

[18] Yuan Ding, Fanghui Cao, Jinke Li, Jin Wang, Anwen Liu, Yan Tan, and Shuiming Hu. Saturated absorption spectroscopy of methane around 1667 nm. *Chin. J. Chem. Phys.*, 37:721–728, 2024.

[19] Walther Ritz. On a new law of series spectra. *ApJ*, 28:237–243, 1908.

[20] E. Kagi and K. Kawaguchi. Microwave spectroscopy of MgO in the $a^3\Pi$ and $X\,^1\Sigma$ states. *J. Mol. Spectrosc.*, 795:179–184, 2006.

[21] Peter R Griffiths. Fourier transform infrared spectrometry. *Science*, 222:297–302, 1983.

[22] E. D. Hinkley and P. L. Kelley. Detection of Air Pollutants with Tunable Diode Lasers. *Science*, 171:635–639, 1971.

[23] Anthony O'Keefe and David A. G. Deacon. Cavity ring-down optical spectrometer for absorption measurements using pulsed laser sources. *Rev. Sci. Instrum.*, 59:2544–2551, 1988.

[24] Fritz Keilmann, Christoph Gohle, and Ronald Holzwarth. Time-domain mid-infrared frequency-comb spectrometer. *Opt. Lett.*, 29:1542–1544, 2004.

[25] Tara Fortier and Esther Baumann. 20 years of developments in optical frequency comb technology and applications. *Commun. Phys.*, 2:153, 2019.

[26] Vinicius Silva de Oliveira, Isak Silander, Lucile Rutkowski, Grzegorz Soboń, Ove Axner, Kevin K Lehmann, and Aleksandra Foltynowicz. Sub-Doppler optical-optical double-resonance spectroscopy using a cavity-enhanced frequency comb probe. *Nat. Commun.*, 15:161, 2024.

[27] Adrian Hjältén, Vinicius Silva de Oliveira, Isak Silander, Andrea Rosina, Michael Rey, Lucile Rutkowski, Grzegorz Soboń, Kevin K Lehmann, and Aleksandra Foltynowicz. Measurement and assignment of J= 5 to 9 rotational energy levels in the 9070–9370 cm^{-1} range of methane using optical frequency comb double-resonance spectroscopy. *J. Chem. Phys.*, 161(12), 2024.

[28] Marco Lamperti, Lucile Rutkowski, Daniele Ronchetti, Davide Gatti, Riccardo Gotti, Giulio Cerullo, Franck Thibault, Hubert Jóźwiak, Szymon Wójtewicz, Piotr Masłowski, et al. Stimulated Raman scattering metrology of molecular hydrogen. *Commun. Phys.*, 6:67, 2023.

[29] James PR Day, Katrin F Domke, Gianluca Rago, Hideaki Kano, Hiro-o Hamaguchi, Erik M Vartiainen, and Mischa Bonn. Quantitative coherent anti-Stokes Raman scattering (CARS) microscopy. *J. Phys. Chem. B*, 115:7713–7725, 2011.

[30] E Jourdanneau, F Chaussard, R Saint-Loup, T Gabard, and H Berger. The methane Raman spectrum from 1200 to 5500 cm^{-1}: A first step toward tem-

perature diagnostic using methane as a probe molecule in combustion systems. *J. Mol. Spectrosc.*, 233:219–230, 2005.

[31] Kristina F Chang, Daniel Lesko, Carter Mashburn, Peter Chang, Eugene Tsao, Alexander J Lind, and Scott A Diddams. A multi-harmonic NIR-UV dual-comb spectrometer. *arXiv preprint arXiv:2312.08492*, 2023.

[32] Takashi Yoshikawa, Yoshihiro Sumiyoshi, Hideyuki Takada, Kennosuke Hoshina, and Yasuki Endo. Laser induced fluorescence spectroscopy of NC_3O. *J. Chem. Phys.*, 128, 2008.

[33] J. J. Wang, N. T. Van-Oanh, D. Bellert, W. H. Breckenridge, M. A. Gaveau, E. Gloaguen, B. Soep, and J. M. Mestdagh. Laser spectroscopic studies of the $E\,^1\Sigma^+$ 'Rydberg' state of the MgO molecule. *Chem. Phys. Lett.*, 392:62–67, 2004.

[34] J. J. Wang and W. H. Breckenridge. Laser spectroscopic studies of several Rydberg states of MgO. *J. Chem. Phys.*, 124:124308, 2006.

[35] NASA Science. Exoplanets: Planet types. `https://science.nasa.gov/exoplanets/planet-types/`.

[36] NASA Exoplanet Archive. Exoplanet and candidate statistics.

[37] W. S. Jacob. On certain Anomalies presented by the Binary Star 70 Ophiuchi. *MNRAS*, 15:228, 1855.

[38] T. J. J. See. Researches on the orbit of 70 Ophiuchi, and on a periodic perturbation in the motion of the system arising from the action of an unseen body. *AJ*, 16:17–23, 1896.

[39] W. D. Heintz. The binary star 70 Ophiuchi revisited. *JRASC*, 82:140–145, 1988.

[40] David W Latham, Tsevi Mazeh, Robert P Stefanik, Michel Mayor, and Gilbert Burki. The unseen companion of HD114762: a probable brown dwarf. *Nature*, 339:38–40, 1989.

[41] Bruce Campbell, G. A. H. Walker, and S. Yang. A Search for Substellar Companions to Solar-type Stars. *ApJ*, 331:902, 1988.

[42] T Nakajima, BR Oppenheimer, SR Kulkarni, DA Golimowski, K Matthews, and ST Durrance. Discovery of a cool brown dwarf. N*ature*, 378:463–465, 1995.

[43] Rafael Rebolo, MR Zapatero Osorio, and EL Martín. Discovery of a brown dwarf in the Pleiades star cluster. *Nature*, 377:129–131, 1995.

[44] A. Wolszczan and D. A. Frail. A planetary system around the millisecond pulsar PSR1257 + 12. *Nature*, 355:145–147, 1992.

[45] Michel Mayor and Didier Queloz. A Jupiter-mass companion to a solar-type star. *Nature*, 378:355–359, 1995.

[46] David F Gray. A planetary companion for 51 Pegasi implied by absence of pulsations in the stellar spectra. *Nature*, 391:153–154, 1998.

[47] Davide Cenadelli and Andrea Bernagozzi. *The Discovery of the First Exoplanets*, pages 1–20. Springer Nature Switzerland, 2025.

[48] R. Paul Butler, Geoffrey W. Marcy, Debra A. Fischer, Timothy M. Brown, Adam R. Contos, Sylvain G. Korzennik, Peter Nisenson, and Robert W. Noyes. Evidence for Multiple Companions to ∪ Andromedae*. *ApJ*, 526:916, 1999.

[49] NC Santos, M Mayor, D Naef, F Pepe, D Queloz, S Udry, and M Burnet. The CORALIE survey for southern extra-solar planets-VI. New long period giant planets around HD 28185 and HD 213240. *A&A*, 379:999–1004, 2001.

[50] D Charbonneau, T M Brown, R W Noyes, and R L Gilliland. Detection of an extrasolar planet atmosphere. *ApJ*, 568:377–384, 2002.

[51] David Charbonneau, Lori E Allen, S Thomas Megeath, Guillermo Torres, Roi Alonso, Timothy M Brown, Ronald L Gilliland, David W Latham,

Georgi Mandushev, Francis T O'Donovan, et al. Detection of thermal emission from an extrasolar planet. *ApJ*, 626:523, 2005.

[52] Drake Deming, Sara Seager, L Jeremy Richardson, and Joseph Harrington. Infrared radiation from an extrasolar planet. *Nature*, 434:740–743, 2005.

[53] J.-L. Birkby. Exoplanet Atmospheres at High Spectral Resolution. *arXiv e-prints*, 2018.

[54] COMMISSIONING PHASE. Setting new standards with HARPS. *The Messenger*, 114:20, 2003.

[55] Steven S Vogt, Steven L Allen, Bruce C Bigelow, L Bresee, William E Brown, T Cantrall, Albert Conrad, M Couture, C Delaney, Harland W Epps, et al. HIRES: the high-resolution echelle spectrometer on the Keck 10-m Telescope. In *Instrumentation in Astronomy VIII*, volume 2198, pages 362–375. SPIE, 1994.

[56] F Pepe, Stefano Cristiani, R Rebolo, NC Santos, H Dekker, A Cabral, Paolo Di Marcantonio, P Figueira, G Lo Curto, C Lovis, et al. ESPRESSO at VLT-On-sky performance and first results. *A&A*, 645:A96, 2021.

[57] William J. Borucki, David Koch, Gibor Basri, Natalie Batalha, Timothy Brown, Douglas Caldwell, John Caldwell, Jørgen Christensen-Dalsgaard, William D. Cochran, Edna DeVore, Edward W. Dunham, Andrea K. Dupree, Thomas N. Gautier, John C. Geary, Ronald Gilliland, Alan Gould, Steve B. Howell, Jon M. Jenkins, Yoji Kondo, David W. Latham, Geoffrey W. Marcy, Søren Meibom, Hans Kjeldsen, Jack J. Lissauer, David G. Monet, David Morrison, Dimitar Sasselov, Jill Tarter, Alan Boss, Don Brownlee, Toby Owen, Derek Buzasi, David Charbonneau, Laurance Doyle, Jonathan Fortney, Eric B. Ford, Matthew J. Holman, Sara Seager, Jason H. Steffen, William F. Welsh, Jason Rowe, Howard Anderson, Lars Buchhave, David Ciardi, Lucianne Walkowicz, William Sherry, Elliott Horch, Howard Isaacson, Mark E. Everett, Debra Fischer, Guillermo Torres, John Asher Johnson,

Michael Endl, Phillip MacQueen, Stephen T. Bryson, Jessie Dotson, Michael Haas, Jeffrey Kolodziejczak, Jeffrey Van Cleve, Hema Chandrasekaran, Joseph D. Twicken, Elisa V. Quintana, Bruce D. Clarke, Christopher Allen, Jie Li, Haley Wu, Peter Tenenbaum, Ekaterina Verner, Frederick Bruhweiler, Jason Barnes, and Andrej Prsa. Kepler Planet-Detection Mission: Introduction and First Results. *Science*, 327:977–980, 2010.

[58] George R. Ricker, Joshua N. Winn, Roland Vanderspek, David W. Latham, Gáspár Á. Bakos, Jacob L. Bean, Zachory K. Berta-Thompson, Timothy M. Brown, Lars Buchhave, Nathaniel R. Butler, R. Paul Butler, William J. Chaplin, David B. Charbonneau, Jørgen Christensen-Dalsgaard, Mark Clampin, Drake Deming, John P. Doty, Nathan De Lee, Courtney Dressing, Edward W. Dunham, Michael Endl, François Fressin, Jian Ge, Thomas Henning, Matthew J. Holman, Andrew W. Howard, Shigeru Ida, Jon M. Jenkins, Garrett Jernigan, John Asher Johnson, Lisa Kaltenegger, Nobuyuki Kawai, Hans Kjeldsen, Gregory Laughlin, Alan M. Levine, Douglas Lin, Jack J. Lissauer, Phillip MacQueen, Geoffrey Marcy, Peter R. McCullough, Timothy D. Morton, Norio Narita, Martin Paegert, Enric Palle, Francesco Pepe, Joshua Pepper, Andreas Quirrenbach, Stephen A. Rinehart, Dimitar Sasselov, Bun'ei Sato, Sara Seager, Alessandro Sozzetti, Keivan G. Stassun, Peter Sullivan, Andrew Szentgyorgyi, Guillermo Torres, Stephane Udry, and Joel Villasenor. Transiting Exoplanet Survey Satellite. *J. Astron. Telesc. Instrum. Syst.*, 1:014003, 2014.

[59] Gaia Collaboration, Prusti, T., de Bruijne, J. H. J., Brown, A. G. A., Vallenari, A., Babusiaux, C., Bailer-Jones, C. A. L., Bastian, U., Biermann, M., Evans, D. W., Eyer, L., Jansen, F., Jordi, C., Klioner, S. A., Lammers, U., Lindegren, L., Luri, X., Mignard, F., Milligan, D. J., Panem, C., Poinsignon, V., Pourbaix, D., Randich, S., Sarri, G., Sartoretti, P., Siddiqui, H. I., Soubiran, C., Valette, V., van Leeuwen, F., Walton, N. A., Aerts, C., Arenou, F., Cropper, M., Drimmel, R., Høg, E., Katz, D., Lattanzi, M. G., O'Mullane, W., Grebel, E. K., Holland, A. D., Huc, C., Passot, X., Bramante, L., Cac-

ciari, C., Castañeda, J., Chaoul, L., Cheek, N., De Angeli, F., Fabricius, C., Guerra, R., Hernández, J., Jean-Antoine-Piccolo, A., Masana, E., Messineo, R., Mowlavi, N., Nienartowicz, K., Ordóñez-Blanco, D., Panuzzo, P., Portell, J., Richards, P. J., Riello, M., Seabroke, G. M., Tanga, P., Thévenin, F., Torra, J., Els, S. G., Gracia-Abril, G., Comoretto, G., Garcia-Reinaldos, M., Lock, T., Mercier, E., Altmann, M., Andrae, R., Astraatmadja, T. L., Bellas-Velidis, I., Benson, K., Berthier, J., Blomme, R., Busso, G., Carry, B., Cellino, A., Clementini, G., Cowell, S., Creevey, O., Cuypers, J., Davidson, M., De Ridder, J., de Torres, A., Delchambre, L., Dell'Oro, A., Ducourant, C., Frémat, Y., García-Torres, M., Gosset, E., Halbwachs, J.-L., Hambly, N. C., Harrison, D. L., Hauser, M., Hestroffer, D., Hodgkin, S. T., Huckle, H. E., Hutton, A., Jasniewicz, G., Jordan, S., Kontizas, M., Korn, A. J., Lanzafame, A. C., Manteiga, M., Moitinho, A., Muinonen, K., Osinde, J., Pancino, E., Pauwels, T., Petit, J.-M., Recio-Blanco, A., Robin, A. C., Sarro, L. M., Siopis, C., Smith, M., Smith, K. W., Sozzetti, A., Thuillot, W., van Reeven, W., Viala, Y., Abbas, U., Abreu Aramburu, A., Accart, S., Aguado, J. J., Allan, P. M., Allasia, W., Altavilla, G., Álvarez, M. A., Alves, J., Anderson, R. I., Andrei, A. H., Anglada Varela, E., Antiche, E., Antoja, T., Antón, S., Arcay, B., Atzei, A., Ayache, L., Bach, N., Baker, S. G., Balaguer-Núñez, L., Barache, C., Barata, C., Barbier, A., Barblan, F., Baroni, M., Barrado y Navascués, D., Barros, M., Barstow, M. A., Becciani, U., Bellazzini, M., Bellei, G., Bello García, A., Belokurov, V., Bendjoya, P., Berihuete, A., Bianchi, L., Bienaymé, O., Billebaud, F., Blagorodnova, N., Blanco-Cuaresma, S., Boch, T., Bombrun, A., Borrachero, R., Bouquillon, S., Bourda, G., Bouy, H., Bragaglia, A., Breddels, M. A., Brouillet, N., Brüsemeister, T., Bucciarelli, B., Budnik, F., Burgess, P., Burgon, R., Burlacu, A., Busonero, D., Buzzi, R., Caffau, E., Cambras, J., Campbell, H., Cancelliere, R., Cantat-Gaudin, T., Carlucci, T., Carrasco, J. M., Castellani, M., Charlot, P., Charnas, J., Charvet, P., Chassat, F., Chiavassa, A., Clotet, M., Cocozza, G., Collins, R. S., Collins, P., Costigan, G., Crifo, F., Cross, N. J. G., Crosta, M., Crowley, C., Dafonte,

C., Damerdji, Y., Dapergolas, A., David, P., David, M., De Cat, P., de Felice, F., de Laverny, P., De Luise, F., De March, R., de Martino, D., de Souza, R., Debosscher, J., del Pozo, E., Delbo, M., Delgado, A., Delgado, H. E., di Marco, F., Di Matteo, P., Diakite, S., Distefano, E., Dolding, C., Dos Anjos, S., Drazinos, P., Durán, J., Dzigan, Y., Ecale, E., Edvardsson, B., Enke, H., Erdmann, M., Escolar, D., Espina, M., Evans, N. W., Eynard Bontemps, G., Fabre, C., Fabrizio, M., Faigler, S., Falcão, A. J., Farràs Casas, M., Faye, F., Federici, L., Fedorets, G., Fernández-Hernández, J., Fernique, P., Fienga, A., Figueras, F., Filippi, F., Findeisen, K., Fonti, A., Fouesneau, M., Fraile, E., Fraser, M., Fuchs, J., Furnell, R., Gai, M., Galleti, S., Galluccio, L., Garabato, D., García-Sedano, F., Garé, P., Garofalo, A., Garralda, N., Gavras, P., Gerssen, J., Geyer, R., Gilmore, G., Girona, S., Giuffrida, G., Gomes, M., González-Marcos, A., González-Núñez, J., González-Vidal, J. J., Granvik, M., Guerrier, A., Guillout, P., Guiraud, J., Gúrpide, A., Gutiérrez-Sánchez, R., Guy, L. P., Haigron, R., Hatzidimitriou, D., Haywood, M., Heiter, U., Helmi, A., Hobbs, D., Hofmann, W., Holl, B., Holland, G., Hunt, J. A. S., Hypki, A., Icardi, V., Irwin, M., Jevardat de Fombelle, G., Jofré, P., Jonker, P. G., Jorissen, A., Julbe, F., Karampelas, A., Kochoska, A., Kohley, R., Kolenberg, K., Kontizas, E., Koposov, S. E., Kordopatis, G., Koubsky, P., Kowalczyk, A., Krone-Martins, A., Kudryashova, M., Kull, I., Bachchan, R. K., Lacoste-Seris, F., Lanza, A. F., Lavigne, J.-B., Le Poncin-Lafitte, C., Lebreton, Y., Lebzelter, T., Leccia, S., Leclerc, N., Lecoeur-Taibi, I., Lemaitre, V., Lenhardt, H., Leroux, F., Liao, S., Licata, E., Lindstrøm, H. E. P., Lister, T. A., Livanou, E., Lobel, A., Löffler, W., López, M., Lopez-Lozano, A., Lorenz, D., Loureiro, T., MacDonald, I., Magalhães Fernandes, T., Managau, S., Mann, R. G., Mantelet, G., Marchal, O., Marchant, J. M., Marconi, M., Marie, J., Marinoni, S., Marrese, P. M., Marschalkó, G., Marshall, D. J., Martín-Fleitas, J. M., Martino, M., Mary, N., Matijevič, G., Mazeh, T., McMillan, P. J., Messina, S., Mestre, A., Michalik, D., Millar, N. R., Miranda, B. M. H., Molina, D., Molinaro, R., Molinaro, M., Molnár, L.,

Moniez, M., Montegriffo, P., Monteiro, D., Mor, R., Mora, A., Morbidelli, R., Morel, T., Morgenthaler, S., Morley, T., Morris, D., Mulone, A. F., Muraveva, T., Musella, I., Narbonne, J., Nelemans, G., Nicastro, L., Noval, L., Ordénovic, C., Ordieres-Meré, J., Osborne, P., Pagani, C., Pagano, I., Pailler, F., Palacin, H., Palaversa, L., Parsons, P., Paulsen, T., Pecoraro, M., Pedrosa, R., Pentikäinen, H., Pereira, J., Pichon, B., Piersimoni, A. M., Pineau, F.-X., Plachy, E., Plum, G., Poujoulet, E., Prša, A., Pulone, L., Ragaini, S., Rago, S., Rambaux, N., Ramos-Lerate, M., Ranalli, P., Rauw, G., Read, A., Regibo, S., Renk, F., Reylé, C., Ribeiro, R. A., Rimoldini, L., Ripepi, V., Riva, A., Rixon, G., Roelens, M., Romero-Gómez, M., Rowell, N., Royer, F., Rudolph, A., Ruiz-Dern, L., Sadowski, G., Sagristà Sellés, T., Sahlmann, J., Salgado, J., Salguero, E., Sarasso, M., Savietto, H., Schnorhk, A., Schultheis, M., Sciacca, E., Segol, M., Segovia, J. C., Segransan, D., Serpell, E., Shih, I-C., Smareglia, R., Smart, R. L., Smith, C., Solano, E., Solitro, F., Sordo, R., Soria Nieto, S., Souchay, J., Spagna, A., Spoto, F., Stampa, U., Steele, I. A., Steidelmüller, H., Stephenson, C. A., Stoev, H., Suess, F. F., Süveges, M., Surdej, J., Szabados, L., Szegedi-Elek, E., Tapiador, D., Taris, F., Tauran, G., Taylor, M. B., Teixeira, R., Terrett, D., Tingley, B., Trager, S. C., Turon, C., Ulla, A., Utrilla, E., Valentini, G., van Elteren, A., Van Hemelryck, E., van Leeuwen, M., Varadi, M., Vecchiato, A., Veljanoski, J., Via, T., Vicente, D., Vogt, S., Voss, H., Votruba, V., Voutsinas, S., Walmsley, G., Weiler, M., Weingrill, K., Werner, D., Wevers, T., Whitehead, G., Wyrzykowski, Ł., Yoldas, A., Žerjal, M., Zucker, S., Zurbach, C., Zwitter, T., Alecu, A., Allen, M., Allende Prieto, C., Amorim, A., Anglada-Escudé, G., Arsenijevic, V., Azaz, S., Balm, P., Beck, M., Bernstein, H.-H., Bigot, L., Bijaoui, A., Blasco, C., Bonfigli, M., Bono, G., Boudreault, S., Bressan, A., Brown, S., Brunet, P.-M., Bunclark, P., Buonanno, R., Butkevich, A. G., Carret, C., Carrion, C., Chemin, L., Chéreau, F., Corcione, L., Darmigny, E., de Boer, K. S., de Teodoro, P., de Zeeuw, P. T., Delle Luche, C., Domingues, C. D., Dubath, P., Fodor, F., Frézouls, B., Fries, A., Fustes, D., Fyfe, D., Gallardo,

E., Gallegos, J., Gardiol, D., Gebran, M., Gomboc, A., Gómez, A., Grux, E., Gueguen, A., Heyrovsky, A., Hoar, J., Iannicola, G., Isasi Parache, Y., Janotto, A.-M., Joliet, E., Jonckheere, A., Keil, R., Kim, D.-W., Klagyivik, P., Klar, J., Knude, J., Kochukhov, O., Kolka, I., Kos, J., Kutka, A., Lainey, V., LeBouquin, D., Liu, C., Loreggia, D., Makarov, V. V., Marseille, M. G., Martayan, C., Martinez-Rubi, O., Massart, B., Meynadier, F., Mignot, S., Munari, U., Nguyen, A.-T., Nordlander, T., Ocvirk, P., O'Flaherty, K. S., Olias Sanz, A., Ortiz, P., Osorio, J., Oszkiewicz, D., Ouzounis, A., Palmer, M., Park, P., Pasquato, E., Peltzer, C., Peralta, J., Péturaud, F., Pieniluoma, T., Pigozzi, E., Poels, J., Prat, G., Prod'homme, T., Raison, F., Rebordao, J. M., Risquez, D., Rocca-Volmerange, B., Rosen, S., Ruiz-Fuertes, M. I., Russo, F., Sembay, S., Serraller Vizcaino, I., Short, A., Siebert, A., Silva, H., Sinachopoulos, D., Slezak, E., Soffel, M., Sosnowska, D., Straižys, V., ter Linden, M., Terrell, D., Theil, S., Tiede, C., Troisi, L., Tsalmantza, P., Tur, D., Vaccari, M., Vachier, F., Valles, P., Van Hamme, W., Veltz, L., Virtanen, J., Wallut, J.-M., Wichmann, R., Wilkinson, M. I., Ziaeepour, H., and Zschocke, S. The Gaia mission. *A&A*, 595:A1, 2016.

[60] D. Spergel, N. Gehrels, C. Baltay, D. Bennett, J. Breckinridge, M. Donahue, A. Dressler, B. S. Gaudi, T. Greene, O. Guyon, C. Hirata, J. Kalirai, N. J. Kasdin, B. Macintosh, W. Moos, S. Perlmutter, M. Postman, B. Rauscher, J. Rhodes, Y. Wang, D. Weinberg, D. Benford, M. Hudson, W. S. Jeong, Y. Mellier, W. Traub, T. Yamada, P. Capak, J. Colbert, D. Masters, M. Penny, D. Savransky, D. Stern, N. Zimmerman, R. Barry, L. Bartusek, K. Carpenter, E. Cheng, D. Content, F. Dekens, R. Demers, K. Grady, C. Jackson, G. Kuan, J. Kruk, M. Melton, B. Nemati, B. Parvin, I. Poberezhskiy, C. Peddie, J. Ruffa, J. K. Wallace, A. Whipple, E. Wollack, and F. Zhao. Wide-Field InfrarRed Survey Telescope-Astrophysics Focused Telescope Assets WFIRST-AFTA 2015 Report, 2015.

[61] Sarah Ballard, Daniel Fabrycky, Francois Fressin, David Charbonneau, Jean-Michel Desert, Guillermo Torres, Geoffrey Marcy, Christopher J. Burke,

Howard Isaacson, Christopher Henze, Jason H. Steffen, David R. Ciardi, Steven B. Howell, William D. Cochran, Michael Endl, Stephen T. Bryson, Jason F. Rowe, Matthew J. Holman, Jack J. Lissauer, Jon M. Jenkins, Martin Still, Eric B. Ford, Jessie L. Christiansen, Christopher K. Middour, Michael R. Haas, Jie Li, Jennifer R. Hall, Sean McCauliff, Natalie M. Batalha, David G. Koch, and William J. Borucki. The Kepler-19 System: A Transiting 2.2 $R_\oplus$ Planet and a Second Planet Detected via Transit Timing Variations. *ApJ*, 743:200, 2011.

[62] Willy Benz, Christopher Broeg, Andrea Fortier, Nicola Rando, Thomas Beck, Mathias Beck, Didier Queloz, David Ehrenreich, PFL Maxted, KG Isaak, et al. The CHEOPS mission. *Exp. Astron.*, 51:109–151, 2021.

[63] George Hobbs, A Archibald, Zaven Arzoumanian, D Backer, Matthew Bailes, NDR Bhat, M Burgay, Sarah Burke-Spolaor, D Champion, Ismaël Cognard, et al. The international pulsar timing array project: using pulsars as a gravitational wave detector. *Classical and Quantum Gravity*, 27:084013, 2010.

[64] Andrzej Udalski, Michał Krzysztof Szymański, and Grzegorz Szymański. OGLE-IV: fourth phase of the optical gravitational lensing experiment. *arXiv preprint arXiv:1504.05966*, 2015.

[65] I. A. Bond, N. J. Rattenbury, J. Skuljan, F. Abe, R. J. Dodd, J. B. Hearnshaw, M. Honda, J. Jugaku, P. M. Kilmartin, A. Marles, K. Masuda, Y. Matsubara, Y. Muraki, T. Nakamura, G. Nankivell, S. Noda, C. Noguchi, K. Ohnishi, M. Reid, To. Saito, H. Sato, M. Sekiguchi, D. J. Sullivan, T. Sumi, M. Takeuti, Y. Watase, S. Wilkinson, R. Yamada, T. Yanagisawa, and P. C. M. Yock. Study by MOA of extrasolar planets in gravitational microlensing events of high magnification. *MNRAS*, 333:71–83, 2002.

[66] Seung-Lee Kim, Chung-Uk Lee, Byeong-Gon Park, Dong-Jin Kim, Sang-Mok Cha, Yongseok Lee, Cheongho Han, Moo-Young Chun, and Insoo Yuk.

KMTNET: a network of 1.6 m wide-field optical telescopes installed at three southern observatories. *J. Korean Astron. Soc.*, 49:37–44, 2016.

[67] Samson A Johnson, Matthew Penny, B Scott Gaudi, Eamonn Kerins, Nicholas J Rattenbury, Annie C Robin, Sebastiano Calchi Novati, and Calen B Henderson. Predictions of the nancy grace roman space telescope galactic exoplanet survey. II. Free-floating planet detection rates. *AJ.*, 160:123, 2020.

[68] Bruce Macintosh, James Graham, David Palmer, Rene Doyon, Don Gavel, James Larkin, Ben Oppenheimer, Leslie Saddlemyer, J Kent Wallace, Brian Bauman, et al. The Gemini planet imager. In *Advances in Adaptive Optics II*, volume 6272, pages 177–188. SPIE, 2006.

[69] J-L Beuzit, Arthur Vigan, David Mouillet, Kjetil Dohlen, Raffaele Gratton, Anthony Boccaletti, J-F Sauvage, Hans Martin Schmid, Maud Langlois, Cyril Petit, et al. SPHERE: the exoplanet imager for the Very Large Telescope. *A&A*, 631:A155, 2019.

[70] N. Jovanovic, F. Martinache, O. Guyon, C. Clergeon, G. Singh, T. Kudo, V. Garrel, K. Newman, D. Doughty, J. Lozi, J. Males, Y. Minowa, Y. Hayano, N. Takato, J. Morino, J. Kuhn, E. Serabyn, B. Norris, P. Tuthill, G. Schworer, P. Stewart, L. Close, E. Huby, G. Perrin, S. Lacour, L. Gauchet, S. Vievard, N. Murakami, F. Oshiyama, N. Baba, T. Matsuo, J. Nishikawa, M. Tamura, O. Lai, F. Marchis, G. Duchene, T. Kotani, and J. Woillez. The Subaru Coronagraphic Extreme Adaptive Optics System: Enabling High-Contrast Imaging on Solar-System Scales. *PASP*, 127:890, 2015.

[71] Sara Seager. The future of spectroscopic life detection on exoplanets. *Proc. Nat. Acad. Sci. U. S. A.*, 111:12634–12640, 2014.

[72] Ryan J. Oelkers, Luke M. Schmidt, Erika Cook, Mary Anne Limbach, D. L. DePoy, J. L. Marshall, Jimmy Ardoin, Mitchell Barry, Evan Batteas, Alexandra Boone, Brant Conway, Silvana Delgado Adrande, John D. Dixon,

Enrique Gonzalez-Vega, Alexandra Guajardo, Landon Holcomb, Christian Lambert, Shravan Menon, Divya Mishra, Jacob Purcell, Zachary Reed, Nathan Sala, Noah Siebersma, Nhu Ngoc Ton, Raenessa M. L. Walker, Z. Franklin Wang, and Kaitlin Webber. Ground-based Reconnaissance Observations of 21 Exoplanet Atmospheres with the Exoplanet Transmission Spectroscopy Imager. *AJ.*, 169:134, 2025.

[73] S. Seager and D. D. Sasselov. Theoretical Transmission Spectra during Extrasolar Giant Planet Transits. *ApJ*, 537:916–921, 2000.

[74] E. M.-R. Kempton, R. E. Lupu, A. Owusu-Asare, P. Slough, and B. Cale. Exo-Transmit: An Open-Source Code for Calculating Transmission Spectra for Exoplanet Atmospheres of Varied Composition. *PASP*, 129:044402, 2017.

[75] Sujan Sengupta, Aritra Chakrabarty, and Giovanna Tinetti. Optical transmission spectra of hot jupiters: effects of scattering. *ApJ*, 889:181, 2020.

[76] Lendl, M., Cubillos, P. E., Hagelberg, J., Müller, A., Juvan, I., and Fossati, L. Signs of strong Na and K absorption in the transmission spectrum of WASP-103b. *A&A*, 606:A18, 2017.

[77] Chen, G., Casasayas-Barris, N., Pallé, E., Yan, F., Stangret, M., Cegla, H. M., Allart, R., and Lovis, C. Detection of Na, K, and Hα absorption in the atmosphere of WASP-52b using ESPRESSO. *A&A*, 635:A171, 2020.

[78] Enric Pallé, María Rosa Zapatero Osorio, Rafael Barrena, Pilar Montañés-Rodríguez, and Eduardo L Martín. Earth's transmission spectrum from lunar eclipse observations. *Nature*, 459:814–816, 2009.

[79] Evelyn JR Macdonald and Nicolas B Cowan. An empirical infrared transit spectrum of Earth: opacity windows and biosignatures. *MNRAS*, 489:196–204, 2019.

[80] Evelyn JR Macdonald and Nicolas B Cowan. Erratum: An empirical infrared transit spectrum of Earth: opacity windows and biosignatures. *MNRAS*, 492:651–652, 2020.

[81] Laura Kreidberg, Jacob L Bean, Jean-Michel Désert, Michael R Line, Jonathan J Fortney, Nikku Madhusudhan, Kevin B Stevenson, Adam P Showman, David Charbonneau, Peter R McCullough, et al. A precise water abundance measurement for the hot jupiter wasp-43b. *ApJL*, 793:L27, 2014.

[82] Robert T. Zellem, Nikole K. Lewis, Heather A. Knutson, Caitlin A. Griffith, Adam P. Showman, Jonathan J. Fortney, Nicolas B. Cowan, Eric Agol, Adam Burrows, David Charbonneau, Drake Deming, Gregory Laughlin, and Jonathan Langton. The 4.5 μm Full-orbit Phase Curve of the Hot Jupiter HD 209458b. *ApJ*, 790:53, 2014.

[83] Louis-Philippe Coulombe, Bjorn Benneke, Ryan Challener, Anjali A. A. Piette, Lindsey S. Wiser, Megan Mansfield, Ryan J. MacDonald, Hayley Beltz, Adina D. Feinstein, Michael Radica, Arjun B. Savel, Leonardo A. Dos Santos, Jacob L. Bean, Vivien Parmentier, Ian Wong, Emily Rauscher, Thaddeus D. Komacek, Eliza M. R. Kempton, Xianyu Tan, Mark Hammond, Neil T. Lewis, Michael R. Line, Elspeth K. H. Lee, Hinna Shivkumar, Ian J. M. Crossfield, Matthew C. Nixon, Benjamin V. Rackham, Hannah R. Wakeford, Luis Welbanks, Xi Zhang, Natalie M. Batalha, Zachory K. Berta-Thompson, Quentin Changeat, Jean-Michel Desert, Nestor Espinoza, Jayesh M. Goyal, Joseph Harrington, Heather A. Knutson, Laura Kreidberg, Mercedes Lopez-Morales, Avi Shporer, David K. Sing, Kevin B. Stevenson, Keshav Aggarwal, Eva-Maria Ahrer, Munazza K. Alam, Taylor J. Bell, Jasmina Blecic, Claudio Caceres, Aarynn L. Carter, Sarah L. Casewell, Nicolas Crouzet, Patricio E. Cubillos, Leen Decin, Jonathan J. Fortney, Neale P. Gibson, Kevin Heng, Thomas Henning, Nicolas Iro, Sarah Kendrew, Pierre-Olivier Lagage, Jeremy Leconte, Monika Lendl, Joshua D. Lothringer, Luigi Mancini, Thomas Mikal-Evans, Karan Molaverdikhani, Nikolay K. Nikolov,

Kazumasa Ohno, Enric Palle, Caroline Piaulet, Seth Redfield, Pierre-Alexis Roy, Shang-Min Tsai, Olivia Venot, and Peter J. Wheatley. A broadband thermal emission spectrum of the ultra-hot Jupiter WASP-18b. *Nature*, 620:292–298, 2023.

[84] Giovanna Tinetti, Thérèse Encrenaz, and Athena Coustenis. Spectroscopy of planetary atmospheres in our Galaxy. *A&ARv*, 21:1–65, 2013.

[85] Thomas J Fauchez, Benjamin V Rackham, Elsa Ducrot, Kevin B Stevenson, and Julien de Wit. Stellar Models Also Limit Exoplanet Atmosphere Studies in Emission. *arXiv preprint arXiv:2502.19585*, 2025.

[86] Nicolas B. Cowan and Eric Agol. Inverting Phase Functions to Map Exoplanets. *ApJL*, 678:L129, 2008.

[87] Heather A. Knutson, David Charbonneau, Lori E. Allen, Jonathan J. Fortney, Eric Agol, Nicolas B. Cowan, Adam P. Showman, Curtis S. Cooper, and S. Thomas Megeath. A map of the day-night contrast of the extrasolar planet HD 189733b. *Nature*, 447:183–186, 2007.

[88] Heather A. Knutson, David Charbonneau, Nicolas B. Cowan, Jonathan J. Fortney, Adam P. Showman, Eric Agol, Gregory W. Henry, Mark E. Everett, and Lori E. Allen. Multiwavelength constraints on the day-night circulation patterns of HD 189733b. *ApJ*, 690:822–836, 2009.

[89] Adam P Showman and Tristan Guillot. Atmospheric circulation and tides of "51 Pegasus b-like" planets. *A&A*, 385:166–180, 2002.

[90] Daniel J. Stevens and B. Scott Gaudi. A Posteriori Transit Probabilities. *PASP*, 125:933, 2013.

[91] Callie E. Hood, Jonathan J. Fortney, Michael R. Line, Emily C. Martin, Caroline V. Morley, Jayne L. Birkby, Zafar Rustamkulov, Roxana E. Lupu, and Richard S. Freedman. Prospects for Characterizing the Haziest Sub-Neptune Exoplanets with High-resolution Spectroscopy. *AJ.*, 160:198, 2020.

[92] Siddharth Gandhi, Matteo Brogi, and Rebecca K Webb. Seeing above the clouds with high-resolution spectroscopy. *MNRAS*, 498:194–204, 2020.

[93] Jerry W. Xuan, Jason Wang, Jean-Baptiste Ruffio, Heather Knutson, Dimitri Mawet, Paul Molli‘ere, Jared Kolecki, Arthur Vigan, Sagnick Mukherjee, Nicole Wallack, Ji Wang, Ashley Baker, Randall Bartos, Geoffrey A. Blake, Charlotte Z. Bond, Marta Bryan, Benjamin Calvin, Sylvain Cetre, Mark Chun, Jacques-Robert Delorme, Greg Doppmann, Daniel Echeverri, Luke Finnerty, Michael P. Fitzgerald, Katelyn Horstman, Julie Inglis, Nemanja Jovanovic, Ronald López, Emily C. Martin, Evan Morris, Jacklyn Pezzato, Sam Ragland, Bin Ren, Garreth Ruane, Ben Sappey, Tobias Schofield, Andrew Skemer, Taylor Venenciano, J. Kent Wallace, and Peter Wizinowich. A Clear View of a Cloudy Brown Dwarf Companion from High-resolution Spectroscopy. *ApJ*, 937:54, 2022.

[94] J. P. Beaulieu, S. Carey, I. Ribas, and G. Tinetti. Primary Transit of the Planet HD 189733b at 3.6 and 5.8 μm. *ApJ*, 677:1343, 2008.

[95] Michael Radica, Luis Welbanks, Néstor Espinoza, Jake Taylor, Louis-Philippe Coulombe, Adina D Feinstein, Jayesh Goyal, Nicholas Scarsdale, Loïc Albert, Priyanka Baghel, Jacob L Bean, Jasmina Blecic, David Lafreni‘ere, Ryan J MacDonald, Maria Zamyatina, Romain Allart, Étienne Artigau, Natasha E Batalha, Neil James Cook, Nicolas B Cowan, Lisa Dang, René Doyon, Marylou Fournier-Tondreau, Doug Johnstone, Michael R Line, Sarah E Moran, Sagnick Mukherjee, Stefan Pelletier, Pierre-Alexis Roy, Geert Jan Talens, Joseph Filippazzo, Klaus Pontoppidan, and Kevin Volk. Awesome SOSS: transmission spectroscopy of WASP-96b with NIRISS/SOSS. *MNRAS*, 524:835–856, 2023.

[96] Thomas P Greene, Taylor J Bell, Elsa Ducrot, Achrène Dyrek, Pierre-Olivier Lagage, and Jonathan J Fortney. Thermal emission from the earth-sized exoplanet trappist-1 b using jwst. *Nature*, 618:39–42, 2023.

[97] Giovanna Tinetti, Pierre Drossart, Paul Eccleston, Paul Hartogh, Astrid Heske, Jérémy Leconte, Giusi Micela, Marc Ollivier, Göran Pilbratt, Ludovic Puig, et al. A chemical survey of exoplanets with ariel. *Exp. Astron.*, 46:135–209, 2018.

[98] I A G Snellen. A new method for probing the atmospheres of transiting exoplanets. *MNRAS*, 353:L1–L6, 2004.

[99] Ignas A. G. Snellen, Remco J. de Kok, Ernst J. W. de Mooij, and Simon Albrecht. The orbital motion, absolute mass and high-altitude winds of exoplanet HD-209458b. *Nature*, 465:1049–1051, 2010.

[100] Ignas Snellen. High-dispersion spectroscopy of extrasolar planets: from CO in hot Jupiters to O_2 in exo-Earths. *Phil. Trans. Royal Soc. London A*, 372:20130075, 2014.

[101] Matteo Brogi and Jayne Birkby. High-resolution Spectroscopy. In *ExoFrontiers*, 2514-3433, pages 8–1 to 8–10. IOP Publishing, 2021.

[102] Snellen, I., de Kok, R., Birkby, J. L., Brandl, B., Brogi, M., Keller, C., Kenworthy, M., Schwarz, H., and Stuik, R. Combining high-dispersion spectroscopy with high contrast imaging: Probing rocky planets around our nearest neighbors. *A&A*, 576:A59, 2015.

[103] H. J. Hoeijmakers, R. J. de Kok, I. A. G. Snellen, M. Brogi, J. L. Birkby, and H. Schwarz. A search for TiO in the optical high-resolution transmission spectrum of HD 209458b: Hindrance due to inaccuracies in the line database. *A&A*, 575:A20, 2015.

[104] I. E. Gordon, L. S. Rothman, R. J. Hargreaves, R. Hashemi, E. V. Karlovets, F. M. Skinner, E. K. Conway, C. Hill, R. V. Kochanov, Y. Tan, P. Wcisło, A. A. Finenko, K. Nelson, P. F. Bernath, M. Birk, V. Boudon, A. Campargue, K. V. Chance, A. Coustenis, B. J. Drouin, J.-M. Flaud, R. R. Gamache, J. T. Hodges, D. Jacquemart, E. J. Mlawer, A. V. Nikitin, V. I. Perevalov,

M. Rotger, J. Tennyson, G. C. Toon, H. Tran, V. G. Tyuterev, E. M. Adkins, A. Baker, A. Barbe, E. Canè, A. G. Császár, A. Dudaryonok, O. Egorov, A. J. Fleisher, H. Fleurbaey, A. Foltynowicz, T. Furtenbacher, J. J. Harrison, J.-M. Hartmann, V.-M. Horneman, X. Huang, T. Karman, J. Karns, S. Kassi, I. Kleiner, V. Kofman, F. Kwabia-Tchana, N. N. Lavrentieva, T. J. Lee, D. A. Long, A. A. Lukashevskaya, O. M. Lyulin, V. Yu. Makhnev, W. Matt, S. T. Massie, M. Melosso, S. N. Mikhailenko, D. Mondelain, H. S. P. Müller, O. V. Naumenko, A. Perrin, O. L. Polyansky, E. Raddaoui, P. L. Raston, Z. D. Reed, M. Rey, C. Richard, R. Tóbiás, I. Sadiek, D. W. Schwenke, E. Starikova, K. Sung, F. Tamassia, S. A. Tashkun, J. Vander Auwera, I. A. Vasilenko, A. A. Vigasin, G. L. Villanueva, B. Vispoel, G. Wagner, A. Yachmenev, and S. N. Yurchenko. The HITRAN2020 molecular spectroscopic database. *J. Quant. Spectrosc. Radiat. Transf.*, 277:107949, 2022.

[105] L.S. Rothman, I.E. Gordon, R.J. Barber, H. Dothe, R.R. Gamache, A. Goldman, V.I. Perevalov, S.A. Tashkun, and J. Tennyson. HITEMP, the high-temperature molecular spectroscopic database. *J. Quant. Spectrosc. Radiat. Transf.*, 111:2139 – 2150, 2010.

[106] H. J. Hoeijmakers, R. J. de Kok, I. A. G. Snellen, M. Brogi, J. L. Birkby, and H. Schwarz. A search for TiO in the optical high-resolution transmission spectrum of HD 209458b: Hindrance due to inaccuracies in the line database. *A&A*, 575:A20, 2015.

[107] S. de Regt, A. Y. Kesseli, I. A. G. Snellen, S. R. Merritt, and K. L. Chubb. A quantitative assessment of the VO line list: Inaccuracies hamper high-resolution VO detections in exoplanet atmospheres. *A&A*, 661:A109, 2022.

[108] Matteo Brogi, Ignas A. G. Snellen, Remco J. de Kok, Simon Albrecht, Jayne Birkby, and Ernst J. W. de Mooij. The signature of orbital motion from the dayside of the planet τ Boötis b. *Nature*, 486:502–504, 2012.

[109] Nikku Madhusudhan. Exoplanetary Atmospheres: Key Insights, Challenges, and Prospects. *ARA&A*, 57:617–663, 2019.

[110] R. Follert, R. J. Dorn, E. Oliva, J. L. Lizon, A. Hatzes, N. Piskunov, A. Reiners, U. Seemann, E. Stempels, U. Heiter, T. Marquart, M. Lockhart, G. Anglada-Escude, T. Löwinger, D. Baade, J. Grunhut, P. Bristow, B. Klein, Y. Jung, D. J. Ives, F. Kerber, E. Pozna, J. Paufique, H. U. Kaeufl, L. Origlia, E. Valenti, D. Gojak, M. Hilker, L. Pasquini, A. Smette, and J. Smoker. CRIRES+: a cross-dispersed high-resolution infrared spectrograph for the ESO VLT. In *Ground-based and Airborne Instrumentation for Astronomy V*, volume 9147, page 914719, 2014.

[111] A Quirrenbach, PJ Amado, JA Caballero, R Mundt, A Reiners, I Ribas, W Seifert, M Abril, J Aceituno, FJ Alonso-Floriano, et al. CARMENES instrument overview. In *Ground-based and airborne instrumentation for astronomy V*, volume 9147, pages 531–542, 2014.

[112] Ian S McLean, Eric E Becklin, Oddvar Bendiksen, George Brims, John Canfield, Donald Frank Figer, James R Graham, Jonah Hare, Fred Lacayanga, James E Larkin, et al. Design and development of NIRSPEC: a near-infrared echelle spectrograph for the Keck II telescope. In *Infrared astronomical instrumentation*, volume 3354, pages 566–578. SPIE, 1998.

[113] M Tamura, H Suto, J Nishikawa, T Kotani, B Sato, W Aoki, T Usuda, T Kurokawa, K Kashiwagi, S Nishiyama, et al. Infrared Doppler instrument for the Subaru telescope (IRD). In *Ground-based and airborne instrumentation for astronomy IV*, volume 8446, pages 638–647. SPIE, 2012.

[114] Enric Palle, Katia Biazzo, Emeline Bolmont, Paul Mollière, Katja Poppenhaeger, Jayne Birkby, Matteo Brogi, Gael Chauvin, Andrea Chiavassa, Jens Hoeijmakers, et al. Ground-breaking exoplanet science with the ANDES spectrograph at the ELT. *Exp. Astron.*, 59:1–84, 2025.

[115] Ignas AG Snellen, Bernhard R Brandl, Remco J De Kok, Matteo Brogi, Jayne

Birkby, and Henriette Schwarz. Fast spin of the young extrasolar planet β Pictoris b. *Nature*, 509:63–65, 2014.

[116] D. A. Fischer, A. W. Howard, G. P. Laughlin, B. Macintosh, S. Mahadevan, J. Sahlmann, and J. C. Yee. Exoplanet Detection Techniques. In *Protostars and Planets VI*, pages 715–737, 2014.

[117] Nikku Madhusudhan. Exoplanetary Atmospheres: Key Insights, Challenges, and Prospects. *ARA&A*, 57:617–663, 2019.

[118] William B. Sparks and Holland C. Ford. Imaging Spectroscopy for Extrasolar Planet Detection. *ApJ*, 578:543–564, 2002.

[119] Hoeijmakers, H. J., Schwarz, H., Snellen, I. A. G., de Kok, R. J., Bonnefoy, M., Chauvin, G., Lagrange, A. M., and Girard, J. H. Medium-resolution integral-field spectroscopy for high-contrast exoplanet imaging - Molecule maps of the β Pictoris system with SINFONI. *A&A*, 617:A144, 2018.

[120] Petit dit de la Roche, D. J. M., Hoeijmakers, H. J., and Snellen, I. A. G. Molecule mapping of HR8799b using OSIRIS on Keck - Strong detection of water and carbon monoxide, but no methane. *A&A*, 616:A146, 2018.

[121] J. Tennyson and S. N. Yurchenko. ExoMol: molecular line lists for exoplanet and other atmospheres. *MNRAS*, 425:21–33, 2012.

[122] S. N. Yurchenko, J. Tennyson, Jeremy Bailey, Morgan D J Hollis, and Giovanna Tinetti. Spectrum of hot methane in astronomical objects using a comprehensive computed line list. *Proc. Nat. Acad. Sci.*, 111:9379–9383, 2014.

[123] J. Tennyson, C. Hill, and S. N. Yurchenko. Data structures for ExoMol: Molecular line lists for exoplanet and other atmospheres. In *6^{th} international conference on atomic and molecular data and their applications ICAMDATA-2012*, volume 1545 of *AIP Conference Proceedings*, pages 186–195. AIP, New York, 2013.

[124] R J Barber, J K Strange, C Hill, O L Polyansky, G Ch Mellau, S N Yurchenko, and Jonathan Tennyson. ExoMol line lists – III. An improved hot rotation-vibration line list for HCN and HNC. *MNRAS*, 437:1828–1835, 2014.

[125] E J Barton, C Chiu, S Golpayegani, S. N. Yurchenko, J. Tennyson, Daniel J. Frohman, and Peter F Bernath. ExoMol Molecular linelists – V. The ro-vibrational spectra of NaCl and KCl. *MNRAS*, 442:1821–1829, 2014.

[126] C. Sousa-Silva, A. F. Al-Refaie, J. Tennyson, and S. N. Yurchenko. ExoMol line lists - VII. the rotation-vibration spectrum of phosphine up to 1500 K. *MNRAS*, 446:2337–2347, 2015.

[127] A. F. Al-Refaie, S. N. Yurchenko, A. Yachmenev, and J. Tennyson. ExoMol line lists - VIII: A variationally computed line list for hot formaldehyde. *MNRAS*, 448:1704–1714, 2015.

[128] A. T. Patrascu, J. Tennyson, and S. N. Yurchenko. ExoMol molecular linelists - IX: The spectrum of AlO. *MNRAS*, 449:3613–3619, 2015.

[129] T. Rivlin, L. Lodi, S. N. Yurchenko, J. Tennyson, and R J Le Roy. ExoMol line lists X: The spectrum of sodium hydride. *MNRAS*, 451:5153–5157, 2015.

[130] A. I. Pavlyuchko, S. N. Yurchenko, and J. Tennyson. ExoMol line lists XI: A Hot Line List for nitric acid. *MNRAS*, 452:1702–1706, 2015.

[131] G Paulose, E J Barton, S. N. Yurchenko, and J. Tennyson. ExoMol Molecular linelists – XII. Line lists for eight isotopologues of CS. *MNRAS*, 454:1931–1939, 2015.

[132] S. N. Yurchenko, Audra Blissett, Usama Asari, Marcus Vasilios, Christian Hill, and J. Tennyson. ExoMol Molecular linelists – XIII. The spectrum of CaO. *MNRAS*, 456:4524–4532, 2016.

[133] D. S. Underwood, J. Tennyson, S. N. Yurchenko, Xinchuan Huang, David W. Schwenke, Timothy J. Lee, S. Clausen, and A. Fateev. ExoMol line lists XIV: A line list for hot SO_2. *MNRAS*, 459:3890–3899, 2016.

[134] A. F. Al-Refaie, O. L. Polyansky, R. I. Ovsyannikov, J. Tennyson, and S. N. Yurchenko. ExoMol line lists XV: A hot line-list for hydrogen peroxide. *MNRAS*, 461:1012–1022, 2016.

[135] A. A. A. Azzam, S. N. Yurchenko, J. Tennyson, and O. V. Naumenko. ExoMol line lists XVI: A Hot Line List for H_2S. *MNRAS*, 460:4063–4074, 2016.

[136] D. S. Underwood, J. Tennyson, S. N. Yurchenko, S. Clausen, and A. Fateev. ExoMol line lists XVII: A line list for hot SO_3. *MNRAS*, 462:4300–4313, 2016.

[137] O. L. Polyansky, A. A. Kyuberis, L. Lodi, J. Tennyson, R. I. Ovsyannikov, and N.F. Zobov. ExoMol molecular line lists XIX: high accuracy computed line lists for $H_2{}^{17}O$ and $H_2{}^{18}O$. *MNRAS*, 466:1363–1371, 2017.

[138] I. I. Mizus, A. Alijah, N. F. Zobov, A. A. Kyuberis, S. N. Yurchenko, J. Tennyson, and O. L. Polyansky. ExoMol molecular line lists XX: a comprehensive line list for H_3^+. *MNRAS*, 468:1717–1725, 2017.

[139] A. Owens, S. N. Yurchenko, A. Yachmenev, W. Thiel, and J. Tennyson. ExoMol molecular line lists XXII. The rotation-vibration spectrum of silane up to 1200 K. *MNRAS*, 471:5025–5032, 2017.

[140] L. Prajapat, P. Jagoda, L. Lodi, M. N. Gorman, S. N. Yurchenko, and J. Tennyson. ExoMol molecular line lists XXIII. Spectra of PO and PS. *MNRAS*, 472:3648–3658, 2017.

[141] S. N. Yurchenko, Frances Sinden, Lorenzo Lodi, Christian Hill, Maire N. Gorman, and J. Tennyson. ExoMol Molecular linelists – XXIV: A new hot line list for silicon monohydride, SiH. *MNRAS*, 473:5324–5333, 2018.

[142] Apoorva Upadhyay, Eamon K. Conway, J. Tennyson, and S. N. Yurchenko. ExoMol Molecular linelists – XXV: A hot line list for silicon sulphide, SiS. *MNRAS*, 477:1520–1527, 2018.

[143] S. N. Yurchenko, W. Bond, M. N. Gorman, L. Lodi, L. K. McKemmish, W. Nunn, R. Shah, and J. Tennyson. ExoMol Molecular linelists – XXVI: spectra of SH and NS. *MNRAS*, 478:270–282, 2018.

[144] B. P. Mant, A. Yachmenev, J. Tennyson, and S. N. Yurchenko. ExoMol molecular line lists - XXVII: spectra of C_2H_4. *MNRAS*, 478:3220 – 3232, 2018.

[145] A. Owens, A. Yachmenev, J. Tennyson, W. Thiel, and S. N. Yurchenko. ExoMol Molecular line lists XXIX: The rotation-vibration spectrum of methyl chloride up to 1200 K. *MNRAS*, 479:3002–3010, 2018.

[146] O. L. Polyansky, A. A. Kyuberis, N. F. Zobov, J. Tennyson, S. N. Yurchenko, and L. Lodi. ExoMol molecular line lists XXX: a complete high-accuracy line list for water. *MNRAS*, 480:2597–2608, 2018.

[147] S. N. Yurchenko, Istvan Szabo, Elizaveta Pyatenko, and J. Tennyson. ExoMol Molecular line lists XXXI: The spectrum of C_2. *MNRAS*, 480:3397–3411, 2018.

[148] H.-Y. Li, J. Tennyson, and S. N. Yurchenko. ExoMol molecular line lists XXXII: the rovibronic spectrum of MgO. *MNRAS*, 486:2351–2365, 2019.

[149] L. K. McKemmish, T. Masseron, J Hoeijmakers, V. V. Pérez-Mesa, S. L. Grimm, S. N. Yurchenko, and J. Tennyson. ExoMol Molecular line lists – XXXIII. The spectrum of Titanium Oxide. *MNRAS*, 488:2836–2854, 2019.

[150] J Langleben, Sergei N. Yurchenko, and Jonathan Tennyson. ExoMol line list XXXIV: A Rovibrational Line List for Phosphinidene (PH) in its $X\,^3\Sigma^-$ and $a\,^1\Delta$ Electronic States. *MNRAS*, 488:2332, 2019.

[151] P. A. Coles, Sergei N. Yurchenko, and Jonathan Tennyson. ExoMol molecular line lists XXXV: a rotation-vibration line list for hot ammonia. *MNRAS*, 490:4638–4647, 2019.

[152] M N Gorman, S. N. Yurchenko, and J. Tennyson. ExoMol Molecular linelists – XXXVI. $X\ ^2\Pi$ – $X\ ^2\Pi$ and $A\ ^2\Sigma^+$ – $X\ ^2\Pi$ transitions of SH. *MNRAS*, 490:1652–1665, 2019.

[153] K L Chubb, J. Tennyson, and S. N. Yurchenko. ExoMol Molecular linelists – XXXVII: spectra of acetylene. *MNRAS*, 493:1531–1545, 2020.

[154] A Owens, E K Conway, J. Tennyson, and S. N. Yurchenko. ExoMol Molecular linelists – XXXVIII: High-temperature molecular line list of silicon dioxide (SiO_2). *MNRAS*, 495:1927–1933, 2020.

[155] S. N. Yurchenko, Thomas M. Mellor, Richard S. Freedman, and J. Tennyson. ExoMol molecular line lists XXXIX: Ro-vibrational molecular line list for CO_2. *MNRAS*, 496:5282–5291, 2020.

[156] S. N. Yurchenko, J. Tennyson, Steve Miller, V. V. Melnikov, J. O'Donoghue, and L. Moore. ExoMol molecular line lists XL: Ro-vibrational molecular line list for the hydronium ion (H_3O^+). *MNRAS*, 497:2340–2351, 2020.

[157] A. Owens, J. Tennyson, and S. N. Yurchenko. ExoMol line lists – XLI. High-temperature molecular line lists for the alkali metal hydroxides KOH and NaOH. *MNRAS*, 502:1128–1135, 2021.

[158] Qianwei Qu, Sergei N. Yurchenko, and Jonathan Tennyson. ExoMol molecular line lists – XLII: Rovibronic molecular line list for the low-lying states of NO. *MNRAS*, 504:5768–5777, 2021.

[159] G. B. Mitev, S. Taylor, J. Tennyson, S. N. Yurchenko, A. A. Buchachenko, and A. V. Stolyarov. ExoMol molecular line lists – XLIII: Rovibronic transitions corresponding to the close-lying X $^2\Pi$ and A $^2\Sigma^+$ states of NaO. *MNRAS*, 511:2349–2355, 2022.

[160] S. N. Yurchenko, J. Tennyson, A.-M. Syme, A. Y. Adam, V. H. J. Clark, B. Cooper, C. P. Dobney, S. T. E. Donnelly, M. N. Gorman, A. E. Lynas-Gray, T. Meltzer, A. Owens, Q. Qu, M. Semenov, W. Somogyi, A. Upadhyay, S. Wright, and J. C. Zapata Trujillo. ExoMol line lists – XLIV. Infrared and ultraviolet line list for silicon monoxide ($^{28}Si^{16}O$). *MNRAS*, 510:903–919, 2022.

[161] A. Owens, S. Dooley, L. McLaughlin, B. Tan, G. Zhang, S. N. Yurchenko, and J. Tennyson. ExoMol line lists – XLV. Rovibronic molecular line lists of calcium monohydride (CaH) and magnesium monohydride (MgH). *MNRAS*, 511:5448–5461, 2022.

[162] T Mellor, A. Owens, S. N. Yurchenko, and J. Tennyson. ExoMol line lists – LI. Rvibronic molecular line list for thioformaldehyde (H_2CS). *MNRAS*, 520:1997–2008, 2022.

[163] S. N. Yurchenko, E. Nogué, A. A. A. Azzam, and J. Tennyson. ExoMol line lists – IL. Rovibronic spectrum of aluminium monochloride (AlCl). *MNRAS*, 520:5183–5191, 2023.

[164] C. A. Bowesman, I. I. Mizus, N. F. Zobov, O. L. Polyansky, J. Sarka, B. Poirier, M. Pezzella, S. N. Yurchenko, and J. Tennyson. ExoMol line lists - L: High-resolution line lists of H_3^+, H_2D^+, D_2H^+ and D_3^+. *MNRAS*, 519:6333–6348, 2023.

[165] Alec Owens, Sam O M Wright, Yakiv Pavlenko, Alexander Mitrushchenkov, Jacek Koput, Sergei N Yurchenko, and Jonathan Tennyson. ExoMol line lists - LI. Molecular line list for lithium hydroxide (LiOH). *MNRAS*, 527:731–738, 2024.

[166] O. Pearce, S. N. Yurchenko, and J. Tennyson. ExoMol line lists – LII. Line Lists for the Methylidyne Cation (CH^+). *MNRAS*, 527:10726–10736, 2024.

[167] S. N. Yurchenko, R. P. Brady, J. Tennyson, A. N. Smirnov, O. A. Vasilyev,

and V. G. Solomonik. ExoMol line lists – LIII. Empirical Rovibronic spectra Yttrium Oxide (YO). *MNRAS*, 527:4899–4912, 2024.

[168] S. N. Yurchenko, W. Szajna, R. Hakalla, M. Semenov, A ov, J. Tennyson, Y. Pavlenko, and M. R. Schmidt. ExoMol line lists – LIV. Empirical line lists for AlH and AlD and Emission spectroscopy of AlD in $A\ ^1\Pi$ ($v = 0, 1, 2$). *MNRAS*, 527:9736–9756, 2024.

[169] C. A. Bowesman, Qianwei Qu, L. K. McKemmish, S. N. Yurchenko, and J. Tennyson. ExoMol line lists – LV: Hyperfine-resolved molecular line list for vanadium monoxide ($^{51}V^{16}O$). *MNRAS*, 529:1321–1332, 2024.

[170] R. P. Brady, S. N. Yurchenko, J. Tennyson, and G.-S. Kim. ExoMol line lists – LVI. The SO line list, MARVEL analysis of experimental transition data and refinement of the spectroscopic model. *MNRAS*, 527:6675–6690, 2024.

[171] A. Owens, , S. N. Yurchenko, and J. Tennyson. ExoMol line lists - LVIII. High-temperature molecular line list of carbonyl sulphide (OCS). *MNRAS*, 530:4004–4015, 2024.

[172] S. N. Yurchenko, T Mellor, and J Tennyson. ExoMol line lists – LIX. High-temperature line list for N_2O. *MNRAS*, 534:1364–1375, 2024.

[173] G. B. Mitev, C. A. Bowesman, Jingxin Zhang, S. N. Yurchenko, and J. Tennyson. ExoMol Line Lists – LXI: A trihybrid linelist for rovibronic transitions of the hydroxyl radical (OH). *MNRAS*, 536:3401–3420, 2025.

[174] A. E. Lynas-Gray, O. L. Polyansky, J. Tennyson, S. N. Yurchenko, and N. F. Zobov. ExoMol Line Lists – LXII: Ro-Vibrational Energy Levels and Line-Strengths for the Propadienediylidene (C_3) electronic Ground-State. *MNRAS*, 535:1439–1448, 2024.

[175] I. I. Mizus, N. F. Zobov, M Pezzella, Oleg V. Boyarkin, Maxim A. Koshelev, Dmitry S. Makarov, S. N. Yurchenko, J. Tennyson, and O. L. Polyansky. Ex-

oMol Line Lists – LXIII: Ro-Vibrational Energy Levels and Line-Strengths HDO. *MNRAS*, 2025.

[176] Mikhail Semenov, Nayla El-Kork, Sergei N. Yurchenko, and Jonathan Tennyson. ExoMol Line Lists – LXIV: Empirical rovibronic spectra of phosphorous mononitride (PN) covering the IR and UV regions. *MNRAS*, 536:714–727, 2025.

[177] J. Tennyson and S. N. Yurchenko. The ExoMol atlas of molecular opacities. *Atoms*, 6:26, 2018.

[178] K. L. Chubb, M. Rocchetto, S. N. Yurchenko, M. Min, I. Waldmann, J. K. Barstow, P. Molliere, A. F. Al-Refaie, M. Phillips, and J. Tennyson. The ExoMolOP Database: Cross-sections and k-tables for Molecules of Interest in High-Temperature Exoplanet Atmospheres. *A&A*, 646:A21, 2021.

[179] Jingxin Zhang, J. Tennyson, and Sergei N. Yurchenko. PyExoCross: a Python program for generating spectra and cross-sections from molecular line lists. *RASTI*, 3:257–287, 2024.

[180] Jingxin Zhang, Christian Hill, J. Tennyson, and Sergei N. Yurchenko. ExoMolHR: A Relational Database of Empirical High-Resolution Molecular Spectra. *ApJS*, 276:67, 2025.

[181] Hans-Joachim Werner, Peter J. Knowles, Gerald Knizia, Frederick R. Manby, and Martin Schütz. Molpro: a general-purpose quantum chemistry program package. *WIREs Comput. Mol. Sci.*, 2:242–253, 2012.

[182] Sergei N. Yurchenko, Lorenzo Lodi, Jonathan Tennyson, and Andrey V. Stolyarov. Duo: A general program for calculating spectra of diatomic molecules. *Comput. Phys. Commun.*, 202:262 – 275, 2016.

[183] J. Tennyson, M. A. Kostin, P. Barletta, G. J. Harris, O. L. Polyansky, J. Ramanlal, and N. F. Zobov. DVR3D: a program suite for the calculation of

rotation-vibration spectra of triatomic molecules. *Comput. Phys. Commun.*, 163:85–116, 2004.

[184] Alexander O. Mitrushchenkov. A new general Renner-Teller (including $\varepsilon \geq 1$) spectroscopic formalism for triatomic molecules. *J. Chem. Phys.*, 136:024108, 2012.

[185] Sergei N. Yurchenko, Walter Thiel, and Per Jensen. Theoretical ROVibrational Energies (TROVE): A robust numerical approach to the calculation of rovibrational energies for polyatomic molecules. *J. Mol. Spectrosc.*, 245:126–140, 2007.

[186] Robert C Hilborn. Einstein coefficients, cross sections, f values, dipole moments, and all that. *arXiv preprint physics/0202029*, 2002.

[187] Peter F Bernath. MoLLIST: Molecular Line Lists, Intensities and Spectra. *J. Quant. Spectrosc. Radiat. Transf.*, 240:106687, 2020.

[188] Tibor Furtenbacher, Attila G. Császár, and Jonathan Tennyson. MARVEL: measured active rotational-vibrational energy levels. *J. Mol. Spectrosc.*, 245:115–125, 2007.

[189] T. Furtenbacher and A. G. Császár. MARVEL: measured active rotational-vibrational energy levels. II. Algorithmic improvements. *J. Quant. Spectrosc. Radiat. Transf.*, 113:929–935, 2012.

[190] T. Furtenbacher and A. G. Császár. The role of intensities in determining characteristics of spectroscopic networks. *J. Molec. Struct.*, 1009:123 – 129, 2012.

[191] Roland Tóbiás, Tibor Furtenbacher, Jonathan Tennyson, and Attila G. Császár. Accurate empirical rovibrational energies and transitions of $H_2{}^{16}O$. *Phys. Chem. Chem. Phys.*, 21:3473–3495, 2019.

[192] A. G. Császár and T. Furtenbacher. Spectroscopic networks. *J. Mol. Spectrosc.*, 266:99 – 103, 2011.

[193] Attila G Császár, Gábor Czakó, Tibor Furtenbacher, and Edit Mátyus. An active database approach to complete rotational–vibrational spectra of small molecules. *Annu. Rep. Comput. Chem.*, 3:155–176, 2007.

[194] Tibor Furtenbacher, Péter Árendás, Georg Mellau, and Attila G Császár. Simple molecules as complex systems. *Sci. Rep.*, 4:4654, 2014.

[195] J. Tennyson, T. Furtenbacher, S. N. Yurchenko, and A. G. Császár. Empirical rovibrational energy levels for nitrous oxide. *J. Quant. Spectrosc. Radiat. Transf.*, 316:108902, 2024.

[196] J Correira, A C Aikin, J M Grebowsky, W D Pesnell, and J P Burrows. Seasonal variations of magnesium atoms in the mesosphere-thermosphere. *Geophys. Res. Lett.*, 35:L06103, 2008.

[197] M. Sarantos, R. M. Killen, W. E. McClintock, E. T. Bradley, R. J. Vervack, Jr., M. Benna, and J. A. Slavin. Limits to Mercury's magnesium exosphere from MESSENGER second flyby observations. *Planet Space Sci.*, 59:1992–2003, 2011.

[198] Karen R. Stockstill-Cahill, Timothy J. McCoy, Larry R. Nittler, Shoshana Z. Weider, and Steven A. Hauck II. Magnesium-rich crustal compositions on Mercury: Implications for magmatism from petrologic modeling. *J. Geophys. Res.-Planets*, 117(E12), 2012.

[199] B. E. Turner and T. C. Steimle. Interstellar MgO. *ApJ*, 299:956, 1985.

[200] S. Sakamoto, G. J. White, K. Kawaguchi, M. Ohishi, K. S. Usuda, and T. Hasegawa. A search for absorption of Mg and Ca compounds in molecular clouds towards Galactic continuum sources. *MNRAS*, 301:872–880, 1998.

[201] Shuning Pan, Tianheng Huang, Allona Vazan, Zhixin Liang, Cong Liu, Junjie Wang, Chris J Pickard, Hui-Tian Wang, Dingyu Xing, and Jian Sun. Magnesium oxide-water compounds at megabar pressure and implications on planetary interiors. *Nat. Comms.*, 14:1165, 2023.

[202] S. Maclean and W. W. Duley. Spectroscopic evidence for interstellar magnesium oxide particles. *ApJ*, 252:L25–L27, 1982.

[203] M. Mogren Al Mogren, Y. Ajili, S. Almania, D. Ben Abdallah, and M. Hochlaf. Collisional excitation of MgO by He. *MNRAS*, 452:1561–1566, 2015.

[204] S. Yoneda and L. Grossman. Condensation of CaO-MgO-Al2O3-SiO2 liquids from cosmic gases. *Geochim. Cosmochim. Acta*, 59:3413–3444, 1995.

[205] T. Nozawa, T. Kozasa, H. Umeda, K. Maeda, and K. Nomoto. Dust in the early universe: Dust formation in the ejecta of population III supernovae. *ApJ*, 598:785–803, 2003.

[206] J. Tennyson and S. N. Yurchenko. Laboratory spectra of hot molecules: data needs for hot super-earth exoplanets. *Mol. Astrophys.*, 8:1–18, 2017.

[207] Laura Schaefer, Katharina Lodders, and Bruce Fegley. Vaporization of the Earth: Application to Exoplanet Atmospheres. *ApJ*, 755:41, 2012.

[208] M. Zilinskas, C. P. A. van Buchem, Y. Miguel, A. Louca, R. Lupu, S. Zieba, and W. van Westrenen. Observability of evaporating lava worlds star. *A&A*, 661:A126, 2022.

[209] Aurélien Falco, Pascal Tremblin, Sébastien Charnoz, Robert J Ridgway, and Pierre-Olivier Lagage. Hydrogenated atmospheres of lava planets: atmospheric structure and emission spectra. *A&A*, 683:A194, 2024.

[210] Yoshiro Azuma, Thomas R. Dyke, Gretchen K. Gerke, and T. C. Steimle. Laser-induced fluorescence and microwave-optical double-resonance study of the $B\,^1\Sigma+ - X\,^1\Sigma+$ system of magnesium monoxide. *J. Mol. Spectrosc.*, 108:137–142, 1984.

[211] T. C. Steimle, Y. Azuma, and P. G. Carrick. Laboratory measurements of the millimeter-wave spectrum of magnesium monoxide. *ApJ*, 277:L21, 1984.

[212] T. Törring and J. Hoeft. The microwave absorption spectrum of MgO. *Chem. Phys. Lett.*, 126:477–480, 1986.

[213] P. C.F. Ip, K. J. Cross, R. W. Field, J. Rostas, B. Bourguignon, and J. McCombie. The $B\,^1\Sigma^+$-$a\,^3\Pi_1$ and $D\,^1\Delta$-$a\,^3\Pi_1$ intercombination systems of the MgO molecule. *J. Mol. Spectrosc.*, 146:409–436, 1991.

[214] S. Civis, H. G. Hedderich, and C. E. Blom. The infrared-spectrum of magnesium-oxide: A diode-laser study using the discharge-enhanced reaction between hot magnesium vapor and N_2O. *Chem. Phys. Lett.*, 176:489–494, 1991.

[215] E. Kagi, T. Hirano, S. Takano, and K. Kawaguchi. Fourier-transform infrared-spectroscopy of the $A^1\Pi$-$X^1\Sigma^+$ system of Mgo. *J. Mol. Spectrosc.*, 168:109–125, 1994.

[216] P. Mürtz, S. Richter, C. Pfelzer, H. Thümmel, and W. Urban. Faraday LMR spectroscopy of the MgO $A^1\Pi$-$X^1\Sigma^+$ (0-2) and $a^3\Pi_{0,1}$-$X^1\Sigma^+$ (0-1) bands. *Mol. Phys.*, 82:989–1007, 1994.

[217] P. Mürtz, H. Thümmel, C. Pfelzer, and W. Urban. New bands of the MgO $A^1\Pi$-$X^1\Sigma^+$ and $a^3\Pi_{0,1}$-$X^1\Sigma^+$ systems by Faraday laser magnetic-resonance spectroscopy. *Mol. Phys.*, 86:513–534, 1995.

[218] Fang-fang Li, Yu-jie Ma, Jia-xing Liu, Dong Yan, Ang Xu, and Feng-yan Wang. Imaging photodissociation dynamics of MgO at 193 nm. *Chin. J. Chem. Phys.*, 35:257–262, 2022.

[219] Tianrui Bai, Zhi Qin, and Linhua Liu. Radiative association for the formation of MgO. *MNRAS*, 500:2496–2502, 2021.

[220] Tianrui Bai, Zhi Qin, and Linhua Liu. Spin-forbidden electronic transition properties of MgO. *J. Quant. Spectrosc. Radiat. Transf.*, 251:UNSP 107086, 2020.

[221] Charles W. Bauschlicher. The convergence of the coupled cluster approach for MgO. *Chem. Phys. Lett.*, 711:27–31, 2018.

[222] Charles W. Bauschlicher and David W. Schwenke. The low-lying electronic states of MgO. *Chem. Phys. Lett.*, 683:62–67, 2017.

[223] S. Stojadinović, M. Perić, J. Radić-Perić, R. Vasilić, M. Petković, and Lj Zeković. Luminescence of the B1Σ+–X1Σ+ band system of MgO during plasma electrolytic oxidation of magnesium alloy. *Surface Coatings Tech.*, 206:2905–2913, 2012.

[224] A. Maatouk, A. Ben Houria, O. Yazidi, N. Jaidane, and M. Hochlaf. Electronic states of MgO: Spectroscopy, predissociation, and cold atomic Mg and O production. *J. Chem. Phys.*, 133:144302, 2010.

[225] V V Sobolev. Exciton spectra of MgO. *Inorganic Materials*, 40:1169–1172, 2004.

[226] D. Bellert, K. L. Burns, N. T. Van-Oanh, J. J. Wang, and W. H. Breckenridge. Spectroscopic characterization of the $F\,^1\Pi_1$ 'Rydberg' state of the MgO molecule. *Chem. Phys. Lett.*, 381:725–728, 2003.

[227] J. W. Daily, C. S. Dreyer, A. Abbud-Madrid, and M. C. Branch. Transition probabilities in the $B\,^1\Sigma^+$-$X\,^1\Sigma^+$ and the $B\,^1\Sigma^+$-$A\,^1\Pi$ electronic systems of MgO. *J. Mol. Spectrosc.*, 214:111–116, 2002.

[228] C. B. Dreyer, J. W. Daily, A. Abbud-Madrid, and M. C. Branch. Laser-induced fluorescence excitation spectroscopy of the magnesium oxide $B\,^1\Sigma^+$-$A\,^1\Pi$ system. *Appl. Optics*, 40:2561–2570, 2001.

[229] J. H. Kim, X. Li, L. S. Wang, H. L. de Clercq, C. A. Fancher, O. C. Thomas, and K. H. Bowen. Vibrationally resolved photoelectron spectroscopy of MgO^- and ZnO^- and the low-lying electronic states of MgO, MgO^-, and ZnO. *J. Phys. Chem. A*, 105:5709–5718, 2001.

[230] X Gerbaux, A Hadni, M Tazawa, and J C Villegier. FAR-INFRARED SPECTRA OF MAGNESIUM-OXIDE. *Appl. Optics*, 33:57–59, 1994.

[231] B. Bourguignon and J. Rostas. The $D^3\Delta_i$-$A^3\Pi_i$ and $D^3\Delta_2$-$A^1\Pi$ systems of the Mgo molecule. *J. Mol. Spectrosc.*, 146:437–454, 1991.

[232] M Matsui. Molecular-Dynamics Study of the Structural and Thermodynamic Properties of MgO Crystal with Quantum Correction. *J. Chem. Phys.*, 91:489–494, 1989.

[233] David R. Yarkony. Spin-forbidden radiative decay involving quasidegenerate states. Application to the $B\,^1\Sigma^+ \rightarrow a\,^3\Pi$ transition in MgO. *J. Chem. Phys.*, 89:7324–7333, 1988.

[234] C. W. Bauschlicher, D. M. Silver, and D. R. Yarkony. An SCF and MCSCF description of the low-lying states of MgO. *J. Chem. Phys.*, 73:2867–2870, 1980.

[235] Louise Pasternack, A. P. Baronavski, and J. R. McDonald. Application of saturation spectroscopy for measurement of atomic Na and MgO in acetylene flames. *J. Chem. Phys.*, 69:4830–4837, 1978.

[236] Tatsuya Ikeda, Ning Bew Wong, David O. Harris, and Robert W. Field. Argon ion and dye laser induced MgO B1Σ+-X1Σ+ and B1Σ+-A1Π photoluminescence spectra. *J. Mol. Spectrosc.*, 68:452–487, 1977.

[237] A. Antic-Jovanovic, V. Bojovic, and D. S. Pesic. A new electronic band system of MgO in the ultraviolet region. *J. Phys.B-At. Mol. Phys.*, 9:L575–L577, 1976.

[238] J. Schamps and G. Gandara. A 3Δ-3Π transition in the near-ultraviolet spectrum of MgO. *J. Mol. Spectrosc.*, 62:80–84, 1976.

[239] M Singh. G1 Π - X1 Σ and G1 Π - A1 Π Transitions of MgO. *J. Phys.B-At. Mol. Phys.*, 6:1917–&, 1973.

[240] M Singh. A new electronic transition F1Π - X1Σ of MgO. *J. Phys.B-At. Mol. Phys.*, 6:1339–1343, 1973.

[241] N B Manson, W Vonderoh, and S L Chodos. SECOND-ORDER RAMAN SPECTRUM OF MGO. *Phys. Rev. B*, 3:1968–&, 1971.

[242] M Singh. New electronic state of MgO. *J. Phys.B-At. Mol. Phys.*, 4:565–&, 1971.

[243] Sandor Trajmar and George E. Ewing. The Near-Ultraviolet Bands of MgO: Analysis of the D1Δ - A1Π and C1Σ - A1Π Systems. *ApJ*, 142:77, 1965.

[244] R w Nicholls. Franck-Condon factors to high vibrational quantum numbers .2. SiO, MgO, SrO, AlO, VO, NO. *Journal of Research of the National Bureau of Standards Section A-Physics and Chemistry*, 66:227+, 1962.

[245] Leo Brewer, S. Trajmar, and R. A. Berg. Analysis of the Ulitraviolet System of Magnesium Oxide. *ApJ*, 135:955, 1962.

[246] A. Lagerqvist and U. Uhler. Red bands of MgO. *Nature*, 164:665–666, 1949.

[247] P. C. Mahanti. The band spectra of MgO, CaO and SrO. *Phys. Rev.*, 42:609–621, 1932.

[248] P N Ghosh, P C Mahanti, and B C Mukkerjee. The vibrational quantum analysis of the blue-green bands of magnesium oxide. *Phys. Rev.*, 35:1491–1494, 1930.

[249] C. A. Bowesman, Meiyin Shuai, Sergei N. Yurchenko, and Jonathan Tennyson. A high resolution line list for AlO. *MNRAS*, 508:3181–3193, 2021.

[250] Andy Wong, S. N. Yurchenko, Peter Bernath, Holger S. P. Mueller, Stephanie McConkey, and J. Tennyson. ExoMol Line List XXI: Nitric Oxide (NO). *MNRAS*, 470:882–897, 2017.

[251] Ya. V. Pavlenko, S. N. Yurchenko, L. K. McKemmish, and Jonathan Tennyson. Analysis of the TiO isotopologues in stellar optical spectra. *A&A*, 42:A77, 2020.

[252] T. Furtenbacher, R. Tóbiás, J. Tennyson, O. L. Polyansky, A. A. Kyuberis, R. I. Ovsyannikov, N. F. Zobov, and A. G. Császár. W2020: A Database of Validated Rovibrational Experimental Transitions and Empirical Energy Levels Part II. $H_2{}^{17}O$ and $H_2{}^{18}O$ with an Update to $H_2{}^{16}O$. *J. Phys. Chem. Ref. Data*, 49:043103, 2020.

[253] L. K. McKemmish, A. M. Syme, J. Borsovszky, S. N. Yurchenko, J Tennyson, T. Furtenbacher, and A. G. Császár. An update to the MARVEL data set and ExoMol line list for $^{12}C_2$. *MNRAS*, 497:1081–1097, 2020.

[254] Anna-Maree Syme and Laura K. McKemmish. Full spectroscopic model and trihybrid experimental-perturbative-variational line list for CN. *MNRAS*, 505:4383–4395, 2021.

[255] Armando N. Perri, Fadia Taher, and Laura K. McKemmish. Full spectroscopic model and trihybrid experimental-perturbative-variational line list for ZrO. *MNRAS*, 524:4631–4641, 2023.

[256] Sergei N Yurchenko, Charles A Bowesman, Ryan P Brady, Elizabeth R Guest, Kyraki Kefala, Georgi B Mitev, Alec Owens, Armando N Perri, Marco Pezzella, Oleksiy Smola, Andrei Sokolov, Jingxin Zhang, and Jonathan Tennyson. ExoMol line lists –LX. Molecular line list for the ammonia isotopologue $^{15}NH_3$. *MNRAS*, 533:3442–3456, 2024.

[257] B. A. Voronin, J. Tennyson, T. Yu. Chesnokova, A. V. Chentsov, and A. D. Bykov. The infrared absorption spectrum of the $H_2{}^{14}O$ radioactive isotopologue of water. *Mol. Phys.*, 122:e2333474, 2024.

[258] Boris A. Voronin, Jonathan Tennyson, Sergey N. Yurchenko, Tatyana Yu. Chesnokova, Aleksei V. Chentsov, Aleksandr D. Bykov, Maria V. Makarova,

Svetlana S. Voronina, and Flávio C. Cruz. The infrared absorption spectrum of radioactive water isotopologue $H_2{}^{15}O$. *Spectroc. Acta Pt. A-Molec. Biomolec. Spectr.*, 311:124007, 2024.

[259] B. A. Voronin, J. Tennyson, S. N. Yurchenko, T. Yu. Chesnokova, A. V. Chentsov, A. D. Bykov, and F. C. Cruz. The spectrum of radioactive water vapor: the $H_2{}^{19}O$ radio-isotopologue. *J. Radioanal. Nucl. Chem.*, 333:4945–4954, 2024.

[260] L. N. Sinitsa, N. F. Zobov, M. A. Rogov, J. Tennyson, and O.L. Polyansky. Study of $HD^{17}O$ spectrum. Theory and experiment. *J. Mol. Spectrosc.*, 407:111965, 2025.

[261] S. Wyckoff and P. Wehinger. Titanium isotopes in Omicron Ceti. *ApJ*, 178:481, 1972.

[262] D. L. Lambert and R. E. Luck. Isotopes of titanium in Aldebaran. *ApJ*, 211:443–452, 1977.

[263] R. E. S. Clegg, D. L. Lambert, and R. A. Bell. Isotopes of titanium in cool stars. *ApJ*, 234:188–199, 1979.

[264] F. Allard, P. H. Hauschildt, and D. Schwenke. TiO and H_2O absorption lines in cool stellar atmospheres. *ApJ*, 540:1005–1015, 2000.

[265] Aomawa L. Shields, Sarah Ballard, and John Asher Johnson. The habitability of planets orbiting M-dwarf stars. *Phys. Rep.*, 663:1–38, 2016.

[266] R. Alvarez and M. O. Mennessier. Determination of Miras temperatures from TiO and VO bands. Estimates of distances. *A&A*, 317:761–768, 1997.

[267] P. A. Couch, T. L. Evans, and P. J. Sarre. The cool circumstellar environment of IRAS 08182-6000: radiative transfer modelling of TiO absorption bands. *MNRAS*, 346:153–162, 2003.

[268] R. Jurdana-Sepic and D. Kotnik-Karuza. Atmospheric thermal structure of a sample of M type giants. II. *Astrophys. Space Sci.*, 289:15–21, 2004.

[269] B. Davies, R.-P. Kudritzki, B. Plez, S. Trager, A. Lancon, Z. Gazak, M. Bergemann, C. Evans, and A. Chiavassa. The temperatures of red supergiants. *ApJ*, 767:3, 2013.

[270] F. Allard, P. H. Hauschildt, and A. Schweitzer. Spherically symmetric model atmospheres for low-mass pre-main-sequence stars with effective temperatures between 2000 and 6800 K. *ApJ*, 539:366–371, 2000.

[271] L. A. Hillenbrand, G. R. Knapp, D. L. Padgett, L. M. Rebull, and P. M. McGehee. Optical TiO and VO band emission in two embedded protostars: IRAS 04369+2539 and IRAS 05451+0037. *AJ.*, 143:37, 2012.

[272] Mayank Narang, P Manoj, Himanshu Tyagi, Prasanta K Nayak, Saurabh Sharma, Arun Surya, Bihan Banerjee, Blesson Mathew, Arpan Ghosh, and Aayushi Verma. Optical spectroscopy of Gaia detected protostars with DOT: Can we probe protostellar photospheres? *A&A*, 44:92, 2023.

[273] Qinglin Ouyang, Wei Wang, Meng Zhai, Guo Chen, Patricio Rojo, Yujuan Liu, Fei Zhao, Jia-Sheng Huang, and Gang Zhao. Tentative detection of titanium oxide in the atmosphere of WASP-69 b with a 4m ground-based telescope. *MNRAS*, 521:5860–5879, 2023.

[274] Stevanus K. Nugroho, Hajime Kawahara, Kento Masuda, Teruyuki Hirano, Takayuki Kotani, and Akito Tajitsu. High-resolution Spectroscopic Detection of TiO and a Stratosphere in the Day-side of WASP-33b. *ApJ*, 154:221, 2017.

[275] Korey Haynes, Avi M. Mandell, Nikku Madhusudhan, Drake Deming, and Heather Knutson. Spectroscopic Evidence for a Temperature Inversion in the Dayside Atmosphere of Hot Jupiter WASP-33b. *ApJ*, 806:146, 2015.

[276] Dilovan B. Serindag, Stevanus K. Nugroho, Paul Molliere, Ernst J. W. de Mooij, Neale P. Gibson, and Ignas A. G. Snellen. Is TiO emission present

in the ultra-hot Jupiter WASP-33b? A reassessment using the improved ExoMol TOTO line list. *A&A*, 645:A90, 2021.

[277] C. Jiang, G. Chen, F. Murgas, E. Pallé, H. Parviainen, and Y. Ma. Confirmation of TiO absorption and tentative detection of MgH and CrH in the atmosphere of HAT-P-41b. *A&A*, 2023.

[278] Kyle B. Sheppard, Luis Welbanks, Avi M. Mandell, Nikku Madhusudhan, Nikolay Nikolov, Drake Deming, Gregory W. Henry, Michael H. Williamson, David K. Sing, Mercedes López-Morales, Jegug Ih, Jorge Sanz-Forcada, Panayotis Lavvas, Gilda E. Ballester, Thomas M. Evans, Antonio García Muñoz, and Leonardo A. dos Santos. The Hubble PanCET Program: A Metal-rich Atmosphere for the Inflated Hot Jupiter HAT-P-41b. *ApJ*, 161:51, 2021.

[279] E Palle, G Chen, J Prieto-Arranz, G Nowak, F Murgas, L Nortmann, D Pollacco, K Lam, P Montanes-Rodriguez, H Parviainen, et al. Feature-rich transmission spectrum for WASP-127b-Cloud-free skies for the puffiest known super-Neptune? *A&A*, 602:L15, 2017.

[280] J.-M. Desert, A. Vidal-Madjar, A. L. des Etangs, D. Sing, D. Ehrenreich, G. Hebrard, and R. Ferlet. TiO and VO broad band absorption features in the optical spectrum of the atmosphere of the hot-Jupiter HD 209458b. *A&A*, 492:585–592, 2008.

[281] Vanesa Ramírez, Alexander J Cridland, and Paul Mollière. Tracing bulk elemental ratios in exoplanetary atmospheres with TiO chemistry. *A&A*, 641:A87, 2020.

[282] Kevin B. Stevenson, Jacob L. Bean, Andreas Seifahrt, Jean-Michel Desert, Nikku Madhusudhan, Marcel Bergmann, Laura Kreidberg, and Derek Homeier. Transmission Spectroscopy of the Hot Jupiter WASP-12b from 0.7 TO 5 μm. *ApJ*, 147:161, 2014.

[283] Michael D Himes and Joseph Harrington. On the dayside atmosphere of WASP-12b. *ApJ*, 931:86, 2022.

[284] Akinsanmi, B., Barros, S. C. C., Lendl, M., Carone, L., Cubillos, P. E., Bekkelien, A., Fortier, A., Florén, H.-G., Collier Cameron, A., Boué, G., Bruno, G., Demory, B.-O., Brandeker, A., Sousa, S. G., Wilson, T. G., Deline, A., Bonfanti, A., Scandariato, G., Hooton, M. J., Correia, A. C. M., Demangeon, O. D. S., Smith, A. M. S., Singh, V., Alibert, Y., Alonso, R., Asquier, J., Bárczy, T., Barrado Navascues, D., Baumjohann, W., Beck, M., Beck, T., Benz, W., Billot, N., Bonfils, X., Borsato, L., Broeg, C., Buder, M., Charnoz, S., Csizmadia, Sz., Davies, M. B., Deleuil, M., Delrez, L., Ehrenreich, D., Erikson, A., Farinato, J., Fossati, L., Fridlund, M., Gandolfi, D., Gillon, M., Güdel, M., Günther, M. N., Heitzmann, A., Helling, Ch., Hoyer, S., Isaak, K. G., Kiss, L. L., Lam, K. W. F., Laskar, J., Lecavelier des Etangs, A., Magrin, D., Maxted, P. F. L., Mecina, M., Mordasini, C., Nascimbeni, V., Olofsson, G., Ottensamer, R., Pagano, I., Pallé, E., Peter, G., Piazza, D., Piotto, G., Pollacco, D., Queloz, D., Ragazzoni, R., Rando, N., Rauer, H., Ribas, I., Santos, N. C., Ségransan, D., Simon, A. E., Stalport, M., Szabó, Gy. M., Thomas, N., Udry, S., Van Grootel, V., Venturini, J., Villaver, E., and Walton, N. A. The tidal deformation and atmosphere of WASP-12 b from its phase curve. *A&A*, 685:A63, 2024.

[285] Elyar Sedaghati, Henri M. J. Boffin, Ryan J. MacDonald, Siddharth Gandhi, Nikku Madhusudhan, Neale P. Gibson, Mahmoudreza Oshagh, Antonio Claret, and Heike Rauer. Detection of titanium oxide in the atmosphere of a hot Jupiter. *Nature*, 549:238–241, 2017.

[286] C. M. Huitson, D. K. Sing, F. Pont, J. J. Fortney, A. S. Burrows, P. A. Wilson, G. E. Ballester, N. Nikolov, N. P. Gibson, D. Deming, S. Aigrain, T. M. Evans, G. W. Henry, A. Lecavelier des Etangs, A. P. Showman, A. Vidal-Madjar, and K. Zahnle. An HST optical-to-near-IR transmission spectrum of

the hot Jupiter WASP-19b: detection of atmospheric water and likely absence of TiO. *MNRAS*, 434:3252–3274, 2013.

[287] Néstor Espinoza, Benjamin V Rackham, Andrés Jordán, Dániel Apai, Mercedes López-Morales, David J Osip, Simon L Grimm, Jens Hoeijmakers, Paul A Wilson, Alex Bixel, Chima McGruder, Florian Rodler, Ian Weaver, Nikole K Lewis, Jonathan J Fortney, and Jonathan Fraine. ACCESS: a featureless optical transmission spectrum for WASP-19b from Magellan/IMACS. *MNRAS*, 482:2065–2087, 2018.

[288] Bibiana Prinoth, H. Jens Hoeijmakers, Daniel Kitzmann, Elin Sandvik, Julia Seidel, V, Monika Lendl, Nicholas W. Borsato, Brian Thorsbro, David R. Anderson, David Barrado, Kateryna Kravchenko, Romain Allart, Vincent Bourrier, Heather M. Cegla, David Ehrenreich, Chloe Fisher, Christophe Lovis, Andrea Guzman-Mesa, Simon Grimm, Matthew Hooton, Brett M. Morris, Maria Oreshenko, Lorenzo Pino, and Kevin Heng. Titanium oxide and chemical inhomogeneity in the atmosphere of the exoplanet WASP-189 b. *Nature Astr.*, 6:449–457, 2022.

[289] B. Prinoth, H. J. Hoeijmakers, S. Pelletier, D. Kitzmann, B. M. Morris, A. Seifahrt, D. Kasper, H. H. Korhonen, M. Burheim, J. L. Bean, B. Benneke, N. W. Borsato, M. Brady, S. L. Grimm, R. Luque, J. Stuermer, and B. Thorsbro. Time-resolved transmission spectroscopy of the ultra-hot Jupiter WASP-189 b. *A&A*, 678, 2023.

[290] Thomas M. Evans, David K. Sing, Hannah R. Wakeford, Nikolay Nikolov, Gilda E. Ballester, Benjamin Drummond, Tiffany Kataria, Neale P. Gibson, David S. Amundsen, and Jessica Spake. Detection of H_2O and evidence for TiO/VO in an ultra-hot exoplanet atmosphere. *ApJ*, 822:L4, 2016.

[291] Stephanie R. Merritt, Neale P. Gibson, Stevanus K. Nugroho, Ernst J. W. de Mooij, Matthew J. Hooton, Shannon M. Matthews, Laura K. McKemmish, Thomas Mikal-Evans, Nikolay Nikolov, David K. Sing, Jessica J.

Spake, and Chris A. Watson. Non-detection of TiO and VO in the atmosphere of WASP-121b using high-resolution spectroscopy, 2020.

[292] Thomas M Evans, David K Sing, Jayesh M Goyal, Nikolay Nikolov, Mark S Marley, Kevin Zahnle, Gregory W Henry, Joanna K Barstow, Munazza K Alam, Jorge Sanz-Forcada, et al. An optical transmission spectrum for the ultra-hot Jupiter WASP-121b measured with the Hubble Space Telescope. *AJ.*, 156:283, 2018.

[293] Hoeijmakers, H. J., Kitzmann, D., Morris, B. M., Prinoth, B., Borsato, N. W., Thorsbro, B., Pino, L., Lee, E. K. H., Akın, C., Seidel, J. V., Birkby, J. L., Allart, R., and Heng, Kevin. The Mantis Network - IV. A titanium cold trap on the ultra-hot Jupiter WASP-121 b. *A&A*, 685:A139, 2024.

[294] Gibson, Neale P and Nugroho, Stevanus K and Lothringer, Joshua and Maguire, Cathal and Sing, David K. Relative abundance constraints from high-resolution optical transmission spectroscopy of WASP-121b, and a fast model-filtering technique for accelerating retrievals. *MNRAS*, 512:4618–4638, 2022.

[295] Hoeijmakers, H. J., Seidel, J. V., Pino, L., Kitzmann, D., Sindel, J. P., Ehrenreich, D., Oza, A. V., Bourrier, V., Allart, R., Gebek, A., Lovis, C., Yurchenko, S. N., Astudillo-Defru, N., Bayliss, D., Cegla, H., Lavie, B., Lendl, M., Melo, C., Murgas, F., Nascimbeni, V., Pepe, F., Ségransan, D., Udry, S., Wyttenbach, A., and Heng, K. Hot Exoplanet Atmospheres Resolved with Transit Spectroscopy (HEARTS) - IV. A spectral inventory of atoms and molecules in the high-resolution transmission spectrum of WASP-121 b. *A&A*, 641:A123, 2020.

[296] Cathal Maguire, Neale P Gibson, Stevanus K Nugroho, Swaetha Ramkumar, Mark Fortune, Stephanie R Merritt, and Ernst de Mooij. High-resolution atmospheric retrievals of WASP-121b transmission spectroscopy

with ESPRESSO: Consistent relative abundance constraints across multiple epochs and instruments. *MNRAS*, 519:1030–1048, 2022.

[297] Joshua D. Lothringer, Zafar Rustamkulov, David K. Sing, Neale P. Gibson, Jamie Wilson, and Kevin C. Schlaufman. A New Window into Planet Formation and Migration: Refractory-to-Volatile Elemental Ratios in Ultra-hot Jupiters. *ApJ*, 914:12, 2021.

[298] Ivan Hubeny, Adam Burrows, and David Sudarsky. A possible bifurcation in atmospheres of strongly irradiated stars and planets. *ApJ*, 594:1011, 2003.

[299] J. J. Fortney, K. Lodders, M. S. Marley, and R. S. Freedman. A unified theory for the atmospheres of the hot and very hot Jupiters: Two classes of irradiated atmospheres. *ApJ*, 678:1419–1435, 2008.

[300] L Jeremy Richardson, Drake Deming, Karen Horning, Sara Seager, and Joseph Harrington. A spectrum of an extrasolar planet. *Nature*, 445:892–895, 2007.

[301] Joseph Harrington, Statia Luszcz, Sara Seager, Drake Deming, and L Jeremy Richardson. The hottest planet. *Nature*, 447:691–693, 2007.

[302] Anjali A. A. Piette, Nikku Madhusudhan, Laura K. McKemmish, Siddharth Gandhi, Thomas Masseron, and Luis Welbanks. Assessing spectra and thermal inversions due to TiO in hot Jupiter atmospheres. *MNRAS*, 496:3870–3886, 2020.

[303] Alexander Roth, Vivien Parmentier, and Mark Hammond. Hot Jupiter diversity and the onset of TiO/VO revealed by a large grid of non-grey global circulation models. *MNRAS*, 531:1056–1083, 2024.

[304] J. G. Collins and T. D. Fay. Radiative opacities for Alpha-systems, Gamma-systems and PHi-systems of titanium monoxide. *J. Quant. Spectrosc. Radiat. Transf.*, 14:1259–1272, 1974.

[305] J. G. Collins. Band-head analysis of Gamma' system of TiO. *J. Phys. B-At. Mol. Opt. Phys.*, 8:304–307, 1975.

[306] B Plez. Spherical opacity sampling model atmospheres for m-giants and supergiants. ii-a grid. *ApJS*, 94:527–552, 1992.

[307] U. G. Jorgensen. Effects of TiO in stellar atmospheres. *A&A*, 284:179–186, 1994.

[308] D. W. Schwenke. Opacity of TiO from a coupled electronic state calculation parametrized by ab initio and experimental data. *Faraday Discuss.*, 109:321–334, 1998.

[309] B. Plez. A new TiO line list. *A&A*, 337:495–500, 1998.

[310] L. K. McKemmish, T. Masseron, S. Sheppard, E. Sandeman, Z. Schofield, T. Furtenbacher, A. G. Császár, J. Tennyson, and C. Sousa-Silva. MARVEL analysis of the measured high-resolution spectra of ^{48}Ti^{16}O. *ApJS*, 228:15, 2017.

[311] Peter Bernath and W. Doug Cameron. Near-infrared Opacity of Late M Dwarfs and Hot Jupiters: The E-3 pi-X-3 Delta Transition of TiO. *ApJ*, 904:24, 2020.

[312] W. Doug Cameron and Peter Bernath. Visible Opacity of M Dwarfs and Hot Jupiters: The TiO $B^3\Pi$-$X^3\Delta$ Band System. *ApJ*, 926:39, 2022.

[313] Alexander A Breier, Björn Waßmuth, Guido W Fuchs, Jürgen Gauss, and Thomas F Giesen. Mass-independent analysis of the stable isotopologues of gas-phase titanium monoxide - TiO. *J. Mol. Spectrosc.*, 355:46–58, 2019.

[314] Daniel Witsch, Alexander A. Breier, Eileen Döring, Koichi M. T. Yamada, Thomas F. Giesen, and Guido W. Fuchs. The rotationally resolved infrared spectrum of TiO and its isotopologues. *J. Mol. Spectrosc.*, 377:111439, 2021.

[315] J. G. Phillips. Molecular-constants of TiO molecule. *ApJS*, 26:313–331, 1973.

[316] K. Kobayashi, G. E. Hall, J. T. Muckerman, T. J. Sears, and A. J. Merer. The E (3)Pi-X (3)Delta transition of jet-cooled TiO observed in absorption. *J. Mol. Spectrosc.*, 212:133–141, 2002.

[317] B. Simard and P. A. Hackett. Spectroscopy and photophysics of refractory molecules at low-temperature: Rotational analysis of the E3-PI-X3-DELTA (0,0) band of titanium monoxide. *J. Mol. Spectrosc.*, 148:128–135, 1991.

[318] Ken Anderson, Paul Sallis, and Sinan Uyanik. 24 - Anaerobic treatment processes. In Duncan Mara and Nigel Horan, editors, *Handbook of Water and Wastewater Microbiology*, pages 391–426. Academic Press, London, 2003.

[319] Mark Maslin, Matthew Owen, Richard Betts, Simon Day, Tom Dunkley Jones, and Andrew Ridgwell. Gas hydrates: past and future geohazard? *Philos. Trans. R. Soc. A.*, 368:2369–2393, 2010.

[320] Fiona M O'Connor, O Boucher, N Gedney, CD Jones, GA Folberth, R Coppell, P Friedlingstein, WJ Collins, J Chappellaz, J Ridley, et al. Possible role of wetlands, permafrost, and methane hydrates in the methane cycle under future climate change: A review. *Rev. Geophys.*, 48, 2010.

[321] Edward J Dlugokencky, L Paul Steele, Patricia M Lang, and Kenneth A Masarie. The growth rate and distribution of atmospheric methane. *JGR-Atm*, 99:17021–17043, 1994.

[322] Martin Heimann. Enigma of the recent methane budget. *Nature*, 476:157–158, 2011.

[323] Benjamin Thomas, Gregory David, Christophe Anselmo, Elodie Coillet, Katja Rieth, Alain Miffre, Jean-Pierre Cariou, and Patrick Rairoux. Remote sensing of methane with broadband laser and optical correlation spectroscopy on the Q-branch of the $2\nu_3$ band. *J. Mol. Spectrosc.*, 291:3–8, 2013.

[324] Sara E. Mikaloff Fletcher and Hinrich Schaefer. Rising methane: A new climate challenge. *Science*, 364(6444):932–933, 2019.

[325] R B Jackson, M Saunois, A Martinez, J G Canadell, X Yu, M Li, B Poulter, P A Raymond, P Regnier, P Ciais, S J Davis, and P K Patra. Human activities now fuel two-thirds of global methane emissions. *Environ. Res. Lett.*, 19:101002, 2024.

[326] Marielle Saunois, Robert B Jackson, Philippe Bousquet, Ben Poulter, and JG Canadell. The growing role of methane in anthropogenic climate change. *Environ. Res. Lett.*, 11:120207, 2016.

[327] Tingzhen Ming, Wei Li, Qingchun Yuan, Philip Davies, Renaud de Richter, Chong Peng, Qihong Deng, Yanping Yuan, Sylvain Caillol, and Nan Zhou. Perspectives on removal of atmospheric methane. *Advances in Applied Energy*, 5:100085, 2022.

[328] X. Lan, K.W. Thoning, and E.J. Dlugokencky. Trends in globally-averaged CH4, N2O, and SF6 determined from NOAA Global Monitoring Laboratory measurements, 2025.

[329] F. Dentener, D. Stevenson, J. Cofala, R. Mechler, M. Amann, P. Bergamaschi, F. Raes, and R. Derwent. The impact of air pollutant and methane emission controls on tropospheric ozone and radiative forcing: CTM calculations for the period 1990-2030. *Atmos. Chem. Phys.*, 5:1731–1755, 2005.

[330] John Houghton. Global warming. *Rep. Prog. Phys.*, 68:1343, 2005.

[331] George C. Rhoderick and William D. Dorko. Standards Development of Global Warming Gas Species: Methane, Nitrous Oxide, Trichlorofluoromethane, and Dichlorodifluoromethane. *Environ. Sci. Technol.*, 38:2685–2692, 2004.

[332] EM Bridges and NH Batjes. Soil gaseous emissions and global climatic change. *Geography*, 81:155–169, 1996.

[333] Andre Van Amstel. Methane. a review. *Journal of Integrative Environmental Sciences*, 9:5–30, 2012.

[334] Zosia Staniaszek, Paul T Griffiths, Gerd A Folberth, Fiona M O'Connor, N Luke Abraham, and Alexander T Archibald. The role of future anthropogenic methane emissions in air quality and climate. *npj Climate and Atmospheric Science*, 5:21, 2022.

[335] Daniel J Jacob, Alexander J Turner, Joannes D Maasakkers, Jianxiong Sheng, Kang Sun, Xiong Liu, Kelly Chance, Ilse Aben, Jason McKeever, and Christian Frankenberg. Satellite observations of atmospheric methane and their value for quantifying methane emissions. *Atmos. Chem. Phys.*, 16:14371–14396, 2016.

[336] Mirosław Kwaśny and Aneta Bombalska. Optical methods of methane detection. *J. Sens.*, 23:2834, 2023.

[337] A. K. Petersen, T. Warneke, C. Frankenberg, P. Bergamaschi, C. Gerbig, J. Notholt, M. Buchwitz, O. Schneising, and O. Schrems. First ground-based FTIR observations of methane in the inner tropics over several years. *Atmos. Chem. Phys.*, 10:7231–7239, 2010.

[338] Yihao Wang, Leizi Jiao, Chunjiang Zhao, Wentao Dong, Wenwen Gong, and Daming Dong. The impact of biodegradable plastics on methane and carbon dioxide emissions in soil ecosystems: a Fourier transform infrared spectroscopy approach. *Sci. Rep.*, 15:7678, 2025.

[339] Nathalie Picqué and Theodor W Hänsch. Frequency comb spectroscopy. *Nature Photonics*, 13:146–157, 2019.

[340] Lavista Tyagi, Rajni Devi, Shrestha Tyagi, Vinay Kumar, Kavita Sharma, Yogendra K. Gautam, Anuj Kumar, Saurabh Kapoor, Aman Bhardwaj, and Ashwani Kumar and. Environmental impacts and recent advancements in the sensing of methane: a review. *Environ. Technol. Rev.*, 14:191–212, 2025.

[341] JP Dakin, MJ Gunning, P Chambers, and ZJ Xin. Detection of gases by correlation spectroscopy. *Sens. Actuators B-Chem.*, 90:124–131, 2003.

[342] G Ehret, C Kiemle, M Wirth, A Amediek, A Fix, and S Houweling. Space-borne remote sensing of CO_2, CH_4, and N_2O by integrated path differential absorption lidar: a sensitivity analysis. *Appl. Phys. B.*, 90:593–608, 2008.

[343] Andrés Guzmán-Marmolejo and Antígona Segura. Methane in the Solar System. *Boletín de la Sociedad Geológica Mexicana*, 67:377–385, 2015.

[344] F W Taylor, S K Atreya, Th Encrenaz, D M Hunten, P G J Irwin, and T C Owen. The composition of the atmosphere of Jupiter. *Jupiter: The planet, satellites and magnetosphere*, pages 59–78, 2004.

[345] L. N. Fletcher, G. S. Orton, N. A. Teanby, P. G. J. Irwin, and G. L. Bjoraker. Methane and its isotopologues on Saturn from Cassini/CIRS observations. *Icarus*, 199:351–367, 2009.

[346] V. G. Teifel. Methane abundance in the atmosphere of Uranus. *Icarus*, 53:389–398, 1983.

[347] Kevin H. Baines, Michael E. Mickelson, Lee E. Larson, and David W. Ferguson. The Abundances of Methane and Ortho/Para Hydrogen on Uranus and Neptune: Implications of New Laboratory 4-0 H_2 Quadrupole Line Parameters. *Icarus*, 114:328–340, 1995.

[348] V. I. Oyama, G. C. Carle, F. Woeller, J. B. Pollack, R. T. Reynolds, and R. A. Craig. Pioneer Venus gas chromatography of the lower atmosphere of Venus. *J. Geophys. Res.-Space*, 85:7891–7902, 1980.

[349] H B Niemann, S K Atreya, S J Bauer, G R Carignan, J E Demick, R L Frost, D Gautier, J A Haberman, D N Harpold, Donald M Hunten, et al. The abundances of constituents of Titan's atmosphere from the GCMS instrument on the Huygens probe. *Nature*, 438:779–784, 2005.

[350] J. Hunter Waite, Hasso Niemann, Roger V. Yelle, Wayne T. Kasprzak, Thomas E. Cravens, Janet G. Luhmann, Ralph L. McNutt, Wing-Huen Ip, David Gell, Virginie De La Haye, Ingo Müller-Wordag, Brian Magee, Nathan Borggren, Steve Ledvina, Greg Fletcher, Erin Walter, Ryan Miller, Stefan Scherer, Rob Thorpe, Jing Xu, Bruce Block, and Ken Arnett. Ion Neutral Mass Spectrometer Results from the First Flyby of Titan. *Science*, 308:982–986, 2005.

[351] Vincent Boudon, Jean-Paul Champion, Tony Gabard, Michel Loëte, Athéna Coustenis, Catherine De Bergh, Bruno Bézard, Emmanuel Lellouch, Pierre Drossart, Mathieu Hirtzig, et al. Methane in Titan's atmosphere: from fundamental spectroscopy to planetology. *Europhysics News*, 40:17–20, 2009.

[352] Emmanuel Lellouch, Catherine de Bergh, Bruno Sicardy, S Ferron, and H-U Käufl. Detection of CO in Triton's atmosphere and the nature of surface-atmosphere interactions. *A&A*, 512:L8, 2010.

[353] W. M. Grundy and L A. Young. Near-infrared spectral monitoring of Triton with IRTF/SpeX I: establishing a baseline for rotational variability. *Icarus*, 172:455–465, 2004.

[354] Dale P. Cruikshank and Jerome Apt. Methane on Triton: Physical state and distribution. *Icarus*, 58:306–311, 1984.

[355] F. Merlin, E. Lellouch, E. Quirico, and B. Schmitt. Triton's surface ices: Distribution, temperature and mixing state from VLT/SINFONI observations. *Icarus*, 314:274–293, 2018.

[356] Vladimir A. Krasnopolsky, Jean Pierre Maillard, and Tobias C. Owen. Detection of methane in the martian atmosphere: evidence for life? *Icarus*, 172:537–547, 2004.

[357] Christopher R. Webster. Measuring methane and its isotopes $^{12}CH_4$, $^{13}CH_4$, and CH_3D on the surface of Mars with in situ laser spectroscopy. *Appl. Optics*, 44:1226–1235, 2005.

[358] Kevin Zahnle, Richard S. Freedman, and David C. Catling. Is there methane on Mars? *Icarus*, 212:493–503, 2011.

[359] Christopher R Webster, Paul R Mahaffy, Sushil K Atreya, Gregory J Flesch, Kenneth A Farley, and MSL Science Team. Low upper limit to methane abundance on Mars. *Science*, 342:355—357, 2013.

[360] Marco Giuranna, Sébastien Viscardy, Frank Daerden, Lori Neary, Giuseppe Etiope, Dorothy Oehler, Vittorio Formisano, Alessandro Aronica, Paulina Wolkenberg, Shohei Aoki, et al. Independent confirmation of a methane spike on Mars and a source region east of Gale Crater. *Nature Geoscience*, 12:326–332, 2019.

[361] Oleg Korablev, Ann Carine Vandaele, Franck Montmessin, Anna A Fedorova, Alexander Trokhimovskiy, François Forget, Franck Lefèvre, Frank Daerden, Ian R Thomas, Loïc Trompet, et al. No detection of methane on Mars from early ExoMars Trace Gas Orbiter observations. *Nature*, 568:517–520, 2019.

[362] J. L. Grenfell, F. Wunderlich, M. Sinnhuber, K. Herbst, R. Lehmann, M. Scheucher, S. Gebauer, G. Arnold, and H. Rauer. Atmospheric processes affecting methane on Mars. *Icarus*, 382:114940, 2022.

[363] Vladimir A Krasnopolsky. Some problems related to the origin of methane on Mars. *Icarus*, 180:359–367, 2006.

[364] Yuk L Yung, Pin Chen, Kenneth Nealson, Sushil Atreya, Patrick Beckett, Jennifer G Blank, Bethany Ehlmann, John Eiler, Giuseppe Etiope, James G Ferry, et al. Methane on Mars and habitability: challenges and responses. *Astrobiology*, 18:1221–1242, 2018.

[365] M. Allen, M. Delitsky, W. Huntress, Y. Yung, and W. H. Ip. Evidence for methane and ammonia in the coma of comet P/Halley. *A&A*, 187:502–512, 1987.

[366] E. L. Gibb, M. J. Mumma, N. Dello Russo, M. A. DiSanti, and K. Magee-Sauer. Methane in Oort cloud comets. *Icarus*, 165:391–406, 2003.

[367] J Apt, N P Carleton, and C D MacKay. Methane on Triton and Pluto - new CCD Spectra. *ApJ*, 270:342–350, 1983.

[368] Ben Burningham, D. J. Pinfield, S. K. Leggett, M. Tamura, P. W. Lucas, D. Homeier, A. Day-Jones, H. R. A. Jones, J. R. A. Clarke, M. Ishii, M. Kuzuhara, N. Lodieu, M. R. Zapatero Osorio, B. P. Venemans, D. J. Mortlock, D. Barrado y Navascués, E. L. Martin, and A. Magazzù. Exploring the substellar temperature regime down to $\sim$ 550 K. *MNRAS*, 391:320–333, 2008.

[369] M. Janson, J. Carson, C. Thalmann, M. W. McElwain, M. Goto, J. Crepp, J. Wisniewski, L. Abe, W. Brandner, A. Burrows, S. Egner, M. Feldt, C. A. Grady, T. Golota, O. Guyon, J. Hashimoto, Y. Hayano, M. Hayashi, S. Hayashi, T. Henning, K. W. Hodapp, M. Ishii, M. Iye, R. Kandori, G. R. Knapp, T. Kudo, N. Kusakabe, M. Kuzuhara, T. Matsuo, S. Mayama, S. Miyama, J. I. Morino, A. Moro-Martín, T. Nishimura, T. S. Pyo, E. Serabyn, H. Suto, R. Suzuki, M. Takami, N. Takato, H. Terada, B. Tofflemire, D. Tomono, E. L. Turner, M. Watanabe, T. Yamada, H. Takami, T. Usuda, and M. Tamura. Near-infrared Multi-band Photometry of the Substellar Companion GJ 758 B. *ApJ*, 728:85, 2011.

[370] C. G. Tinney, J. Davy Kirkpatrick, Jacqueline K. Faherty, Gregory N. Mace, Mike Cushing, Christopher R. Gelino, Adam J. Burgasser, Scott S. Sheppard, and Edward L. Wright. New Y and T Dwarfs from WISE Identified by Methane Imaging. *ApJS*, 236:28, 2018.

[371] Callie E. Hood, Jonathan J. Fortney, Michael R. Line, and Jacqueline K. Faherty. Brown Dwarf Retrievals on FIRE!: Atmospheric Constraints and Lessons Learned from High Signal-to-noise Medium-resolution Spectroscopy of a T9 Dwarf. *AJ.*, 953:170, 2023.

[372] B. R. Oppenheimer, S. R. Kulkarni, K. Matthews, and T. Nakajima. Infrared Spectrum of the Cool Brown Dwarf Gl 229B. *Science*, 270:1478–1479, 1995.

[373] T Nakajima, BR Oppenheimer, SR Kulkarni, DA Golimowski, K Matthews, and ST Durrance. Discovery of a cool brown dwarf. *Nature*, 378:463–465, 1995.

[374] Peter F. Bernath. Molecular astronomy of cool stars and sub-stellar objects. *Intern. Rev. Phys. Chem.*, 28:681–709, 2009.

[375] P. H. Hauschildt, R. Warmbier, R. Schneider, and T. Barman. Methane line opacities in very cool stellar objects. *A&A*, 504:225–229, 2009.

[376] J Davy Kirkpatrick, I Neill Reid, James Liebert, Roc M Cutri, Brant Nelson, Charles A Beichman, Conard C Dahn, David G Monet, John E Gizis, and Michael F Skrutskie. Dwarfs cooler than "M": The definition of spectral type "L" using discoveries from the 2-Micron All-Sky Survey (2MASS). *ApJ*, 519:802, 1999.

[377] Adam J Burgasser, J Davy Kirkpatrick, Michael E Brown, I Neill Reid, Adam Burrows, James Liebert, Keith Matthews, John E Gizis, Conard C Dahn, David G Monet, et al. The spectra of T dwarfs. I. Near-infrared data and spectral classification. *ApJ*, 564:421, 2002.

[378] C. G. Tinney, Adam J. Burgasser, J. Davy Kirkpatrick, and Michael W. McElwain. The 2MASS Wide-Field T Dwarf Search. IV. Hunting Out T Dwarfs with Methane Imaging. *AJ.*, 130:2326, 2005.

[379] Adam Burrows and C. M. Sharp. Chemical Equilibrium Abundances in Brown Dwarf and Extrasolar Giant Planet Atmospheres. *ApJ*, 512:843, 1999.

[380] Giovanna Tinetti, Mao-Chang Liang, Alfred Vidal-Madjar, David Ehrenreich, Alain Lecavelier des Etangs, and Yuk L. Yung. Infrared transmission spectra for extrasolar giant planets. *ApJ*, 654:L99–L102, 2007.

[381] Adam Burrows, WB Hubbard, JI Lunine, and James Liebert. The theory of brown dwarfs and extrasolar giant planets. *Rev. Mod. Phys.*, 73:719, 2001.

[382] Keith S. Noll, T. R. Geballe, S. K. Leggett, and Mark S. Marley. The Onset of Methane in L Dwarfs. *ApJ*, 541:L75, 2000.

[383] Tadashi Nakajima, Takashi Tsuji, and Kenshi Yanagisawa. H- and K-Band Methane Features in an L Dwarf, 2MASS 0920+35. *ApJL*, 561:L119–L122, 2001.

[384] Brittany E. Miles, Andrew J. Skemer, Travis S. Barman, Katelyn N. Allers, and Jordan M. Stone. Methane in Analogs of Young Directly Imaged Exoplanets. *ApJ*, 869:18, 2018.

[385] Michael C. Cushing, J. Davy Kirkpatrick, Christopher R. Gelino, Roger L. Griffith, Michael F. Skrutskie, A. Mainzer, Kenneth A. Marsh, Charles A. Beichman, Adam J. Burgasser, Lisa A. Prato, Robert A. Simcoe, Mark S. Marley, D. Saumon, Richard S. Freedman, Peter R. Eisenhardt, and Edward L. Wright. The Discovery of Y Dwarfs Using Data From the Wide-Field Infrared Survey Explorer (WISE). *ApJ*, 743:50, 2011.

[386] J. Davy Kirkpatrick, Christopher R. Gelino, Michael C. Cushing, Gregory N. Mace, Roger L. Griffith, Michael F. Skrutskie, Kenneth A. Marsh, Edward L. Wright, Peter R. Eisenhardt, Ian S. McLean, Amanda K. Mainzer, Adam J. Burgasser, C. G. Tinney, Stephen Parker, and Graeme Salter. Further Defining Spectral Type "Y" and Exploring the Low-Mass End of the Field Brown Dwarf Mass Function. *ApJ*, 753:156, 2012.

[387] Jeremy Bailey. The dawes review 3: The atmospheres of extrasolar planets and brown dwarfs. *Publ. Astron. Soc. Aust.*, 31:e043, 2014.

[388] C. Sagan, W. R. Thompson, R. Carlson, D. Gurnett, and C. Hord. A search for life on earth from the Galileo spacecraft. *Nature*, 365:715–721, 1993.

[389] Trent L Schindler and James F Kasting. Synthetic spectra of simulated terrestrial atmospheres containing possible biomarker gases. *Icarus*, 145:262–271, 2000.

[390] Karin I. Öberg, Ruth Murray-Clay, and Edwin A. Bergin. The Effects of Snowlines on C/O in Planetary Atmospheres. *ApJ*, 743:L16, 2011.

[391] Mark R. Swain, Gautam Vasisht, and Giovanna Tinetti. The presence of methane in the atmosphere of an extrasolar planet. *Nature*, 452:329–331, 2008.

[392] M R Swain, G Tinetti, G Vasisht, P Deroo, C Griffith, J Bouwman, Pin Chen, Y Yung, A Burrows, L R Brown, et al. Water, methane, and carbon dioxide present in the dayside spectrum of the exoplanet HD 209458b. *ApJ*, 704:1616, 2009.

[393] Giovanna Tinetti, P Deroo, M R Swain, C A Griffith, G Vasisht, L R Brown, C Burke, and P McCullough. Probing the terminator region atmosphere of the hot-Jupiter XO-1b with transmission spectroscopy. *ApJL*, 712:L139, 2010.

[394] G Guilluy, Alessandro Sozzetti, M Brogi, ALDO STEFANO Bonomo, Paolo Giacobbe, Riccardo Claudi, and SERENA Benatti. Exoplanet atmospheres with GIANO-II. Detection of molecular absorption in the dayside spectrum of HD 102195b. *A&A*, 625:A107, 2019.

[395] Guilluy, G., Giacobbe, P., Carleo, I., Cubillos, P. E., Sozzetti, A., Bonomo, A. S., Brogi, M., Gandhi, S., Fossati, L., Nascimbeni, V., Turrini, D., Schisano, E., Borsa, F., Lanza, A. F., Mancini, L., Maggio, A., Malavolta, L., Micela, G., Pino, L., Rainer, M., Bignamini, A., Claudi, R., Cosentino, R., Covino, E., Desidera, S., Fiorenzano, A., Harutyunyan, A., Lorenzi, V., Knapic, C., Molinari, E., Pacetti, E., Pagano, I., Pedani, M., Piotto, G., and Poretti, E. The GAPS Programme at TNG - XXXVIII. Five molecules in the atmo-

sphere of the warm giant planet WASP-69b detected at high spectral resolution. *A&A*, 665:A104, 2022.

[396] Jiang, C., Chen, G., Pallé, E., Murgas, F., Parviainen, H., Yan, F., and Ma, Y. Evidence for stellar contamination in the transmission spectra of HAT-P-12b. *A&A*, 656:A114, 2021.

[397] Kevin B Stevenson, Joseph Harrington, Sarah Nymeyer, Nikku Madhusudhan, Sara Seager, William C Bowman, Ryan A Hardy, Drake Deming, Emily Rauscher, and Nate B Lust. Possible thermochemical disequilibrium in the atmosphere of the exoplanet GJ 436b. *Nature*, 464:1161–1164, 2010.

[398] J. P. Beaulieu, G. Tinetti, D. Kipping, I. Ribas, R. J. Barber, J. Y-K. Cho, I. Polichtchouk, J. Tennysson, S. N. Yurchenko, C. A. Griffith, I. Waldmann, S. Miller, S. Carey, O. Mousis, S. J. Fossey, and A. Aylward. Methane in the atmosphere of the transiting hot Neptune GJ436b? *ApJ*, 731:16, 2011.

[399] Akihiko Fukui, Norio Narita, Kenji Kurosaki, Masahiro Ikoma, Kenshi Yanagisawa, Daisuke Kuroda, Yasuhiro Shimizu, Yasuhiro H Takahashi, Hiroshi Ohnuki, Masahiro Onitsuka, et al. Optical-to-near-infrared simultaneous observations for the hot Uranus GJ3470b: a hint of a cloud-free atmosphere. *ApJ*, 770:95, 2013.

[400] Olivia Venot, Marcelino Agúndez, Franck Selsis, Marcell Tessenyi, and Nicolas Iro. The atmospheric chemistry of the warm Neptune GJ 3470b: Influence of metallicity and temperature on the CH_4/CO ratio. *A&A*, 562:A51, 2014.

[401] David K Sing, Zafar Rustamkulov, Daniel P Thorngren, Joanna K Barstow, Pascal Tremblin, Catarina Alves de Oliveira, Tracy L Beck, Stephan M Birkmann, Ryan C Challener, Nicolas Crouzet, et al. A warm Neptune's methane reveals core mass and vigorous atmospheric mixing. *Nature*, 630:831–835, 2024.

[402] Yayaati Chachan, Heather A. Knutson, Peter Gao, Tiffany Kataria, Ian Wong, Gregory W. Henry, Bjorn Benneke, Michael Zhang, Joanna Barstow, Jacob L. Bean, Thomas Mikal-Evans, Nikole K. Lewis, Megan Mansfield, Mercedes López-Morales, Nikolay Nikolov, David K. Sing, and Hannah Wakeford. A Hubble PanCET Study of HAT-P-11b: A Cloudy Neptune with a Low Atmospheric Metallicity. *AJ.*, 158:244, 2019.

[403] M. Basilicata, P. Giacobbe, A. S. Bonomo, G. Scandariato, M. Brogi, V. Singh, A. Di Paola, L. Mancini, A. Sozzetti, A. F. Lanza, P. E. Cubillos, M. Damasso, S. Desidera, K. Biazzo, A. Bignamini, F. Borsa, L. Cabona, I. Carleo, A. Ghedina, G. Guilluy, A. Maggio, G. Mainella, G. Micela, E. Molinari, M. Molinaro, D. Nardiello, M. Pedani, L. Pino, E. Poretti, J. Southworth, M. Stangret, and D. Turrini. The GAPS Programme at TNG. LV. Multiple molecular species in the atmosphere of HAT-P-11 b and review of the HAT-P-11 planetary system. *A&A*, 686:A127, 2024.

[404] Ilaria Carleo, Paolo Giacobbe, Gloria Guilluy, Patricio E. Cubillos, Aldo S. Bonomo, Alessandro Sozzetti, Matteo Brogi, Siddharth Gandhi, Luca Fossati, Diego Turrini, Katia Biazzo, Francesco Borsa, Antonino F. Lanza, Luca Malavolta, Antonio Maggio, Luigi Mancini, Giusi Micela, Lorenzo Pino, Ennio Poretti, Monica Rainer, Gaetano Scandariato, Eugenio Schisano, Gloria Andreuzzi, Andrea Bignamini, Rosario Cosentino, Aldo Fiorenzano, Avet Harutyunyan, Emilio Molinari, Marco Pedani, Seth Redfield, and Hristo Stoev. The GAPS Programme at TNG XXXIX. Multiple Molecular Species in the Atmosphere of the Warm Giant Planet WASP-80 b Unveiled at High Resolution with GIANO-B. *AJ.*, 164:101, 2022.

[405] Taylor J Bell, Luis Welbanks, Everett Schlawin, Michael R Line, Jonathan J Fortney, Thomas P Greene, Kazumasa Ohno, Vivien Parmentier, Emily Rauscher, Thomas G Beatty, et al. Methane throughout the atmosphere of the warm exoplanet WASP-80b. *Nature*, 623:709–712, 2023.

[406] Nikku Madhusudhan, Subhajit Sarkar, Savvas Constantinou, Måns Holm-

berg, Anjali A. A. Piette, and Julianne I. Moses. Carbon-bearing Molecules in a Possible Hycean Atmosphere. *ApJL*, 956:L13, 2023.

[407] B. Macintosh, J. R. Graham, T. Barman, R. J. De Rosa, Q. Konopacky, M. S. Marley, C. Marois, E. L. Nielsen, L. Pueyo, A. Rajan, J. Rameau, D. Saumon, J. J. Wang, J. Patience, M. Ammons, P. Arriaga, E. Artigau, S. Beckwith, J. Brewster, S. Bruzzone, J. Bulger, B. Burningham, A. S. Burrows, C. Chen, E. Chiang, J. K. Chilcote, R. I. Dawson, R. Dong, R. Doyon, Z. H. Draper, G. Duchêne, T. M. Esposito, D. Fabrycky, M. P. Fitzgerald, K. B. Follette, J. J. Fortney, B. Gerard, S. Goodsell, A. Z. Greenbaum, P. Hibon, S. Hinkley, T. H. Cotten, L.-W. Hung, P. Ingraham, M. Johnson-Groh, P. Kalas, D. Lafreniere, J. E. Larkin, J. Lee, M. Line, D. Long, J. Maire, F. Marchis, B. C. Matthews, C. E. Max, S. Metchev, M. A. Millar-Blanchaer, T. Mittal, C. V. Morley, K. M. Morzinski, R. Murray-Clay, R. Oppenheimer, D. W. Palmer, R. Patel, M. D. Perrin, L. A. Poyneer, R. R. Rafikov, F. T. Rantakyrö, E. L. Rice, P. Rojo, A. R. Rudy, J.-B. Ruffio, M. T. Ruiz, N. Sadakuni, L. Saddlemyer, M. Salama, D. Savransky, A. C. Schneider, A. Sivaramakrishnan, I. Song, R. Soummer, S. Thomas, G. Vasisht, J. K. Wallace, K. Ward-Duong, S. J. Wiktorowicz, S. G. Wolff, and B. Zuckerman. Discovery and spectroscopy of the young jovian planet 51 Eri b with the Gemini Planet Imager. *Science*, 350:64–67, 2015.

[408] Travis S. Barman, Quinn M. Konopacky, Bruce Macintosh, and Christian Marois. Simultaneous Detection of Water, Methane, and Carbon Monoxide in the Atmosphere of Exoplanet HR 8799 b. *ApJ*, 804:61, 2015.

[409] A. Borysow, J. P. Champion, U. G. Jorgensen, and C. Wenger. Preliminary CH_4 line list data for stellar atmospheres. In I. Hubeny, D. Mihalas, and K. Werner, editors, *Stellar atmosphere modeling*, volume 288 of *ASP Conference Series*, pages 352–356, 2003.

[410] S. N. Yurchenko and J. Tennyson. ExoMol line lists IV: The rotation-vibration spectrum of methane up to 1500 K. *MNRAS*, 440:1649–1661, 2014.

[411] A.V. Nikitin, O.M. Lyulin, S.N. Mikhailenko, V.I. Perevalov, N.N. Filippov, I.M. Grigoriev, I. Morino, Y. Yoshida, and T. Matsunaga. GOSAT-2014 methane spectral line list. *J. Quant. Spectrosc. Radiat. Transf.*, 154:63–71, 2015.

[412] R. J. Hargreaves, P. F. Bernath, J. Bailey, and M. Dulick. Empirical Line Lists and Absorption Cross Sections for Methane at High Temperatures. *ApJ*, 813:12, 2015.

[413] Robert J. Hargreaves, Iouli E. Gordon, Michael Rey, andrei V. Nikitin, Vladimir G. Tyuterev, Roman V. Kochanov, and Laurence S. Rothman. An Accurate, Extensive, and Practical Line List of Methane for the HITEMP Database. *ApJS*, 247:55, 2020.

[414] S. N. Yurchenko, D. S. Amundsen, J. Tennyson, and I P Waldmann. A hybrid line list for CH_4 and hot methane continuum. *A&A*, 605:A95, 2017.

[415] Michaël Rey, Andrei V Nikitin, Yurii L Babikov, and Vladimir G Tyuterev. TheoReTS–An information system for theoretical spectra based on variational predictions from molecular potential energy and dipole moment surfaces. *J. Mol. Spectrosc.*, 327:138–158, 2016.

[416] J. I. Canty, P. W. Lucas, S. N. Yurchenko, J. Tennyson, S. K. Leggett, C. G. Tinney, H. R. A. Jones, B. Burningham, D. J. Pinfield, and R. L. Smart. Methane and ammonia in the near-infrared spectra of late-t dwarfs. *MNRAS*, 450:454–480, 2015.

[417] Jonathan Tennyson and Sergei N Yurchenko. ExoMol at 10. *Astron. Geophys.*, 62:6.16–6.21, 2021.

[418] M Lendl, Sz Csizmadia, A Deline, L Fossati, Daniel Kitzmann, Kevin Heng, S Hoyer, Sébastien Salmon, Willy Benz, Christopher Broeg, et al. The hot dayside and asymmetric transit of WASP-189 b seen by CHEOPS. *A&AS*, 643:A94, 2020.

[419] Quentin Changeat, Billy Edwards, Ahmed F Al-Refaie, Mario Morvan, Angelos Tsiaras, Ingo P Waldmann, and Giovanna Tinetti. KELT-11 b: Abundances of water and constraints on carbon-bearing molecules from the hubble transmission spectrum. *AJ.*, 160:260, 2020.

[420] Nour Skaf, Michelle Fabienne Bieger, Billy Edwards, Quentin Changeat, Mario Morvan, Flavien Kiefer, Doriann Blain, Tiziano Zingales, Mathilde Poveda, Ahmed Al-Refaie, et al. ARES. II. Characterizing the Hot Jupiters WASP-127 b, WASP-79 b, and WASP-62b with the Hubble Space Telescope. *AJ.*, 160:109, 2020.

[421] Paolo Giacobbe, Matteo Brogi, Siddharth Gandhi, Patricio E Cubillos, Aldo S Bonomo, Alessandro Sozzetti, Luca Fossati, Gloria Guilluy, Ilaria Carleo, Monica Rainer, et al. Five carbon-and nitrogen-bearing species in a hot giant planet's atmosphere. *Nature*, 592:205–208, 2021.

[422] Taylor J Bell, Nicolas Crouzet, Patricio E Cubillos, Laura Kreidberg, Anjali AA Piette, Michael T Roman, Joanna K Barstow, Jasmina Blecic, Ludmila Carone, Louis-Philippe Coulombe, et al. Nightside clouds and disequilibrium chemistry on the hot Jupiter WASP-43b. *Nature astronomy*, 8:879–898, 2024.

[423] Matthew C Nixon, Anjali AA Piette, Eliza M-R Kempton, Peter Gao, Jacob L Bean, Maria E Steinrueck, Alexandra S Mahajan, Jason D Eastman, Michael Zhang, and Leslie A Rogers. New Insights into the Internal Structure of GJ 1214 b Informed by JWST. *ApJL*, 970:L28, 2024.

[424] Adina D Feinstein, Michael Radica, Luis Welbanks, Catriona Anne Murray, Kazumasa Ohno, Louis-Philippe Coulombe, Néstor Espinoza, Jacob L Bean, Johanna K Teske, Björn Benneke, et al. Early Release Science of the exoplanet WASP-39b with JWST NIRISS. *Nature*, 614:670–675, 2023.

[425] Marylou Fournier-Tondreau, Ryan J. MacDonald, Michael Radica, David Lafreniere, Luis Welbanks, Caroline Piaulet, Louis-Philippe Coulombe, Ro-

main Allart, Kim Morel, Etienne Artigau, Loic Albert, Olivia Lim, Rene Doyon, Bjorn Benneke, Jason F. Rowe, Antoine Darveau-Bernier, Nicolas B. Cowan, Nikole K. Lewis, Neil J. Cook, Laura Flagg, Frederic Genest, Stefan Pelletier, Doug Johnstone, Lisa Dang, Lisa Kaltenegger, Jake Taylor, and Jake D. Turner. Near-infrared transmission spectroscopy of HAT-P-18 b with NIRISS: Disentangling planetary and stellar features in the era of JWST. *MNRAS*, 528:3354–3377, 2024.

[426] A. Tsiaras, M. Rocchetto, I. P. Waldmann, G. Tinetti, R. Varley, G. Morello, E. J. Barton, S. N. Yurchenko, and J. Tennyson. Detection of an atmosphere around the super-Earth 55 Cancri e. *ApJ*, 820:99, 2016.

[427] Louis-Philippe Coulombe, Michael Radica, Björn Benneke, Élyse D'Aoust, Lisa Dang, Nicolas B Cowan, Vivien Parmentier, Loïc Albert, David Lafrenière, Jake Taylor, et al. Highly reflective white clouds on the western dayside of an exo-Neptune. *Nat. Astron*, pages 1–14, 2025.

[428] Billy Edwards, Quentin Changeat, Robin Baeyens, Angelos Tsiaras, Ahmed Al-Refaie, Jake Taylor, Kai Hou Yip, Michelle Fabienne Bieger, Doriann Blain, Amélie Gressier, and et al. ARES I: WASP-76 b, A Tale of Two HST Spectra. *ApJ*, 160:8, Jun 2020.

[429] Maria Oreshenko, Baptiste Lavie, Simon L. Grimm, Shang-Min Tsai, Matej Malik, Brice-Olivier Demory, Christoph Mordasini, Yann Alibert, Willy Benz, Sascha P. Quanz, Roberto Trotta, and Kevin Heng. Retrieval Analysis of the Emission Spectrum of WASP-12b: Sensitivity of Outcomes to Prior Assumptions and Implications for Formation History. *ApJL*, 847:L3, 2017.

[430] Abhijith Rajan, Julien Rameau, Robert J. De Rosa, Mark S. Marley, James R. Graham, Bruce Macintosh, Christian Marois, Caroline Morley, Jennifer Patience, Laurent Pueyo, Didier Saumon, Kimberly Ward-Duong, S. Mark Ammons, Pauline Arriaga, Vanessa P. Bailey, Travis Barman, Joanna Bulger,

Adam S. Burrows, Jeffrey Chilcote, Tara Cotten, Ian Czekala, Rene Doyon, Gaspard Duchêne, Thomas M. Esposito, Michael P. Fitzgerald, Katherine B. Follette, Jonathan J. Fortney, Stephen J. Goodsell, Alexandra Z. Greenbaum, Pascale Hibon, Li-Wei Hung, Patrick Ingraham, Mara Johnson-Groh, Paul Kalas, Quinn Konopacky, David Lafrenière, James E. Larkin, Jérôme Maire, Franck Marchis, Stanimir Metchev, Maxwell A. Millar-Blanchaer, Katie M. Morzinski, Eric L. Nielsen, Rebecca Oppenheimer, David Palmer, Rahul I. Patel, Marshall Perrin, Lisa Poyneer, Fredrik T. Rantakyrö, Jean-Baptiste Ruffio, Dmitry Savransky, Adam C. Schneider, Anand Sivaramakrishnan, Inseok Song, Rémi Soummer, Sandrine Thomas, Gautam Vasisht, J. Kent Wallace, Jason J. Wang, Sloane Wiktorowicz, and Schuyler Wolff. Characterizing 51 Eri b from 1 to 5 μm: A Partly Cloudy Exoplanet. *AJ.*, 154:10, 2017.

[431] Baptiste Lavie, João M. Mendonça, Christoph Mordasini, Matej Malik, Mickaël Bonnefoy, Brice-Olivier Demory, Maria Oreshenko, Simon L. Grimm, David Ehrenreich, and Kevin Heng. HELIOS–RETRIEVAL: An Open-source, Nested Sampling Atmospheric Retrieval Code; Application to the HR 8799 Exoplanets and Inferred Constraints for Planet Formation. *AJ.*, 154:91, 2017.

[432] Jean-Loup Baudino, Paul Mollière, Olivia Venot, Pascal Tremblin, Bruno Bézard, and Pierre-Olivier Lagage. Toward the Analysis of JWST Exoplanet Spectra: Identifying Troublesome Model Parameters. *ApJ*, 850:150, 2017.

[433] A. Tsiaras, I. P. Waldmann, T. Zingales, M. Rocchetto, G. Morello, M. Damiano, K. Karpouzas, G. Tinetti, L. K. McKemmish, J. Tennyson, and S. N. Yurchenko. A population study of gaseous exoplanets. *AJ.*, 155:156, 2018.

[434] Mollière, P., Wardenier, J. P., van Boekel, R., Henning, Th., Molaverdikhani, K., and Snellen, I. A. G. petitRADTRANS - A Python radiative transfer package for exoplanet characterization and retrieval. *A&A*, 627:A67, 2019.

[435] Katy L. Chubb and Michiel Min. Exoplanet Atmosphere Retrievals in 3D Using Phase Curve Data with ARCiS: Application to WASP-43b. *A&A*, 665:A2, 2022.

[436] Megan E Tannock, Stanimir Metchev, Callie E Hood, Gregory N Mace, Jonathan J Fortney, Caroline V Morley, Daniel T Jaffe, and Roxana Lupu. A 1.46–2.48 μm spectroscopic atlas of a T6 dwarf (1060 K) atmosphere with IGRINS: first detections of H2S and H2, and verification of H_2O, CH_4, and NH_3 line lists. *MNRAS*, 514:3160–3178, 2022.

[437] Jonathan Tennyson. *Astronomical spectroscopy : an introduction to the atomic and molecular physics of astronomical spectra*. World Scientific, Singapore, 2 edition, 2011.

[438] Philip Bunker and Per Jensen. *Fundamentals of Molecular Symmetry*. IOP Publishing, 11 2004.

[439] Philip R Bunker and Per Jensen. *Molecular symmetry and spectroscopy*, volume 46853. NRC research press, 2006.

[440] V Boudon, M Rey, and M Loete. The vibrational levels of methane obtained from analyses of high-resolution spectra. *J. Quant. Spectrosc. Radiat. Transf.*, 98:394–404, 2006.

[441] O. N. Ulenikov, E. S. Bekhtereva, S. Albert, S. Bauerecker, H. M. Niederer, and M. Quack. Survey of the high resolution infrared spectrum of methane ($^{12}CH_4$ and $^{13}CH_4$): Partial vibrational assignment extended towards 12 000 cm^{-1}. *J. Chem. Phys.*, 141:234302, 2014.

[442] Sergei N. Yurchenko, Walter Thiel, and Per Jensen. Theoretical rovibrational energies (trove): A robust numerical approach to the calculation of rovibrational energies for polyatomic molecules. *Journal of Molecular Spectroscopy*, 245(2):126–140, OCT 2007.

[443] C. Bray, A. Cuisset, F. Hindle, G. Mouret, R. Bocquet, and V. Boudon. Spectral lines of methane measured up to 2.6 THz at sub-MHz accuracy with a CW-THz photomixing spectrometer: Line positions of rotational transitions induced by centrifugal distortion. *J. Quant. Spectrosc. Radiat. Transf.*, 203:349–354, 2017.

[444] V. Boudon, O. Pirali, P. Roy, J.-B. Brubach, L. Manceron, and J. Vander Auwera. The high-resolution far-infrared spectrum of methane at the SOLEIL synchrotron. *J. Quant. Spectrosc. Radiat. Transf.*, 111:1117–1129, 2010.

[445] R F Curl. Infrared-Radio Frequency Double-Resonance Observations of Pure Rotational Q-Branch Transitions of Methane. *J. Mol. Spectrosc.*, 48:165–173, 1973.

[446] M. Oldani, M. Andrist, A. Bauder, and A. G. Robiette. Pure rotational spectra of methane and methane-D4 in the vibrational ground state observed by microwave Fourier transform spectroscopy. *J. Mol. Spectrosc.*, 110:93–105, 1985.

[447] C W Holt, M C L Gerry, and I Ozier. The distortion moment microwave spectrum of $^{12}CH_4$ in the ground vibronic state. *Can. J. Phys.*, 53:1791–1805, 1975.

[448] M Oldani, A Bauder, J C Hilico, M Loete, and J P Champion. Microwave Fourier-Transform Spectroscopy of Rovibrational Transitions in the $\nu_2 - \nu_4$ Dyads of Methane-^{12}C and Methane-^{13}C. *Europhys. Lett.*, 4:29–33, 1987.

[449] J C Hilico, L Loete, J P Champion, J L Destomes, and M Bogey. The millimeter-wave spectrum of methane. *J. Mol. Spectrosc.*, 122:381–389, 1987.

[450] C. J. Pursell and D. P. Weliky. Pure Rotational Transitions in the ν_3 State of Methane. *J. Mol. Spectrosc.*, 97:773–785, 1992.

[451] M Takami, K Uehara, and K Shimoda. Rotational Transitions of CH_4 in $\nu_3 = 1$ Excited-State Observed by an Infrared-Microwave Double-Resonance Method. *Japanese J. Appl. Phys.*, 12:924–925, 1973.

[452] C. W. Holt, M. C. L. Gerry, and I. Ozier. Microwave Spectrum of $^{12}CH_4$ in the Ground Vibronic State. *Phys. Rev. Lett.*, 31:1033–1036, 1973.

[453] Eszter Dudás, Bastien Vispoel, Robert R. Gamache, Michaël Rey, Vladimir G. Tyuterev, Andrei V. Nikitin, Samir Kassi, Nicolas Suas-David, and Robert Georges. Non-LTE spectroscopy of the tetradecad region of methane recorded in a hypersonic flow. *Icarus*, 394:115421, 2023.

[454] Jinjun Liu, S M Riyadh, Hamzeh Telfah, Ian Jones, Jonathan Bersson, Cunfeng Cheng, Shui-Ming Hu, and David Foote. Mid-Infrared Doppler-Free Saturation Absorption Spectroscopy of the Q Branch of CH_4 $\nu_3 = 1$ Band using a Rapid-Scanning Continuous-Wave Optical Parametric Oscillator. *Opt. Lett*, 49:4230–4233, 2024.

[455] Matthias Germann, Adrian Hjalten, Vincent Boudon, Cyril Richard, Karol Krzempek, Arkadiusz Hudzikowski, Aleksander Gluszek, Grzegorz Sobon, and Aleksandra Foltynowicz. A methane line list with sub-MHz accuracy in the 1250 to 1380 cm^{-1} range from optical frequency comb Fourier transform spectroscopy. *J. Quant. Spectrosc. Radiat. Transf.*, 288:108252, 2022.

[456] A. A. Rodina, A. Nikitin, V, L. Manceron, X. Thomas, L. Daumont, M. Rey, K. Sung, A. E. Protasevich, S. A. Tashkun, and Vl G. Tyuterev. Improved line list of $^{12}CH_4$ in the 4100-4300 cm^{-1} region. *J. Quant. Spectrosc. Radiat. Transf.*, 279:108021, 2022.

[457] Aleksandra Foltynowicz, Lucile Rutkowski, Isak Silander, Alexandra C. Johansson, Vinicius Silva de Oliveira, Ove Axner, Grzegorz Soboń, Tadeusz Martynkien, Paweł Mergo, and Kevin K. Lehmann. Measurement and assignment of double-resonance transitions to the 8900–9100 cm^{-1} levels of methane. *Phys. Rev. A*, 103:022810, 2021.

[458] Sho Okubo, Hajime Inaba, Shoko Okuda, and Hiroyuki Sasada. Frequency measurements of the $2\nu_3$ A_1 – ν_3 band transitions of methane in comb-referenced infrared-infrared double-resonance spectroscopy. *Phys. Rev. A*, 103:022809, 2021.

[459] Jidong Li, Yanjun Ding, Zheng Li, and Zhimin Peng. Quantum cascade laser measurements of CH_4 linestrength and temperature-dependent self-broadening and narrowing parameters at 7.16 μm. *J. Quant. Spectrosc. Radiat. Transf.*, 276:107901, 2021.

[460] L. Yang, H. Lin, M.D. Plimmer, X.-J. Feng, Y.-J. Ma, J.-T. Luo, J.-F. Luo, and J.-T. Zhang. Measurement of the spectral line positions in the $2\nu_3$ R(6) manifold of methane. *J. Quant. Spectrosc. Radiat. Transf.*, 245:106888, 2020.

[461] A. V. Nikitin, A. A. Rodina, X. Thomas, L. Manceron, L. Daumont, M. Rey, K. Sung, A. E. Protasevich, S. A. Tashkun, I. S. Chizhmakova, and Vl. G. Tyuterev. Line list of $^{12}CH_4$ in the 4300–4600 cm^{-1} region. *J. Quant. Spectrosc. Radiat. Transf.*, 253:107061, 2020.

[462] A. S. Pine. Speed-dependent line mixing in the ν_3 band Q branch of methane. *J. Quant. Spectrosc. Radiat. Transf.*, 224:62–77, 2019.

[463] H Lin, L. Yang, X. J. Feng, and J. T. Zhang. Discovery of New Lines in the R9 Multiplet of the $2\nu_3$ Band of $^{12}CH_4$. *Phys. Rev. Lett.*, 122:013002, 2019.

[464] L Yang, H Lin, X J Feng, M D Plimmer, and J T Zhang. Saturation cavity ring-down spectrometry using a dynamical relaxation model. *Opt. Express*, 27:1769–1776, 2019.

[465] A. A. Rodina, A. V. Nikitin, X. Thomas, L. Manceron, L. Daumont, M. Rey, K. Sung, S. A. Tashkun, and Vl. G. Tyuterev. Improved line list of $^{12}CH_4$ in the 3760–4100 cm^{-1} region. *J. Quant. Spectrosc. Radiat. Transf.*, 225:351–362, 2019.

[466] A V Nikitin, A E Protasevich, M Rey, V I Serdyukov, L N Sinitsa, A Lugovskoy, and VI G Tyuterev. Improved line list of $^{12}CH_4$ in the 8850-9180 cm^{-1} region. *J. Quant. Spectrosc. Radiat. Transf.*, 239:106646, 2019.

[467] Hongliang Ma, Shenlong Zha, Xueyuan Cai, Guannan Lin, and Zhensong Cao. Line parameters of $^{12}CH_4$ around 2.008 μm studied by tunable diode laser spectroscopy with a long-path White cell. *J. Opt. Soc. Am. B*, 35:2453–2458, 2018.

[468] M. Ghysels, D. Mondelain, S. Kassi, A. Nikitin, V, M. Rey, and A. Campargue. The methane absorption spectrum near 1.73 μm (5695-5850 cm^{-1}): Empirical line lists at 80 K and 296 K and rovibrational assignments. *J. Quant. Spectrosc. Radiat. Transf.*, 213:169–177, 2018.

[469] Riccardo Gotti, Marco Prevedelli, Samir Kassi, Marco Marangoni, and Daniele Romanini. Feed-forward coherent link from a comb to a diode laser: Application to widely tunable cavity ring-down spectroscopy. *J. Chem. Phys.*, 148:054202, 2018.

[470] L. Yang, H. Lin, X. J. Feng, and J. T. Zhang. Temperature-scanning saturation cavity ring-down spectrometry for Doppler-free spectroscopy. *Opt. Express*, 26:10203–10210, 2018.

[471] Philip A. Kocheril, Charles R. Markus, Anne Marie Esposito, Alex W. Schrader, Thomas S. Dieter, and Benjamin J. McCall. Extended sub-Doppler resolution spectroscopy of the ν_3 band of methane. *J. Quant. Spectrosc. Radiat. Transf.*, 215:9–12, 2018.

[472] V. A. Nikitin, X. Thomas, L. Daumont, M. Rey, K. Sung, G. C. Toon, M. A. H. Smith, A. W. Mantz, A. E. Protasevich, S. A. Tashkun, and Vl G. Tyuterev. Assignment and modelling of $^{12}CH_4$ spectra in the 5550-5695, 5718-5725 and 5792-5814 cm^{-1} regions. *J. Quant. Spectrosc. Radiat. Transf.*, 219:323–332, 2018.

[473] A. V. Nikitin, X. Thomas, L. Daumont, M. Rey, K. Sung, G. C. Toon, M. A. H. Smith, A. W. Mantz, S. A. Tashkun, and V. G. Tyuterev. Measurements and modeling of long-path $^{12}CH_4$ spectra in the 5300-5550 cm^{-1} region. *J. Quant. Spectrosc. Radiat. Transf.*, 202:255–264, 2017.

[474] R. Hashemi, A. Predoi-Cross, A. V. Nikitin, Vi. G. Tyuterev, K. Sung, M. A. H. Smith, and V. Malathy Devi. Spectroscopic line parameters of $^{12}CH_4$ for atmospheric composition retrievals in the 4300-4500 cm^{-1} region. *J. Quant. Spectrosc. Radiat. Transf.*, 186:106–117, 2017.

[475] A. V. Nikitin, M. Rey, S. A. Tashkun, S. Kassi, D. Mondelain, A. Campargue, and Vl. G. Tyuterev. Analyses and modeling of the $^{12}CH_4$ spectrum at 80 K between 6539 and 6800 cm^{-1}. *J. Quant. Spectrosc. Radiat. Transf.*, 168:207 – 216, 2016.

[476] T. Delahaye, S. E. Maxwell, Z. D. Reed, H. Lin, J. T. Hodges, K. Sung, V. M. Devi, T. Warneke, P. Spietz, and H. Tran. Precise methane absorption measurements in the 1.64 μm spectral region for the MERLIN mission. *JGR-Atm*, 121:7360–7370, 2016.

[477] Michael Rey, andrei V. Nikitin, Alain Campargue, Samir Kassi, Didier Mondelain, and Vladimir G. Tyuterev. Ab initio variational predictions for understanding highly congested spectra: rovibrational assignment of 108 new methane sub-bands in the icosad range (6280-7800 cm^{-1}). *Phys. Chem. Chem. Phys.*, 18:176–189, 2016.

[478] V. Malathy Devi, D. Chris Benner, Mary Ann H. Smith, Arlan W. Mantz, Keeyoon Sung, Timothy J. Crawford, and Adriana Predoi-Cross. Self- and air-broadened line shape parameters in the $\nu_2+\nu_3$ band of $^{12}CH_4$: 4500-4630 cm^{-1}. *J. Quant. Spectrosc. Radiat. Transf.*, 152:149–165, 2015.

[479] M. A. H. Smith, D. Chris Benner, A. Predoi-Cross, and V. Malathy Devi. Air- and self-broadened half widths, pressure-induced shifts, and line mixing

in the ν_2 band of $^{12}CH_4$. *J. Quant. Spectrosc. Radiat. Transf.*, 133:217–234, 2014.

[480] A.V. Nikitin, X. Thomas, L. Régalia, L. Daumont, M. Rey, S.A. Tashkun, Vl.G. Tyuterev, and L.R. Brown. Measurements and modeling of long-path $^{12}CH_4$ spectra in the 4800–5300 cm^{-1} region. *J. Quant. Spectrosc. Radiat. Transf.*, 138:116–123, 2014.

[481] A. V. Nikitin, V. Boudon, Ch. Wenger, S. Albert, L. R. Brown, S. Bauerecker, and M. Quack. High resolution spectroscopy and the first global analysis of the Tetradecad region of methane $^{12}CH_4$. *Phys. Chem. Chem. Phys.*, 15:10071–10093, 2013.

[482] Masashi Abe, Kana Iwakuni, Sho Okubo, and Hiroyuki Sasada. Accurate transition frequency list of the ν_3 band of methane from sub-Doppler resolution comb-referenced spectroscopy. *J. Opt. Soc. Am. B*, 30:1027–1035, 2013.

[483] L. Daumont, A. V. Nikitin, X. Thomas, L. Regalia, P. Von der Heyden, VI. G. Tyuterev, M. Rey, V. Boudon, Ch. Wenger, M. Loete, and L. R. Brown. New assignments in the 2 μm transparency window of the $^{12}CH_4$ Octad band system. *J. Quant. Spectrosc. Radiat. Transf.*, 116:101–109, 2013.

[484] A. Campargue, O. Leshchishina, L. Wang, D. Mondelain, and S. Kassi. The WKLMC empirical line lists (5852-7919 cm^{-1}) for methane between 80 K and 296 K: "Final" lists for atmospheric and planetary applications. *J. Mol. Spectrosc.*, 291:16–22, 2013.

[485] A. M. Zolot, F. R. Giorgetta, E. Baumann, W. C. Swann, I. Coddington, and N. R. Newbury. Broad-band frequency references in the near-infrared: Accurate dual comb spectroscopy of methane and acetylene. *J. Quant. Spectrosc. Radiat. Transf.*, 118:26–39, 2013.

[486] Alain Campargue, Le Wang, Didier Mondelain, Samir Kassi, Bruno Bezard, Emmanuel Lellouch, Athena Coustenis, Catherine de Bergh, Mathieu

Hirtzig, and Pierre Drossart. An empirical line list for methane in the 1.26-1.71 μm region for planetary investigations (T=80-300 K). Application to Titan. *Icarus*, 219:110–128, 2012.

[487] Carine Manca Tanner and Martin Quack. Reinvestigation of the $\nu_2 + 2\nu_3$ subband in the overtone icosad of $^{12}CH_4$ using cavity ring-down (CRD) spectroscopy of a supersonic jet expansion. *Mol. Phys.*, 110:2111–2135, 2012.

[488] A. V. Nikitin, X. Thomas, L. Regalia, L. Daumont, P. Von der Heyden, V. G. Tyuterev, L. Wang, S. Kassi, and A. Campargue. First assignment of the $5\nu_4$ and $\nu_2 + 4\nu_4$ band systems of $^{12}CH_4$ in the 6287-6550 cm^{-1} region. *J. Quant. Spectrosc. Radiat. Transf.*, 112:28–40, 2011.

[489] E. Baumann, F. R. Giorgetta, W. C. Swann, A. M. Zolot, I. Coddington, and N. R. Newbury. Spectroscopy of the methane ν_3 band with an accurate mid-infrared coherent dual-comb spectrometer. *Phys. Rev. A*, 84:062513, 2011.

[490] Sho Okubo, Hirotaka Nakayama, Kana Iwakuni, Hajime Inaba, and Hiroyuki Sasada. Absolute frequency list of the ν_3-band transitions of methane at a relative uncertainty level of 10^{-11}. *Opt. Express*, 19:23878–23888, 2011.

[491] A. V. Nikitin, O. M. Lyulin, S. N. Mikhailenko, V. I. Perevalov, N. N. Filippov, I. M. Grigoriev, I. Morino, T. Yokota, R. Kumazawa, and T. Watanabe. GOSAT-2009 methane spectral line list in the 5550-6236 cm^{-1} range. *J. Quant. Spectrosc. Radiat. Transf.*, 111:2211–2224, 2010.

[492] M. A. H. Smith, D. Chris Benner, A. Predoi-Cross, and V. Malathy Devi. Multispectrum analysis of $^{12}CH_4$ in the nu(4) spectral region: II. Self-broadened half widths, pressure-induced shifts, temperature dependences and line mixing. *J. Quant. Spectrosc. Radiat. Transf.*, 111:1152–1166, 2010.

[493] O. M. Lyulin, A. V. Nikitin, V. I. Perevalov, Isamu Morino, Tatsuya Yokota, Ryoichi Kumazawa, and Takeshi Watanabe. Measurements of N_2- and O_2-broadening and shifting parameters of methane spectral lines in the

5550–6236 cm^{-1} region. *J. Quant. Spectrosc. Radiat. Transf.*, 110:654–668, 2009.

[494] Keisuke Takahata, Takumi Kobayashi, Hiroyuki Sasada, Yoshiaki Nakajima, Hajime Inaba, and Feng-Lei Hong. Absolute frequency measurement of sub-Doppler molecular lines using a $3.4-\mu$m difference-frequency-generation spectrometer and a fiber-based frequency comb. *Phys. Rev. A*, 80:032518, 2009.

[495] Ella Sciamma-O'Brien, Samir Kassi, Bo Gao, and Alain Campargue. Experimental low energy values of CH_4 transitions near 1.33 μm by absorption spectroscopy at 81 K. *J. Quant. Spectrosc. Radiat. Transf.*, 110:951–963, 2009.

[496] L R Brown. Empirical line parameters of methane from 1.1 to 2.1 μm. *J. Quant. Spectrosc. Radiat. Transf.*, 96:251–270, 2005.

[497] A. Predoi-Cross, L. R. Brown, V. Malathy-Devi, M. Brawley-Tremblay, and D. Benner. Multispectrum analysis of $^{12}CH_4$ from 4100 to 4635 cm^{-1}: 1. Self-broadening coefficients (widths and shifts). *J. Mol. Spectrosc.*, 232:231–246, 2005.

[498] M Hippler and M Quack. High-resolution Fourier transform infrared and cw-diode laser cavity ringdown spectroscopy of the ν_2+2 nu(3) band of methane near 7510 cm^{-1} in slit jet expansions and at room temperature. *J. Chem. Phys.*, 116:6045–6055, 2002.

[499] I M Grigoriev, N N Filippov, M V Tonkov, J P Champion, T Gabard, and R Le Doucen. Line parameters and shapes of high clusters: R branch of the ν_3 band of CH_4 in He mixtures. *J. Quant. Spectrosc. Radiat. Transf.*, 74:431–443, 2002.

[500] J.-C. Hilico, O. Robert, M. Loëte, S. Toumi, A. S. Pine, and L. R. Brown. Analysis of the Interacting Octad System of $^{12}CH_4$. *J. Mol. Spectrosc.*, 208:1 – 13, 2001.

[501] O Robert, J C Hilico, M Loete, J P Champion, and L R Brown. First assignment and line strengths of the $4\nu_4$ band of $^{12}CH_4$ near 1.9 μm. *J. Mol. Spectrosc.*, 209:14–23, 2001.

[502] L Fejard, J P Champion, L R Brown, and A S Pine. The intensities of methane in the 3 to 5 μm region revisited. *J. Mol. Spectrosc.*, 201:83–94, 2000.

[503] P S Ering, D A Tyurikov, G Kramer, and B Lipphardt. Measurement of the absolute frequency of the methane E-line at 88 THz. *Optics Comms.*, 151:229–234, 1998.

[504] R Georges, M Herman, J C Hilico, and O Robert. High-resolution FTIR spectroscopy using a jet: Sampling the rovibrational spectrum of $^{12}CH_4$. *J. Mol. Spectrosc.*, 187:13–20, 1998.

[505] D. K. Bronnikov, D. V. Kalinin, V. D. Rusanov, Y. G. Filimonov, Yu. G. Selivanov, and J. C. Hilico. Spectroscopy and Non-Equilibrium Distribution of Vibrationally Excited Methane in a Supersonic Jet. *J. Quant. Spectrosc. Radiat. Transf.*, 60:1053–1068, 1998.

[506] R Z Martinez, D Bermejo, J Santos, J P Champion, and J C Hilico. High resolution Raman spectroscopy from vibrationally excited states populated by a stimulated Raman process: $2\nu_1 - \nu_1$ of $^{12}CH_4$. *J. Chem. Phys.*, 107:4864–4874, 1997.

[507] J. C. Hilico, G. S. Baronov, D. K. Bronnikov, S. A. Gavrikov, I. I. Nikolaev, V. D. Rusanov, and Y. G. Filimonov. High-resolution spectroscopy of (pentad–dyad) and (octad–pentad) hot bands of methane in a supersonic jet. *J. Mol. Spectrosc.*, 161:435–444, 1993.

[508] J. C. Hilico, M. Loete, and L. R. Brown. Line Strengths of the $v_3 + v_3$ and $v_3 - v_3$ Bands of Methane ($^{12}CH_4$). *J. Mol. Spectrosc.*, 152:229–251, 1992.

[509] D Bermejo, J Santos, and P Cancio. High-resolution Q-cw SRS spectrum of

$^{12}CH_4$ in the region of the level-crossing between ν_1 and $\nu_2 + \nu_4$. *J. Mol. Spectrosc.*, 156:303–306, 1992.

[510] G Kramer, B Lipphardt, and C O Weiss. Coherent Frequency-Synthesis in the Infrared. In *Proceedings Of The 1992 Ieee Frequency Control Symposium*, pages 39–43. IEEE, Ultrasonics, Ferroelectrics, and Frequency Control Society, 1992.

[511] G Millot, B Lavorel, and J I Steinfeld. Collisional broadening, line shifting, and line mixing in the stimulated Raman $2\nu_2$ Q-branch of CH_4. *J. Chem. Phys.*, 95:7938–7946, 1991.

[512] J C Hilico, J P Champion, S Toumi, V G Tyuterev, and S A Tashkun. New analysis of the pentad system of methane and prediction of the (pentad-pentad) spectrum. *J. Mol. Spectrosc.*, 168:455–476, 1994.

[513] L R Brown. Methane line parameters from 3700 to 4136 cm^{-1}. *Appl. Optics*, 27:3275–3279, 1988.

[514] V P Chebotayev, V M Klementyev, M V Nikitin, B A Timchenko, and V F Zakharyash. Comparison of frequency stabilities of the Rb standard and of the He-Ne/CH_4 laser stabilized to the E line in methane. *Appl. Phys. B Photophysics and Laser Chemistry*, 36:59–61, 1985.

[515] A De Martino, R Frey, and F Pradere. Double-Resonance Observation of the ($2\nu_3$,E) State in Methane. *Chem. Phys. Lett.*, 95:200–204, 1983.

[516] D E Jennings and A G Robiette. Determination of the ν_4 Band Strength of $^{12}CH_4$ from Diode-Laser Line Strength Measurements. *J. Mol. Spectrosc.*, 94:369–379, 1982.

[517] W M Itano and I Ozier. Avoided-Crossing Molecular-Beam Spectroscopy of Methane. *J. Chem. Phys.*, 72:3700–3711, 1980.

[518] D J E Knight, G J Edwards, P R Pearce, and N R Cross. Measurement of the Frequency of the 3.39-μm Methane-Stabilized Laser to ± 3 Parts in 10^{-11}. *IEEE Transactions of Instrumentation and Measurement*, 29:257–264, 1980.

[519] M. Dang-Nhu, A. S. Pine, and A. G. Robiette. Spectral Intensities in the ν_3 Bands of $^{12}CH_4$ and $^{13}CH_4$. *J. Mol. Spectrosc.*, 77:57–68, 1979.

[520] P. Pinson and J. Dupre-Maquaire. The High Resolution Spectrum of CH_4: The Q Branch of the ν_4 Band. *J. Mol. Spectrosc.*, 78:170–174, 1979.

[521] G. Restelli and F. Cappellani. High Resolution Spectroscopy of the ν_4 Band of Methane. *J. Mol. Spectrosc.*, 78:161–169, 1979.

[522] T G Blaney, G J Edwards, B W Jolliffe, D J E Knight, and P T Woods. Absolute frequencies of the methane-stabilized HeNe laser (3.39 μm) and the CO_2, R(32) stabilized laser (10.17 μm). *J. Phys. D: Appl. Phys.*, 9:1323, 1976.

[523] A S Pine. High-Resolution Methane ν_3-Band Spectra Using a Stabilized Tunable Difference-Frequency Laser System. *J. Opt. Soc. Am.*, 66:97–108, 1976.

[524] Jean-Paul Champion and H Berger. A. Spectre Raman à haute résolution de la bande ν_2 de $^{12}CH_4$. *Journal de Physique*, 36:135–139, 1975.

[525] R C Nelson, E K Plyler, and W S Benedict. Absorption Spectra of Methane in the Near Infrared. *J. Res. Natl. Bur. Stand.*, 41:615–621, 1948.

[526] D. R. J. Boyd, H. W. Thompson, and R. L. Williams. Vibration-rotation bands of methane. *Proc. R. Soc. London, Ser. A*, 213:42–54, 1952.

[527] T Feldman, J Romanko, and H L Welsh. The ν_2 Raman band of Methane. *Can. J. Phys.*, 33:138–145, 1955.

[528] D. H. Rank, D. P. Eastman, G. Skorinko, and T. A. Wiggins. Fine Structure in the Lines of the $2\nu_3$ Band of Methane. *J. Mol. Spectrosc.*, 5:78–82, 1960.

[529] J Moretbailly, L Gautier, and J Montagutelli. Cebsch-Gordan Coefficients Adapted to Cubic Symmetry. *J. Mol. Spectrosc.*, 15:355+, 1965.

[530] Jacques Moret-Bailly. Calculation of the frequencies of the lines in a three-fold degenerate fundamental band of a spherical top molecule. *J. Mol. Spectrosc.*, 15:344–354, 1965.

[531] J Herranz, J Morcillo, and A Gómez. The ν_2 infrared band of CH_4 and CD_4. *J. Mol. Spectrosc.*, 19:266–282, 1966.

[532] Robin S McDowell. The ν_3 infrared bands of $^{12}CH_4$ and $^{13}CH_4$. *J. Mol. Spectrosc.*, 21:280–290, 1966.

[533] W R Clements and B P Stoicheff. High-Resolution Raman Spectroscopy of Gases with Laser Excitation. *J. Mol. Spectrosc.*, 33:183, 1970.

[534] L Henry, N Husson, R Andia, and A Valentin. Infrared Absorption Spectrum of Methane from 2884 cm^{-1} to 3141 cm^{-1}. *J. Mol. Spectrosc.*, 36:511–&, 1970.

[535] I Ozier, P N Yi, A Khosla, and N F Ramsey. Direct Observation of Ortho-Para Transitions in Methane. *Phys. Rev. Lett.*, 24:642–&, 1970.

[536] N Husson and M Dang Nhu. Analyse rotationnelle de la bande ν_3 de $^{12}CH_4$ de 2884 a 3141 cm^{-1}. *Journal de Physique*, 32:627–638, 1971.

[537] N Husson and G Poussigue. Analyse rotationnelle de la bande ν_4 de $^{12}CH_4$ de 1225 à 1376 cm^{-1}. *Journal de Physique*, 32:859–865, 1971.

[538] W L Barnes, J Susskind, R H Hunt, and E K Plyler. Measurement and Analysis of the ν_3 Band of Methane. *J. Chem. Phys.*, 56:5160–5172, 1972.

[539] B Bobin. Interpretation of $2\nu_3$ Harmonic Band of Methane $^{12}CH_4$ (From 5890 to 6107 cm^{-1}). *J. Phys.*, 33:345–352, 1972.

[540] J Botineau. Infrared-Absorption of Methane at High-Resolution between 1225 and 1400 cm^{-1}. *J. Mol. Spectrosc.*, 41:182–&, 1972.

[541] A Rosenberg, I Ozier, and A K Kudian. Pure Rotational Spectrum of CH_4. *J. Chem. Phys.*, 57:568+, 1972.

[542] H Berger, M Faivre, J P Champion, and Moret-Bailly J. High-Resolution Raman Spectroscopy of CH_4. *J. Mol. Spectrosc.*, 45:298–301, 1973.

[543] B Bobin and K Fox. Nouvelle interprétation de la bande νs de $^{12}CH_4$, de 2840 à 3167 cm^{-1}. *J. Phys.*, 34:571–582, 1973.

[544] J Cadot and R Delorme. Experimental Determination of J Values for Some Lines of Bands $\nu_2+\nu_3$ and $\nu_3+\nu_4$ of Methane. *J. Mol. Spectrosc.*, 45:443–449, 1973.

[545] R F Curl, T Oka, and D S Smith. Observation of a Pure Rotational Q-Branch Transition of Methane by Infrared-Radio Frequency Double-Resonance. *J. Mol. Spectrosc.*, 46:518–520, 1973.

[546] Lane Darnton and J S Margolis. The temperature dependence of the half widths of some self-and foreign-gas-broadened lines of methane. *J. Quant. Spectrosc. Radiat. Transf.*, 13:969–976, 1973.

[547] Joel Susskind. Analysis of the ν_4 band of CH_4. *J. Mol. Spectrosc.*, 45:457–466, 1973.

[548] H Berger. Simultaneous Study of Vibrational Band-ν_2 and Band-ν_4 of Spherical Tops, Using Irreducible Tensors of O_3. *J. Mol. Spectrosc.*, 55:48–55, 1975.

[549] B Bobin and J C Hilico. Attribution des transitions du type ($R' = J' \pm 2 \leftarrow J_0$) de la bande ($\nu_3+\nu_4$) du méthane $^{12}CH_4$. *Journal de Physique*, 36:225–233, 1975.

[550] Jean-Paul Champion. B. Analyse de la bande fondamentale ν_2 de $^{12}CH_4$. *Journal de Physique*, 36:141–151, 1975.

[551] Arieh Rosenberg and Irving Ozier. The forbidden ($J \rightarrow J+1$) spectrum of CH_4 in the ground vibronic state. *J. Mol. Spectrosc.*, 56:124–132, 1975.

[552] G. Tarrago, M. Dang-Nhu, G. Poussigue, G. Guelachvili, and C. Amiot. The Ground State of Methane $^{12}CH_4$ Through the Forbidden Lines of the ν_3 Band. *J. Mol. Spectrosc.*, 57:246–263, 1975.

[553] D. L. Gray and A. G. Robiette. Simultaneous analysis of the ν_2 and ν_4 bands of methane. *Mol. Phys.*, 32:1609–1625, 1976.

[554] J. L. Hall, C. J. Bordé, and K. Uehara. Direct Optical Resolution of the Recoil Effect Using Saturated Absorption Spectroscopy. *Phys. Rev. Lett.*, 37:1339–1342, 1976.

[555] M R Aliev, D N Kozlov, and V V Smirnov. Coherent spectroscopy of high-resolution Raman-scattering of methane. *JETP Letters*, 26:27–29, 1977.

[556] H Berger. Raman spectrum of $^{12}CH_4$ between 2850 and 3100 cm^{-1}. *J. Mol. Spectrosc.*, 66:55–61, 1977.

[557] Jean-Paul Champion. Développement complet de l'hamiltonien de vibration–rotation adapté à l'étude des interactions dans les molécules toupies sphériques. Application aux bandes ν_2 et ν_4 de $^{12}CH_4$. *Can. J. Phys.*, 55:1802–1828, 1977.

[558] R. A. Toth, L. R. Brown, and R. H. Hunt. Line positions and strengths of methane in the 2862 to 3000 cm $^{-1}$ region. *J. Mol. Spectrosc.*, 67:1–33, 1977.

[559] B Bobin and G Guelachvili. Analyse de la bande de combinaison (ν_3+ ν_4) du méthane $^{12}CH_4$. *Journal de Physique*, 39:33–42, 1978.

[560] A Chedin, N Husson, N A Scott, and D Gautier. $\nu 4$ band of methane ($^{12}CH_4$ and $^{13}CH_4$). Line parameters and evaluation of Jovian atmospheric transmission at 7.7 μm. *J. Mol. Spectrosc.*, 71:343–368, 1978.

[561] Robert H Hunt, Linda R Brown, and Robert A Toth. Line intensities of methane in the 2700–2862-cm^{-1} region. *J. Mol. Spectrosc.*, 69:482–485, 1978.

[562] A D May, M A Henesian, and R L Byer. The CW coherent anti-Stokes Raman spectrum of the ν_1 band of CH_4 and its pressure dependence. *Can. J. Phys.*, 56:248–250, 1978.

[563] A. Owyoung, C. W. Patterson, and R. S. McDowell. CW Stimulated Raman Gain Spectroscopy of the v_4 Fundamental of Methane. *Chem. Phys. Lett.*, 59:156–162, 1978.

[564] Irving Ozier and Arieh Rosenberg. The vibrationally induced rotational spectrum of CH_4 in the $v_4 = 1$ state. *J. Chem. Phys.*, 69:5203–5204, 1978.

[565] R D Blatherwick, A Goldman, BL Lutz, P M Silvaggio, and R W Boese. Infrared methane spectra between 1120 cm^{-1} and 1800 cm^{-1}: a new atlas. *Appl. Optics*, 18:3798–3804, 1979.

[566] J P Boquillon and R Bregier. High-Resolution Coherent Stokes Raman-Spectroscopy of the ν_1 and ν_3 Bands of Methane. *Appl. Phys.*, 18:195–198, 1979.

[567] D. L. Gray and A. G. Robiette. The anharmonic force field and equilibrium structure of methane. *Mol. Phys.*, 37:1901–1920, 1979.

[568] D L Gray, A G Robiette, and A S Pine. Extended Measurement and Analysis of the ν_3-Infrared Band of Methane. *J. Mol. Spectrosc.*, 77:440–456, 1979.

[569] D N Kozlov, A M Prokhorov, and V V Smirnov. Methane-$\nu_1(A_1)$ Vibrational-State Rotational Structure Obtained from High-Resolution CARS-Spectra of the Q-Branch. *J. Mol. Spectrosc.*, 77:21–28, 1979.

[570] J P Champion, G Pierre, H Berger, and J Cadot. Vibration-Rotation Energies of Harmonic and Combination Levels in Tetrahedral XY_4 Molecules - Anal-

ysis of the $2\nu_2$ and $\nu_2+\nu_4$ Bands of $^{12}CH_4$. *J. Mol. Spectrosc.*, 79:281–294, 1980.

[571] J C Hilico, J Degni, J P Champion, and G Guelachvili. Analysis of the $\nu_2+\nu_3$ band of $^{12}CH_4$ and $^{13}CH_4$. *J. Mol. Spectrosc.*, 81:277–302, 1980.

[572] D E Jennings. Intermode Calibration of Diode-Laser Spectra Using Tandem Étalons. *Appl. Optics*, 19:2–4, 1980.

[573] G S Orton and A G Robiette. A line parameter list for the v_2 and v_4 Bands of $^{12}CH_4$ and $^{13}CH_4$, extended to $J^{'}=25$ and its application to planetary-atmospheres. *J. Quant. Spectrosc. Radiat. Transf.*, 24:81–95, 1980.

[574] J J Valentini, P Esherick, and A Owyoung. Use of a Free-Expansion Jet in Ultra-High-Resolution Inverse Raman-Spectroscopy. *Chem. Phys. Lett.*, 75:590–592, 1980.

[575] S Gherissi, A Henry, M Loete, and A Valentin. Transition-Moment and Line Strengths of the ν_3 Band of $^{12}CH_4$. *J. Mol. Spectrosc.*, 86:344–356, 1981.

[576] R H Hunt, L R Brown, R A Toth, and J W Brault. Line Assignments and Intensities for the $\nu_3+\nu_4-\nu_4$ Band of $^{12}CH_4$. *J. Mol. Spectrosc.*, 86:170–183, 1981.

[577] I Ozler, M C L Gerry, and A G Robiette. Microwave spectra of molecules of astrophysical interest. XX. Methane. *J. Phys. Chem. Ref. Data*, 10:1085–1095, 1981.

[578] A G Robiette. Extended Assignment and Analysis of the ν_2 and ν_4 Infrared Bands of $^{12}CH_4$. *J. Mol. Spectrosc.*, 86:143–158, 1981.

[579] R A Toth, L R Brown, R H Hunt, and L S Rothman. Line Parameters of Methane from 2385 to 3200 cm^{-1}. *Appl. Optics*, 20:932–935, 1981.

[580] L. R. Brown and L. S. Rothman. Methane Line Parameters for the 2.3 μm Region. *Appl. Optics*, 21:2425–2427, 1982.

[581] L R Brown, R A Toth, A G Robiette, JE Lolck, R H Hunt, and J W Brault. Analysis of the ν_1 and $\nu_2 + \nu_4$ Bands of $^{12}CH_4$. *J. Mol. Spectrosc.*, 93:317–350, 1982.

[582] J E Lolck, S Brodersen, and A G Robiette. The $2\nu_4$ Isotropic and Anisotropic Raman Bands of CH_4. *J. Raman Spectrosc.*, 12:49–62, 1982.

[583] B L Lutz, C Pierre, G Pierre, and J P Champion. Quantum Assignments and Intensity Measures for Methane between 1100 and 1800 cm^{-1} - a Comparison between Theory and Experiment. *ApJS*, 48:507–530, 1982.

[584] G Restelli and F Cappellani. Tunable Diode-Laser Measurements of Spectral Intensities in the ν_4 Band of $^{12}CH_4$. *Chem. Phys. Lett.*, 92:439–442, 1982.

[585] G Poussigue, E Pascaud, J P Champion, and G Pierre. Rotational Analysis of Vibrational Polyads in Tetrahedral Molecules - Simultaneous Analysis of the Pentad Energy-Levels of $^{12}CH_4$. *J. Mol. Spectrosc.*, 93:351–380, 1982.

[586] L R Brown, J S Margolis, R H Norton, and B D Stedry. Computer Measurement of Line Strengths with Application to the Methane Spectrum. *Appl. Spectrosc.*, 37:287–292, 1983.

[587] H Frunder, D Illig, H Finsterholzl, H W Schrotter, B Lavorel, G Roussel, J C Hilico, J P Champion, G Pierre, G Poussigue, and E Pascaud. Revised Analysis of the Structure of the ν_1 Band of Methane. *Chem. Phys. Lett.*, 100:110–114, 1983.

[588] P Varanasi, L P Giver, and F P J Valero. Intensity Measurements in the ν_4-Fundamental of $^{13}CH_4$ at Planetary Atmospheric Temperatures. *J. Quant. Spectrosc. Radiat. Transf.*, 30:491–495, 1983.

[589] L R Brown and R A Toth. Comparison of the frequencies of NH_3, CO_2, H_2O, N_2O, CO, and CH_4 as infrared calibration standards. *J. Opt. Soc. Am. B*, 2:842–856, 1985.

[590] H Graener and A Laubereau. High-Resolution Fourier-Transform Raman-Spectroscopy with Ultrashort Laser-Pulses. *Optics Comms.*, 54:141–146, 1985.

[591] M M Thiery, D Fabre, and K Kobashi. Raman-Spectra of Solid CH_4 under High-Pressure. III. New High-Pressure Phases in Solid CH_4 and CD_4. *J. Chem. Phys.*, 83:6165–6172, 1985.

[592] C E Keffer, C P Conner, and W H Smith. Pressure broadening of methane lines in the 6190 Å and 6825 Å bands at room and lowtemperatures. *J. Quant. Spectrosc. Radiat. Transf.*, 35:495–499, 1986.

[593] K Kim. Integrated infrared intensities of methane. *J. Quant. Spectrosc. Radiat. Transf.*, 37:107–110, 1987.

[594] V G Tyuterev, J P Champion, G Pierre, and V I Perevalov. Parameters of reduced hamiltonian and invariant parameters of interacting E and F_2 fundamentals of tetrahedral molecules - ν_2 and ν_4 bands of $^{12}CH_4$ and $^{28}Si_4$. *J. Mol. Spectrosc.*, 120:49–78, 1986.

[595] L R Brown, M Loete, and J C Hilico. Linestrengths of the ν_2 and ν_4 Bands of $^{12}CH_4$ and $^{13}CH_4$. *J. Mol. Spectrosc.*, 133:273–311, 1989.

[596] P. Varanasi and S. Chudamani. Measurements of collision-broadened line widths in the ν_4-fundamental band of $^{12}CH_4$ at low temperatures. *J. Quant. Spectrosc. Radiat. Transf.*, 41:335–343, 1989.

[597] P Varanasi and S Chudamani. The Temperature-Dependence of Lineshifts, Linewidths and Line-Intensities of Methane at Low-Temperatures. *J. Quant. Spectrosc. Radiat. Transf.*, 43:1–11, 1990.

[598] C Roche and J P Champion. Analysis of dyad - dyad transitions of $^{12}CH_4$ and $^{13}CH_4$. *Can. J. Phys.*, 69:40–51, 1991.

[599] L R Brown, J S Margolis, J P Champion, J C Hilico, J M JOUVARD, M Loete, C Chackerian, G Tarrago, and D C Benner. Methane and its isotopes - current status and prospects for improvement. *J. Quant. Spectrosc. Radiat. Transf.*, 48:617–628, 1992.

[600] A. S. Pine. Self-broadening, N_2-broadening, O_2-broadening, H_2-broadening, Ar-broadening, and He-broadening in the ν_3 band Q-branch of CH_4. *J. Chem. Phys.*, 97:773–785, 1992.

[601] J Santos, P Cancio, J L Domenech, J Rodriguez, and D Bermejo. Accurate wavenumber measurement in high-resolution stimulated Raman-spectroscopy (SRS) by using an infrared standard. ν_1 fundamental of $^{12}CH_4$. *Laser Chem.*, 12:53–63, 1992.

[602] M A H Smith, C P Rinsland, V M Devi, and D C Benner. Temperature-dependence of broadening and shifts of methane lines in the ν_4 band. *Spectroc. Acta Pt. A-Molec. Biomolec. Spectr.*, 48:1257–1272, 1992.

[603] O Ouardi, J C Hilico, M Loete, and L R Brown. The hot bands of methane between 5 and 10 μm. *J. Mol. Spectrosc.*, 180:311–322, 1996.

[604] C Wenger and J P Champion. Spherical top data system (STDS) software for the simulation of spherical top spectra. *J. Quant. Spectrosc. Radiat. Transf.*, 59:471–480, 1998.

[605] F Menard-Bourcin, L Doyennette, J Menard, and C Boursier. Time-resolved IR-IR double resonance measurements in methane excited to $2\nu_3$(F-2). *J. Phys. Chem.*, 104:5444–5459, 2000.

[606] K Nauta and R E Miller. Rotational and vibrational dynamics of methane in helium nanodroplets. *Chem. Phys. Lett.*, 350:225–232, 2001.

[607] J J O'Brien and H Cao. Absorption spectra and absorption coefficients for methane in the 750-940 nm region obtained by intracavity laser spectroscopy. *J. Quant. Spectrosc. Radiat. Transf.*, 75:323–350, 2002.

[608] M Gharavi and S G Buckley. Diode laser absorption spectroscopy measurement of linestrengths and pressure broadening coefficients of the methane $2\nu_3$ band at elevated temperatures. *J. Mol. Spectrosc.*, 229:78–88, 2005.

[609] D Mondelain, P Chelin, A Valentin, D Hurtmans, and C Camy-Peyret. Line profile study by diode laser spectroscopy in the $^{12}CH_4$ $\nu_2 + \nu_4$ band. *J. Mol. Spectrosc.*, 233:23–31, 2005.

[610] C Boursier, J Menard, A Marquette, and F Menard-Bourcin. Identification of hot band transitions of CH_4 near 3000 cm^{-1}. *J. Mol. Spectrosc.*, 237:104–114, 2006.

[611] Eric Jourdanneau, Tony Gabard, Frederic Chaussard, Robert Saint-Loup, Hubert Berger, Elena Bertseva, and Frederic Grisch. CARS methane spectra: Experiments and simulations for temperature diagnostic purposes. *J. Mol. Spectrosc.*, 246:167–179, 2007.

[612] S. Rudolph, G. Wollny, K. von Haeften, and M. Havenith. Probing collective excitations in helium nanodroplets: Observation of phonon wings in the infrared spectrum of methane. *J. Chem. Phys.*, 126:124318, 2007.

[613] E. H. Wishnow, G. S. Orton, I. Ozier, and H. P. Gush. The distortion dipole rotational spectrum of CH_4: A low temperature far-infrared study. *J. Quant. Spectrosc. Radiat. Transf.*, 103:102–117, 2007.

[614] Hiromichi Hoshina, Dmitry Skvortsov, Boris G. Sartakov, and andrey F. Vilesov. Rotation of methane and silane molecules in He droplets. *J. Chem. Phys.*, 132:074302, 2010.

[615] H. Tran, J.-M. Hartmann, G. Toon, L. R. Brown, C. Frankenberg, T. Warneke, P. Spietz, and F. Hase. The $2\nu_3$ band of CH_4 revisited with line mixing: Consequences for spectroscopy and atmospheric retrievals at 1.67 μm. *J. Quant. Spectrosc. Radiat. Transf.*, 111:1344–1356, 2010.

[616] Robert E. Zillich and K. Birgitta Whaley. Rotational spectra of methane and deuterated methane in helium. *J. Chem. Phys.*, 132:174501, 2010.

[617] M. Sanzharov, J. Vander Auwera, O. Pirali, P. Roy, J.-B. Brubach, L. Manceron, T. Gabard, and V. Boudon. Self and N_2 collisional broadening of far-infrared methane lines measured at the SOLEIL synchrotron. *J. Quant. Spectrosc. Radiat. Transf.*, 113:1874–1886, 2012.

[618] Yu Zhang, Fang-Rong Wang, Yan-Hui Zhao, Yi-Ding Wang, Tian Cui, Ru-Wen Kan, Li-Chun Wu, Tie-Qiang Zhang, and Yuan-Kun Zhang. Experiment research on ellipsoidal structure methane using the absorption characteristics of 3.31 μm mid-infrared spectroscopy. *Infrared Phys. Technol.*, 55:353–356, 2012.

[619] Vladimir Tyuterev, Sergei Tashkun, Michael Rey, Roman Kochanov, andrei Nikitin, and Thibault Delahaye. Accurate Spectroscopic Models for Methane Polyads Derived from a Potential Energy Surface Using High-Order Contact Transformations. *J. Phys. Chem. A*, 117:13779–13805, 2013.

[620] M. Rey, A. V. Nikitin, and Vl G. Tyuterev. Theoretical hot methane line lists up to T=2000 K for astrophysical applications. *ApJ*, 789:2, 2014.

[621] Kiu Liu, Lei Wang, Tu Tan, Guishi Wang, Weijun Zhang, Weidong Chen, and Xiaoming Gao. Highly sensitive detection of methane by near-infrared laser absorption spectroscopy using a compact dense-pattern multipass cell. *Sensors and Actuators B-Chemical*, 220:1000–1005, 2015.

[622] G. Magnotti, U. Kc, P. L. Varghese, and R. S. Barlow. Raman spectra of methane, ethylene, ethane, dimethyl ether, formaldehyde and propane for combustion applications. *J. Quant. Spectrosc. Radiat. Transf.*, 163:80–101, 2015.

[623] Michael Rey, Andrei V. Nikitin, and Vladimir G. Tyuterev. Convergence of normal mode variational calculations of methane spectra: Theoretical linelist

in the icosad range computed from potential energy and dipole moment surfaces. *J. Quant. Spectrosc. Radiat. Transf.*, 164:207–220, 2015.

[624] Andrei V. Nikitin, Alexander E. Protasevich, Michael Rey, and Vladimir G. Tyuterev. Highly excited vibrational levels of methane up to 10 300 cm^{-1}: Comparative study of variational methods (vol 149, 124305, 2018). *J. Chem. Phys.*, 149:159901, 2018.

[625] D. V. Petrov. Raman spectrum of methane in nitrogen, carbon dioxide, hydrogen, ethane, and propane environments. *Spectroc. Acta Pt. A-Molec. Biomolec. Spectr.*, 191:573–578, 2018.

[626] Michael Rey, andrei V. Nikitin, Bruno Bezard, Pascal Rannou, Athena Coustenis, and Vladimir G. Tyuterev. New accurate theoretical line lists of $^{12}CH_4$ and $^{13}CH_4$ in the 0-13400 cm^{-1} range: Application to the modeling of methane absorption in Titan's atmosphere. *Icarus*, 303:114–130, 2018.

[627] T. D. Butterworth, B. Amyay, D. V. D. Bekerom, A. V. D. Steeg, T. Minea, N. Gatti, Q. Ong, C. Richard, C. van Kruijsdijk, J. T. Smits, A. P. van Bavel, V. Boudon, and G. J. van Rooij. Quantifying methane vibrational and rotational temperature with Raman scattering. *J. Quant. Spectrosc. Radiat. Transf.*, 236:106562, 2019.

[628] T. Delahaye, M. Ghysels, J. T. Hodges, K. Sung, R. Armante, and H. Tran. Measurement and Modeling of Air-Broadened Methane Absorption in the MERLIN Spectral Region at Low Temperatures. *JGR-Atm*, 124:3556–3564, 2019.

[629] Ehsan Gharib-Nezhad, Alan N. Heays, Hans A. Bechtel, and James R. Lyons. H_2-induced pressure broadening and pressure shift in the P-branch of the ν_3 band of CH_4 from 300 to 655 K. *J. Quant. Spectrosc. Radiat. Transf.*, 239:106649, 2019.

[630] M. Kiseleva, J. Mandon, S. Persijn, and F. J. M. Harren. Accurate measurements of line strengths and air-broadening coefficients in methane around

1.66 μm using cavity ring down spectroscopy. *J. Quant. Spectrosc. Radiat. Transf.*, 224:9–17, 2019.

[631] Michele Gianella, Akshay Nataraj, Béla Tuzson, Pierre Jouy, Filippos Kapsalidis, Mattias Beck, Markus Mangold, andreas Hugi, Jérôme Faist, and Lukas Emmenegger. High-resolution and gapless dual comb spectroscopy with current-tuned quantum cascade lasers. *Opt. Express*, 28:6197–6208, 2020.

[632] V. D. Petrov, I. I. Matrosov, A. R. Zaripov, A. S. Tanichev, and A. A. Kobzev. Pressure dependence of peak position and shape of ν_1 methane Raman band. In G G Matvienko and O A Romanovskii, editors, *26th International Symposium On Atmospheric And Ocean Optics, Atmospheric Physics*, volume 11560 of *Proc. SPIE*, page 115600E, 2020.

[633] Arnaud Cuisset, Francis Hindle, Gaël Mouret, Robin Bocquet, Jonas Bruckhuisen, Jean Decker, Anastasiia Pienkina, Cédric Bray, Eric Fertein, and Vincent Boudon. Terahertz Rotational Spectroscopy of Greenhouse Gases Using Long Interaction Path-Lengths. *Appl. Sci.*, 11:1229, 2021.

[634] A. Farji, H. Aroui, and J. Vander Auwera. Air-induced collisional parameters in the ν_3 band of methane. *J. Quant. Spectrosc. Radiat. Transf.*, 275:107878, 2021.

[635] Aleksandra Foltynowicz, Lucile Rutkowski, Isak Silander, Alexandra C. Johansson, Vinicius Silva de Oliveira, Ove Axner, Grzegorz Soboń, Tadeusz Martynkien, Paweł Mergo, and Kevin K. Lehmann. Sub-Doppler Double-Resonance Spectroscopy of Methane Using a Frequency Comb Probe. *Phys. Rev. Lett.*, 126:063001, 2021.

[636] Et-touhami Es-sebbar and Aamir Farooq. Line-strengths, collisional coefficients and narrowing parameters in the ν_3 band of methane: H_2, He, N_2, O_2, Ar and CO_2 collider effects. *J. Quant. Spectrosc. Radiat. Transf.*, 272:107758, 2021.

[637] Ning Zhu, Ze Xu, Zhenhai Wang, Zihao Song, Weitian Wang, Xiaoliang Chen, and Xing Chao. Midinfrared Compressed Fourier-Transform Spectroscopy with an Optical Frequency Comb. *Phys. Rev. Appl.*, 18:024025, 2022.

[638] Francesco Mazza, Ona Thornquist, Leonardo Castellanos, Tom Butterworth, Cyril Richard, Vincent Boudon, and Alexis Bohlin. The ro-vibrational ν_2 mode spectrum of methane investigated by ultrabroadband coherent Raman spectroscopy. *J. Chem. Phys.*, 158:094201, 2023.

[639] S. Vasilchenko, T. Delahaye, S. Kassi, A. Campargue, R. Armante, H. Tran, and D. Mondelain. Temperature dependence of the absorption of the R(6) manifold of the $2\nu_3$ band of methane in air in support of the MERLIN mission. *J. Quant. Spectrosc. Radiat. Transf.*, 298:108483, 2023.

[640] A De Martino, R Frey, and F Pradere. Observation of the $\nu_3 - (2\nu_3, A_1)$ Band of Methane. *Chem. Phys. Lett.*, 100:329–333, 1983.

[641] Yu. S. Domnin, M. B. Koshelyayevsky, V. M. Tatarenkov, and P. S. Shumyatsky. He-Ne/CH4 laser frequency measurements (rus). *JETP Letters*, 34:175, 1981.

[642] Yu. S. Domnin, M. B. Koshelyayevsky, V. M. Tatarenkov, and P. S. Shumyatsky. Absolute measurements of frequencies of IR lasers (rus). *JETP Letters*, 30:273, 1979.

[643] Badr Amyay and Vincent Boudon. Vibration-rotation energy levels and corresponding eigenfunctions of $^{12}CH_4$ up to the tetradecad. *J. Quant. Spectrosc. Radiat. Transf.*, 219:85–104, 2018.

[644] A. V. Nikitin, I. S. Chizhmakova, M. Rey, S. A. Tashkun, S. Kassi, D. Mondelain, A. Campargue, and Vl. G. Tyuterev. Analysis of the absorption spectrum of $^{12}CH_4$CH4 in the region 5855-6250 cm^{-1} of the $2\nu_3$ band. *J. Quant. Spectrosc. Radiat. Transf.*, 203:341–348, 2017.

[645] K M Evenson, G W Day, J S Wells, and L O Mullen. Extension of Absolute Frequency Measurements to the cw He–Ne Laser at 88 THz (3.39 μ). *Appl. Phys. Letters*, 20:133–134, 1972.

[646] A Clairon, B Dahmani, and J Rutman. Accurate Absolute Frequency Measurements on Stabilized CO_2 and He-Ne Infrared-Lasers. *IEEE Transactions of Instrumentation and Measurement*, 29:268–272, 1980.

[647] A. Campargue, O. Leshchishina, D. Mondelain, S. Kassi, and A. Coustenis. An improved empirical line list for methane in the region of the $2\nu_3$ band at 1.66 μm. *J. Quant. Spectrosc. Radiat. Transf.*, 118:49–59, 2013.

[648] Rothman L. S. et al. The *HITRAN* 2012 molecular spectroscopic database. *J. Quant. Spectrosc. Radiat. Transf.*, 130:4 – 50, 2013.

[649] Yaye Awa Ba, Christian Wenger, Romain Surleau, Vincent Boudon, Maud Rotger, Ludovic Daumont, David A. Bonhommeau, Vladimir G. Tyuterev, and Marie-Lise Dubernet. MeCaSDa and ECaSDa: Methane and ethene calculated spectroscopic databases for the virtual atomic and molecular data centre. *J. Quant. Spectrosc. Radiat. Transf.*, 130:62–68, 2013.

[650] Michael Zhang, Kimberly Paragas, Jacob L Bean, Joseph Yeung, Yayaati Chachan, Thomas P Greene, Jonathan Lunine, and Drake Deming. Retrievals on NIRCam Transmission and Emission Spectra of HD 189733b with PLATON 6, a GPU Code for the JWST Era. *AJ.*, 169(1):38, 2024.

[651] Schleich, S., Boro Saikia, S., Changeat, Q., Güdel, M., Voigt, A., and Waldmann, I. Knobs and dials of retrieving JWST transmission spectra - I. The importance of P–T profile complexity. *A&A*, 690:A336, 2024.

[652] Stephen P. Schmidt, Ryan J. MacDonald, Shang-Min Tsai, Michael Radica, Le-Chris Wang, Eva-Maria Ahrer, Taylor J. Bell, Chloe Fisher, Daniel P. Thorngren, Nicholas Wogan, Erin M. May, Piero Ferrari, Katherine A. Bennett, Zafar Rustamkulov, Mercedes López-Morales, and David K. Sing. A

Comprehensive Reanalysis of K2-18 b's JWST NIRISS+NIRSpec Transmission Spectrum. *arXiv e-prints*, 2025.

[653] J. Roy-Perez, S. Pérez-Hoyos, N. Barrado-Izagirre, and H. Chen-Chen. The role of cloud particle properties in the WASP-39b transmission spectrum based on JWST/NIRSpec observations. *A&A*, 694:A249, 2025.

[654] Yui Kawashima, Hajime Kawahara, Yui Kasagi, Hiroyuki Tako Ishikawa, Kento Masuda, Takayuki Kotani, Tamoyuki Kudo, Teruyuki Hirano, Masayuki Kuzuhara, Stevanus K Nugroho, et al. Atmospheric retrieval of Subaru/IRD high-resolution spectrum of the archetype T-type brown dwarf Gl 229 B. *arXiv preprint arXiv:2410.11561*, 2024.

[655] N Husson, G Poussigue, A Valentin, and C Amiot. Étude de la bande $\nu_1 + \nu_4$ de $^{12}CH_4$ de 4136 à 4288 cm^{-1}. *Revue di Physique Applique*, 7:267–278, 1972.

[656] G Pierre, J C Hilico, C DeBergh, and J P Maillard. The Region of the $3\nu_3$ Band of Methane. *J. Mol. Spectrosc.*, 82:379–393, 1980.

[657] R H Hunt, J Lolck, A G Robiette, L R Brown, and R A Toth. Measurement and Analysis of the Infrared-Absorption Spectrum of the $2\nu_2$ Band of $^{12}CH_4$. *J. Mol. Spectrosc.*, 92:246–256, 1982.

[658] G Pierre, J P Champion, G Guelachvili, E Pascaud, and G Poussigue. Rotational Analysis of Vibrational Polyads in Tetrahedral Molecules - Line Parameters of the Infrared-Spectrum of $^{12}CH_4$ in the Range 2250-3260 cm^{-1} - Theory versus Experiment. *J. Mol. Spectrosc.*, 102:344–360, 1983.

[659] A De Martino, R Frey, and F Pradere. Double-Resonance Observation of the ($3\upsilon_3$,A1) State of Methane. *Chem. Phys. Lett.*, 111:113–116, 1984.

[660] J. C. Hilico, M. Loete, and L. R. Brown. Line Strengths of the $\nu_3 - \nu_4$ Band of Methane. *J. Mol. Spectrosc.*, 111:119–137, 1985.

[661] A De Martino, R Frey, and F Pradere. Double-Resonance Spectroscopy in Methane - Theoretical Vibration-Rotation Intensities and Experimental Investigation of the Lower ($3\nu_3$, F_2) Level. *Mol. Phys.*, 55:731–749, 1985.

[662] J. S. Margolis. Measured Line Positions and Strengths of Methane Between 5500 and 6180 cm^{-1}. *Appl. Optics*, 27:4038–4051, 1988.

[663] J. S. Margolis. Empirical Values of the Ground State Energies for Methane Transitions Between 5500 and 6150 cm^{-1}. *Appl. Optics*, 29:2295–2302, 1990.

[664] A Campargue, M Chenevier, and F Stoeckel. Intracavity-laser absorption spectroscopy of the visible overtone transition of methane in a supersonically cooled jet. *Chem. Phys. Lett.*, 183:153–157, 1991.

[665] A Lucchesini, I Longo, C Gabbanini, S Gozzini, and L Moi. Diode-Laser spectroscopy of methane overtone transitions. *Appl. Optics*, 32:5211–5216, 1993.

[666] K Boraas, Z Li, and J P Reilly. High-resolution study of methane's $3\nu_1 + \nu_3$ vibrational overtone band. *J. Chem. Phys.*, 100:7916–7927, 1994.

[667] A. Campargue, D. Permogorov, and R. Jost. Interactivity absorption spectroscopy of the third streching overtone transition of jet cooled methane. *J. Chem. Phys.*, 102:5910–5916, 1995.

[668] K Singh and J J O'Brien. Laboratory measurements of absorption-coefficients for the 727 nm band of methane at 77 K and comparison with results derived from spectra of the giants planets. *J. Quant. Spectrosc. Radiat. Transf.*, 54:607–619, 1995.

[669] T Tsukamoto and H Sasada. Extended assignments of the $3\nu_1 + \nu_3$ band of methane. *J. Chem. Phys.*, 102:5126–5140, 1995.

[670] K Singh and J J O'Brien. Absorption coefficients for the 727 nm band of methane at 77 K determined by intracavity laser spectroscopy. *Astrophys. Space Sci.*, 236:97–109, 1996.

[671] A. S. Pine. N_2 and Ar broadening and line mixing in the P and R branches of the ν_3 band of CH_4. *J. Quant. Spectrosc. Radiat. Transf.*, 57:157–176, 1997.

[672] C Boussin, L Regalia, JJ Plateaux, and A Barbe. Line intensities and self-broadening coefficients for methane lines between 5500 and 6180 cm^{-1} retrieved with a multispectrum fitting technique. *J. Mol. Spectrosc.*, 191:381–383, 1998.

[673] R Nassar and P Bernath. Hot methane spectra for astrophysical applications. *J. Quant. Spectrosc. Radiat. Transf.*, 82:279–292, 2003.

[674] A. Lucchesini and S. Gozzini. Methane diode laser overtone spectroscopy at 840 nm. *J. Quant. Spectrosc. Radiat. Transf.*, 103:209–216, 2007.

[675] C. Frankenberg, T. Warneke, A. Butz, I. Aben, F. Hase, P. Spietz, and L. R. Brown. Pressure broadening in the $2\nu_3$ band of methane and its implication on atmospheric retrievals. *Atmos. Chem. Phys.*, 8:5061–5075, 2008.

[676] Samir Kassi, Bo Gao, Daniele Romanini, and Alain Campargue. The near-infrared (1.30-1.70 μm) absorption spectrum of methane down to 77 K. *Phys. Chem. Chem. Phys.*, 10:4410–4419, 2008.

[677] Bo Gao, Samir Kassi, and Alain Campargue. Empirical low energy values for methane transitions in the 5852-6181 cm^{-1} region by absorption spectroscopy at 81 K. *J. Mol. Spectrosc.*, 253:55–63, 2009.

[678] Alain Campargue, Le Wang, Samir Kassi, Milan Masat, and Ondrej Votava. Temperature dependence of the absorption spectrum of CH_4 by high resolution spectroscopy at 81 K: (II) The icosad region (1.49-1.30 μm). *J. Quant. Spectrosc. Radiat. Transf.*, 111:1141–1151, 2010.

[679] D. Mondelain, S. Kassi, L. Wang, and A. Campargue. The 1.28 μm transparency window of methane (7541-7919 cm^{-1}): empirical line lists and temperature dependence (80 K-300 K). *Phys. Chem. Chem. Phys.*, 13:7985–7996, 2011.

[680] Le Wang, Didier Mondelain, Samir Kassi, and Alain Campargue. The absorption spectrum of methane at 80 and 294 K in the icosad (6717-7589 cm^{-1}): Improved empirical line lists, isotopologue identification and temperature dependence. *J. Quant. Spectrosc. Radiat. Transf.*, 113:47–57, 2012.

[681] Gao Wei, Chen Wei-Dong, Zhang Wei-Jun, Yuan Yi-Qian, and Gao Xiao-Ming. Low temperature laser absorption spectra of methane in the near-infrared at 1.65 μm for lower state energy determination. *Chinese Phys. B*, 21:014211, 2012.

[682] Milan Masat, Petr Pracna, Didier Mondelain, Samir Kassi, Alain Campargue, and Ondrej Votava. Spectroscopy of jet-cooled methane in the lower icosad region: Empirical assignments of low-J '' spectral lines from two-temperature analysis. *J. Mol. Spectrosc.*, 291:9–15, 2013.

[683] Serge Beguier, Samir Kassi, and Alain Campargue. An empirical line list for methane in the 1.25 μm transparency window. *J. Mol. Spectrosc.*, 308:1–5, 2015.

[684] S. Beguier, A. W. Liu, and A. Campargue. An empirical line list for methane near 1 μm (9028 – 10435 cm^{-1}). *J. Quant. Spectrosc. Radiat. Transf.*, 166:6–12, 2015.

[685] M. Ghysels, S. Vasilchenko, D. Mondelain, S. Beguier, S. Kassi, and A. Campargue. Laser absorption spectroscopy of methane at 1000 K near 1.7 μm: A validation test of the spectroscopic databases. *J. Quant. Spectrosc. Radiat. Transf.*, 215:59–70, 2018.

[686] V. I. Serdyukov, L. N. Sinitsa, A. A. Lugovskoi, and N. M. Emel'yanov. The $^{12}CH_4$ absorption spectra at 296 K and 200 K in the range between 6000

and 9000 cm^{-1}. In G G Matvienko and O A Romanovskii, editors, *24th International Symposium On Atmospheric And Ocean Optics, Atmospheric Physics*, volume 10833 of *Proc. SPIE*, page 1083309. SPIE, 2018.

[687] Andy Wong, Peter F. Bernath, Michael Rey, Andrei V Nikitin, and Vladimir G. Tyuterev. Atlas of Experimental and Theoretical High-temperature Methane Cross Sections from T=295 to 1000 K in the Near-infrared. *ApJS*, 240:4, 2019.

[688] Lei Yang, Hong Lin, Mark Plimmer, Xiao-Juan Feng, Hong-Wei Chu, Yong-Jian Ma, Jing-Ting Luo, Hui-Bin Sun, and Jin-Tao Zhang. Possible two-photon absorption in the near-infrared region observed by cavity ring-down spectroscopy. *Opt. Express*, 28:39128–39136, 2020.

[689] Nathan A. Malarich, David Yun, Keeyoon Sung, Scott Egbert, Sean C. Coburn, Brian J. Drouin, and Gregory B. Rieker. Dual frequency comb absorption spectroscopy of CH_4 up to 1000 Kelvin from 6770 to 7570 cm^{-1}. *J. Quant. Spectrosc. Radiat. Transf.*, 272:107812, 2021.

[690] A Lucchesini. Diode laser overtone spectroscopy of methane at 780 nm. *arXiv:2202.02187*, 2022.

[691] A. Campargue, E. V. Karlovets, S. S. Vasilchenko, and M. Turbet. The high resolution absorption spectrum of methane in the 10 800-14 000 cm^{-1} region: literature review, new results and perspectives. *Phys. Chem. Chem. Phys.*, 25:32778–32799, 2023.

[692] A. V. Nikitin, M. Rey, A. Campargue, and V. G. Tyuterev. First assignments of the $6\nu_4$, ν_2+$5\nu_4$, and ν_1+$4\nu_4$ Triacontad band system of $^{12}CH_4$ in the 7606-7919 cm^{-1} region. *J. Quant. Spectrosc. Radiat. Transf.*, 325:109098, 2024.

[693] A. V. Nikitin, A. A. Solodov, A. E. Protasevich, M. Rey, A. M. Solodov, and V. G. Tyuterev. Improved line list of methane in the 900–1050 cm^{-1} region. *J. Quant. Spectrosc. Radiat. Transf.*, 331:109286, 2025.

[694] Lovis, C., Snellen, I., Mouillet, D., Pepe, F., Wildi, F., Astudillo-Defru, N., Beuzit, J.-L., Bonfils, X., Cheetham, A., Conod, U., Delfosse, X., Ehrenreich, D., Figueira, P., Forveille, T., Martins, J. H. C., Quanz, S. P., Santos, N. C., Schmid, H.-M., Ségransan, D., and Udry, S. Atmospheric characterization of Proxima b by coupling the SPHERE high-contrast imager to the ESPRESSO spectrograph. *A&A*, 599:A16, 2017.

[695] Rafael Riançо-Silva, Pedro Machado, Zita Martins, Emmanuel Lellouch, Jean-Christophe Loison, Michel Dobrijevic, João A. Dias, and José Ribeiro. A study of very high resolution visible spectra of Titan: Line characterisation in visible CH_4 bands and the search for C_3. *Planet Space Sci.*, 240:105836, 2024.

[696] Evgeniya Starikova, Keeyoon Sung, Andrei V. Nikitin, Michael Rey, and Vladimir Tyuterev. Assignment and modeling of $^{13}CH_4$ spectrum at 298 K in the lower part of the Tetradecad in the 4970–5300 cm^{-1} range. *J. Quant. Spectrosc. Radiat. Transf.*, 329:109196, 2024.

[697] Ana Glidden, Sara Seager, Janusz J. Petkowski, and Shuhei Ono. Can Isotopologues Be Used as Biosignature Gases in Exoplanet Atmospheres? *Life*, 13, 2023.

[698] Ulysse Marboeuf, Amaury Thiabaud, Yann Alibert, and Willy Benz. Isotopic ratios D/H and $^{15}N/^{14}N$ in giant planets. *MNRAS*, 475:2355–2362, 2017.